University of Strathclyde
Department of Mechanical and Aerospace Engineering

Friction stir welding simulation, optimization and design

XINGGUO ZHOU

A thesis presented in fulfilment of the requirements for the degree of Doctor of Philosophy
2013

Authenticity and copyright statement

This thesis is the result of the author's original research. It has been composed by the author and has not been previously submitted for examination which has led to the award of a degree.

Acknowledgements

First of all, I would like to express my sincere gratitude to my supervisors Professor Donald MacKenzie and Dr. Wenke Pan. Professor MacKenzie offers continuous support to my paper writing, thesis revision and other academic activities such as international conferences, offering numerous suggestions and guides to my research. In the past three years, Dr. Pan guides me step by step into the academic palace. I am also grateful for his help on my daily life, so that I can live peacefully in Glasgow, and concentrate on academic research.

My overseas tuition fees are covered by Overseas Research Student Award Scheme (ORSAS) for the first year and Scottish Research Student Award Scheme (SORSAS) for the later 2 years. In addition, Postgraduate Scholarship of University of Strathclyde offers me three year living expense.

Many thanks to Professor Ruidong Fu for offering friction stir welded AA2024 joints for research on small punch beam test, and Dr. Wenzhong Wu for offering help in nano-indentation test.

Thanks to my friends, Dr. Jianping Meng, Dr. Hongjun Li, Dr. Haihu Liu and Dr. Jun Hong, for both academic help and discussion and daily life help. The friendship forms a kind of mental support to me.

Thanks to my sister Dr. Yeyun Zhou and brother-in-law Dr. Rong Long, for their careful revision suggestions to my papers and continuous supporting during my PhD life.

Last but not least, endless thanks to my parents, for their understanding and endless support to my decision to study overseas.

Abstract

Friction stir welding is an advanced welding technology mainly used to join aluminum alloys but with potential for other materials like steel, titanium and its alloys. The aim of this work is to provide a combination of numerical and experiment tools to understand the mechanisms of friction stir welding, optimizing the friction stir welds and characterizing the material properties for welds.

The thesis is broadly divided into three themes. In the first theme, an automatic procedure to estimate friction stir welding model parameters, particularly those difficult to measure directly, is proposed and developed. The proposed methodology is seen to predict heat input power from the welding tool and contact conductivity between the workpiece and its supporting plate in good agreement with experimental temperature history data.

In the second theme, discontinuous and distributed cooling methods, which use periodical and non-uniformly distributed cooling medium flow to cool the welding workpieces, are proposed to reduce the residual stress of friction stir welds and investigated using multi-physics numerical simulation to predict transient temperature field, residual stress and mechanical performance of welds. The discontinuous cooling method is found to be more effective than conventional active cooling, leading to a lower drop in induced welding temperature and reduced residual stress. The distributed cooling provides another method to balance residual stress and welding temperature for butt welding. The effect of discontinuous cooling on microstructure is evaluated using the multi-physics model.

The third part presents small punch beam testing method to characterize material properties of base material, welded material and material property distribution. The small punch beam test utilizes miniaturized specimen and is therefore suited to measuring material properties in local regions of structure, such as the friction stir welding nugget.

Contents

Nomenclature

v: welding velocity, mm/s

t: time, second

X: coordinate of x axis on the welding path, mm

X_0: x axis coordinate of initial position on the welding path, mm

Y: coordinate of y axis on the welding path, mm

x: coordinate of x axis in the workpiece, mm

y: coordinate of y axis in the workpiece, mm

R: distance of a point in the workpiece to the welding tool center, mm

R_0: radius of the welding tool shoulder, mm

H: film coefficient, Wm^{-2}°C^{-1}

Q: total heat input power to the workpiece, W

R_p: radius of the welding tool probe, mm

F_x: friction force components at X direction, N

F_y: friction force components at Y direction, N

F_{total}: the Z axial force, N

Q1: heat flux to the workpiece, W

Q2: rounded film coefficient, Wm^{-2}°C^{-1}

q: heat rate, Wm^{-2}

λ: conductivity, Wm^{-1}°C^{-1}

c: specific heat, Jkg^{-1}°C^{-1}

ρ: density, kgm^{-3}

a: heat flux gradient, m^{2}s^{-1}

$\Phi(u)$: probability integral function, unitless

T: temperature, ^{0}C

δ: objective function for FSW model parameter identification, unitless

Dc: diameter of cooling nozzle, mm

Dt: diameter of the tool, mm

Dcc: centre to centre distance between cooling area and welding tool, mm

Wca: width of cooling area, mm

Lca: length of cooling area, mm

γ: cooling duty, unitless

Ref S1: reference longitudinal residual stress, MPa

Global S1: maximum longitudinal residual stress, MPa

Eff: effectiveness of cooling methods, $10^{-4}\mathrm{MPaW^{-1}m^{2}{}^{o}C}$

R_{trad}: trade-off ratio of cooling methods, unitless

Φ : objective function for SPBT, unitless

d_{LHS}: distance between sampling points in LHS method, unitless

List of Figures

List of Tables

1 Introduction

Friction Stir Welding, FSW, is a solid state joining process invented at The Welding Institute (TWI) in 1991 [1-1].

A typical FSW process consists of four stages: plunge stage, dwell stage, welding stage and retrieve stage, as shown in Figure 1-1. At the plunge stage, the rotating tool moves down to contact and slowly penetrate the workpiece. Temperature of the workpiece is relatively low at the beginning and the material is hard, and then the workpiece is softened by the heat generated by the welding tool. When material near the welding tool is hot enough, the welding tool moves along the welding path and the welding stage starts. At this stage, the material ahead of the tool is heated by friction and material plastic deformation occurs. For butt welds, the welding velocity is usually constant and the temperature field around the moving tool is almost quasi-static. At the end of welding path, the welding tool slows down the rotational speed and lifts up.

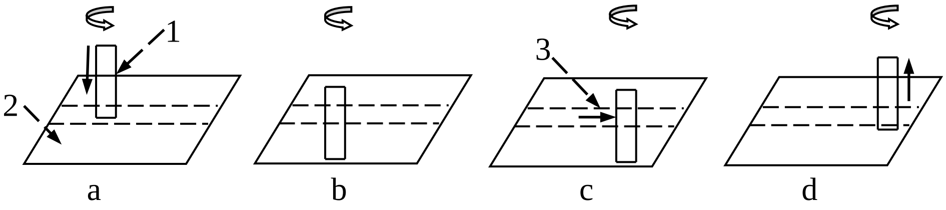

Figure 1-1 Stages of FSW

a: plunge stage, b: dwelling stage, c: welding stage, d: retrieve stage

1: welding tool, 2: workpiece 3: welding path

The rotational speed and travel velocity of the welding tool and the force applied along the rotation axial during the welding stage are significant process parameters. These parameters determine the frictional heat input rate into the workpiece. The welding tool may not be strictly vertical to the workpiece and could be with a tilt angle usually within 5 degrees to control material flow.

FSW has several advantages over conventional fusion welding, including no harmful electromagnetic radiation, no UV emission, low distortion, good mechanical properties and, particularly, the applicability to join high strength aluminum alloys such as the 2000 series. Applications of FSW [1-2]-[1-6] can be found in ship building, aerospace and railway industries etc., including panel joining, wing and fuselage manufacturing and high speed train construction.

A range of analytical and numerical models of the FSW process, or elements of the process, have been developed since it was introduced in 1991. Previously, the frictional heat energy generated between the welding tool and the workpiece was analytically modeled by researchers and then numerous finite element models (FEM) emerged, including thermal models and coupled thermal stress models, was applied to analysis of the transient temperature field and stress field. Computational Fluid Dynamics was also used to analyze the material flow in the vicinity of the welding tool.

The objective of the thesis research is to develop numerical and experimental methods to provide rapid and effective solutions to problems in FSW simulation, optimization and process design. This is achieved through research into three aspects of FSW: automatic identification of major process parameters; multi-physics simulation of the FSW process with active cooling to reduce residual stress and improve microstructure and development of a new method to characterize weld material properties.

In Chapter 2, a detailed review of previous research into FSW is presented, including thermal modeling, stress modeling, material flow modeling and mechanical properties modeling. Thermal source models, methodologies to calculate residual stress, material flow investigation methods and microstructure models are discussed.

In Chapter 3, methodologies employed in the following chapters are introduced, including FEM, genetic algorithms, artificial neural network algorithms and small punch beam testing.

In Chapter 4 a simplified thermal model for FSW is presented and a systematic and automatic procedure to identify model parameters such as thermal loads and boundary conditions is proposed. A genetic algorithm is developed to quantify the heat input power from the welding tool and heat loss rate from the workpiece to the backing plate through comparison of the predicted temperature history and experiment measurements.

Chapter 5 proposes novel discontinuous cooling and distributed cooling methods for controlling and reducing residual stress induced by the FSW process.

Chapter 6 includes an optimization oriented integrated model, incorporating a thermal stress model and a microstructure model for AA2024-T3, to investigate the effect of the discontinuous cooling method on microstructure evolution.

In Chapter 7, a novel weld material (plastic) property measurement system based on a small specimen test machine (small punch beam test) coupled with numerical model is presented. The small punch beam test is first applied to AA2024 base material with the aid of a genetic algorithm and then a neural network approach is introduced to characterize the average material properties of welds. The material property distribution is identified by virtual experiment in the third section.

In Chapter 8, the thesis concludes with a review of the main findings from the research reported and makes recommendations for future work.

1.1 References

[1-1] Thomas, WM; Nicholas, ED; Needham, JC; Murch, MG;Temple-Smith, P;Dawes, CJ.Friction-stir butt welding, GB Patent No. 9125978.8, International patent application No. PCT/GB92/02203, (1991)

[1-2] Qi, X, Chao, Y J (1999). "Heat transfer and Thermo-Mechanical analysis of FSW joining of 6061-T6 plates". 1st International Symposium on FSW (CD ROM). Thousand Oaks, USA: TWI.

[1-3] http://www.boeing.com/news/frontiers/archive/2004/september/i_tt.html

[1-4] http://www.airframer.com/news_story.html?release=8137

[1-5] S. W. Kallee, J. M. Kell, W. M. Thomas und C. S. Wiesner:"Development and implementation of innovative joining processes in the automotive industry", Paper presented at DVS Annual Welding Conference "Große Schweißtechnische Tagung", Essen, Germany, 12–14 September 2005.

[1-6] http://www.twi.co.uk/technical-knowledge/published-papers/trends-in-the-design-and-fabrication-of-rolling-stock-january-2007/

2 Literature Review

This thesis focuses on three aspects of FSW including numerical modelling, residual stress optimization and miniaturized test methods (small punch test). The numerical modelling procedures focus on aspects of thermal models, residual stress predictions, material flow investigations and mechanical property evaluations. Residual stress optimization is divided into process parameter optimization and additional methods to control residual stress. The small punch test method contains applications to characterize fracture, creep and fatigue behaviour of various materials.

2.1 Simulation

FSW is a complex thermo-mechanical process involving multi-discipline mechanisms, such as fluid dynamics and solid mechanics, including thermal and stress analysis. Several researchers have proposed various models to investigate heat transfer, residual stress, material flow, mechanical properties of welds, etc. to gain insight into the mechanisms of the process.

2.1.1 Heat transfer

Song [2-1] developed a heat source model for FSW in which the heat generated by the tool and workpiece interface was divided into two parts, one from the shoulder and another from the probe. The heat energy from the shoulder is assumed to be generated by frictional work and expressed as:

$$q_r = 2\pi\mu F_z rn \qquad 2\text{-}1$$

where q_r is the heat flux in a point with radius r to the tool centre, generated by friction in the shoulder/ workpiece interface, F_z is the axial load onto the shoulder and *n* is rotational speed of the tool.

The heat generation arises from frictional heating of the workpiece by the threaded and bottom surfaces of the probe and plastic deformation of material and is expressed as:

$$Q_p = 2\pi r_p hk\tau \frac{-V_m}{\sqrt{3}} + \frac{2\mu k\bar{\tau}\pi r_p hV_{rp}}{\sqrt{3(1+\mu^2)}} + \frac{4F_x\mu V_m cos\theta}{\pi} \qquad 2\text{-}2$$

where $\theta = 90° - \gamma - tan^{-1}(\mu)$, $V_m = \frac{r_p \omega sin\gamma}{sin(180° - \theta - \gamma)}$, $V_{rp} = \frac{r_p \omega sin\theta}{sin(180° - \theta - \gamma)}$, r_p is the pin's radius, h is workpiece's thickness, F_x is the translation force, $\bar{\tau}$ is the average shear stress of workpiece material, γ is the helix angle of pin's thread and k is the heat conductivity.

Vilaca *et al* [2-2] developed an analytic thermal model iSTIR for FSW, in which the asymmetric friction heat generation on the advancing and retreating sides is due to the combined rotation speed and welding velocity. Ignoring the material flow under the tool, the frictional velocity field is shown in Figure 2-1. Considering point A on advancing side and point B on retreating side for example, the velocities can be expressed as follow:

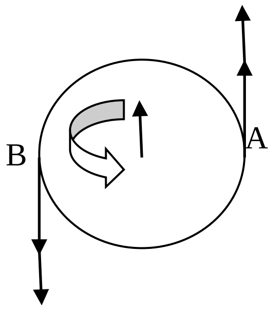

Figure 2-1 Velocity field for asymmetric friction heat

$$V_A = V_x + \omega R, V_B = V_x - \omega R \qquad 2\text{-}3$$

In addition to the analytic thermal source model, Colligan *et al* [2-50] proposed a conceptual model to clarify the relationship between the process parameters, such as rotation speed and welding velocity and the process outcomes, such as force and power, which are related to the thermal transfer model.

Mandal *et al* [2-4] modeled the plunge stage using FEM implemented in ABAQUS and the predicted temperature is compared to a simple experiment in a 'mining' machine. The frictional heat generation is calculated numerically. Johnson-Cook material model was applied and the predicted temperature was found to be in good agreement with experiment.

2.1.2 Residual stress

Chen *et al* [2-5] simulated thermal mechanical FWS of AA6061-T6 plates by FEM, including the mechanical force of the welding tool. Longitudinal stress, transverse stress and through thickness stress were predicted and compared to X-ray residual stress measurement as shown in Figure 2-2. The longitudinal residual stress was found to be greater than the transverse residual stress and higher welding velocity could induce higher longitudinal residual stress.

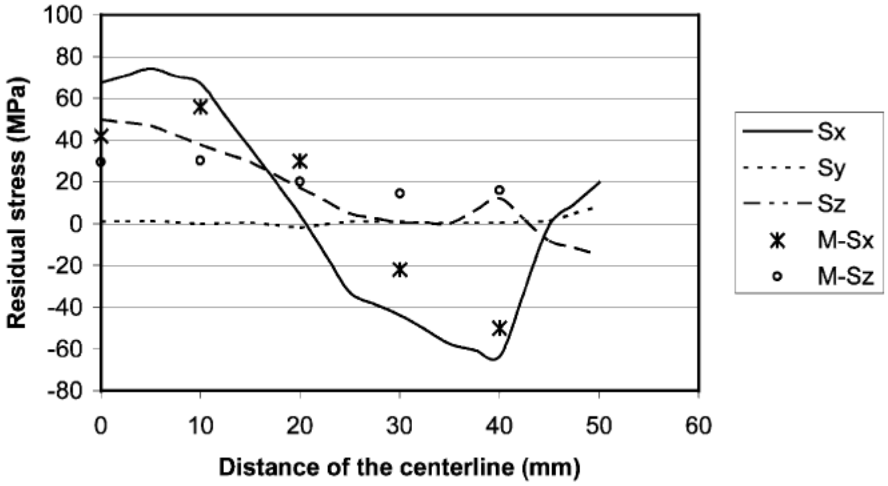

v=140 mm/min

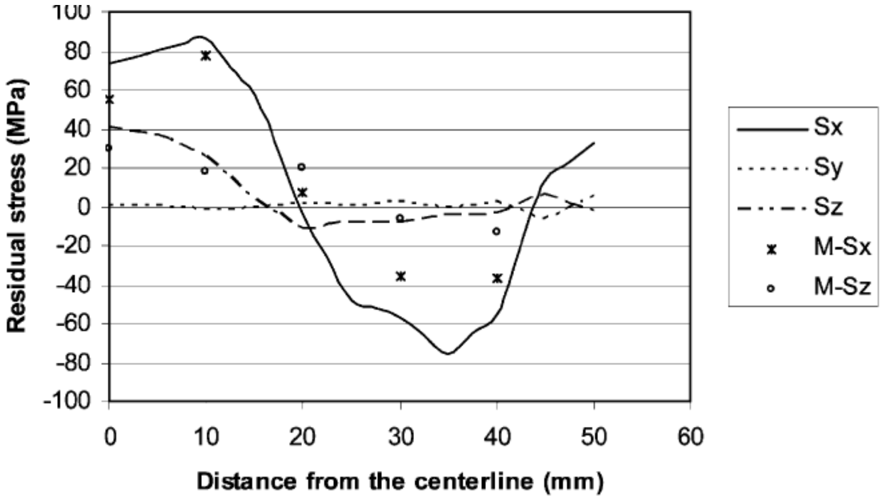

v=350 mm/min

Figure 2-2 [2-5] Predicted stress distribution and measured stresses

Sx: longitudinal stress, Sy: transverse stress, Sz: through thickness stress

M-Sx: measured longitudinal stress, M-Sz: measured through thickness stress

Zhu *et al* [2-6] used experimentally measured temperature at various locations to iteratively estimate the total heat input energy and a fictitious convection coefficient via inverse analysis, while simulating FSW for 304L steel. The predicted values of total heat input energy and fictitious convection coefficient are applied to a thermal mechanical model to calculate residual stress as shown in Figure 2-3. The calculated residual stress was consistent with experimental data. It was also pointed out that the fixture release was important in the computational model, as it significantly decreased residual stress.

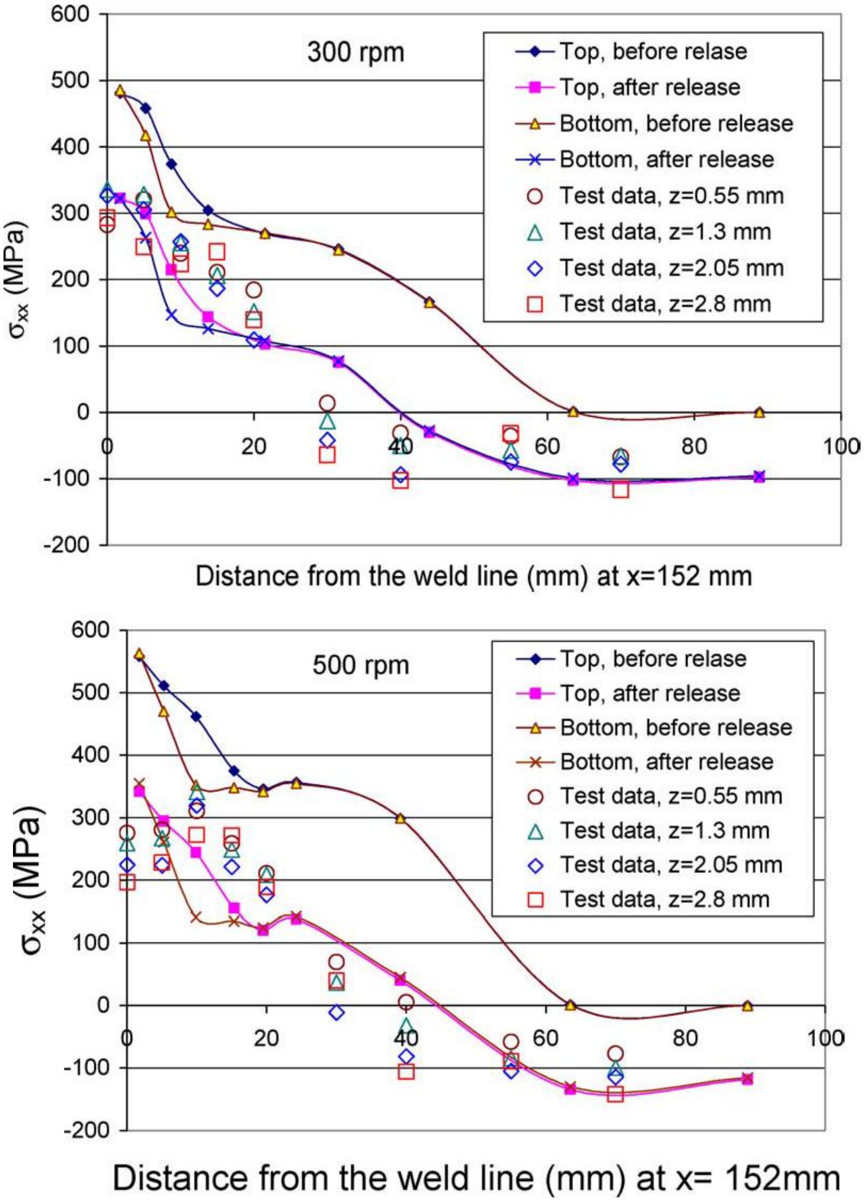

Figure 2-3 [2-6] Calculated longitudinal residual stress distribution from rotational speed 300 and 500 rpm and corresponding measured values.
X coordinates indicate the distance in the weld line from the workpiece edge.
Distance from weld line is transverse distance

Buffa *et al* [2-7] simulated Friction Stir Processing (FSP), which is similar to the FSW, but the tool used in FSP doesn't have a probe, with two different tools, one with a pin and the other without it. As shown in Figure 2-4, results indicated that the residual stresses occurring in friction stir processing operations are mainly determined by friction heat, especially the friction heat generated at the shoulder-workpiece interface.

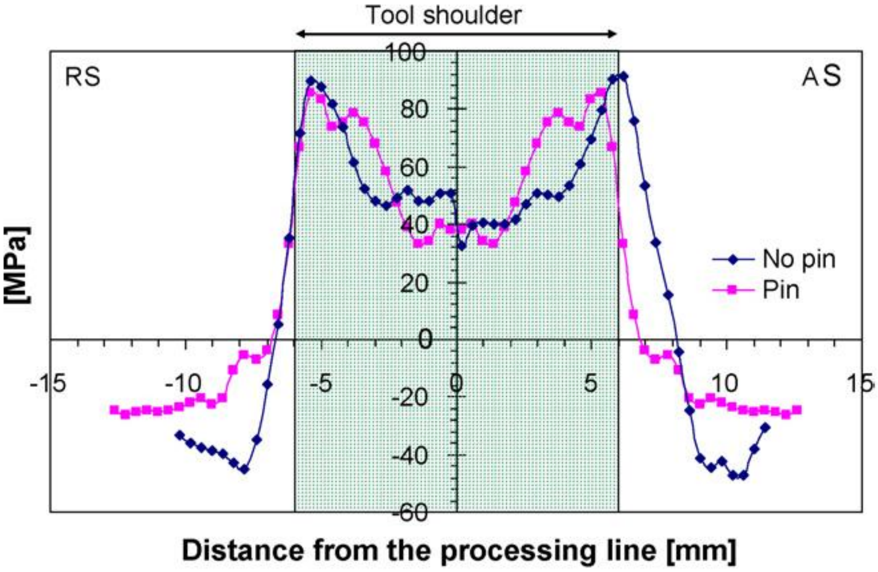

Figure 2-4 [2-7] Measured longitudinal residual stress distribution

Khandka *et al* [2-8] applied a sequentially coupled thermal mechanical model to three different materials; AA2024, AA6061 and SS304L. Thermal history was calculated first and then the temperature field history data was coupled to mechanical model to predict thermal stress in Figure 2-5. The longitudinal residual stress was found to be the biggest residual stress component in all three cases. In addition, the M profile (inverted V profile in some cases) of longitudinal residual stress was in good agreement data with published data.

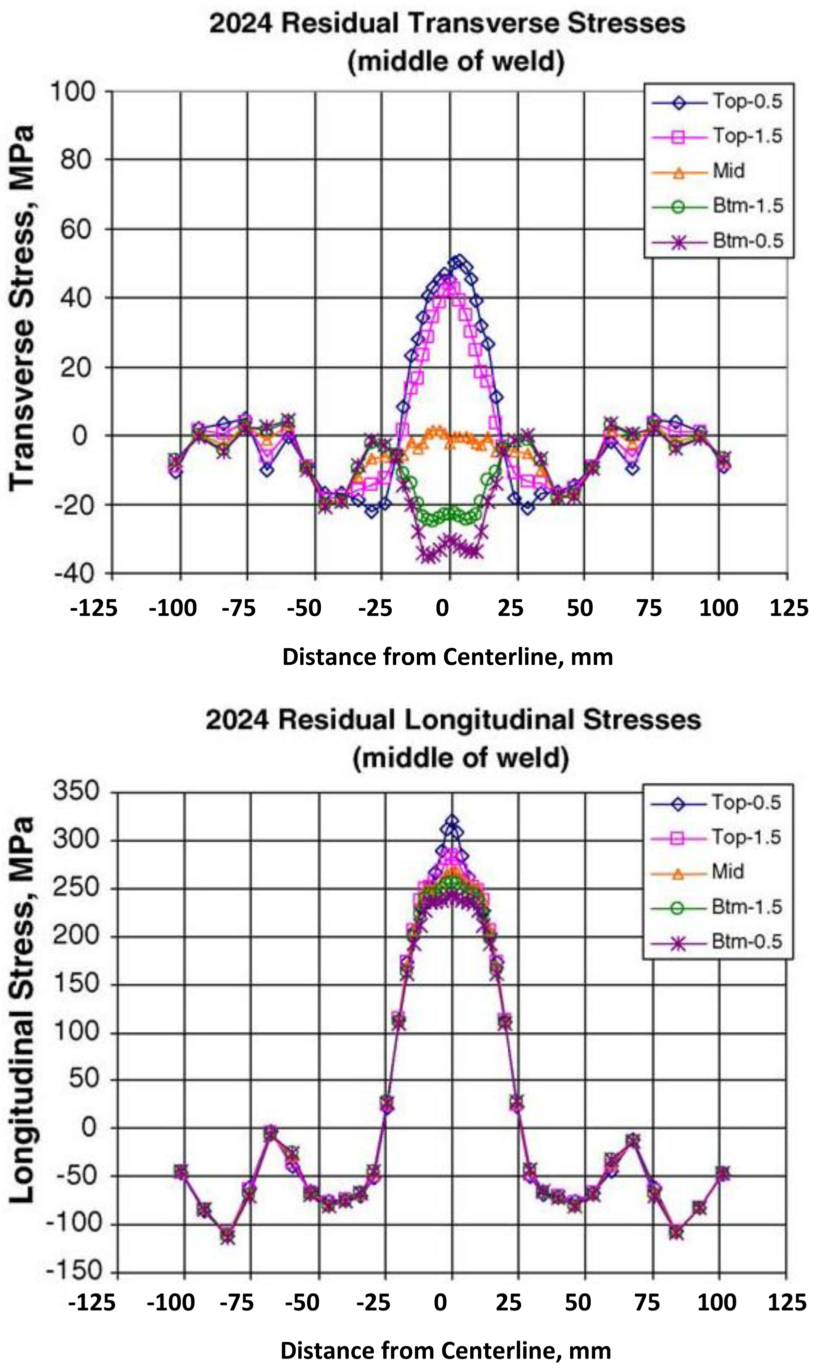

Figure 2-5 [2-8] Transverse and longitudinal residual stress for AA2024 FSW

Soundararajan *et al* [2-9] investigated the boundary conditions for an AA6061 FSW thermal mechanical model. The contact conductivity between the workpiece and the back plate was considered to be dependent on the interface pressure which is shown in Figure 2-6. In addition, thermal stress was found to be the dominant part of active stress. Figure 2-7 compared the temperature prediction with and without considering contact conductivity variation and indicated that the dependence on interface pressure is more reasonable.

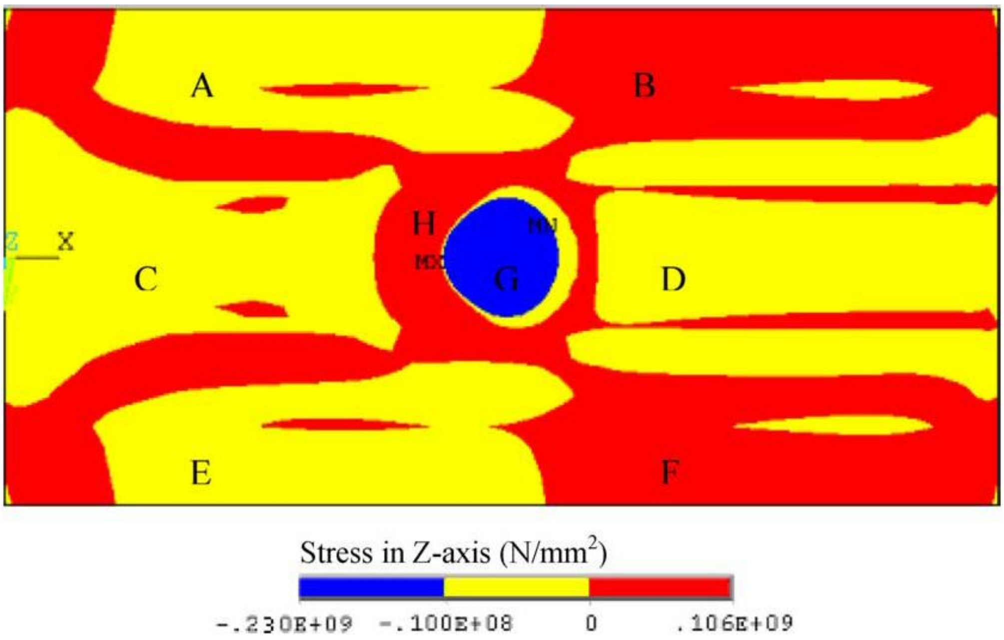

Figure 2-6 [2-9] Z axis stress distribution of material bottom plane

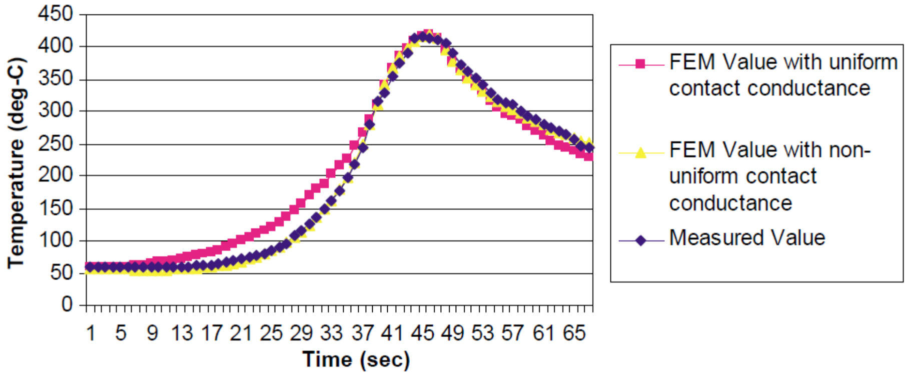

Figure 2-7 [2-9] Comparison of temperature history of uniform and non-uniform contact conductance FEM prediction

Bastier *et al* [2-10] built a 3D mixed finite element and fluid dynamic model to estimate material flow and temperature field. A sequentially steady state algorithm was employed to predict residual state based on a metallurgical model and the scheme is shown in Figure 2-8. The longitudinal residual stress profile agreed well with published experiment data.

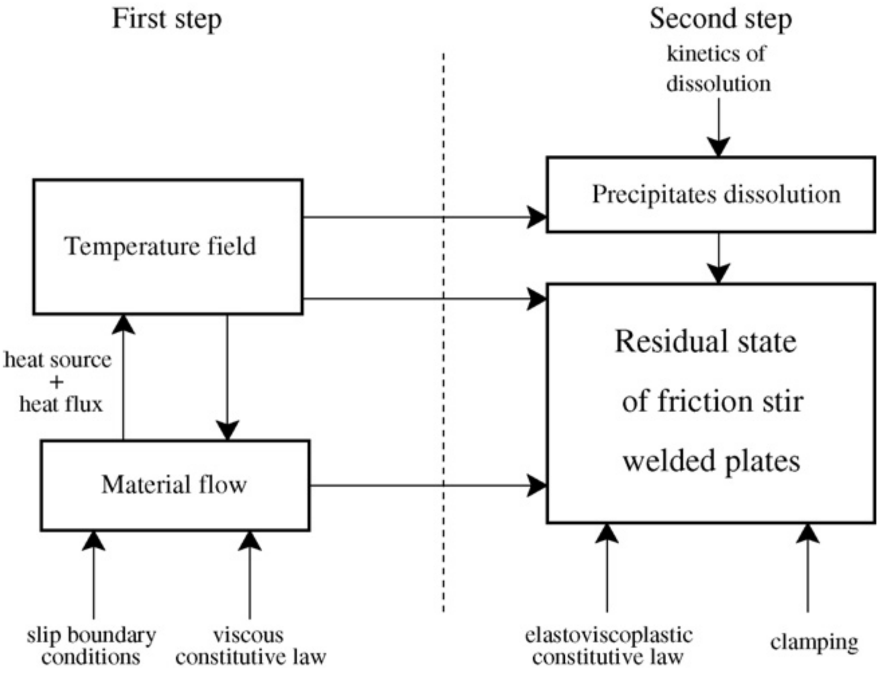

Figure 2-8 [2-10] Model structure

These studies showed that thermal stress is the main contribution to residual stress and longitudinal residual stress is usually bigger than other residual stress components. The M profile of longitudinal residual stress distribution is repeatedly reported.

2.1.3 Material flow

Zhang *et al* [2-11] examined the material flow using trace particles and residual stress and it was found that material in the advancing front side of welds rotated with the pin for several revolutions but the material in retreating side did not rotate with the pin. The location of maximum longitudinal residual stress occurred at R+1~2mm distance from the welding line, where R is the shoulder radius. And the maximum longitudinal residual stress increased with increasing welding velocity.

Colegrove *et al* [2-12] demonstrated the feasibility of computational fluid dynamics code FLUENT to analyze material flow in FSW to understand the effect of threaded tool, though the welding temperature and force were over predicted. Figure 2-9 illustrates the predicted material flow.

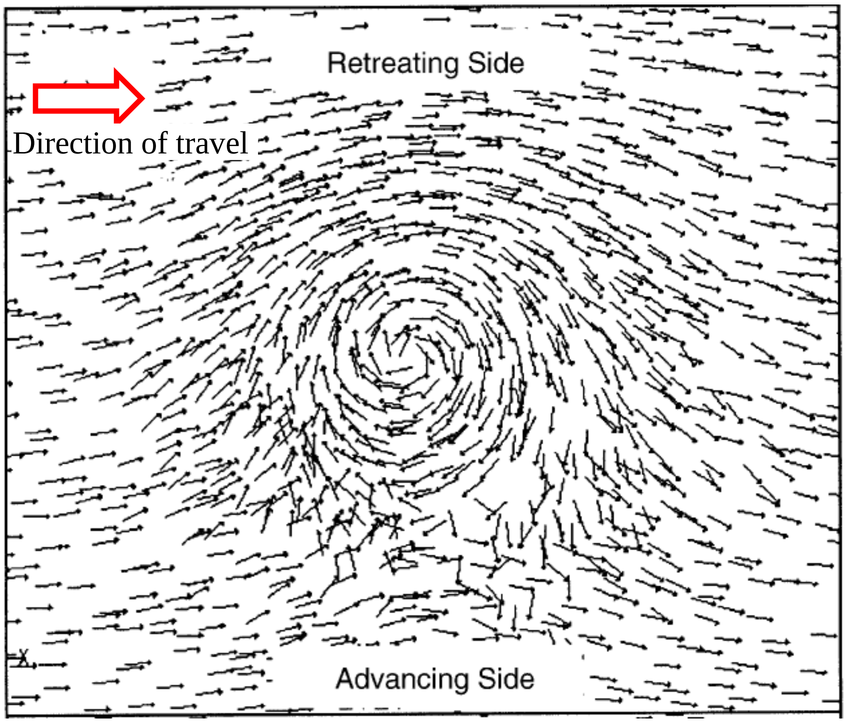

Figure 2-9 [2-12] Velocity field in the vicinity of the tool

Zhang *et al* [2-13] studied the material flow by using a nonlinear finite element technique. It was found that the material in front of the pin on the retreating side moved faster than that behind the pin on the retreating side and that tangent material flow was dominant. As shown in Figure 2-10, if the rotational speed or welding velocity is increased, the material flow speed could be increased.

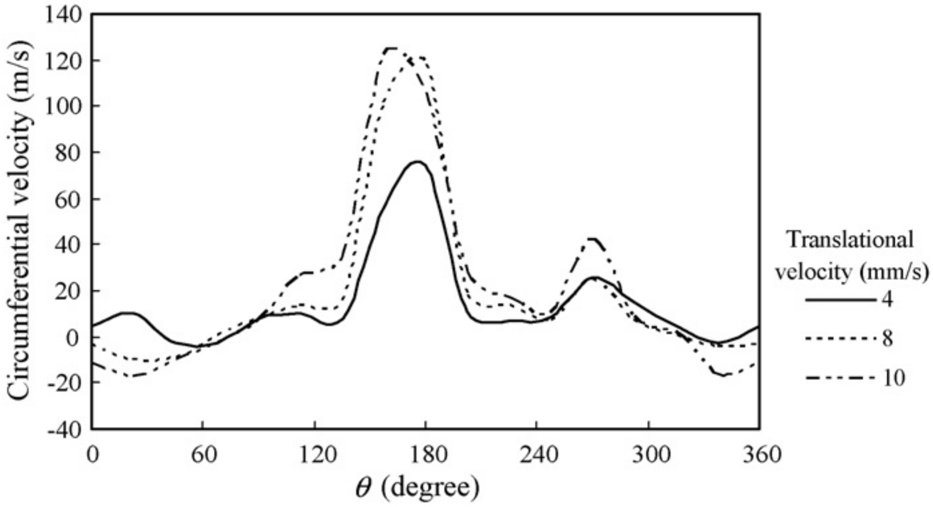

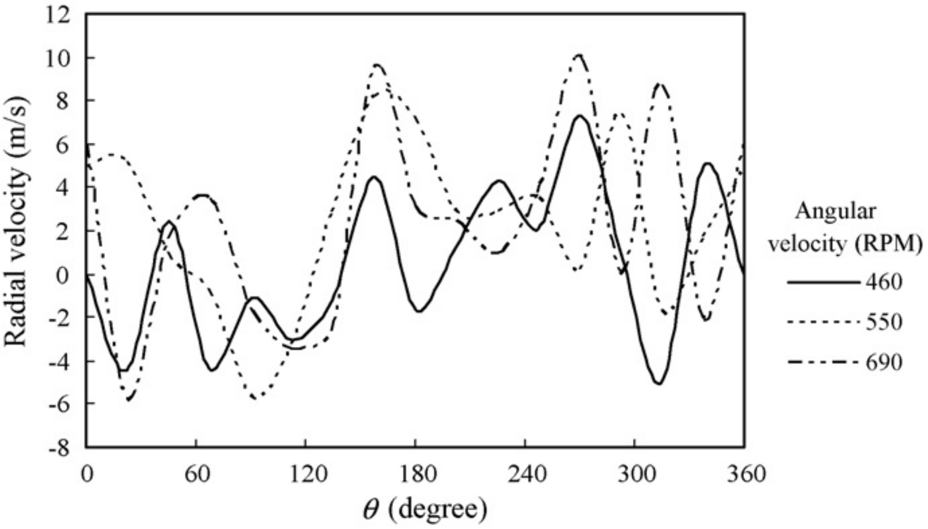

Figure 2-10 [2-13] Tangent and radial flow for material near the tool pin

Nanda *et al* [2-14] modeled the transient temperature field and material for AISI 1018 steel friction stir butt welding. As shown in Figure 2-11, the calculated temperature field was slightly asymmetric due to the friction heat difference in advancing side and retreating side. Plastic flow around the tool is severe and the streamline around the tool from top view was close to circular.

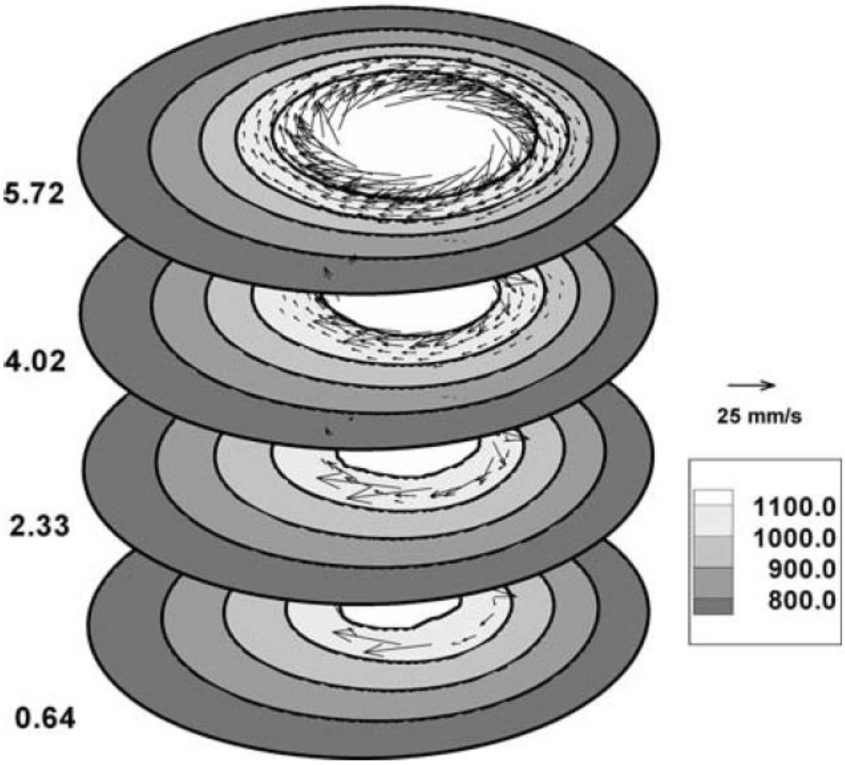

Figure 2-11 [2-14] Material flow velocity near the tool at various thicknesses

Deng *et al* [2-15] developed a plain strain 2D finite element model to simulate FSW progress for AA6061-T6 and the material flow was investigated. Though several assumptions were made, the prediction of post-weld marker positions compared well with experimental measurements as shown in Figure 2-12.

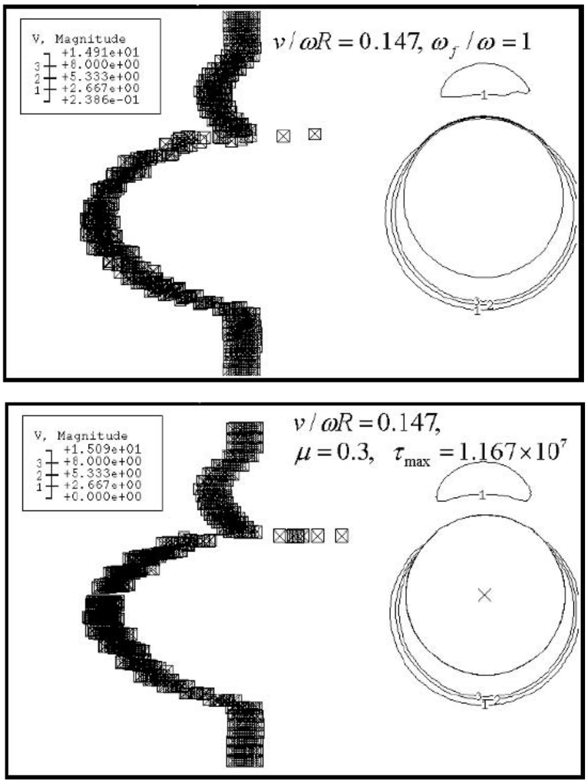

Figure 2-12 [2-15] Predicted and measured post-weld marker position: slipping interface model and frictional contact interface model

The material flow mainly occurs in the vicinity of the tool pin, where the strain rate is also large. Other locations away from the pin are not severely influenced by the pin or the shoulder and flow velocity is relatively small.

2.1.4 Mechanical properties

Boyce *et al* [2-16] proposed a multi scale simulation framework for FSW of polycrystalline material, namely a finite element model followed by crystal level microscopic model. The predicted shape profile matched well with experiments and the calculated lattice strain change was accurate compared to experimental results.

Okuyucu *et al* [2-17] applied an artificial neural network to FSW for aluminum plates and established a correlation between process parameters and mechanical properties. Structure of applied artificial neural network is shown in Figure 2-13. The tensile strength, yield strength, elongation, hardness of weld nugget and HAZ were mapped to welding velocity and rotational speed of the tool. High relevance between mechanical properties and process parameters were observed as all the R^2 values (coefficient of determination) were larger than 0.985.

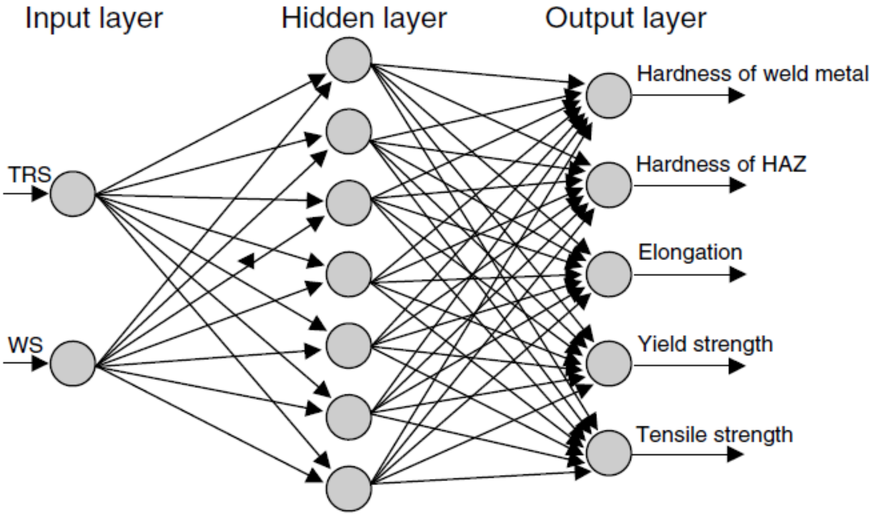

Figure 2-13 [2-17] Three layer neural network structure for mechanical properties prediction

Buffa *et al* [2-18] examined the continuous dynamic recrystallization occurring in FSW for 3mm thick AA7075-T6 blanks both experimentally and numerically. Two different analytical models were used to calculate the final average grain size in weld nugget zone and the predictions were found to be close to experimental measurement. AA6082-T6 [2-19] was also examined.

Kamp *et al* [2-20], [2-21] proposed a combined model for 7000 series aluminum alloy FSW, including a thermal model, a microstructure model and a structural model. The combined model was initially built and calibrated for AA7449 but then extended to another 7000 series alloy, AA7150. The microstructure was found to be highly dependent on peak temperature, heating rate and cooling rate experienced during thermal cycles. The predicted precipitation was in good agreement with measured particle size in most areas of welds.

Gallais *et al* [2-22] characterized and modeled the precipitation microstructures after FSW for AA6056 in both T4 and T78 initial temper states. No precipitation was found in the stir zone directly after welding and the lowest hardness zone could be resulted by coarse and extensive precipitation.

Heurtier *et al* [2-23] applied a semi-analytical model to estimate temperature field and micro hardness in various weld zones. The micro hardness model was based on thermal history of various weld zones and calibrated with heat treated samples experiencing the same thermal cycle corresponding to the weld zones. The predicted micro hardness distribution generally agrees with measured values.

Lockwood *et al* [2-24] [2-25] built a 2D finite element model based on measured full field strain and determined local constitutive data in various zones. The weld zones are assumed to composite material consisting of various thin materials, while the distribution in through thickness is assumed uniform for each zone. These studies of mechanical properties show that, in general, the mechanical property models capture the characteristics of the microstructure evolution during FSW and the microstructure evolution is dominated by thermal history except for the weld nugget zone and nearby.

2.2 Process optimization

2.2.1 Parameter optimization

Hattingh *et al* [2-26] investigated the correlation between tool geometry and tensile strength of 5083-H321 aluminum alloy friction stir welds. The flute number, depth and taper angle, pin diameter and taper and the pitch of thread were taken into account. It was found that the most successful tools were likely to incorporate three tapered flutes, a pin diameter taper and a pitch 10% of pin diameter and 15% of plate thickness.

Fernandez *et al* [2-27] studied tool wear and self-optimization during FSW for AL-SiC composite. It was found that welds become more homogeneous when the tool is optimally shaped.

Lombard *et al* [2-28] presented a systematic method to optimize FSW process parameters, including welding velocity and rotation speed of the tool. Figure 2-14 shows the scheme of the used method. The residual stress was experimentally measured by X-ray diffraction. The research indicated that the rotation speed is essential to tensile strength and fatigue performance.

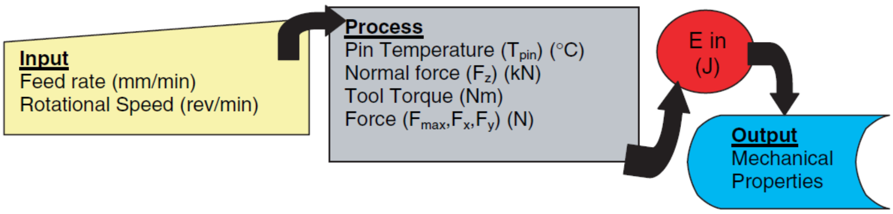

Figure 2-14 [2-28] Schematic relationship between input parameters and mechanical property outcomes

Amancio-Filho *et al* [2-29] examined process parameter optimization for dissimilar FSW, namely AA2024-T351 and 6056-T4. Welding velocity and rotation speed were taken into account in range of 150-400 mm/min and 500-1200 rpm. It was shown that in dissimilar FSW, the weaker component determined the performance of the joint.

Lakshminarayanan *et al* [2-30] applied the Taguchi approach to determine the most significant factors affecting tensile strength of FSW for RDE-40 aluminum alloy. Figure 2-15 shows the various process parameters considered and their relationship to ultimate strength. Three parameters, namely welding velocity, rotation speed of the tool and axial force were found to be significant to tensile strength of the joint.

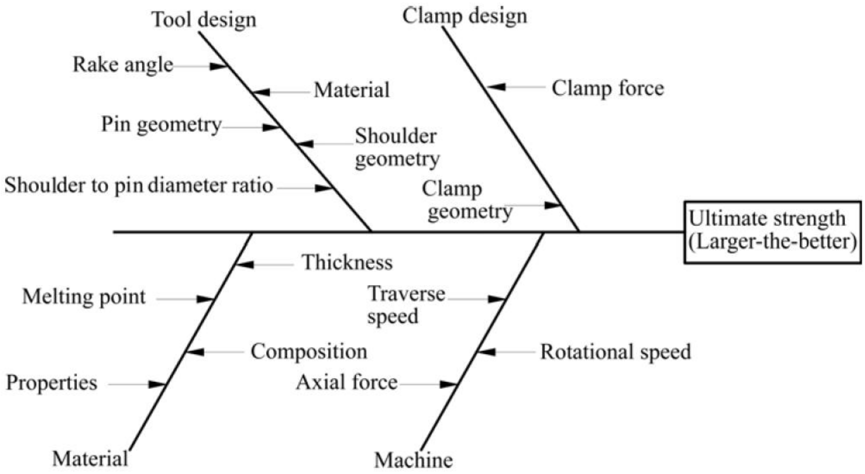

Figure 2-15 [2-30] Schematic of Taguchi approach for process parameter optimization

2.2.2 Other methods

Though adjusting process parameters helps to reduce residual stress and improve mechanical properties, introduction of additional means to further optimize FSW is necessary.

Staron *et al* [2-31] pointed out that performance of welded components, such as fatigue performance and corrosion performance, could be influenced by residual stress induced by FSW and applying mechanical tensioning to AA2024 sheet was attempted. Experimental results shown in Figure 2-16 indicated that compressive residual stress could be achieved in the weld by preloaded tensioning.

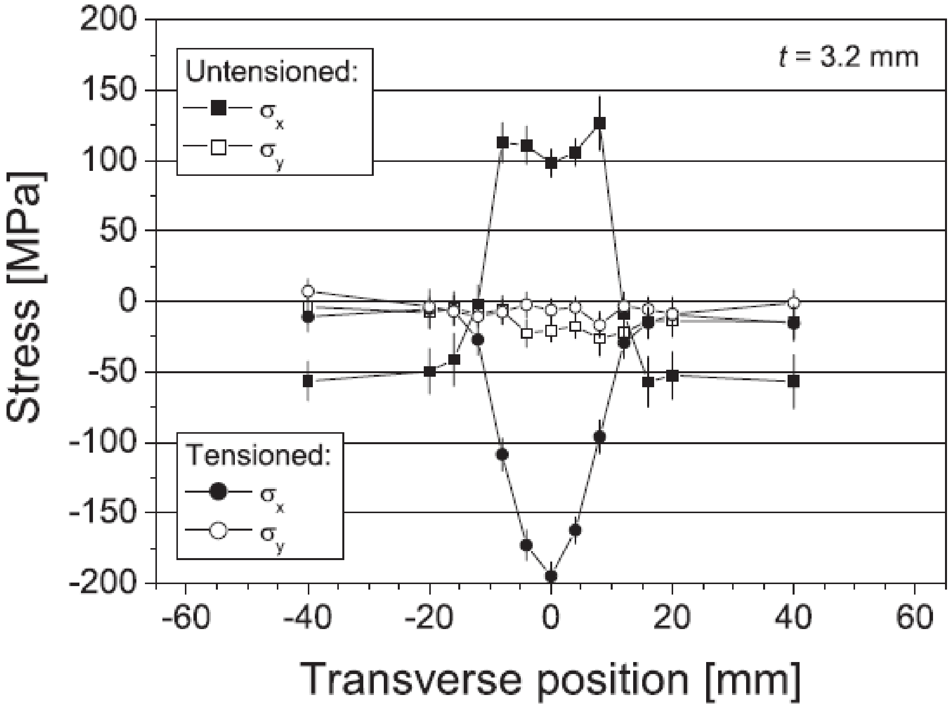

Figure 2-16 [2-31] Effect of applying preloaded mechanical tensioning in FSW. σx and σy are longitudinal and transverse residual stress respectively

Altenkirch *et al* [2-32] investigated the influence of mechanical tensioning and sectioning on residual stress. Around 35% of the yield strength of the base material at room temperature was applied to the workpieces. The welds were then sectioned into shorter length. It was found that applied load could reduce the longitudinal residual stress to almost zero and the residual stress was progressively relaxed by sectioning.

Richards *et al* [2-33] modeled the effect of mechanical tensioning for residual stress control after FSW by FEM. Figure 2-17 shows that under various heat inputs from the tool and various welding velocity the mechanical tensioning could effectively reduce residual stress. The residual stress reduction was attributed to reduction of compressive plastic straining ahead of the tool and increase of tensile plastic straining behind. As shown in Figure 2-18, pre-tensioning was more effective than post weld tensioning.

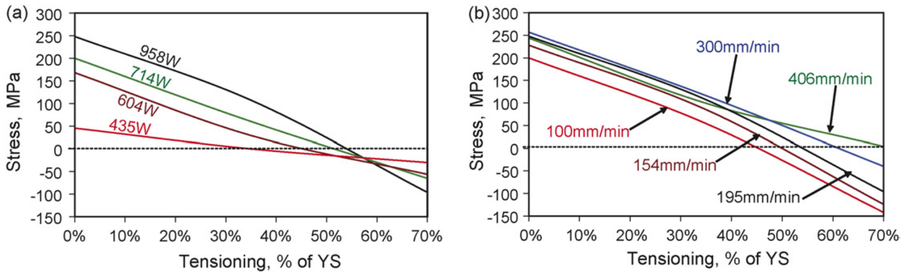

Figure 2-17 [2-33] Predicted effect of preloaded mechanical tensioning under various heat input from the tool (a) and various welding velocity (b)

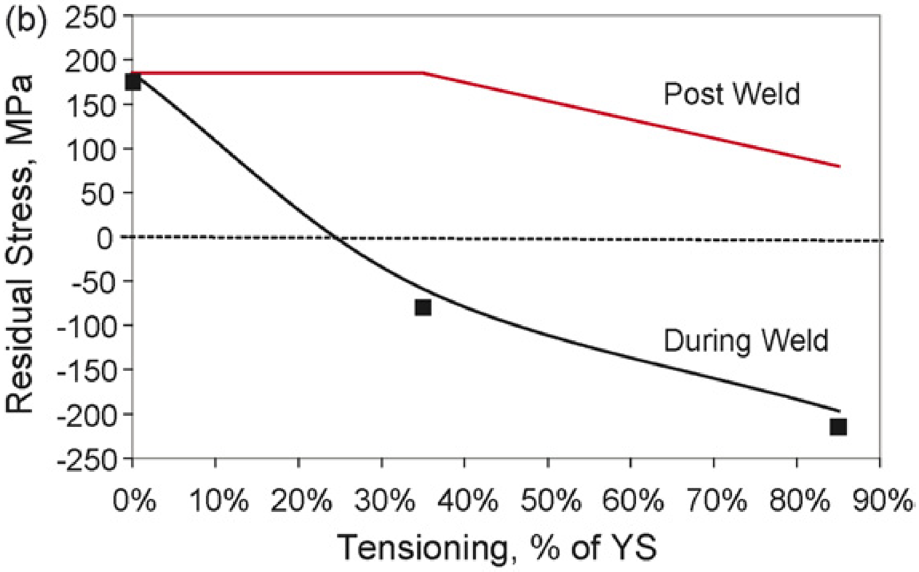

Figure 2-18 [2-33] Comparison of post welding and preloaded mechanical tensioning

Kuo *et al* [2-34] studied the mechanism of 304 stainless steel vibration welding. The residual stress was found to be reduced to 206 MPa, which was 21% smaller than the residual stress without vibration. The residual stress relief was mainly contributed to dislocation followed by dislocation breakdown.

Zhao *et al* [2-35] built a finite element model for vibration induced stress relief and both non-resonant vibration and resonant vibration were examined. Vibration amplitude was found essential in reducing residual stress for non-resonant vibration, while vibration frequency was significant in resonant vibration and the amplitude could be small.

Process parameter optimization is one the most simple methods to improve mechanical performance, but the effect to some extent is limited. Mechanical tensioning is very effective in residual stress reduction, but only good for butt welding. Coupling mechanical vibration into FSW is still subject to discussion due the interference to the welding tool.

2.3 The small punch test

Small punch beam test is a miniaturized testing method, whose testing procedures and applications are related to part of the thesis research (small punch beam test).The small punch test system configuration is shown in Figure 2-19. The disk-shaped specimen is deformed by a punch with spherical head and the forced applied to the specimen and corresponding displacement of specimen center are recorded. The force VS displacement data could be used to estimate strain stress curve for specimen material. Compared to conventional test method, the specimen is much small and usually the dimensions are diameter 10 mm and thickness 0.5 mm.

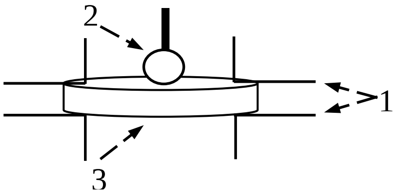

Figure 2-19 Schematic for small punch test

1: fixture, 2: punch with spherical head, 3: specimen

2.3.1 Applications

Misawa *et al* [2-36] employed the small punch test to evaluate ductile-brittle transition temperature (DBTT) using miniaturized transmission electron microscopy (TEM) disk specimen made of HT-9 and JFMS ferritic steels. It was found that the small punch testing could give reliable information on DBTT by using statistical analysis. The small punch test was also introduced to characterize resistance to stress corrosion cracking of austenitic and ferritic steels [2-37] successfully, namely 304 and HT-9.

Kameda *et al* [2-38] evaluated the DBTT shift induced by temper embrittlement and neutron irradiation by the small punch test. The specimens were impurity-doped steel plates of size 10 x 10 x 0.5 mm. The obtained upper limit and lower limit of DBTT showed dependency on dopant (metallic or nonmetallic elements of steel) concentrations.

Mao *et al* [2-39] developed a further miniaturized small punch test using a 3 mm diameter and 0.25 mm thickness TEM disk specimen. The deformation progress was found to comprise of elastic bending, plastic bending and plastic membrane stretching stages. The yield stress and ultimate stress could be predicted and the ductile fracture toughness could be linearly mapped to the biaxial equivalent fracture strain.

Fleury *et al* [2-40] applied the small punch test to assess the mechanical properties of materials used in steam power plants to evaluate the remaining life of components. Mechanical characteristics from the small punch test correlated well with uniaxial tensile test and the tensile stress strain data was accurately predicted in the temperature range 25-600 ^{0}C. The small punch test was then extended to characterize fracture toughness of materials [2-41]. As shown in Figure 2-20, the calculated small punch (SP) DBTT and conventional Charpy fractural appearance transition temperature (FATT) agreed well. The simulation results are calculated based on estimated strain-stress curve and numerical model of small punch test.

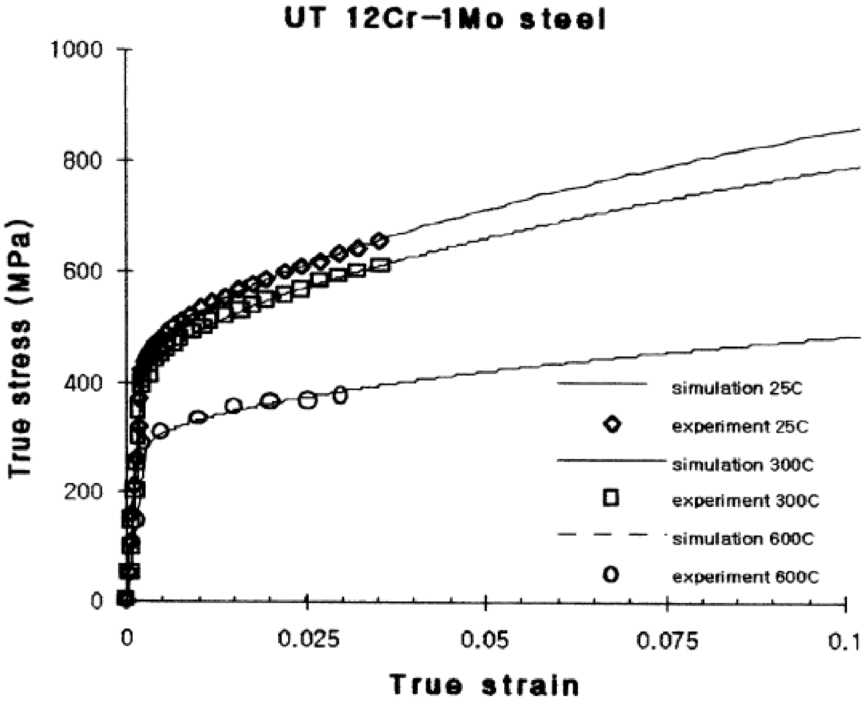

Figure 2-20 [2-40] Comparison of predicted and experimentally measured strain stress curves in range 25 to 600 ℃ for 12Cr-1Mo steel

Ule *et al* [2-42] compared the small punch creep test with a conventional creep test for service exposed components. As shown in Figure 2-21, the repeatability of the small punch creep test was demonstrated by carrying out experiments within laboratories or using the same testing equipment. Temperature was identified as the greatest factor affecting accuracy.

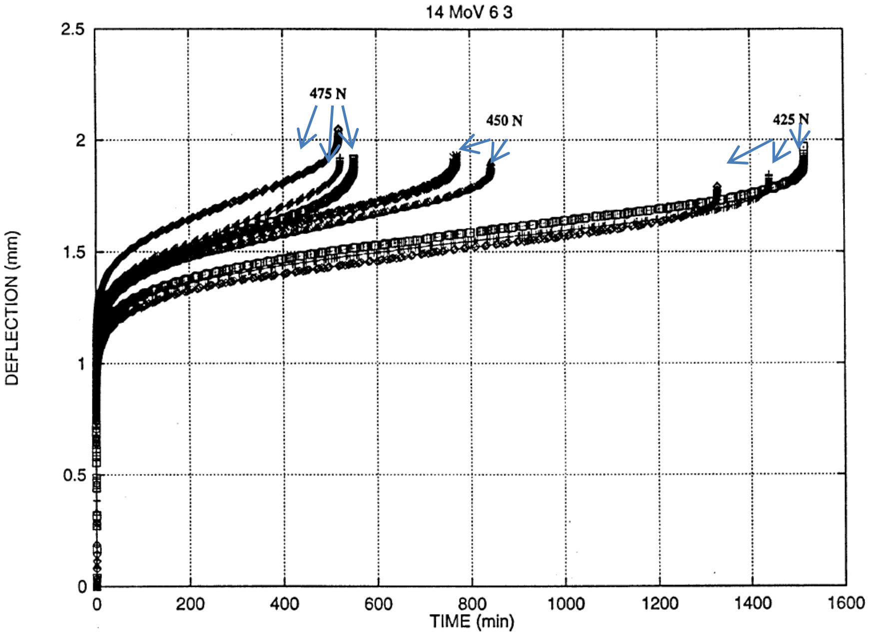

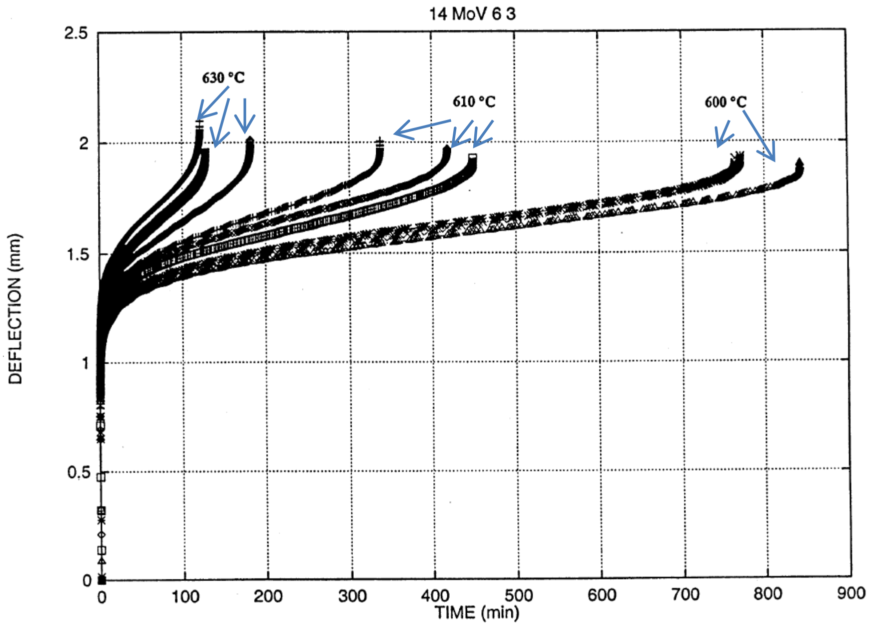

Figure 2-21 [2-42] Measured deflection-time curves for 14MoV63 steel under different loads and temperatures

Cheon *et al* [2-43] performed the small punch test on CF8 stainless steel to assess thermal aging embrittlement. The general trend and repeatability of small punch load-displacement curves were shown in Figure 2-22 and found to be similar to that for ferritic steels and the yield strength increased with increasing aging degree. The inverse procedure of the small punch test was also investigated [2-44], which uses the load-force curves to determine material property parameters in numerical models. The objective function was the error between experiment force vector and numerically predicted force vector and the simulated annealing algorithm was employed to minimize the objective function. In the meanwhile, an Artificial Neural Network, ANN, was introduced to predict numerical load-displacement curves.

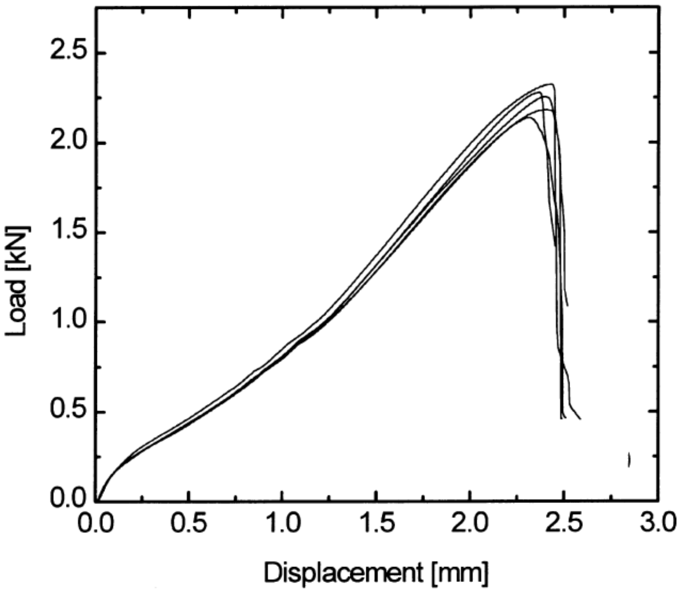

Figure 2-22 [2-43] Repeatability of the small punch test for CF8 steel

Saucedo-Munoz *et al* [2-45] investigated the relationship between fracture toughness and equivalent fracture strain from the small punch test. The fracture toughness was found to be linearly dependent on equivalent fracture strain for steels JN1, JJ1 and JK2. Analysis showed that the small punch test could provide useful information to assess fracture toughness degradation in small areas.

Dobes *et al* [2-46] performed comparisons between small punch creep test and conventional uniaxial creep test for chromium steel and low alloy steel. Results in Figure 2-23 showed that the relationship between time to fracture and minimum deflection rate in the small punch test was similar to corresponding quantities in conventional creep test. The comparison was also applied to mechanically alloyed Al-C-O alloys and the findings were similar. The findings were confirmed in P91 steel creep testing [2-47].

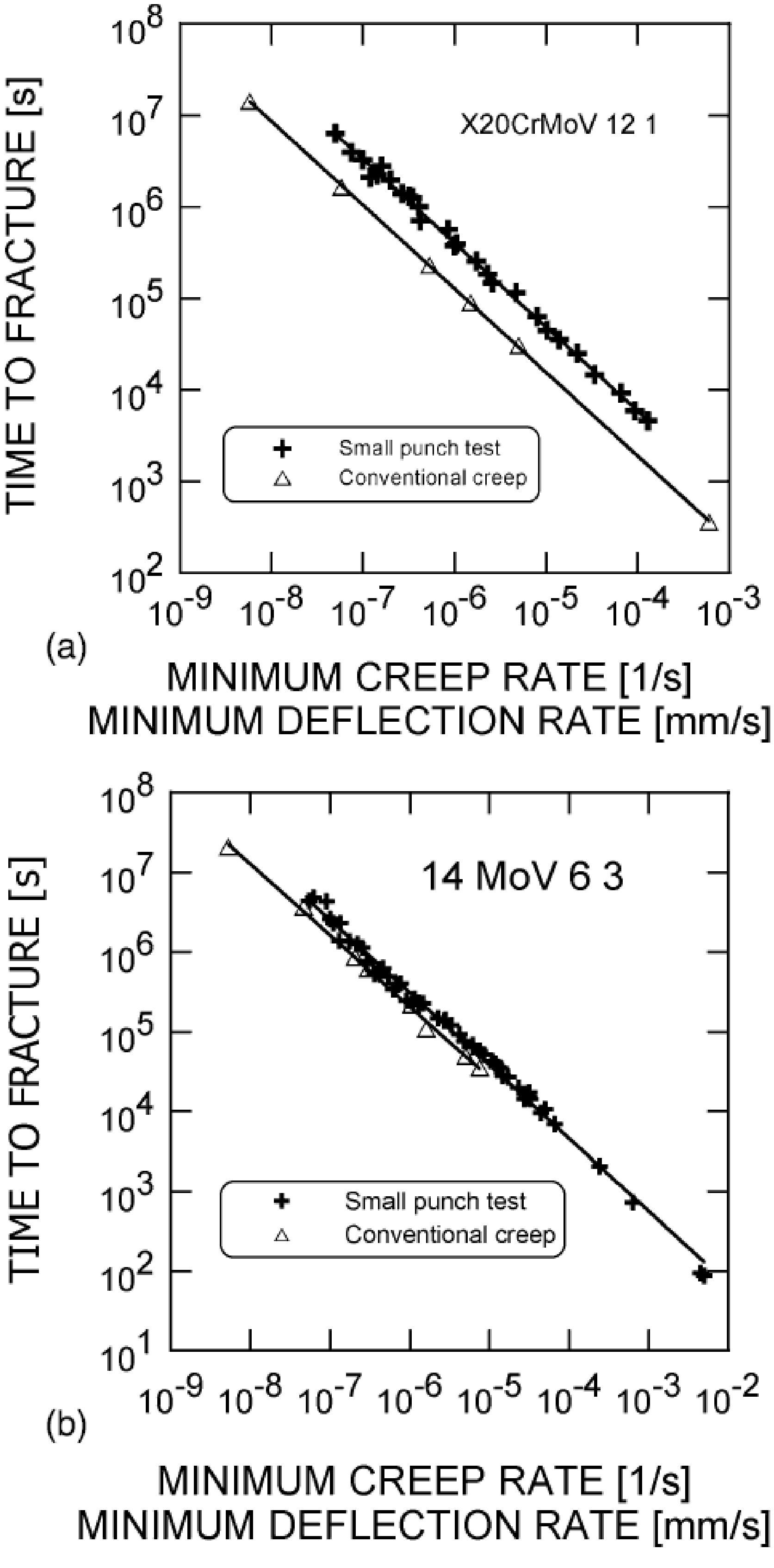

Figure 2-23 [2-46] Comparison between the small punch test and conventional creep test on time to fracture and minimum creep rate curves

Yang *et al* [2-48] studied complicated creep strain behavior in the small punch test. The relationship of specimen central creep deflection to central creep strain was assumed to be approximate to the relationship between central non-creep deflection and central non-creep strain.

Leon *et al* [2-49] tested tensile strength of Al/Ni-Sic composites via the small punch test. Tensile strength was found in range of 220 to 250 MPa varying with the particle size reinforcement and matrix composition.

Jia *et al* [2-50] conducted the small punch test for steels F82H and T91 at temperature from -190 to 80 ^{0}C and also Optimax-A irradiated. Results in Figure 2-24 demonstrated that the irradiation hardening calculated by the small punch test was in agreement with conventional tensile test and increased irradiation dose could improve yield strength, while the total displacement at failure decreased. The DBTT was also found to increase with increasing irradiation dose.

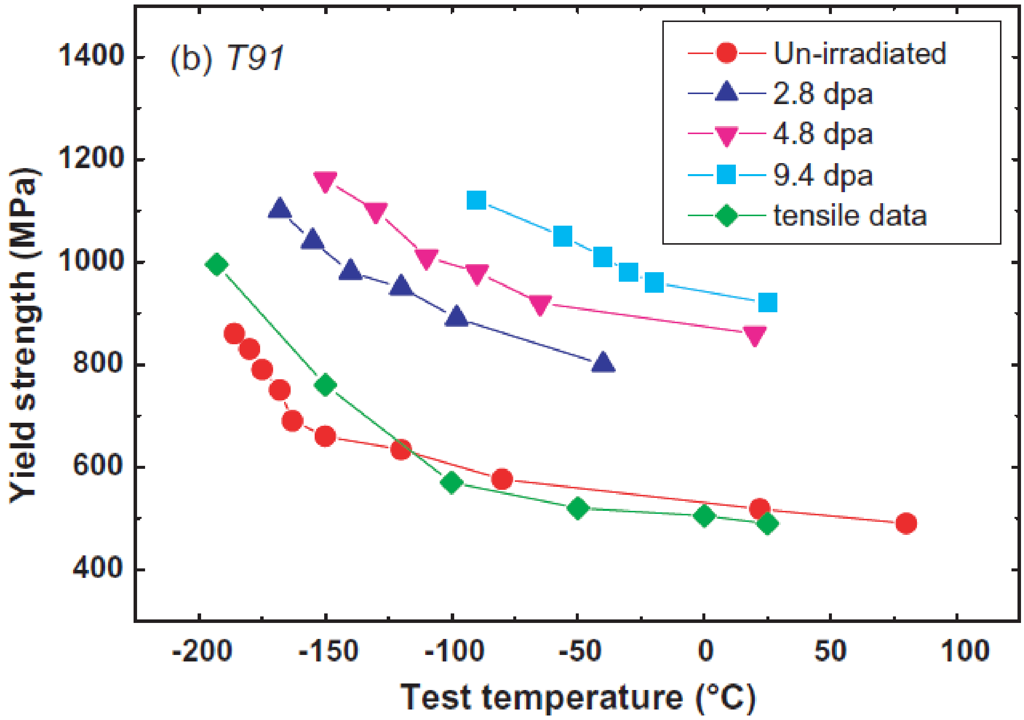

Figure 2-24 [2-50] Yield strength predicted by the small punch test and comparison with conventional tensile test

Ju *et al* [2-51] obtained fracture toughness of SA 508 steel based on fracture mechanics by the small punch test. The specimens were sharply notched and the fracture toughness was successfully predicted.

Abendroth *et al* [2-52] coupled the small punch test and neural network algorithm to identify plastic deformation and failure properties of ductile materials. Experimental load-displacement curves are shown in Figure 2-25. Material property parameters were predicted and verified by testing and simulation. Ductile damage and fracture parameters were also identified by the small punch test and neural network [2-53].

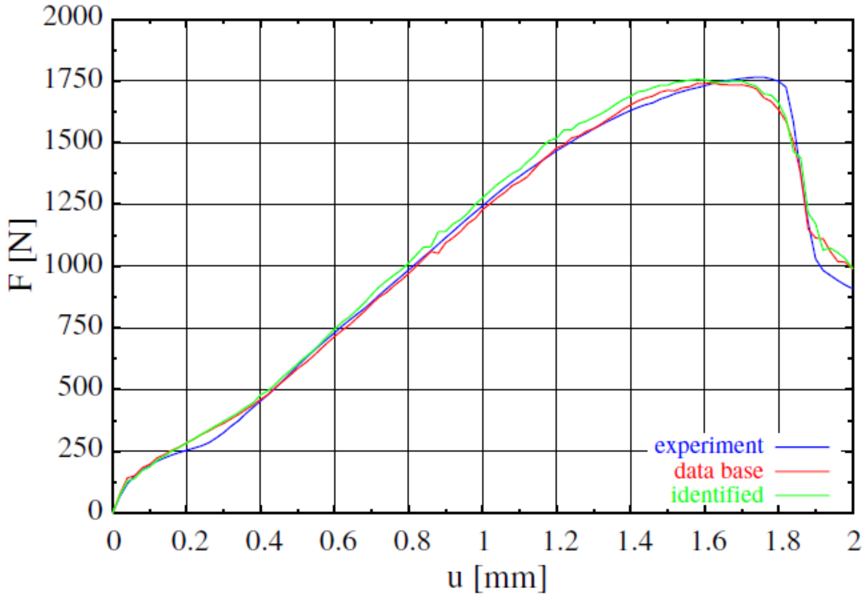

Figure 2-25 [2-52] Predicted and experimental load-displacement curves of 10MnMoNi555

Shekhter *et al* [2-54] used three methods to assess temper embrittlement of a serviced 1Cr1Mo25V rotor; namely Charpy V-notch test, fracture toughness test and the small punch test. Results and analysis showed that the small punch test could be used to directly characterise fracture toughness.

Kim *et al* [2-55] evaluated PRV steels' ductile-brittle transition temperature in non-irradiated and neutron irradiated condition by the small punch test. The determined transition temperatures correlated linearly with the Charpy index temperature as well as the reference temperature.

Finarelli *et al* [2-56] characterized mechanical properties of 316L austenitic steel and martensitic steel Optifer after exposure to irradiation source SINQ. Yield strength, ductility and fracture energy were predicted.

Ling *et al* [2-57] performed small punch creep test for 304 stainless steel at 650 ^{0}C to characterize Kachanov-Rabotnov creep damage properties. The calculated data by finite element model was found to be in good agreement with experimental results.

Serre *et al* [2-58] investigated the embrittlement sensitivity of T91 martensitic steel subject to liquid lead bismuth eutectic by the small punch test. The ductile to brittle transition caused by liquid metal was observed and confirmed. And the small punch test seemed to be sensitive to reveal this kind of embrittlement.

Egan *et al* [2-59] introduced profilometry into the small punch test by modification of full field low coherence interferometry. The 3D micrometer profile of deformed specimen was measured by random depth access as shown in Figure 2-26. This technique had advantages over single point deflection measurement methods and didn't contact the specimen. It has been successfully applied to true strain stress relationship identification for annealed mild steels [2-60].

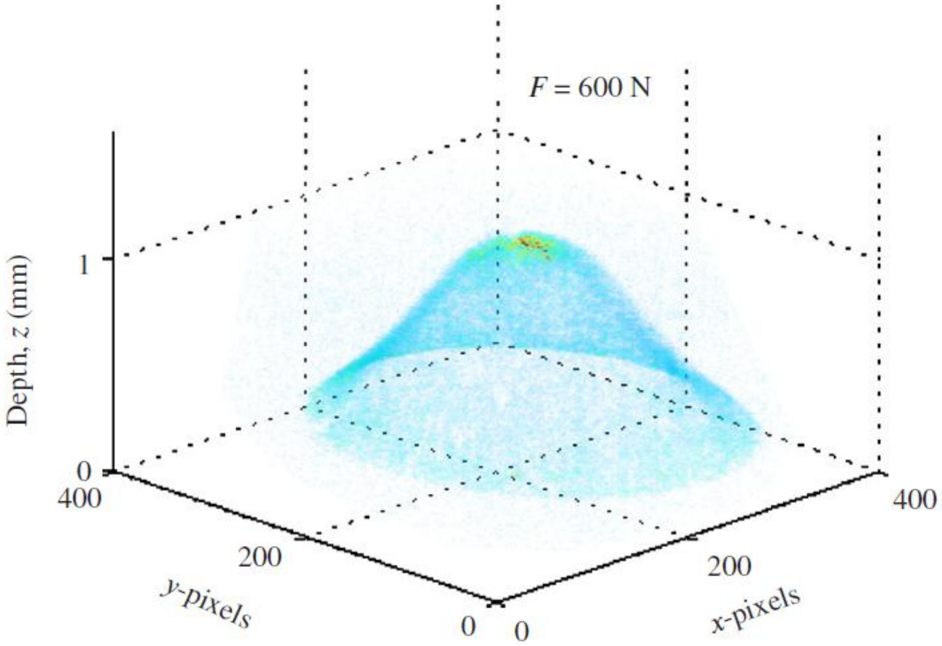

Figure 2-26 [2-59] Measured profile of the small punch test deformed specimen under load 500N

Chang *et al* [2-61] assessed fracture resistance for typical nuclear materials using the small punch test. It was proven that the proposed simple small punch specimen was feasible for identifying J-R curves of virgin materials at room temperature.

Kim *et al* [2-62] examined local creep performance of P92 steel welds by the small punch test. The local microstructures in different zones were observed under microscopy and various specimens were sampled from different locations. The Type IV region was found to be the weakest zone of the whole weld.

Linse *et al* [2-63] characterized reactor vessel steels in brittle-ductile transition region by the small punch test. A neural network algorithm was developed to calculate hardening parameters and Weibull parameters, reducing computational time.

Lzaki *et al* [2-64] applied the small punch test to studied boiler pipes' creep life. Results from small punch creep tests and conventional uniaxial creep tests were correlated. Base material, pre-crept material, welded material and service aged material of 2.25Cr-1Mo steel were sampled and tested. As shown in Figure 2-27, the measured load of small punch creep test and uniaxial creep stress at the same rupture time were found to be linear and independent on test conditions or materials.

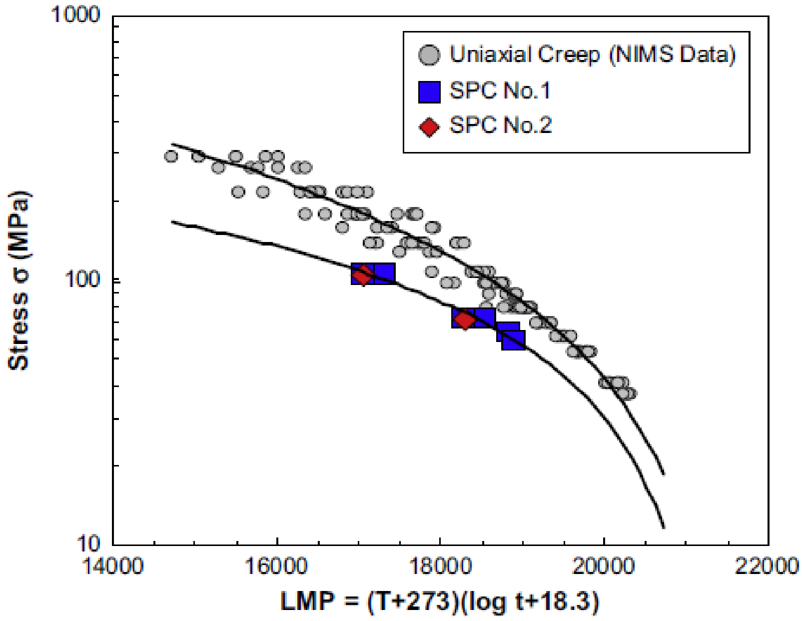

Figure 2-27 [2-64] Comparisons between uniaxial creep test results of original material and the small punch test results of serviced exposed material

Blagoeva *et al* [2-65] applied the CEN small punch creep testing code on repair welded P91 pipe. Creep strengths of the original material and service exposed base material tested at 600 ^{0}C were similar in both small punch creep test and in the first stage of conventional uniaxial test.

Komazaki *et al* [2-66][2-67] carried out both small punch tests and small punch creep tests using a further miniaturized plate specimen to evaluate the high temperature strength distribution of welded ferritic steel. The distribution of the maximum load in the small punch test at temperature 873K was close to the results of Vickers hardness measurements as shown in Figure 2-28. The load-stress conversion coefficient agreed well with that in finite element analysis.

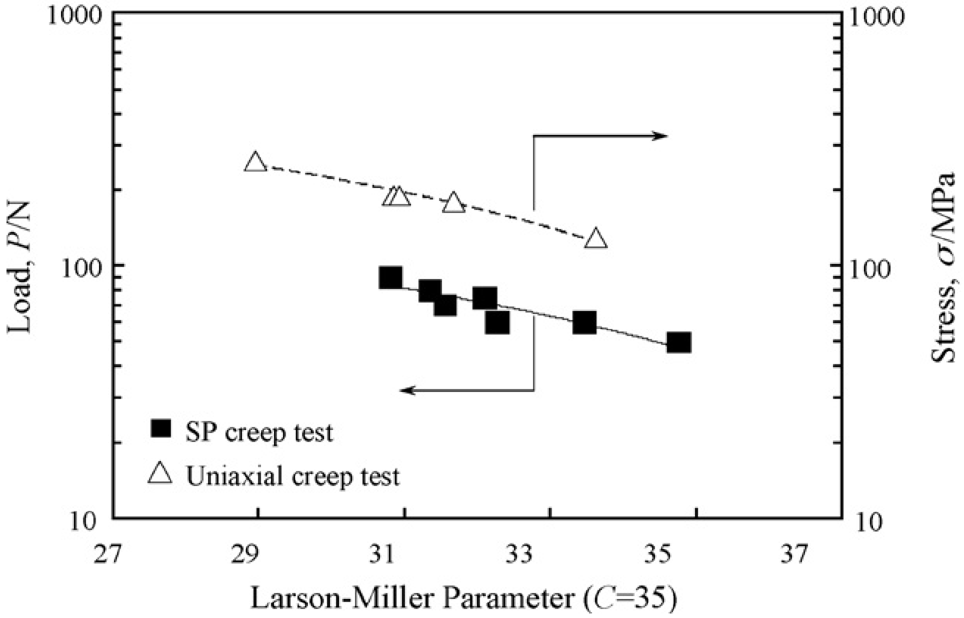

Figure 2-28 [2-66] Comparison of small punch creep test and conventional creep test

Tanaka *et al* [2-68] evaluated high temperature fracture toughness for CrMoV cast steel using the small punch test. The specimens were pre-cracked and the crack extension was experimentally measured by electric potential drop method. Estimated fracture toughness degradation correlated with those from conventional test.

Okuda *et al* [2-69] identified anisotropic fracture behavior of ODS ferritic steels by the small punch test, which was applied in advanced nuclear systems. The results demonstrated that DBTTs in longitudinal and transverse directions were not the same and it was explained by the elongated grain of OSD ferritic steels.

Hu *et al* [2-70] modeled the small punch test for Zirconium, employing the Gurson-Tvergaard-Needleman plastic damage constitutive model. As shown in Figure 2-29, results of damage occurrence and growth were in good agreement with experiment observation.

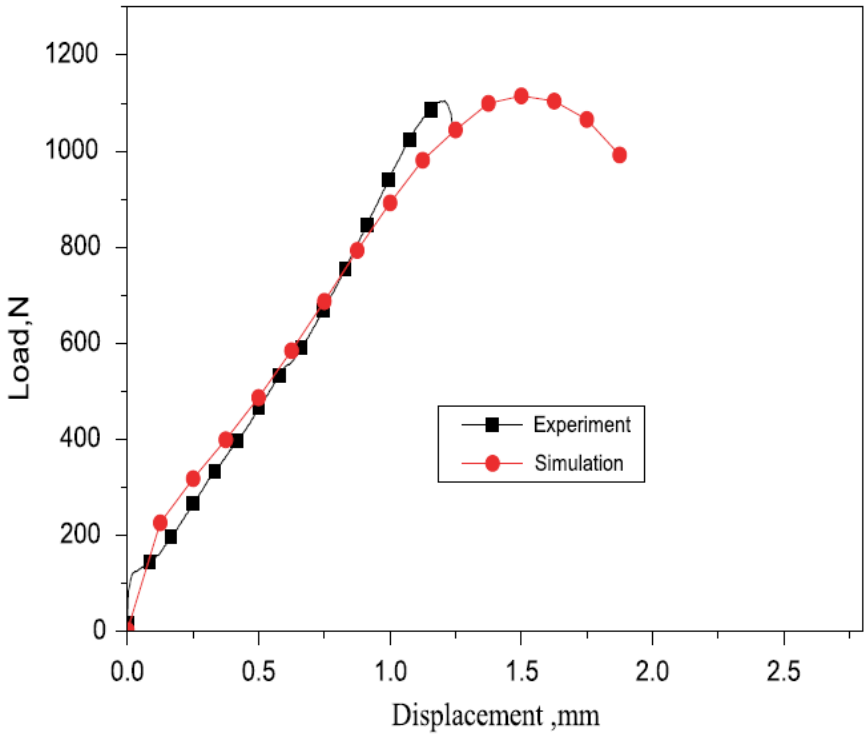

Figure 2-29 [2-70] Comparison of simulation and experiment results

2.4 References

[2-1] M. Song, R. Kovacevic, Thermal modeling of friction stir welding in a moving coordinate system and its validation, International Journal of Machine Tools and Manufacture, Volume 43, Issue 6, May 2003, Pages 605-615

[2-2] Pedro Vilaça, Luísa Quintino, Jorge F. dos Santos, iSTIR—Analytical thermal model for friction stir welding, Journal of Materials Processing Technology, Volume 169, Issue 3, 1 December 2005, Pages 452-465

[2-3] Kevin J. Colligan, Rajiv S. Mishra, A conceptual model for the process variables related to heat generation in friction stir welding of aluminum, Scripta Materialia, Volume 58, Issue 5, March 2008, Pages 327-331

[2-4] S. Mandal, J. Rice, A.A. Elmustafa, Experimental and numerical investigation of the plunge stage in friction stir welding, Journal of Materials Processing Technology, Volume 203, Issues 1–3, 18 July 2008, Pages 411-419

[2-5] C.M. Chen, R. Kovacevic, Finite element modeling of friction stir welding—thermal and thermomechanical analysis, International Journal of Machine Tools and Manufacture, Volume 43, Issue 13, October 2003, Pages 1319-1326

[2-6] X.K Zhu, Y.J Chao, Numerical simulation of transient temperature and residual stresses in friction stir welding of 304L stainless steel, Journal of Materials Processing Technology, Volume 146, Issue 2, 28 February 2004, Pages 263-27

[2-7] G. Buffa, L. Fratini, S. Pasta, R. Shivpuri, On thermo-mechanical loads and the resultant residual stresses in friction stir processing operations, CIRP Annals - Manufacturing Technology, Volume 57, Issue 1, 2008, Pages 287-290

[2-8] Mir Zahedul H. Khandkar, Jamil A. Khan, Anthony P. Reynolds, Michael A. Sutton, Predicting residual thermal stresses in friction stir welded metals, Journal of Materials Processing Technology, Volume 174, Issues 1–3, 25 May 2006, Pages 195-203

[2-9] Vijay Soundararajan, Srdja Zekovic, Radovan Kovacevic, Thermo-mechanical model with adaptive boundary conditions for friction stir welding of Al 6061, International Journal of Machine Tools and Manufacture, Volume 45, Issue 14, November 2005, Pages 1577-1587

[2-10] A. Bastier, M.H. Maitournam, F. Roger, K. Dang Van, Modelling of the residual state of friction stir welded plates, Journal of Materials Processing Technology, Volume 200, Issues 1–3, 8 May 2008, Pages 25-37

[2-11] H.W. Zhang, Z. Zhang, J.T. Chen, The finite element simulation of the friction stir welding process, Materials Science and Engineering: A, Volume 403, Issues 1–2, 25 August 2005, Pages 340-348

[2-12] Paul A. Colegrove, Hugh R. Shercliff, 3-Dimensional CFD modelling of flow round a threaded friction stir welding tool profile, Journal of Materials Processing Technology, Volume 169, Issue 2, 10 November 2005, Pages 320-327

[2-13] H.W. Zhang, Z. Zhang, J.T. Chen, 3D modeling of material flow in friction stir welding under different process parameters, Journal of Materials Processing Technology, Volume 183, Issue 1, 5 March 2007, Pages 62-70

[2-14] R. Nandan, G.G. Roy, T.J. Lienert, T. Debroy, Three-dimensional heat and material flow during friction stir welding of mild steel, Acta Materialia, Volume 55, Issue 3, February 2007, Pages 883-895

[2-15] Xiaomin Deng, Shaowen Xu, Two-Dimensional Finite Element Simulation of Material Flow in the Friction Stir Welding Process, Journal of Manufacturing Processes, Volume 6, Issue 2, 2004, Pages 125-133

[2-16] D.E. Boyce, P.R. Dawson, B. Sidle, T. Gnäupel-Herold, A multiscale methodology for deformation modeling applied to friction stir welded steel, Computational Materials Science, Volume 38, Issue 1, November 2006, Pages 158-175

[2-17] Hasan Okuyucu, Adem Kurt, Erol Arcaklioglu, Artificial neural network application to the friction stir welding of aluminum plates, Materials & Design, Volume 28, Issue 1, 2007, Pages 78-84

[2-18] G. Buffa, L. Fratini, R. Shivpuri, CDRX modelling in friction stir welding of AA7075-T6 aluminum alloy: Analytical approaches, Journal of Materials Processing Technology, Volume 191, Issues 1–3, 1 August 2007, Pages 356-359

[2-19] Livan Fratini, Gianluca Buffa, CDRX modelling in friction stir welding of aluminium alloys, International Journal of Machine Tools and Manufacture, Volume 45, Issue 10, August 2005, Pages 1188-1194

[2-20] N. Kamp, A. Sullivan, J.D. Robson, Modelling of friction stir welding of 7xxx aluminium alloys, Materials Science and Engineering: A, Volume 466, Issues 1–2, 25 September 2007, Pages 246-255

[2-21] N. Kamp, A. Sullivan, R. Tomasi, J.D. Robson, Modelling of heterogeneous precipitate distribution evolution during friction stir welding process, Acta Materialia, Volume 54, Issue 8, May 2006, Pages 2003-2014

[2-22] C. Gallais, A. Denquin, Y. Bréchet, G. Lapasset, Precipitation microstructures in an AA6056 aluminium alloy after friction stir welding: Characterisation and modelling, Materials Science and Engineering: A, Volume 496, Issues 1–2, 25 November 2008, Pages 77-89

[2-23] P. Heurtier, M.J. Jones, C. Desrayaud, J.H. Driver, F. Montheillet, D. Allehaux, Mechanical and thermal modelling of Friction Stir Welding, Journal of Materials Processing Technology, Volume 171, Issue 3, 1 February 2006, Pages 348-357

[2-24] William D Lockwood, Borislav Tomaz, A.P Reynolds, Mechanical response of friction stir welded AA2024: experiment and modeling, Materials Science and Engineering: A, Volume 323, Issues 1–2, 31 January 2002, Pages 348-353

[2-25] W.D. Lockwood, A.P. Reynolds, Simulation of the global response of a friction stir weld using local constitutive behavior, Materials Science and Engineering: A, Volume 339, Issues 1–2, 2 January 2003, Pages 35-42

[2-26] D.G. Hattingh, C. Blignault, T.I. van Niekerk, M.N. James, Characterization of the influences of FSW tool geometry on welding forces and weld tensile strength using an instrumented tool, Journal of Materials Processing Technology, Volume 203, Issues 1–3, 18 July 2008, Pages 46-57

[2-27] G.J Fernandez, L.E Murr, Characterization of tool wear and weld optimization in the friction-stir welding of cast aluminum 359+20% SiC metal-matrix composite, Materials Characterization, Volume 52, Issue 1, March 2004, Pages 65-75

[2-28] H. Lombard, D.G. Hattingh, A. Steuwer, M.N. James, Optimising FSW process parameters to minimise defects and maximise fatigue life in 5083-H321 aluminium alloy, Engineering Fracture Mechanics, Volume 75, Issues 3–4, February–March 2008, Pages 341-354

[2-29] S.T. Amancio-Filho, S. Sheikhi, J.F. dos Santos, C. Bolfarini, Preliminary study on the microstructure and mechanical properties of dissimilar friction stir welds in aircraft aluminium alloys 2024-T351 and 6056-T4, Journal of Materials Processing Technology, Volume 206, Issues 1–3, 12 September 2008, Pages 132-142

[2-30] A.K. Lakshminarayanan, V. Balasubramanian, Process parameters optimization for friction stir welding of RDE-40 aluminium alloy using Taguchi technique, Transactions of Nonferrous Metals Society of China, Volume 18, Issue 3, June 2008, Pages 548-554

[2-31] P Staron, M Koçak, S Williams, A Wescott, Residual stress in friction stir-welded Al sheets, Physica B: Condensed Matter, Volume 350, Issues 1–3, Supplement, 15 July 2004, Pages E491-E493

[2-32] J. Altenkirch, A. Steuwer, M. Peel, D.G. Richards, P.J. Withers, The effect of tensioning and sectioning on residual stresses in aluminium AA7749 friction stir welds, Materials Science and Engineering: A, Volume 488, Issues 1–2, 15 August 2008, Pages 16-24

[2-33] D.G. Richards, P.B. Prangnell, S.W. Williams, P.J. Withers, Global mechanical tensioning for the management of residual stresses in welds, Materials Science and Engineering: A, Volume 489, Issues 1–2, 20 August 2008, Pages 351-362

[2-34] Che-Wei Kuo, Chi-Ming Lin, Gen-Huey Lai, Yu-Che Chen, Yung-Tse Chang and Weite Wu, Characterization and Mechanism of 304 Stainless Steel Vibration Welding, Special Issue on Solidification Science and Processing for Advanced Materials, Vol. 48, No. 9 (2007) pp. 2319 to 2323

[2-35] X.C. Zhao, Y.D. Zhang, H.W. Zhang, Q. Wu, Simulation of vibration stress relief after welding based on FEM, Acta Metallurgica Sinica (English Letters), Volume 21, Issue 4, August 2008, Pages 289-294

[2-36] T. Misawa, T. Adachi, M. Saito, Y. Hamaguchi, The small punch tests for evaluating ductile-brittle transition behavior of irradiated ferritic steels, Journal of Nuclear Materials, Volume 150, Issue 2, October 1987, Pages 194-202

[2-37] T. Misawa, Y. Hamaguchi, M. Saito, Stress corrosion cracking and hydrogen embrittlement studies of austenitic and ferritic steels by the small punch test, Journal of Nuclear Materials, Volumes 155–157, Part 2, 2 July 1988, Pages 749-753

[2-38] J. Kameda, O. Buck, Evaluation of the ductile-to-brittle transition temperature shift due to temper embrittlement and neutron irradiation by means of a small-punch test, Materials Science and Engineering, Volume 83, Issue 1, October 1986, Pages 29-38

[2-39] Xinyuan Mao, Hideaki Takahashi, Development of a further-miniaturized specimen of 3 mm diameter for tem disk (ø 3 mm) the small punch tests, Journal of Nuclear Materials, Volume 150, Issue 1, September 1987, Pages 42-52

[2-40] E. Fleury, J.S. Ha, The small punch tests to estimate the mechanical properties of steels for steam power plant: I. Mechanical strength, International Journal of Pressure Vessels and Piping, Volume 75, Issue 9, August 1998, Pages 699-706

[2-41] J.S. Ha, E. Fleury, The small punch tests to estimate the mechanical properties of steels for steam power plant: II. Fracture toughness, International Journal of Pressure Vessels and Piping, Volume 75, Issue 9, August 1998, Pages 707-713.

[2-42] B Ule, T Šuštar, F Dobeš, K Milička, V Bicego, S Tettamanti, K Maile, C Schwarzkopf, M.P Whelan, R.H Kozlowski, J Klaput, The small punch test method assessment for the determination of the residual creep life of service exposed components: outcomes from an interlaboratory exercise, Nuclear Engineering and Design, Volume 192, Issue 1, 2 August 1999, Pages 1-11

[2-43] Jin Sik Cheon, In Sup Kim, Evaluation of thermal aging embrittlement in CF8 duplex stainless steel by the small punch test, Journal of Nuclear Materials, Volume 278, Issue 1, February 2000, Pages 96-103

[2-44] Jin-Sik Cheon, Cheol-Hong Joo, The small punch test for determining a flow stress by using a hybrid inverse procedure, Computational Materials Science, Volume 43, Issue 4, October 2008, Pages 744-751

[2-45] Maribel L Saucedo-Muñoz, Shi Cheng Liu, Toshiyuki Hashida, Hideaki Takahashi, Hideo Nakajima, Correlationship between JIC and equivalent fracture strain determined by small-punch tests in JN1, JJ1 and JK2 austenitic stainless steels, Cryogenics, Volume 41, Issue 10, October 2001, Pages 713-719

[2-46] F. Dobeš, K. Milička, On the Monkman–Grant relation for the small punch test data, Materials Science and Engineering: A, Volume 336, Issues 1–2, 25 October 2002, Pages 245-248

[2-47] F. Dobeš, K. Milička, Application of creep the small punch testing in assessment of creep lifetime, Materials Science and Engineering: A, Volumes 510–511, 15 June 2009, Pages 440-443

[2-48] Zhen Yang, Zhi-wen Wang, Relationship between strain and central deflection in small punch creep specimens, International Journal of Pressure Vessels and Piping, Volume 80, Issue 6, June 2003, Pages 397-404

[2-49] C.A León, R.A.L Drew, The small punch testing for assessing the tensile strength of gradient Al/Ni–SiC composites, Materials Letters, Volume 56, Issue 5, November 2002, Pages 812-816

[2-50] X. Jia, Y. Dai, The small punch tests on martensitic/ferritic steels F82H, T91 and Optimax-A irradiated in SINQ Target-3, Journal of Nuclear Materials, Volume 323, Issues 2–3, 1 December 2003, Pages 360-367

[2-51] Jang-Bog Ju, Jae-il Jang, Dongil Kwon, Evaluation of fracture toughness by small-punch testing techniques using sharp notched specimens, International Journal of Pressure Vessels and Piping, Volume 80, Issue 4, April 2003, Pages 221-228

[2-52] Martin Abendroth, Meinhard Kuna, Determination of deformation and failure properties of ductile materials by means of the small punch test and neural networks, Computational Materials Science, Volume 28, Issues 3–4, November 2003, Pages 633-644

[2-53] Martin Abendroth, Meinhard Kuna, Identification of ductile damage and fracture parameters from the small punch test using neural networks, Engineering Fracture Mechanics, Volume 73, Issue 6, April 2006, Pages 710-725

[2-54] A Shekhter, S Kim, D.G Carr, A.B.L Croker, S.P Ringer, Assessment of temper embrittlement in an ex-service 1Cr–1Mo–0.25V power generating rotor by Charpy V-Notch testing, KIc fracture toughness and the small punch test, International Journal of Pressure Vessels and Piping, Volume 79, Issues 8–10, August 2002, Pages 611-615

[2-55] Min-Chul Kim, Yong Jun Oh, Bong Sang Lee, Evaluation of ductile–brittle transition temperature before and after neutron irradiation for RPV steels using the small punch tests, Nuclear Engineering and Design, Volume 235, Issues 17–19, August 2005, Pages 1799-1805

[2-56] D Finarelli, M Roedig, F Carsughi, The small punch tests on austenitic and martensitic steels irradiated in a spallation environment with 530 MeV protons, Journal of Nuclear Materials, Volume 328, Issues 2–3, 1 July 2004, Pages 146-150

[2-57] Xiang Ling, Yangyan Zheng, Yingjun You, Yuxin Chen, Creep damage in small punch creep specimens of Type 304 stainless steel, International Journal of Pressure Vessels and Piping, Volume 84, Issue 5, May 2007, Pages 304-309

[2-58] I. Serre, J.-B. Vogt, Liquid metal embrittlement of T91 martensitic steel evidenced by the small punch test, Nuclear Engineering and Design, Volume 237, Issue 7, April 2007, Pages 677-685

[2-59] Patrick Egan, Maurice P. Whelan, Fereydoun Lakestani, Michael J. Connelly, Random depth access full-field low-coherence interferometry applied to a the small punch test, Optics and Lasers in Engineering, Volume 45, Issue 4, April 2007, Pages 523-529

[2-60] Patrick Egan, Maurice P. Whelan, Fereydoun Lakestani, Michael J. Connelly, The small punch test: An approach to solve the inverse problem by deformation shape and finite element optimization, Computational Materials Science, Volume 40, Issue 1, July 2007, Pages 33-39

[2-61] Yoon-Suk Chang, Jong-Min Kim, Jae-Boong Choi, Young-Jin Kim, Min-Chul Kim, Bong-Sang Lee, Derivation of ductile fracture resistance by use of small punch specimens, Engineering Fracture Mechanics, Volume 75, Issue 11, July 2008, Pages 3413-3427

[2-62] Bumjoon Kim, Byeongsoo Lim, Local creep evaluation of P92 steel weldment by small punch creep test, Acta Mechanica Solida Sinica, Volume 21, Issue 4, August 2008, Pages 312-317

[2-63] T. Linse, M. Kuna, J. Schuhknecht, H.-W. Viehrig, Usage of the small-punch-test for the characterisation of reactor vessel steels in the brittle–ductile transition region, Engineering Fracture Mechanics, Volume 75, Issue 11, July 2008, Pages 3520-3533

[2-64] Toru Izaki, Toshimi Kobayashi, Junichi Kusumoto, Akihiro Kanaya, A creep life assessment method for boiler pipes using small punch creep test, International Journal of Pressure Vessels and Piping, Volume 86, Issue 9, September 2009, Pages 637-642

[2-65] D.T. Blagoeva, R.C. Hurst, Application of the CEN (European Committee for Standardization) small punch creep testing code of practice to a representative repair welded P91 pipe, Materials Science and Engineering: A, Volumes 510–511, 15 June 2009, Pages 219-223

[2-66] Shin-ichi Komazaki, Taichiro Kato, Yutaka Kohno, Hiroyasu Tanigawa, Creep property measurements of welded joint of reduced-activation ferritic steel by the small-punch creep test, Materials Science and Engineering: A, Volumes 510–511, 15 June 2009, Pages 229-233, ISSN 0921-5093, 10.1016/j.msea.2008.04.132.

[2-67] Taichiro Kato, Shin-ichi Komazaki, Yutaka Kohno, Hiroyasu Tanigawa, Akira Kohyama, High-temperature strength analysis of welded joint of RAFs by the small punch test, Journal of Nuclear Materials, Volumes 386–388, 30 April 2009, Pages 520-524

[2-68] Kenichi Tanaka, Toshio Amita, Takashi Satou, Kimihiro Koba, Junichi Kusumoto, Akihiro Kanaya, Evaluation on high temperature fracture toughness of CrMoV cast steel by the small punch testing, International Journal of Pressure Vessels and Piping, Volume 86, Issue 9, September 2009, Pages 643-648

[2-69] Naoyuki Okuda, Ryuta Kasada, Akihiko Kimura, Statistical evaluation of anisotropic fracture behavior of ODS ferritic steels by using the small punch tests, Journal of Nuclear Materials, Volumes 386–388, 30 April 2009, Pages 974-978

[2-70] Ruomei Hu, Xiang Ling, Three-dimensional numerical simulation on plastic damage in small punch specimen of Zirconium, International Journal of Pressure Vessels and Piping, Volume 86, Issue 12, December 2009, Pages 813-817

3 Numerical & Experimental Methods

The research reported in this thesis utilized a range of computational and experimental methods reviewed in Chapter 2 to investigate the FSW process. Several different types of finite element models were created and applied during the project, ranging in complexity from relatively simple thermal analysis models to advanced multiphysics models. Optimization algorithms based on Genetic Algorithm and Artificial Neural Network procedures were developed to identify and optimize key FSW process parameters. A new miniaturized material testing method, the small punch beam test, was implemented for experimental characterization and measurement of material properties associated with the welded workpiece. This chapter provides an overview of these tools and procedures, with application reported in detail in later chapters.

3.1 FEM Models

FEM is a numerical analysis method frequently applied in engineering area and helps to understand the mechanisms of various manufacturing processes. The basic idea of FEM is to discretize the solution space into finite elements and evaluate the numerical solution on the nodes. Solutions elsewhere are interpolated by the constructed shape functions. For heat transfer or structural stress analysis involved in the FSW process, the solution space is the three dimensional (3D) space occupied by the workpiece.

The general FEM procedure for solving structural stress problems can be divided into 6 steps, as follows:

1. Discretize the structure by appropriate elements. The type, size and distribution should be considered.
2. Determine the appropriate shape functions for the elements.
3. Form the element stiffness matrix. The matrix can be derived either by equilibrium or variational principles.
4. Assemble all element stiffness matrices and loads to form equilibrium equations

5. Apply boundary conditions and update the equilibrium equations accordingly.
6. Solve the displacement for all nodes and calculate strain and stress according to specific material properties.

The steps for solving heat transfer problems are similar except the specific governing functions and equilibrium conditions. For fully coupled thermal stress analysis (thermal model and stress model are interactive in every small time increment), the solution data are synchronized at each step increment.

The FEM models utilized in this thesis include a thermal model, a fully coupled thermal stress model and a thermal stress microstructure model. The thermal model describes the heat transfer phenomenon of the FSW, while the thermal stress model takes the heat transfer and heat induced stress, including temperature dependent mechanical properties and the effect of displacement on heat transfer. For thermal stress microstructure model, it incorporates the thermal stress model and microstructure model to predict transient and ultimate mechanical properties induced by the heating cycles. All the three types of models are created in ABAQUS.

ABAQUS is a powerful commercial finite element analysis software package from DASSAULT SYSTEMS, including pre-processor, solver and post-processor. ABAQUS is capable of building thermal models, structural stress models and thermal stress couple models. In addition it offers two kinds of Application Program Interfaces (APIs) for secondary development, allowing advanced users to apply complex boundary conditions, loads and material properties, as well as build models automatically.

ABAQUS provides user subroutines DFLUX, DLOAD, FILM and USDFLD etc. to precisely describe the physical issues, and these user subroutines are written in the FORTRAN programming langue, which is efficient in computational analysis. Utility routines, which can be called in the user subroutines, are provided to extract model related information when the models are running. Model related information includes solutions such as temperature, stress and its components, material properties and node properties including their coordinates and connections. The Model related information offers flexibility in the user subroutines.

ABAQUS also provides PYTHON scripting interfaces, allowing expert users to fully control the progress of FEA, including pre-processor, solver and post-processor. By using PYTHON scripting interfaces, it is possible to integrate user implemented algorithms and ABAQUS based models, making the analysis procedure automatic.

ABAQUS based FEM modelling procedures can be divided into 3 stages: model configuration, job submission and results analysis. In the model configuration stage, the geometry of workpiece, material properties, element types, mesh size and distribution, analysis types, steps and output variables etc. have to be determined. If applicable, user subroutines should be prepared according to specific requirements. The model configuration and user subroutines should be checked to ensure it is correct and reasonable; otherwise errors may occur in the proceeding procedure. Then jobs should be created for the models and parallel simulation modes could be selected according to hardware and software specifications. After the jobs are finished, output database (ODB) files can be read to plot the solution results. All the above procedures can be done either by graphic interface ABAQUS CAE or PYTHON scripting interface, or a combination of them.

The thermal models for FSW are used to calculate transient temperature field induced by heat input from the interaction between the tool and workpiece material. The temperature field is the key factor to the establishment of residual stress and the microstructure change in welds, thus the thermal model is very important.

The thermal models utilize the implicit method. Compared with the explicit method, the implicit method performs Newton-Raphson iterations to balance the internal structural forces and externally applied forces, rather than updating stiffness matrix at the beginning of each increment. In this way, the implicit procedure does not accumulate errors and can be more stable than the explicit procedure.

The thermal models used in the thesis consider only the welding stage (heat and cooling cycles are included) and accordingly contain only one step (consisting of many small time increments). The time increment is automatically controlled to avoid convergence problems. Initial attempt increment is 0.1 second and the maximum increment is no bigger than 0.3 second. Usually maximum 5 attempts are allowed at each increment.

The heat generated by the interaction between the tool and workpiece is very complicated. The heat energy consists of at least 3 fractions, namely the friction heat between the shoulder and workpiece, the friction heat between the pin and workpiece and the plasticity energy released by deformed workpiece material. The generated heat, especially for the heat between the tool and workpiece, would transfer to both the tool and workpiece and the fraction depends on thermal conductivities and contact pressure etc. In the thermal model, the tool is not modeled and all the heat energy transferred to the workpiece is rounded into a moving heat source.

The moving heat source is modeled as a surface heat flux with symmetric profile to the welding line. The position of heat flux profile center is named as reference position. The surface heat flux moves at the welding speed with the same initial reference position as the tool.

In ABAQUS, the moving heat source is first defined as a user defined load in the model and then implemented by user subroutine DFLUX [3-1][3-2]. The user subroutine DFLUX is written in FORTRAN programming language and it defines the heat flux distribution and variation with time. At each increment, the user subroutine DFLUX will be called and the heat flux values for proper integration points are updated.

The input parameters of the user subroutine DFLUX include step time, total time, coordinates, flux type and surface name etc. The step time and total time can be used to calculate the reference position based on welding velocity. The coordinates are current coordinates of current point and are represented by an array. The flux type offers information of flux type, in case there are multiple types of heat flux involved, for example, body flux and surface flux. The surface name helps to identify different surface heat fluxes in different surfaces.

The output parameters or the parameters to be defined, in the user subroutine DFLUX are magnitude of flux flowing into the current point and its corresponding flux rate with aspect to time. The latter doesn't influence the accuracy of solution in current increment, but the convergence rate can be improved if proper value is given.

The construction of the user subroutine DFLUX can be divided into three steps, as shown in Figure 3-1. The X coordinate of reference position in DFLUX is calculated at the beginning of each call, which is aligned with the welding direction. The X coordinate can be expressed as:

$$X = v * t + X_0 \quad 3\text{-}1$$

Where X_0 is the start position of welds, v is the welding velocity and t represents step time.

The Y coordinate of reference position is constant and the same as the corresponding coordinate of the welding line.

Based on updated reference position at the beginning of each call, the distance between current point and the reference position can be calculated by:

$$R = \sqrt{(x - X)^2 + (y - Y)^2} \quad 3\text{-}2$$

Where x and y are coordinates of current point and R is the distance between current point and the reference position.

A judgment of flux type and surface name is made to ensure that the correct type of flux is applied to the correct surface and then the heat flux for this point is calculated and updated.

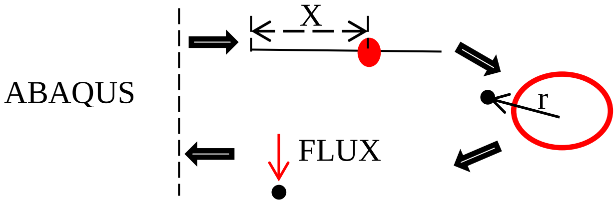

Figure 3-1 Construction procedure of the user subroutine DFLUX

The contact pressure distribution between the workpiece and the backing plate is non-uniform, thus the contact conductivity in areas are much lower than that right under the tool. In addition, due to the fact that the contact pressure varies with the moving tool, the contact conductivity between the workpiece and the backing plate also varies with the tool position.

The coordinate and time dependent contact pressure is first defined as user defined interaction and then implemented by user subroutine FILM [3-1]. At each increment, the user subroutine FILM will be called and the film conditions for proper integration points are updated.

The input parameters of the user subroutine FILM include step time, total time, coordinates, flux type and surface name etc. The step time and total time can be used to calculate the tool position based on the welding velocity. The coordinates are current coordinates of current point and are represented by an array. The interaction type offers information of film condition type, in case there are multiple types of non-uniform film conditions involved. The surface name helps to identify different surface film conditions to different surfaces.

The to be defined parameters in the user subroutines FILM include film coefficient and sink temperature for current point and film coefficient rate with aspect to time. The film coefficient rate can improve convergence rate if proper value is given.

The structure of the user subroutine FILM is similar to that of the user subroutine DFLUX. The tool position is updated according to step time at the beginning of each call, then the distance between current point and the tool position is calculated to make judgment if current point is directly under the tool. And the film coefficient is applied accordingly:

$$H = \begin{cases} H_1, R > R_0 \\ H_0, R \leq R_0 \end{cases} \quad 3\text{-}3$$

Where R_0 is the radius of the tool shoulder, H_0 and H_1 are film coefficient for the area under the tool and the other areas. The values of H_0 and H_1 depend on specific cases and assumptions.

The thermal stress model is a fully coupled model, in which the thermal and mechanical solutions are calculated simultaneously rather than sequentially. This fully coupled model is able to predict transient temperature field and transient stress field. The model can take account heat input to the workpiece, frictional and axial forces imposed by the tool and externally active cooling source into consideration and it describes the welding stage and cooling stage, thus there are two steps in the model with different loads and boundary conditions.

In this model, the heat input of the workpiece is extended to a 3D profile. Not only the heat generated between the tool shoulder and workpiece is considered, but also the heat generated between the tool probe and workpiece. The heat energy between the tool probe and workpiece is simplified to a ring distribution through the thickness and a uniform circular distribution on the bottom surface. The through thickness ring heat distribution is simplified to body heat flux, where others remain surface heat flux. The 3D heat input in this model is simplified 3D moving heat source and implemented by the user subroutine DFLUX.

The structure of DFLUX in the thermal stress model is similar to that used in the thermal model. The first step is to determine the transient reference position at the beginning of each call. Then judgment is made to determine whether the heat flux type is surface flux or body flux. If the type is body flux, the heat flux magnitude is calculated by:

$$H_b = C_b Q/(2\pi R_p * L_p) \quad 3\text{-}4$$

Where H_b is the body flux returned by the user subroutine DFLUX and Q is the total input power to the workpiece, C_b is a fraction, R_p is the radius of the tool probe and $\mathrm{L_p}$ is the length of the tool probe.

If the type is surface flux, a further judgment based on surface name must be made to determine whether current point is on the top surface or not. If yes, the heat flux magnitude is then calculated according to flux distribution between the tool shoulder and workpiece. If no, the heat flux magnitude is calculated according to flux distribution between the tool probe and workpiece.

An active cooling source can be introduced in this model. In contrast to the heating source, the active cooling source absorbs energy from workpiece and usually the heat transfer rate from workpiece to cooling medium is relatively large, thus the temperature of workpiece near the cooling source drops quickly.

The active cooling source is modeled as film conditions in this model and is implemented by the user subroutine FILM. The user subroutine FILM for traditional active cooling source is similar to that in thermal model. But for discontinuous cooling source, it is more complicated.

Figure 3-2 shows structure of the user subroutine FILM for a discontinuous cooling source. The first step in FILM is to calculate reference position according updated step time at each call. Then judgment is made to determine whether the current step time is within designated cooling time slot. If yes, the coordinates of current point is compared to the reference position to determine if it is with the cooling area. Uniform film coefficient magnitude is assigned to points in cooling area. Otherwise, the coefficient magnitudes are zeros.

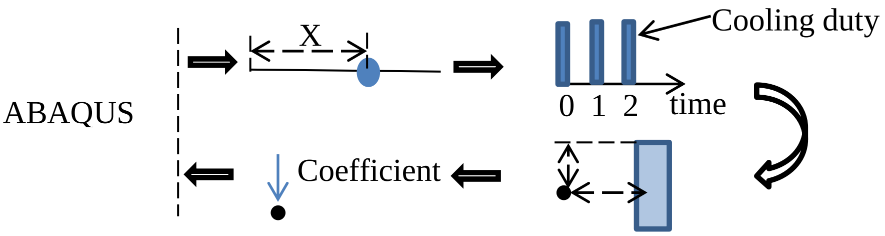

Figure 3-2 Structure of user subroutine FILM for discontinuous cooling source

The forces imposed by the tool mainly consist of axial pressure and frictional force. The pressure distribution is considered uniform under the tool shoulder, thus can be calculated by axial force divided by area of the tool shoulder. The frictional force is not symmetric because of longitudinal welding velocity. In this model, the friction coefficient is considered, thus the magnitude of frictional force for each point is the same. The direction of frictional force varies and depends on relative coordinates to reference position of tool.

The forces are implemented in user subroutine DLOAD [3-1][3-3]. The user subroutine DLOAD is called at each increment for each integration point to update load for this model.

The input parameters of the user subroutine DLOAD include step time, total time, coordinates, flux type and surface name etc. The step time and total time can be used to calculate the reference position based on welding velocity. The coordinates are current coordinates of current point and are represented by an array. The load type offers information of loads, in case there are multiple types of loads involved, for example, body forces and surface pressure. The surface name helps to identify different pressure loads applied to different surfaces.

The output parameters of the user subroutine DLOAD are the forces and loading rate, while the loading rate mainly serves to improve the convergence rate.

Figure 3-3 shows the structure of the user subroutine DLOAD. Similar to the other user subroutines, the first step in DLOAD is to calculate the transient reference position and next the load type is determined. If the load is axial pressure, then the force is calculated based on the distance between current point and the reference position. Otherwise, the load is surface frictional force and then the coordinates of current point are used to determine the relative location to the reference position. Components of friction forces are calculated from:

$$F_x = \begin{cases} -\frac{F_{total}}{\pi {R_s}^2} * \mu * \frac{abs(x-X)}{r0.0005}, y - Y > 0 \\ \frac{F_{total}}{\pi {R_s}^2} * \mu * \frac{abs(x-X)}{r0.0005}, y - Y \leq 0 \end{cases} \quad 3\text{-}5$$

$$F_y = \begin{cases} \frac{F_{total}}{\pi {R_s}^2} * \mu * \frac{abs(y-Y)}{r0.0005}, x - X > 0 \\ -\frac{F_{total}}{\pi {R_s}^2} * \mu * \frac{abs(y-Y)}{r0.0005}, x - X \leq 0 \end{cases} \quad 3\text{-}6$$

Where F_x and F_y are friction force components at X and Y axis directions, F_{total} is the Z axial force, R_s is the radius of the tool shoulder, μ presents the friction coefficient and the constant 0.0005 indicates the frictional forces are only applied to the workpiece within a thickness of 0.5 mm.

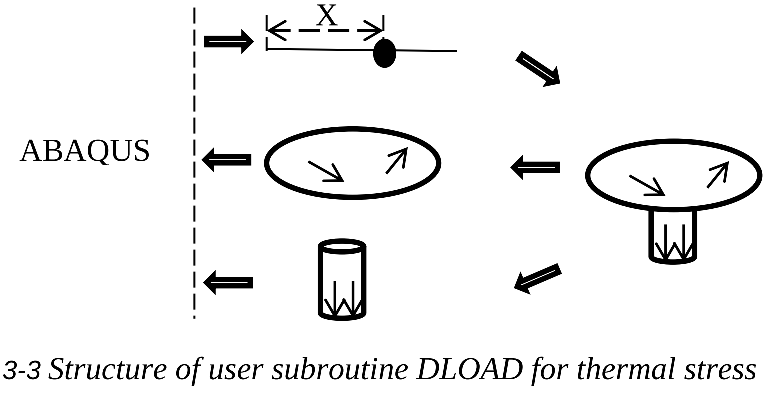

Figure 3-3 Structure of user subroutine DLOAD for thermal stress model

The thermal-stress-microstructure model couples a thermal model, stress model and microstructure model. In this model, physical based material properties are used and a simplified precipitation model is established, which is able to predict ultimate hardness / strength distribution for friction stir welds.

The physical based material properties depend on both transient temperature and historical temperature experienced, in other words, the constitutive relation is solution dependent. In this model, the strain stress relationship is implemented by user subroutine USDFLD [3-1].

The yield strength is defined to be linear with a user defined variable, which is updated by the user subroutine USDFLD at each increment. Input parameters for the user subroutine USDFLD include step time, total time and time increment for this increment, coordinates and other parameters necessary for utility routines. Must-to-be defined variables of the user subroutine USDFLD are user defined variables, which are predefined in the model and usually are an array. Alternatively to be defined variables are state variables, which are passed into the user subroutine USDFLD for information.

Figure 3-4 shows the structure of the user subroutine USDFLD for constitutive model. The first step is to call utility routine GETVRM [3-1] to retrieve transient temperature of current point and compare it with state variable historical peak temperature, whose initial value is ambient temperature. If the transient temperature is bigger than the historical peak temperature, then the historical peak temperature is updated with the same value of the transient temperature and the user defined variable for yield strength is calculated according to the transient temperature. Otherwise, the user defined variable for yield strength is dependent to both the transient temperature and the historical peak temperature.

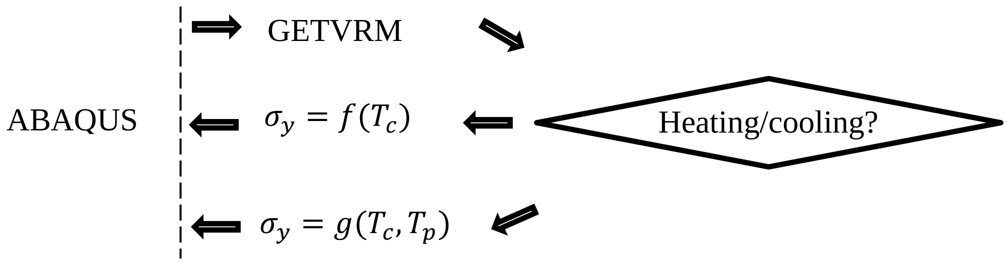

Figure 3-4 Structure of the user subroutine USDFLD for physical based constitutive model

The microstructure model takes heating and cooling history as input, including historical peak temperature and the 'heating duration' and calculates hardness / strength as output. In addition, a time-saving technique identifying a zone of interest is applied by setting flags for material points.

Figure 3-5 shows the structure of the user subroutine USDFLD for the microstructure model. The first step is similar to the user subroutine of the constitutive model. If the transient temperature is above the critical temperature, a flag is set and the hardness / strength model applied. Two state variables T_p and T_c are used to track the heating duration which are essential for hardness / strength prediction. H is an user defined variable indicating the reference value of hardness.

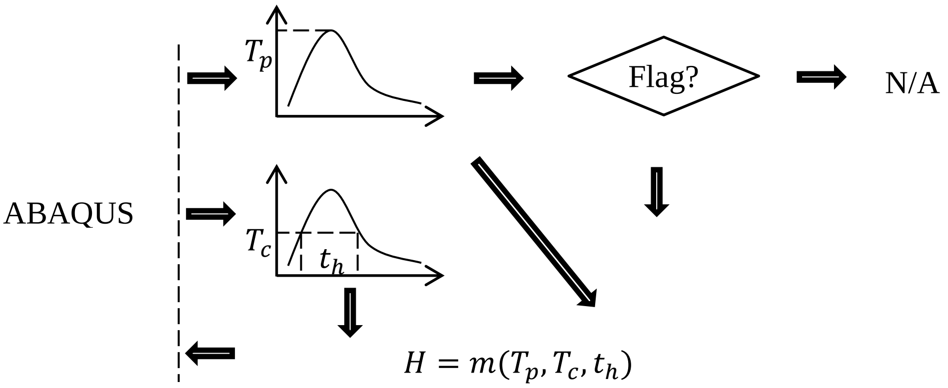

Figure 3-5 Structure of the user subroutine USDFLD for microstructure model

The time increment is semi-manually controlled in the user subroutine USDFLD. In step setting, the estimated time increment is automatically controlled by an ABAQUS algorithm. To precisely control cooling duty, which is essential to the temperature of the workpiece material and therefore significant to the microstructure model, the time increment is fine tuned to ensure the discontinuous cooling starts exactly when step time is rounded seconds and stops exactly after cooling duty. The semi-manual time increment control can be expressed as:

$$t_{inc} = \begin{cases} 0.8 * t_{inc}^{e}, t + t_{inc}^{e} > floor(t) + 1 \\ 0.8 * t_{inc}^{e}, t + t_{inc}^{e} > floor(t) + 0.2 \ and \ t < floor(t) + 0.2 \\ t_{inc}^{e}, other \ conditions \end{cases}$$

Where t_{inc}^{e} is the step time increment estimated by ABAQUS algorithms, t_{inc} is the step time increment suggested by the user subroutine USDFLD, t represents the step time in second unit and $floor(t)$ is the function which return the next lower integer to t.By control the step time increment, the active cooling can precisely start at rounded seconds and last 0.2 second at the frequency of 1Hz.

3.1.1 Python Scripts

Python script [3-6] is a general purpose, interpreted and high level programming language. It features comprehensive standard libraries and has a large group of users and developers continuing to enrich and optimize the libraries. Python is also the programing language for ABAQUS, which offer numerous application interface (API) [3-4]. Taking advantages of API from ABAQUS, Python script can be used to create finite element models, submit jobs and monitor job status and extract output from ODB databases or result files [3-5], making the analysis procedure automatic and saving modeling effects.

Parametric models are frequently used in investigating influence of variables or parameter optimizations and usually involve modification or assignment of parameter values in model files such as FORTRAN files for user subroutines. Python script is used to implement parametric models and the procedure is described as follow. After a template model is built, Python script starts to search the position (line number and column number) of parameters in the model files and change the parameter values according to designated ranges and intervals. Then the new model files are numbered and saved sequentially.

After the parametric models are generated, they are parallel submitted to a high performance cluster (HPC). Figure 3-6 shows the structure of the HPC [3-7], including headnodes and standard nodes. The headnodes provides interfaces to end users via secured remote login, such as uploading files to the HPC, downloading files from HPC to local drive, monitoring current status of HPC and submitting jobs to HPC, while the standard nodes are parallel computing nodes, which actually run the jobs when required. The HPC is shared among a group of users and usually under heavy utilization, so the best way to avoid interrupting other users while maximizing the usage of HPC is adjusting parallel running jobs to avoid load peak and increasing parallel running jobs when the load is relatively lower; for example, at night or on holidays. As license tokens for ABAQUS are very limited in the research programme compared to demands, it is also necessary to monitor the available tokens into account to determine the number of parallel jobs. In addition, the running jobs might be interrupted by kinds of errors, for example, hardware failure, which is relatively common in distributed computing systems. So job status should be monitored and actions should be taken if abnormal status is detected.

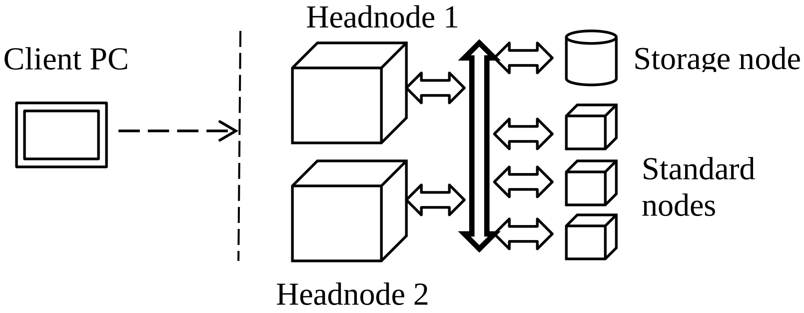

Figure 3-6 Structure of HPC

Another technique for parametric models is extracting solution data from output database, which contains various solutions of the models. ABAQUS offers API to extract results from ODB files by Python script. Figure 3-7 shows the structure of output databases. The databases are comprised of model data and solutions data. For model data, the parts, sections and materials are included; for solutions data, there are steps, field output data and history output data.

Based on the structure of ABAQUS output database, procedure to extract field output data by Python script, for example, node temperature is divided into three steps. First, the step is identified if the model output results in multi steps. The steps can be identified either by their sequence starting from 0 or their names. Once the correct step is selected, step time should be determined, which can be acquired by inquiring the frames sequentially. Next the solutions data can be found by their names, for example, node temperature can be identified by ‘NT11’ [3-3]. The solutions data are actually arrays of solutions for nodes or elements and can be distinguished by their labels.

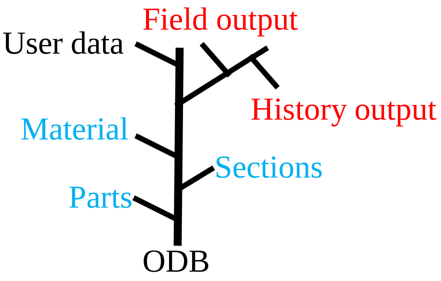

Figure 3-7 Structure of ABAQUS output database

Usually an automatic procedure logically links the parametric model generation procedure, job submission and monitor procedure, data extraction procedure and optimization algorithms, as shown in Figure 3-8. The main optimization algorithms used in the thesis are genetic algorithms and artificial neural network algorithm, which are introduced in section 3.2 and section 3.3 respectively.

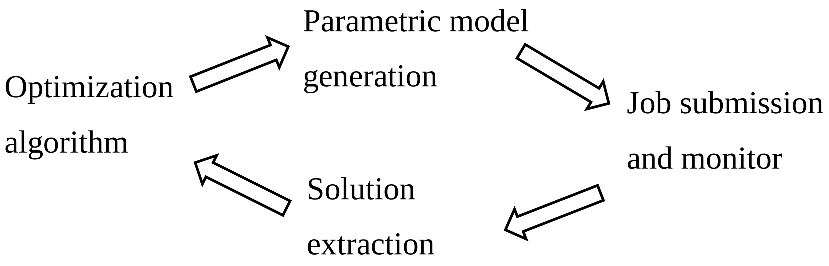

Figure 3-8 Schematic of automatic optimization procedure

3.2 Genetic Algorithms

Invented by John Holland, genetic algorithm is an evolutional optimization algorithm that modifies variables iteratively. A genetic algorithm simulates the natural evolution by using crossover and mutation operations to reproduce new variables for next iteration, which are similar to DNA reproduction. Genetic algorithms offer progressive optimizations and don’t require explicit information between parameters and/or the optimization objectives. They have already been used to optimize structural loading, adaptively control robots and solve mathematic problems numerically, etc.

The groups of variables in genetic algorithm are called seeds and the group of seeds in an iteration is called one generation. Seeds are presented by integers in range from 0 to 255 in the format of 8 binary digits.

The procedure of genetic algorithm mainly consists of initialization, fitness ranking and reproduction steps. At the initialization step, the necessary parameters are initialized, for example, the amount of variables to be optimized and the size of each iteration / generation. Then values of the variables are mapped from integer domain to real domain according to their search/definition spaces to be assigned to parametric models. The solutions of the parametric models are then extracted and used to calculate the fitness of corresponding seeds. If the highest fitness is lower than critical fitness, then the seeds of current generation are crossed over and mutated to reproduce seeds for next generation. These steps would be repeated until the highest fitness is no less than critical fitness or the number of generation reaches designated value.

The crossover operation is shown in Figure 3-9(a). Two seeds in the same generation are randomly selected and then crossover digit is randomly determined. Then the digits before the crossover digit are exchanged, while other digits remind unchanged. By this way, two new seeds for next generation are prepared.

The mutation operation is shown in Figure 3-9(b). Only one seed is randomly selected for each mutation operation and the mutation digit is determined by random selection function. Once the seed and the mutation digit are selected, the binary value of the mutation digit is reversed. By this way, one new seed is prepared after each mutation operation.

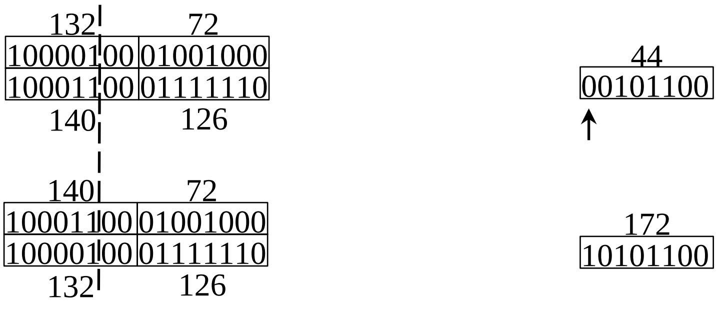

(a) (b)

Figure 3-9 Reproduction procedures: crossover and mutation

The genetic algorithm in the thesis is implemented by Python script. In addition to the genetic algorithm, the automatic parametric model generation, intelligent job submission and monitor and data extraction, special care is taken to allow restoration from interruption since usually the genetic algorithm runs for a relatively long time and might be interrupted by various unexpected circumstances. Restoring the genetic algorithm can avoid wasting previous work and make the algorithm more stable.

The restoring procedure includes interruption field determination and field processing. First information of the interrupted generation is determined by searching the database recording the running status of generation algorithm. The information includes the seeds of the interrupted generation and the incomplete parametric models. Next the incomplete models are submitted and results are retrieved after completion. Then the procedure goes into the normal procedure and the restoring procedure ends.

3.3 Artificial Neural Network

An artificial neural network is a computational model with similar structure to biological neural network. Applications of artificial neural network include vehicle control, object recognition, data mining, etc. In most cases, the artificial neural network [3-8] is comprised of connected artificial neurons and can be expressed in a format of three layer structure, namely input layer, hidden layer and output layer, as shown in Figure 3-10. Each neuron in the artificial neural network represents a non-linear operator with several adaptive parameters. The outputs of all neurons in the input layer are input of neurons in the hidden layer and accordingly the inputs of neurons in the output layer are the output of all neurons in the hidden layer.

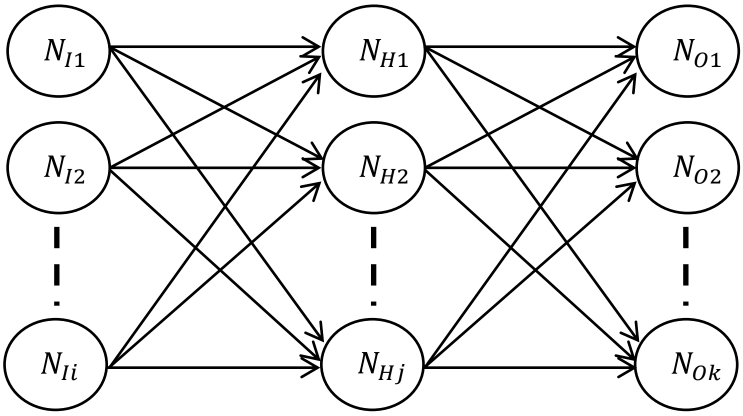

Figure 3-10 Structure of artificial neural network

The artificial neural network applied in the thesis is a back-propagation (BP) neural network, which uses supervised learning paradigm to adjust parameters of the neurons. A BP neural network can approximate the complex relationship between input data set and target data set by adjusting the parameters to minimize the error between target data set and output data set. Application of the BP neural network algorithm usually involves database preparation, neural network training and prediction. In this thesis, the database preparation provides the input data set and the target data set by numerical methods. The input data set are parameters of finite element models, while the target data sets are solutions of the models, for example, load forces. During the training progress, the parameters of the neurons are first randomly assigned and then adjusted based on the error between target data set and output data set at each epoch according to learning algorithms. This progress ends until the error between target data set and output data set is lower than designated value and the BP neural network is trained. Output of the trained neural network from input data which is not included in the training database is called prediction. The accuracy of prediction depends on the training progress.

The BP neural network is implemented in MATLAB using the neural network toolbox. The database preparation is done by Python script and then the input data set (load forces at different displacements) and target data set (material property parameters in small punch beam test) are extracted. Three layer structures is established and the amount of neurons in the input layer is the same to the dimensions of input data (the dimension of load force vectors) and the amount of neurons in the output layer is the same to the dimensions of the target data (the amount of material property parameters), while the amount of neurons in the hidden layer is estimated by empirical equation:

$$j = \sqrt{i * k} + a \quad 3\text{-}7$$

Where $i, j, and\ k$ are the amount of neurons in the input layer, the hidden layer and the output layer and a is an integer in the range of 1 and 9.

When the BP neural network is trained, the experiment force vector is then used to predict material property parameters.

3.4 Small Punch Beam Test

Compared to conventional material property test methods, the small punch test - a miniaturized testing method - is characterized by the small specimen size used. The miniaturized specimens are usually disks with diameter 10 mm and thickness 0.5 mm and such a small volume of material could be removed from relatively large components without weakening the strength and safety of the components. Primary applications of the small punch test include charactering degraded material properties of in-service pressure vessels and pipes in power plants without requirement of suspending service or post-test repairing.

The small punch beam testing method in this research uses a low-cost and easily manufactured punch, compared to small punch test’s spherical punch, and can be used to identify mechanical property distribution of welds in a single test. The specimens for the small punch beam test can be easily sampled from welded components. A new type of tool testing system, shown in Figure 3-11, was developed as part of the research programme. The tool consists of a top and bottom blocks, each having a narrow through slot. The test beam specimen is located in a shallow slot perpendicular to the through slot. The punch is a rectangular bar with a half-cylinder profile contact surface, overcoming the manufacturing difficulties associated with a hemispherical punch. The radius of the punch head is 1.25 mm and the width of the punch is 8 mm. The test specimen shown in Figure 3-12 is a beam with rectangular cross section with width of 2 mm and height of 1.6 mm. The height of the beam is slightly greater than the depth of the shallow slot, such that when the four fixing screws are tightened the beam sample is fully clamped. The central part of the beam is 8 mm and an additional 8 mm material is included at both ends to hold the beam. Chamfers with size 0.2 mm * 45^o were created on the bottom slot to avoid stress singularity. The four screws were tightened with same torque using a torque wrench to keep the top and bottom surfaces parallel. The punch is guided by the slot in the top block. The bottom block is made of two pieces, making the chamber easier to manufacture. The top and bottom blocks and punch are made of stainless steel, while the tested specimen is aluminum AA2024. The specimen material Young’s modulus and Poisson’s ratio are 73.1 GPa and 0.3 respectively. Lubricant was applied to the punch top surface and the side surface to reduce the friction between the punch and specimen and punch and the top block slot.

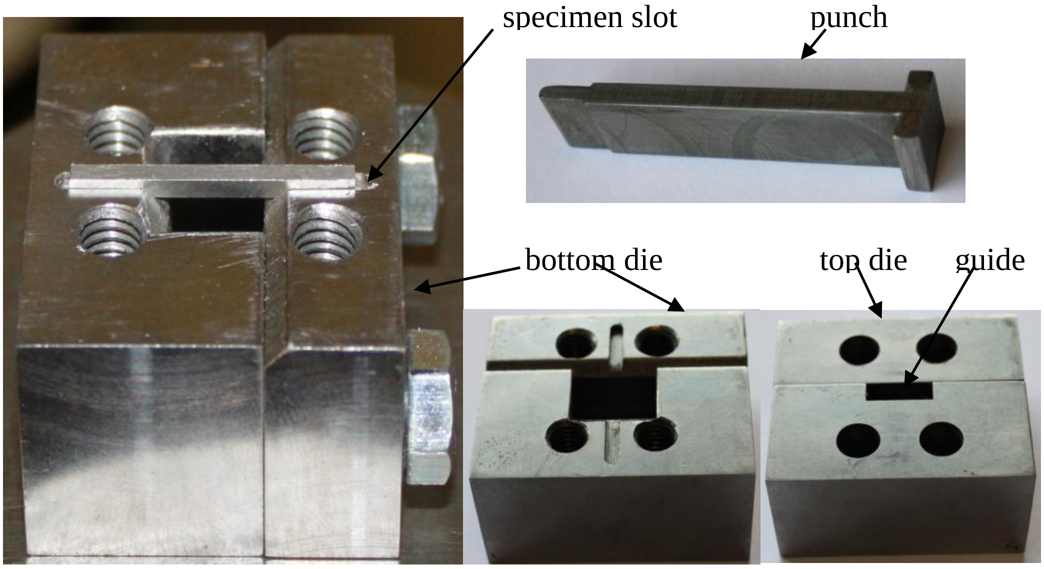

Figure 3-11 Small punch tool system

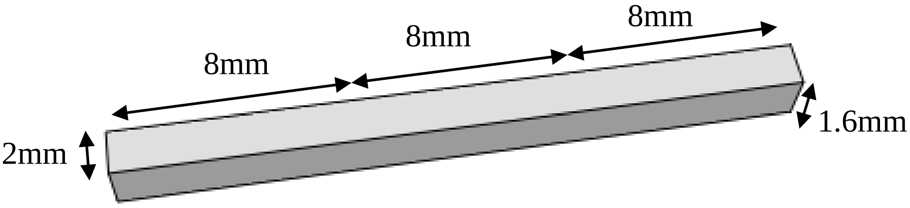

Figure 3-12 Specimen for small punch tool system

3.5 References

[3-1] Abaqus 6.09 User Subroutines Reference Manual

[3-2] Abaqus/CAE 6.09 User's Manual

[3-3] Abaqus Analysis User's Manual

[3-4] Abaqus Scripting User's Manual

[3-5] Abaqus Scripting Reference Manual

[3-6] Core Python Programming 2nd Edition, Wesley J. Chun, published by Prentice Hall, September 18, 2006

[3-7] Handouts of HPC training courses

[3-8] MATLAB manual

4 FSW model Parameter Identification

The temperature history plays a very important role in FSW, as it affects final grain size and distribution and dissolution of precipitates and consequently affects the mechanical properties of the weld.

Gould [4-1] investigated the temperature distribution in the FSW workpiece using the Rosenthal equation, assuming that heat was solely generated by the work done by the friction force between the workpiece and tool shoulder. Vilaca, *et al* [4-2] also used the Rosenthal equation to derive an analytical solution for thermal distribution by placing the point heat source at the middle plane along the thickness direction of the workpiece and considered the heat generated from both the translation and rotation of the welding tool.

Several types of numerical thermal modeling methods have also been investigated. Chao [4-3] *et al*. initially presented a 3-D thermal model including heat generation from the shoulder. Later, they used an inverse method to obtain thermal parameters with the analysis of the separated models of workpiece and tool [4-4]. In Colegrove's model [4-5], heat generated from shearing of the material and friction on the vertical and threaded surface of the pin were studied. The 3-D thermal model of Khandkar *et al* [4-6] correlated the heat input and the experimentally measured torque, considering different types of contact conditions including sliding, sticking and partial sliding/sticking. A detailed review on the simplified FSW thermal model can be found in [4-7].

However, FSW is a complicated thermal-mechanical process and some modeling parameters such as film coefficient and thermal radiation of the work pieces may be technically difficult and/or expensive to measure experimentally. Previous research on numerical FSW thermal modeling mainly focused on trial and error methods to obtain these thermal parameters. This may be very time consuming or difficult to obtain optimal values. Therefore, it is important to establish a systematic procedure to identify FSW process parameters.

In this chapter, an automatic genetic algorithm method for characterization of FSW thermal parameters Q1 and Q2 is presented, where Q1 and Q2 are the heat input rate to the workpiece generated by the tool and conductive heat loss from the workpiece to the backing plate. Experiment results from reference [4-4] are used to validate the proposed method. In the following section, a brief introduction of how ABAQUS Python commands are used to manage a high performance cluster by allocating finite element jobs to different nodes to perform parallel simulation is given. An investigation of a basic finite element thermal model, which was used for thermal parameters identification in the later simulation, is then presented.

4.1 ABAQUS python scripts for parallel simulation

The identification process for FSW thermal parameters Q1 and Q2 includes:

a. Build a trial FEM thermal model with guess values for the parameters to be identified.
b. Employ a genetic algorithm (GA) method to obtain the optimal values for these parameters
c. Use a high performance cluster for FEM simulation, with the thermal parameters updated by the GA procedure.

Due to the large amount of FEM modeling involved, a systematic procedure was developed. Use of ABAQUS python scripts provided an effective way to deal with the problem. Before the start of the ABAQUS python procedure, a basic FEM thermal model is established as described in Chapter 3. The basic FEM loaded with a continuous point heat source is compared with theoretical resolution for verification purpose.

Figure 4-1 shows the flow chart used for thermal parameters optimization. Firstly, the basic ABAQUS model file is called and the heat input and surface film coefficient user subroutines are prepared. Secondly, the GA module is called to modify thermal parameters in user subroutines. Each GA generation consists of 20 seeds, therefore 20 FEM models are prepared. Thirdly, 20 different ABAQUS jobs are allocated and submitted to different HPC nodes. Fourthly, after these jobs have finished, the ABAQUS post-processing program is called to extract the temperature history data at the points of interest for all the models. The calculated results are then compared with the experimental results and the procedure stopped if the convergence criterion is satisfied or the total iteration number reached. Specifically for this chapter, the criterion can be satisfied if objective function (defined later in equation 4-2) is no larger than 3.5% or the iteration number is larger than 30. Otherwise, go to second step and repeat the second step to fourth step until the defined criterion is satisfied.

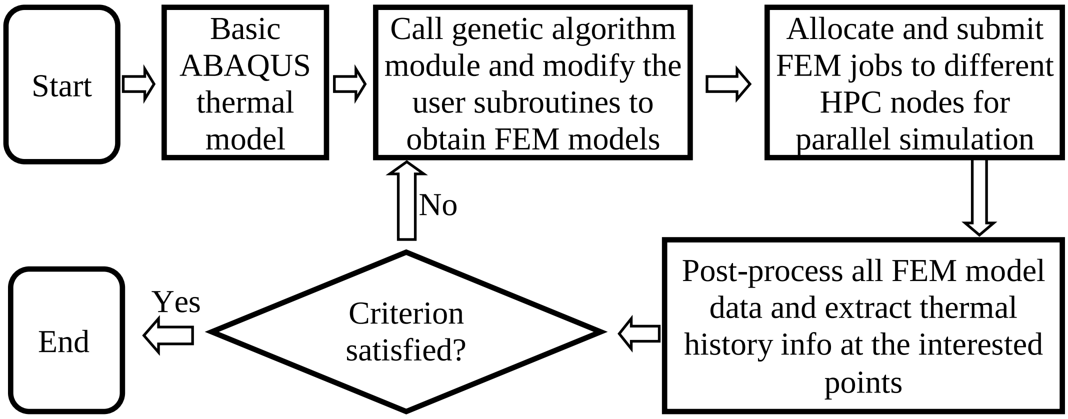

Figure 4-1 ABAQUS python procedure for parameters optimization

4.2 FSW Finite element thermal model

To validate the proposed FSW process thermal parameters identification method, the FSW experiment results from [4-4], in which two aluminum plates of length of 610 mm, width 102 mm and thickness 8.1 mm are friction stir welded, are used for comparison. The case with tool traverse speed of 2.36 mm/sec is considered. Thermal history data at the point 5 mm from the weld line on top surface, named as Point C, is used for thermal parameter characterization, while the temperature variation with time at another point, named as point D, on middle thickness plane of the plate and 12.7 mm distance from the central line is employed for validation.

To obtain the optimized values for the FSW thermal parameters, large numbers of FEM models have to be analyzed. Because only thermal parameters are to be identified, a basic FEM model is analyzed and serves as a model for other simulations. The only change for other models is the modification of Q1 and Q2 and their values are written into the models through ABAQUS user subroutines.

4.2.1 Basic thermal model

Figure 4-2 shows a simplified FSW 3D transient thermal model with a continuous point heat source applied at point A, i.e. the center point along the welding line. As two identical aluminum plates are to be welded, a half model is analyzed. The ABAQUS 3D 8-node brick element is employed and the model contains 19215 nodes and 14560 elements. The material thermal conductivity and specific heat are taken from reference [4-4]. Assuming no heat dissipation from the workpiece, the numerical results can be compared with analytical solution where a point heat source is applied to an infinite plate. The analytical temperature formulation for any point at time *t* is given in Equation 4-1 [4-8].

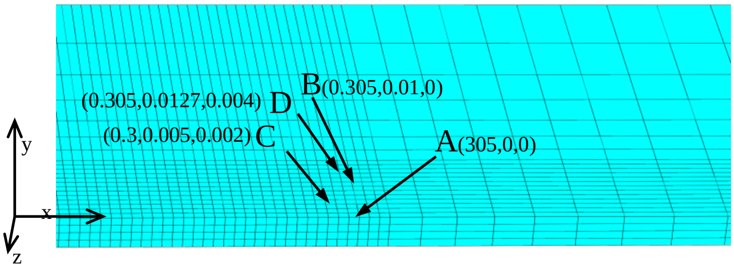

Figure 4-2 FEM mesh of simplified FSW 3D ABAQUS thermal model. A point heat source is applied at the central point along the weld line

$$T(R,t) = \frac{q}{2\pi\lambda R}\left[1-\Phi\left(\frac{R}{\sqrt{4at}}\right)\right] \quad \text{4-1}$$

Where the heat rate q, conductivity λ, specific heat c and density ρ are 1000 W, 120 W/m2, 1000 W/m3 and 2700 kg/m3 respectively, $a = \lambda/(c*\rho)$ and $\Phi(u)$ is the probability integral function, *R* is the distance from the heat source and *t* is time in second.

Figure 4-3 is the comparison of the temperature history between the numerical and theoretical solution at point B (10 mm from point A along the line perpendicular to the weld line). From this figure, it can be seen that the numerical results are in good agreement with that of the analytical results for time *t* up to 1.1 seconds. However, as time increases beyond 1.1 seconds the error increases. This error is mainly because heat can be accumulated in the numerical model with small thickness, while for the theoretical model the heat can be transferred to the far field. The error is not caused by the mesh and integration step time, therefore this model serves as a basic model for the later simulation.

4.2.2 FSW FEM model for thermal parameters characterization

The thermal model used for FSW is based on the basic thermal model. Instead of a continuous point heat source, an undefined moving heat source with a constant total heat input rate *q(r)* from the tool shoulder is assumed. This total heating power is labeled as Q1, The heat input rate for each point under the shoulder will be proportional to the distance (r) from the point to the center of the shoulder, as shown in Figure 4-4, where r_o is the radius of the tool shoulder.

The undefined heat transferred from the workpiece to the support plate Q2 is assumed to have uniform distribution and is modeled using a thermal film coefficient. The advantage of introducing $Q2$ is that there is no need to include the support plate into the FEM model. Hence, the total CPU time for the simulation is saved.

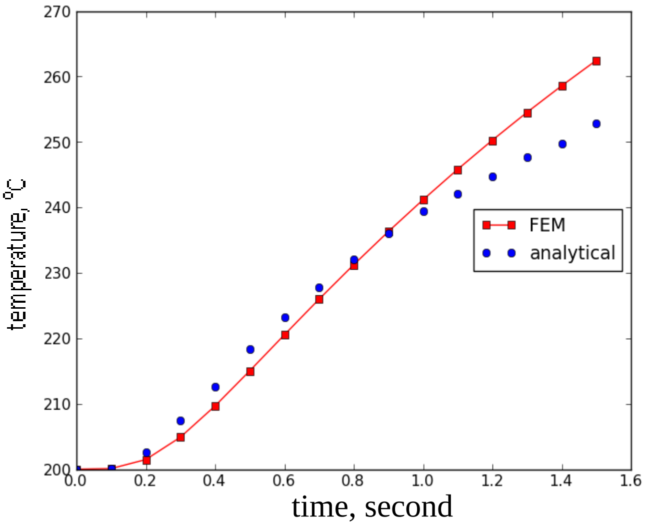

Figure 4-3 Comparison of temperature result between FEM and analytical model

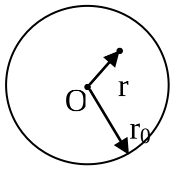

$$q(r) = \frac{3Q_1 r}{2\pi r_0^3} \quad [4\text{-}4]$$

Figure 4-4 Heat input rate distribution under the tool shoulder

The heat dissipated from the side and the top surfaces of the workpiece to air is considered through the use of thermal film coefficient with a value of 30w/m^2 in the FE model. Due to symmetry, no heat exchange occurs on the middle plane along the weld line. The initial temperature for the whole workpiece is assumed to be 25^{o}C. Material properties, including specific heat and conductivity, are assumed to vary with temperature and are listed in Table 4-1 and Table 4-2 respectively [4-4].

Table 4-1 Conductivity property of workpiece [4-4]

conductivity	90	100	110	120	130	140	150
temperature	0	50	100	150	200	250	300

Table 4-2 Specific heat of workpiece [4-4]

Specific heat	900	1000	1077	1100
temperature	0	150	250	300

4.3 Genetic algorithm for thermal parameters characterization

The combined effect of parameters to be identified in the definition space can't and analytically solved. The GA optimization method doesn't require it and suitable in this case. In addition, parallel simulations can be easily adopted in genetic algorithms' iterations, which could accelerate the optimization progress. Here, optimal values for Q1 and Q2 are to be identified. In using GA, Q1 and Q2 will be represented by an integer (in 8 bits binary format) with the range of 0 to 255. The real values of Q1 and Q2 can be calculated from the integer using the formulation shown in Figure 4-5, with a given range for Q1 and Q2, vice versa. In this case, the assumed searching ranges for Q1 and Q2 are [1000 W, 2000 W] and [100 W/m^2/^{o}C, 500 W/m^2/^{o}C] respectively.

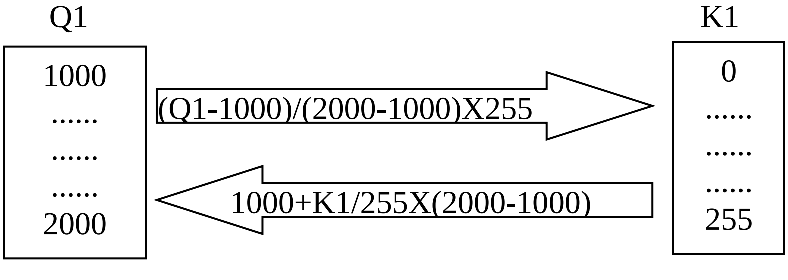

Figure 4-5 Real value of Q1 can be transferred to integral from 0 to 255, vice versa

The flow chart of the GA process is shown in Figure 4-6. Initially, 20 sets of chromosomes corresponding to Q1 and Q2 are randomly generated. The real values of Q1 and Q2 are then calculated. Following this, 20 FEM thermal model jobs are prepared and submitted to the HPC. After the solutions are complete, the temperature history data is extracted at the points of interest, such as points C and D defined in Figure 4-2.

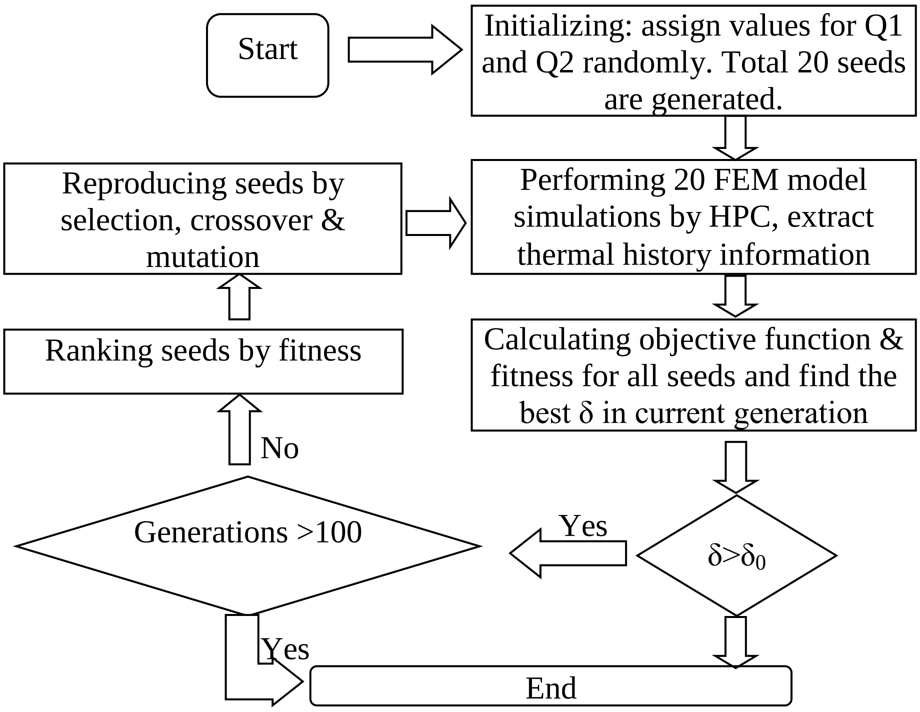

Figure 4-6 GA flow chart for identification of FSW process thermal parameters

The value of the objective function δ for each seed is then calculated, where:

$$\delta = \sqrt{\frac{1}{n}\sum_{i=1}^{n}\left(\frac{T_{cal}^{i}-T_{exp}^{i}}{T_{exp}^{i}}\right)^{2}} \quad \text{4-2}$$

δT^{i}_{exp} and T^{i}_{cal} are the experimental and calculated temperature for the *i*th seed respectively and n represents the total points extracted from the temperature vs. time curves.

The fitness for each seed is defined as $f = 1/\delta$ and is the largest value of fitness in one generation, which is selected to characterize the fitness of that generation. If the value of δ is smaller than a specified criterion value or the total number of generation is larger than 100, the GA process stops. Otherwise, new off-spring for the next generation will be created through selection, cross-over and mutation. These steps are repeated until the criterion is satisfied.

4.4 Numerical results

The GA module and ABAQUS Python codes based on the GA flowchart shown in Figure 4-6 and the ABAQUS Python procedure shown in *Figure 4-1*, were developed. The temperature history [4-4] at point C (see Figure 4-2) are divided into 20 segments, therefore 21 experiment data points are used for calculating the GA objective function value.

The data points were chosen after 100 seconds of welding because the temperature is not sensitive to the welding time at an earlier stage. After GA evolution to the 35th generation, the average relative error between the experimental and numerical results is smaller than 5%. The values for thermal parameters Q1 and Q2 obtained are 1714 W and 462 W/m^2. Using these identified parameters and performing ABAQUS simulation again, the comparison of experimental and numerical results at point C shown in Figure 4-7 is obtained. It generally agrees with the results experiment except for the peak temperature value. This may be explained by the measurement error and evidence of distorted measured temperature data can be observed from [4-4]. The thermal history at point D was also predicted for validation purpose, as shown in Figure 4-8. The comparison at Point D shows that the proposed numerical model is reliable and accurate, as the measured point D temperature data at was not utilized in the thermal parameters characterization procedure. The relative error between the predicted and experimental results is plotted against GA iteration number in Figure 4-9.

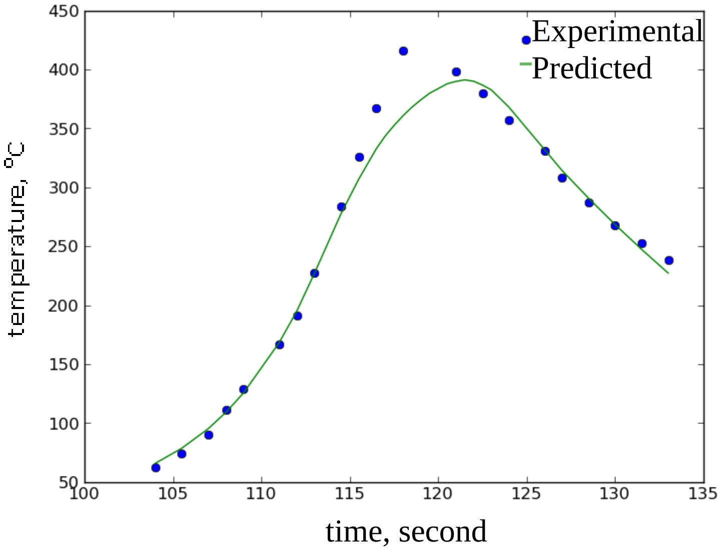

Figure 4-7 Comparison of experimental [4-4] & predicted temperature at point C

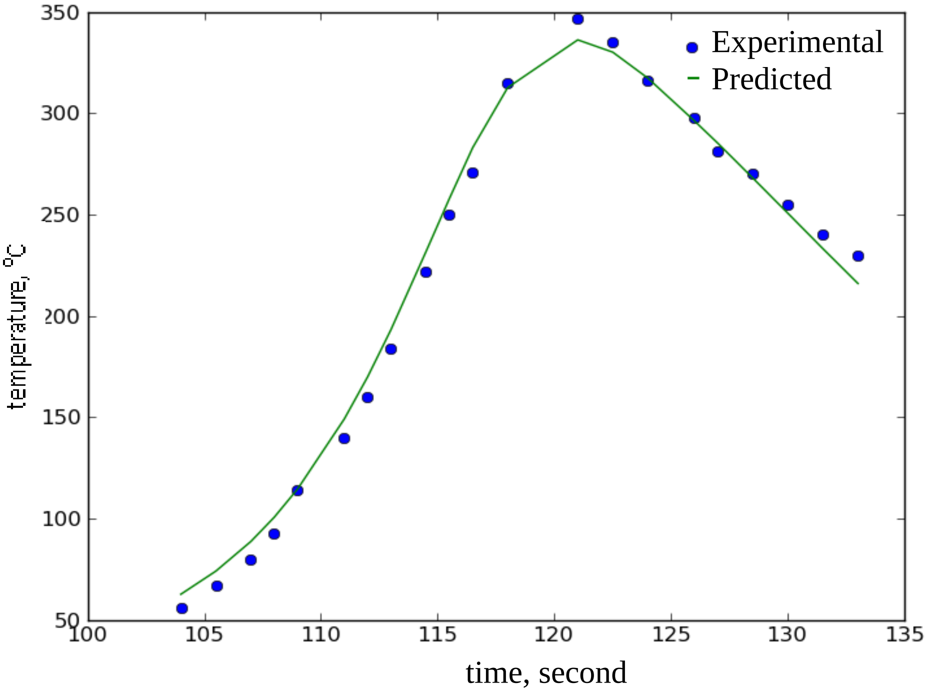

Figure 4-8 Comparison of experimental [4-4] & predicted temperature at point D

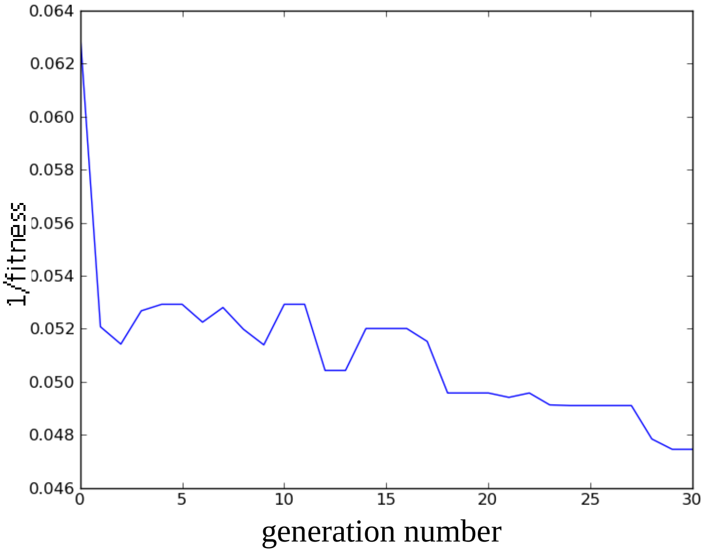

Figure 4-9 Fitness evolution history

4.5 References

[4-1] J. Gould, ‘Heat Flow Model for Friction Stir Welding of Aluminum Alloys’, J. of Materials Processing and Manufacturing Science, Vol.7, 1998, pp185-194.

[4-2] P. Vilaca, L. Quintino and J.F., Santos, “iSTIR-Analystical Thermal Model for Friction Stir Welding”, J. of Materials processing Technology, Vol.169, Issue 3, 2005, pp452-465.

[4-3] Y.J. Chao, X. Qi, ‘Thermal and Thermo-mechanical Modelling of Friction Stir Welding of Aluminum Alloy 6061-T6 plates’, Journal of materials Processing and Manufacturing Science, Vol. 7, pp. 215-233, 1998

[4-4] Y.J. Chao, X. Qi and W. Tang, ‘Heat Transfer in Friction Stir Welding-Experimental and Numerical Studies’, Journal of Manufacturing Science and Engineering, Vol. 125, pp. 138-145, 2003

[4-5] P. Colegrove, ‘3-Dimentional Flow and Thermal Modelling of the Friction Stir Welding Process’, Proceedings of the 2nd International Symposium on Friction Stir Welding, Sweden, August 2000.

[4-6] M.Z.H. Khandkar, J.A. Khan, A.P. Reynolds, ‘A Thermal Model of the Friction Stir Welding Process’, Proceedings of IMECE2002, ASME International Mechanical Engineering Congress & Exposition, New Orleans, Louisiana, November, 2002.

[4-7] H.J. Li, “Coupled Thermo-Mechanical Modelling of Friction Stir Welding”, PhD thesis, University of Strathclyde, UK. 2008.

[4-8] W.Y. Zhang, “Heat transfer theory for welding”, Mechanical Industry Press, 1989.10, ISBN 711101667X: P.27-28.

5 Active Cooling in FSW

As an advanced welding technology, FSW has extensive merits in welding traditionally unweldable metals such as high strength aluminum alloys with low distortion [5-1]. The thermal input to the workpiece is relatively low compared to conventional fusion welding and the mechanical action of the process can lead to grain refinement. However, residual stress induced by the process must be considered [5-13], particularly longitudinal residual stress.

Several workers have developed numerical models to investigate the process parameters influencing residual stress. These have mainly focused on thermal stress. H.W. Zhang [5-2] *et al* simplified the process to a 2D model, taking account of the effect of the pin to material flow patterns and concluded that the curve of longitudinal residual stress distribution is symmetrical to the welding path the peak isn't located in the center and the longitudinal residual stress is related to welding velocity. Mir Zahedul H. Khandkar *et al* [5-3] focused on residual stress incurred by heating and cooling cycles via a sequentially coupled 3D simulation. Three different materials AA2024, AA6061 and SS304L were studied and material properties considered to be varying with temperature. The predicted stress profile was found to be in good agreement with reported result and it was concluded that the highest tensile stress in all three cases was the longitudinal stress. Other workers considered more realistic material models, heat source models and boundary conditions [5-4] - [5-10]. In general, it was found that that thermal stress dominated the establishment of residual stress and that the longitudinal residual stress is the highest residual stress component.

Bussu and Irving [5-11] have shown that tensile residual stress has a negative influence on fatigue life, with higher tensile stresses causing shorter fatigue life. Methods for controlling tensile residual stress have therefore mainly focused on how to reduce the maximum longitudinal tensile component Residual stress control methods investigated include global mechanical tensioning, active cooling and roller tensioning. It is reported that the roller tensioning method has little effect on reducing longitudinal residual stress if applied during the welding stage [5-12]. The effect of global mechanical tensioning has been shown to be significantly beneficial when applied to plate butt welding [5-13], but application can become difficult in practice if the welding pattern is changed, for example, to circular welding. Active cooling utilizes high cooling power such as liquid CO_2 to force the material behind the welding tool to cool quickly and is reported to be effective in reducing longitudinal residual stress both by experiment [5-14] and numerical method [5-15].

In [5-15], a FSW process cooled by liquid CO_2 was simulated using FEM. The configuration of active cooling is shown as Figure 5-1. The circle indicates that the cooling nozzle used is a cylinder so its projection to workpiece is a circle with diameter Dc, which is bigger than the diameter of the tool Dt. Cooling rate is assumed to be uniform within the circle.

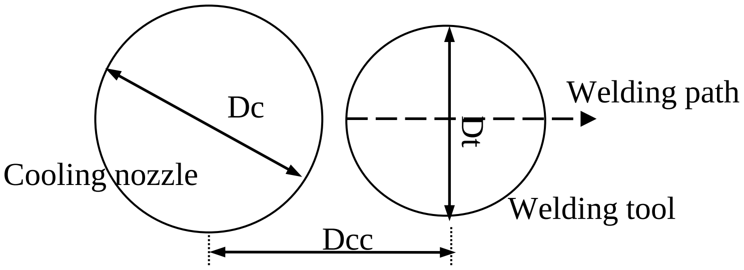

Figure 5-1 Schematics for active cooling in [5-15]

Dcc: centre to centre distance between the cooling area and welding tool, Dt: diameter of the tool, Dc: diameter of cooling nozzle

Here, the active cooling method mentioned in Figure 5-1 is termed as traditional cooling. It is found that a cooling nozzle leading the welding tool has negligible effect on residual stress, so that trailing nozzles were preferable. The authors note that the reversal effect of longitudinal tensile residual stress was contributed by tensile yielding happened between the tool and the nozzle in cases of trailing nozzles. It is also found that it is better to place the cooling nozzle as close as possible to the welding tool and the higher the cooling rate is, the lower the residual stress would be. When the cooling nozzle is placed only 20 mm trailing the welding tool, the maximum welding temperature drops from original nearly 500 ºC to range between 360 ºC and 400 ºC. This excessive temperature drop is not conducive to weld formation and the welding quality could be reduced.

The results found in [5-15] show that traditional cooling can have a positive or negative effect on the establishment of welding residual stress, depending on the specific cooling arrangement considered. Here, the effect of two new approaches to active cooling is investigated to establish their effect on welding temperature and longitudinal residual stress. These new methods are termed discontinuous cooling and distributed cooling.

1. The discontinuous cooling method cools the workpiece periodically using cooling medium such as liquid CO_2, rather than applying cooling medium in the continuous manner of traditional cooling.
2. The distributed cooling method applies the cooling medium in a specific optimized profile relative to the weld tool.

These two cooling methods are investigated in two sections of this Chapter.

In Section 5.1, a methodology is introduced to define an analytical model of discontinuous cooling, including analysis of temperature improvement and temperature gradient improvement. A finite element model for FSW including discontinuous cooling is then presented, describing heat source from the tool, material properties and boundary conditions. An investigation for traditional cooling and discontinuous cooling parameters are presented and results are discussed, including the principles for influence of distance and cooling rate to welding temperature, longitudinal residual stress and efficacy.

In Section 5.2, theory for distributed cooling is introduced. Distributed cooling is defined, prediction of welding temperature improvement and procedure for optimizing welding temperature and longitudinal residual stress and then a simplified finite element model (FEM) for FSW is present, including temperature field and residual stress field, next are results and discussion for comparison of non-distributed cooling and distributed cooling.

5.1 Discontinuous cooling

The physical arrangements for traditional active cooling and discontinuous cooling are similar and shown in Figure 5-2. The circular and rectangular areas represent the projected shapes of the welding tool and cooling nozzle on the workpiece surface, where Lca is the length of the cooling area, Wca is the width of the cooling area, Dcc is the centre to centre distance between the cooling nozzle and welding tool and Dt is the diameter of the tool. . Here, the, tool diameter Dt is set to 20 mm, dimensions for cooling nozzle are Wca=10 mm and Lca=20 mm and both the welding tool and cooling nozzle are located symmetrically on the welding path.

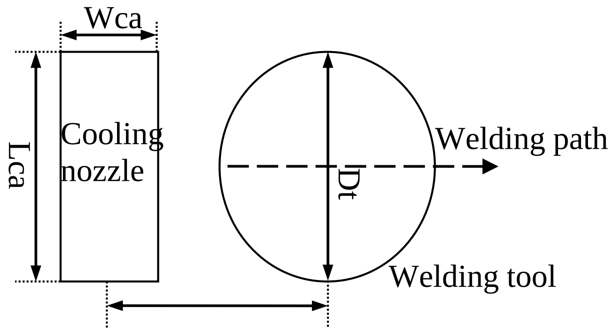

Figure 5-2 Schematic of active cooling model for cooling rate and Dcc investigation

Wca: width of cooling nozzle, Lca: length of cooling nozzle

The difference between traditional cooling and discontinuous cooling is the cooling rate-time curve applied to the workpiece, as shown in Figure 5-3. In Figure 5-3a, the cooling rate for traditional cooling is constant, while in Figure 5-3b, the cooling rate for discontinuous cooling is pulsed, ideally varying between zero and constant values throughout the welding stage. The ratio of cooling time and its cycle: $r = t_c/t_0$ is defined as cooling duty. Here, the total amount of coolant applied during the discontinuous cooling process is equivalent to that used in traditional continuous cooling for the same welding duration, *t*.

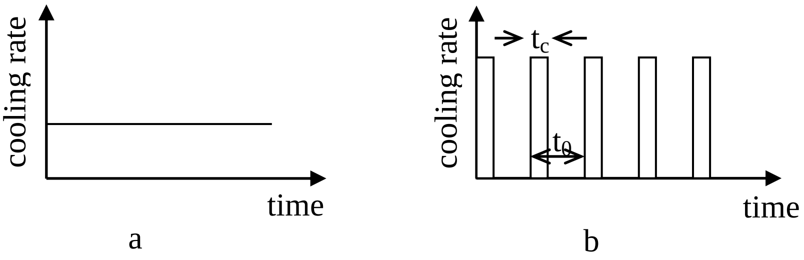

Figure 5-3 Schematic of cooling rate for traditional cooling and discontinuous

a: traditional cooling, b: discontinuous cooling

5.1.1 Welding temperature improvement

In traditional cooling, the heat source from the welding tool and the cooling source from the nozzle are independent, so the temperature of material acted on by the tool and nozzle can be expressed as:

$$T_{tc} = T_{tc}^{tool} + T_{tc}^{cool} \quad 5\text{-}1$$

where T_{tc}, T_{tc}^{tool} and T_{tc}^{cool} represent total temperature increment of the material under the tool, temperature increment contributed by heat input from the tool, temperature increment contributed by continuous cooling nozzle separately. The temperature increment contribution from the tool is considered to be the same in both discontinuous cooling and traditional cooling, such that $T_{tc}^{tool} = T_{dc}^{tool}$. Thus only T_{tc}^{cool} is discussed.

To simplify the problem, the cooling nozzle is replaced by n point heating sources with negative heat input rate q as shown in Figure 5-4a. For point heating source C at time t, heat input within small time increment dt is qdt and its temperature contribution to point P from t to t_0 can be expressed as:

$$dT_{tc}^{cool} = \frac{qdt}{cp[4\pi\alpha(t_0-t)]^{3/2}} exp(\frac{-r^2}{4\alpha(t_0-t)}) \quad 5\text{-}2 \ [5\text{-}19]$$

where dT_{tc}^{cool} is temperature increment contribution for traditional cooling from t to t_0, q is the (negative for cooling sources) heat flux rate , r is the distance to the cooling nozzle, $c, p \ and \ \alpha$ are material related coefficient and considered to be constant in this case and t_0 is the cycle of discontinuous cooling.

If point P is located in the right side of point C, as shown in Figure 5-4b, then:

$$r = \sqrt{(x_0 - vt)^2 + {y_0}^2} \quad 5\text{-}3$$

where x_0 and y_0 are initial distances at x direction and y direction specifically, v represents the moving speed. Positive direction of x axis is set to the same as welding direction. It is assumed that $x_0 - vt_0 > 0$, which means the point C has no contact with cooling area at time t_0.

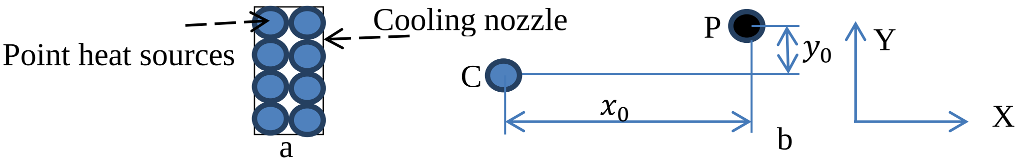

Figure 5-4 Schematic of point heat sources for cooling nozzle and location of point P

Based on Equations 5-2 and 5-3, the temperature contributed by the cooling nozzle from time 0 to t0 can be expressed as:

$$T_{tc}^{cool} = \int_0^{t_0} \frac{qdt}{cp[4\pi\alpha(t_0-t)]^{3/2}} exp(\frac{-[(x_0-vt)^2+{y_0}^2]}{4\alpha(t_0-t)}) \qquad 5\text{-}4$$

For discontinuous cooling, the cooling medium is only applied for a period of εt_0 during its cycle t_0. The temperature increment during the whole cycle can be expressed as:

$$T_{dc}^{cool} = \int_0^{\varepsilon t_0} \frac{qdt/\gamma}{cp[4\pi\alpha(t_0-t)]^{3/2}} exp(\frac{-[(x_0-vt)^2+{y_0}^2]}{4\alpha(t_0-t)}) \qquad 5\text{-}5$$

where γ is the cooling duty, q/γ is the cooling rate for discontinuous cooling, which indicates that the production of cooling rate and cooling duty is kept as the same as that of traditional active cooling.

The difference of temperature increment for discontinuous cooling and traditional cooling from time 0 to t_0 can be expressed as follows for the same initial temperature at time 0:

$$T_{dc}^{cool} - T_{tc}^{cool} =$$

$$\int_0^{\varepsilon t_0} \frac{qdt/\gamma}{cp[4\pi\alpha(t_0-t)]^{3/2}} \exp(\frac{-[(x_0-vt)^2+{y_0}^2]}{4\alpha(t_0-t)}) - \int_0^{t_0} \frac{qdt}{cp[4\pi\alpha(t_0-t)]^{3/2}} \exp(\frac{-[(x_0-vt)^2+{y_0}^2]}{4\alpha(t_0-t)})$$

$$=$$

$$\int_0^{t_0} \frac{qdt}{cp[4\pi\alpha(t_0-\gamma t)]^{3/2}} \exp\left(\frac{-[(x_0-v\gamma t)^2+{y_0}^2]}{4\alpha(t_0-\gamma t)}\right) - \int_0^{t_0} \frac{qdt}{cp[4\pi\alpha(t_0-t)]^{3/2}} \exp(\frac{-[(x_0-vt)^2+{y_0}^2]}{4\alpha(t_0-t)})$$

$$= \int_0^{t_0} \frac{qdt}{cp(4\pi\alpha)^{3/2}} \left[\frac{1}{(t_0-\gamma t)^{3/2}} exp\left(\frac{-[(x_0-v\gamma t)^2+{y_0}^2]}{4\alpha(t_0-\gamma t)}\right) - \frac{1}{(t_0-t)^{3/2}} exp\left(\frac{-[(x_0-vt)^2+{y_0}^2]}{4\alpha(t_0-t)}\right)\right] \qquad 5\text{-}6$$

As $0 < \gamma < 1$ and $0 < t < t_0$:

$$\exp\left(\frac{-[(x_0-v\gamma t)^2+{y_0}^2]}{4\alpha(t_0-\gamma t)}\right) < \exp\left(\frac{-[(x_0-vt)^2+{y_0}^2]}{4\alpha(t_0-t)}\right)$$

Thus:

$$\frac{1}{(t_0-\gamma t)^{3/2}} \exp\left(\frac{-[(x_0-v\gamma t)^2+{y_0}^2]}{4\alpha(t_0-\gamma t)}\right) - \frac{1}{(t_0-t)^{3/2}} \exp\left(\frac{-[(x_0-vt)^2+{y_0}^2]}{4\alpha(t_0-t)}\right) < 0$$

As the cooling nozzle heat input is negative ($q < 0$), the discontinuous and traditional temperature increments must satisfy the condition:

$$T_{dc}^{cool} - T_{tc}^{cool} > 0$$

Thus the discontinuous cooling process leads to a less reduction in temperature. This conclusion can be expanded to the other point heating sources of the nozzle, so the sum of all the point heating sources incur less temperature drop in discontinuous cooling than traditional cooling. In other words, for material under the welding tool and meeting the requirement of $x_0 - vt_0 > 0$, the average temperature in the discontinuous cooling model is higher than that in traditional active cooling for the same given cooling area and time-average cooling rate.

5.1.2 Temperature gradient within γt_0

Discontinuous cooling leads to welding temperature improvement and in addition a higher reversal temperature gradient is generated in the material between the cooling nozzle and the maximum temperature point during time 0 and γt_0. As noted in [5-15], larger temperature gradients increase tensile plastic strain and reduce misfit, thus reduce tensile residual stress.

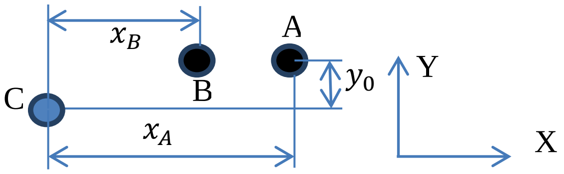

Figure 5-5 Schematic for temperature gradient at welding direction

During time 0 and γt_0, the temperature gradient between point A and B, as shown in Figure 5-5, has contributions from the heat source (the tool) and cooling source (the nozzle). Thus

$$\Delta T = \Delta T^{tool} + \Delta T^{cool} \quad 5\text{-}7$$

where ΔT, $\Delta T^{tool}$and ΔT^{cool} represent the total temperature gradient in the material between the cooling nozzle and maximum temperature point, the temperature gradient contributed by heat input from the tool and the temperature gradient contributed by the cooling nozzle respectively. The temperature gradient contribution from the tool is considered to be the same in both discontinuous cooling and traditional cooling, in other words, $\Delta T_{tc}^{tool} = \Delta T_{dc}^{tool}$, thus only ΔT_{tc}^{cool} and ΔT_{dc}^{cool} during time 0 and εt_0 are discussed.

For traditional active cooling, temperature gradient contributed by the nozzle during time 0 and γt_0 is:

$$\Delta T_{tc}^{cool} = \int_0^t \frac{qdt}{cp[4\pi\alpha(t_0-t)]^{3/2}} \exp\left(\frac{-[(x_A-vt)^2+{y_0}^2]}{4\alpha(t_0-t)}\right) - \int_0^t \frac{qdt}{cp[4\pi\alpha(t_0-t)]^{3/2}} \exp(\frac{-[(x_B-vt\,)^2+{y_0}^2]}{4\alpha(t_0-t)})$$

5-8

For discontinuous cooling, temperature gradient contributed by the nozzle during time 0 and γt_0 is:

$$\Delta T_{dc}^{cool} = \int_0^t \frac{q/\gamma dt}{cp[4\pi\alpha(t_0-t)]^{3/2}} exp\left(\frac{-[(x_A-vt)^2+{y_0}^2]}{4\alpha(t_0-t)}\right) - \int_0^t \frac{qdt}{cp[4\pi\alpha(t_0-t)]^{3/2}} exp(\frac{-[(x_B-vt)^2+{y_0}^2]}{4\alpha(t_0-t)}) \qquad 5\text{-}9$$

As $0 < \gamma < 1$ and $x_A > x_B$:

$$\Delta T_{dc}^{tool} > \Delta T_{tc}^{tool}$$

Thus the discontinuous cooling process gives a l;arger temperature gradient than traditional cooling. This conclusion can also be applied to other point heating sources of the nozzle. Consequently, the temperature gradient from the tool to the nozzle in discontinuous cooling is greater than that in traditional cooling during time 0 and γt_0. This indicates that increasing the cooling rate would increase the temperature gradient in the discontinuous cooling model,. This increased temperature gradient may increase the desired tensile plastic strain or decrease compressive plastic strain, thus reduce tensile longitudinal residual stress [5-15].

5.1.3 Finite Element Simulation

Equations 5-6, 5-8 and 5-9 show that decreasing γ or increasing q would help improve both welding temperature and temperature gradient if production of γq is the same, which may further reduce longitudinal residual stress in discontinuous cooling. This behavior was investigated through several FEA simulations implemented in ABAQUS. Dcc is set to 15 mm, which is the minimum practical distance between the tool and nozzle and cooling liquid flow frequency fixed at 1 Hz, with cooling duty varying from 0.5, 0.25 to 0.15 while keeping cooling liquid volume constant. The corresponding cooling rates are set to 0.8E4, 1.6E4 and 2.7E4 Wm^{-20}C^{-1} specifically. The solution time step is controlled to ensure the cooling duty is correctly applied to the cooling area at appropriate time.

5.1.3.1 FEA model

The finite element model used is a simplified thermal mechanical coupled model. In this model, only stress incurred by thermal load is considered. The material simulated is aluminum alloy AA2024 and the yield stress is defined as temperature dependent. The workpiece material property is assumed to be isotropic. Two stages are used in this model, with a first step of welding followed by a cooling step, which simulate the heating (and active cooling synchronously if applicable) stage and the cooling stage respectively. The step time for welding is set to 26 seconds and cooling stage is set to 174 seconds. The temperature of work piece drops to ambient temperature at the end of cooling step.

The workpiece consists of two plates with dimensions 50 mm*150 mm*3 mm, as shown in Figure 5-6. The tool direction is defined in the positive X axis direction. The finite element mesh is coarse remote from the welding path and refined in the center along welding path.

The thermal conductivity is 121 $\mathrm{Wm^{-1}{}^{0}C^{-1}}$, density is 2780 $\mathrm{kg/m^{3}}$, specific heat capacity is 875 $\mathrm{JKg^{-1}{}^{0}C^{-1}}$, Young's modulus 73.1 GPa, Poisson’s ratio 0.33 and thermal expansion coefficient 2.268E-5 $\mathrm{{}^{0}C^{-1}}$. The temperature dependent plastic properties [5-16] are given in Table 5-1.

Table 5-1 Yield strength variation with temperature

Temperature/°C	25	100	149	204	260	315	371
Yield strength/MPa	324.00	310.00	248.00	131.00	62.00	41.00	27.60

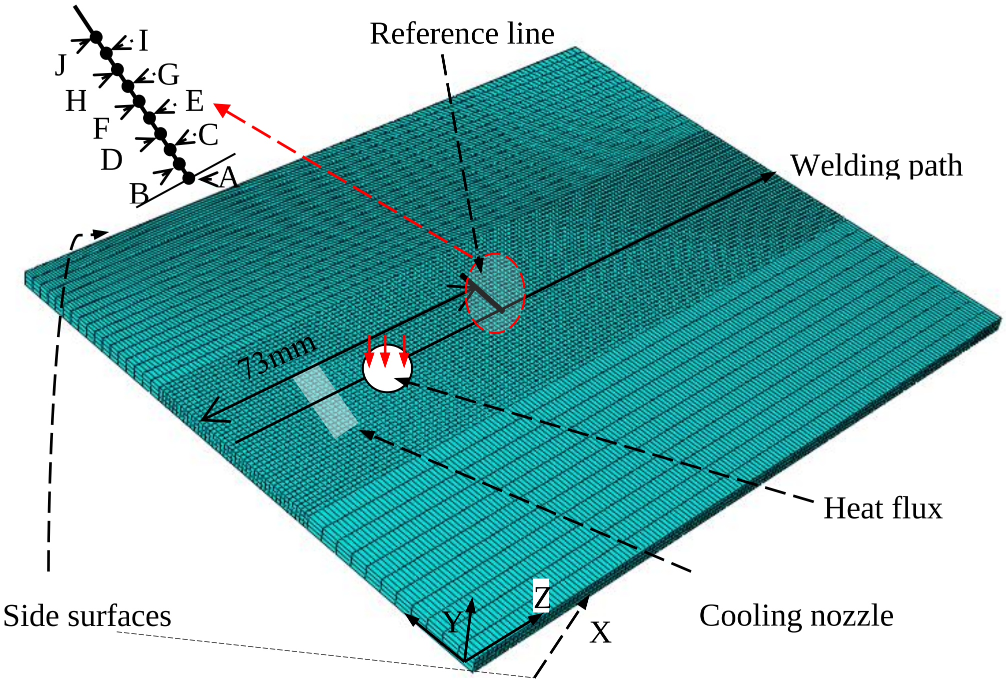

Figure 5-6 Geometry and mesh for thermal mechanical coupled model

Points A to K are reference points

The model boundary conditions are illustrated in Figure 5-6. The work piece is supported at the bottom by a backing plate. To simplify the model and eliminate complex contact which requires large CPU time, the support of the backing plate is treated as a constraint on the Z axis of the workpiece bottom face, with appropriate heat transfer applied. Heat transfer from the workpiece surface to air is represented by convection, using a film coefficient of 15 $Wm^{-2 0}C^{-1}$ on the four edge surfaces and top surface, excluding the cooling area if appropriate. In the welding step, the area of the bottom surface with pressurized contact to the virtual backing plate is set to have a larger convection coefficient of 500 $Wm^{-2 0}C^{-1}$ with sink temperature 20 ^{0}C, compared to other unpressurized area of bottom surface with convection coefficient of 200 $Wm^{-2 0}C^{-1}$, according to findings in [5-5]. The heat source is a moving surface heat flux applied to a radius of 10 mm at the center along welding direction. The heat flux distribution is assumed to be linear with distance to tool center and the total power is set to 700W. The moving speed is set to 5 mm/s and the initial location of tool center is 10 mm away from the left edge of the work piece. If applicable, cooling liquid is assumed to be moving with the same velocity as the tool, but a fixed distance behind. The two surfaces parallel to the welding direction are constrained in the Y axis direction during the welding step. In the cooling step, both the heat source and cooling liquid (if applicable) are removed and the constraint on two parallel surfaces released, while the constrain of Z axis (backing plate) is maintained. The mechanical effects of welding tool, such as pressure and friction force, are neglected.

A mesh convergence study was performed to determine a suitable mesh density at the center of the model. Figure 5-7 shows that, changing mesh size from 1mm*1mm*1mm to 2mm*2mm*2mm has negligible effect on the temperature-time curve. The model chosen for the investigation contains 30600 elements and 41676 nodes.

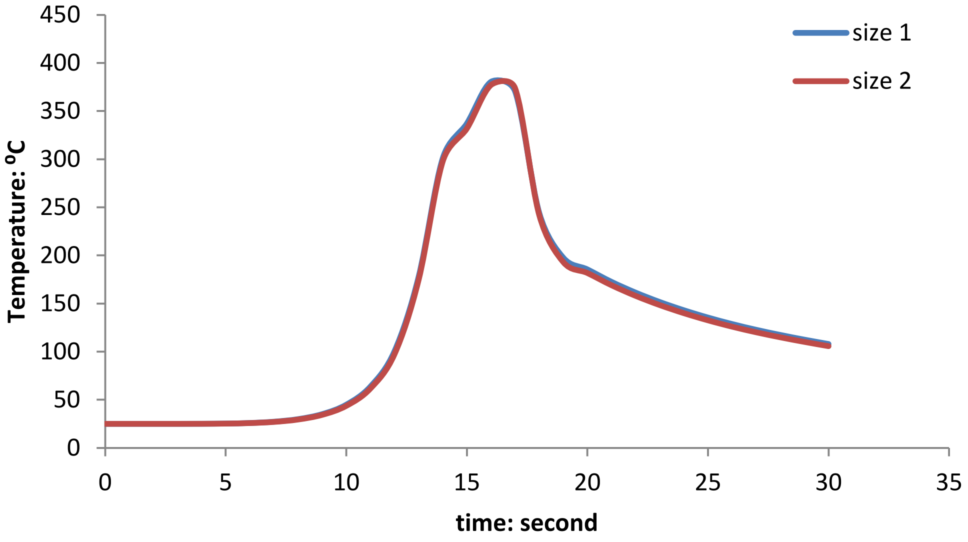

Figure 5-7 Mesh independence for the FEM
*size 1- 1mm*1mm*1mm, size 2- 2mm*2mm*2mm*

5.1.3.2 FE Simulation Results

In the welding stage, the heating process can be considered as quasi-static. Figure 5-8 shows four temperature contour plots at different times for the model with no cooling applied. At step time 14 second, max temperature is 432.9 ^{0}C and the temperature distribution has an oval form around the center of the moving tool. After a further 2 seconds, the maximum temperature reaches 435.2 ^{0}C, which is slightly higher than step time 14 second. The temperature development rate is around 1.15 ^{0}C per second. As step time increases, the temperature increment drops to 0.3 ^{0}C per second at step time 20 second.

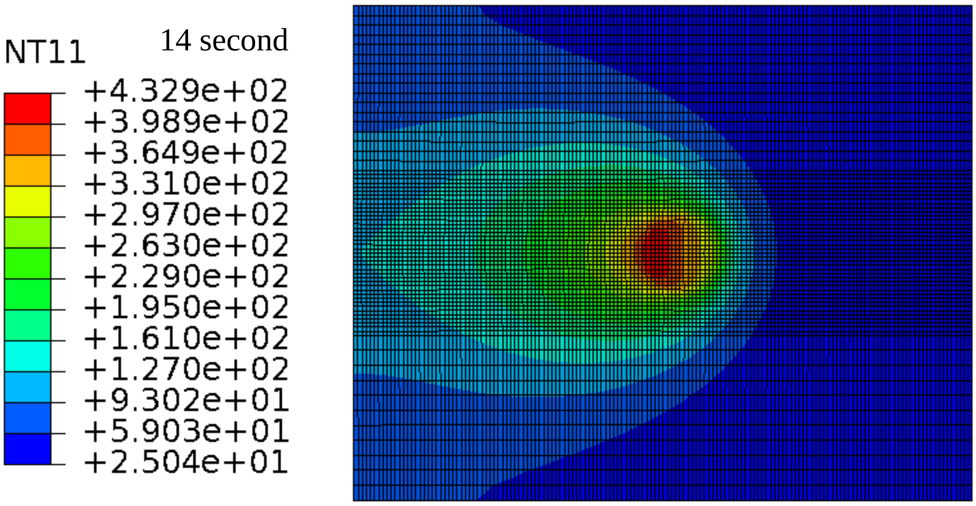
14 second

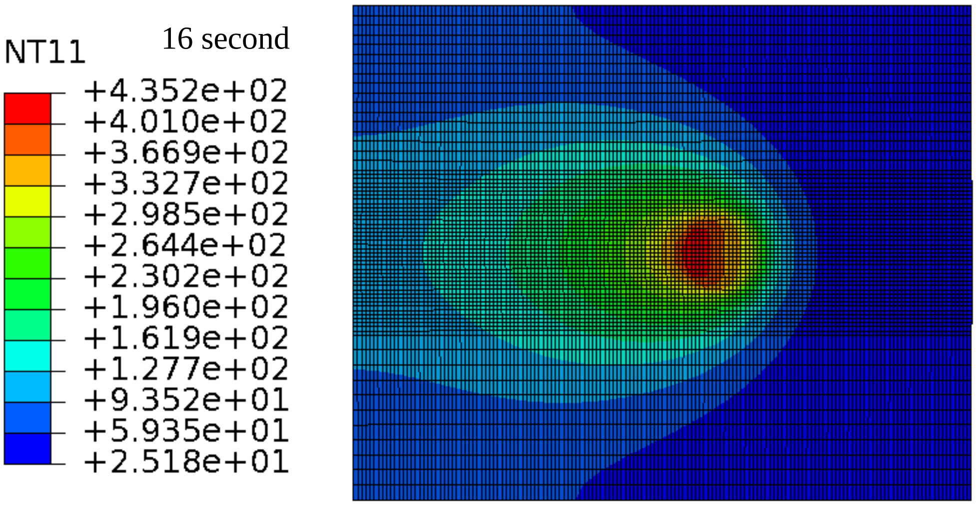
16 second

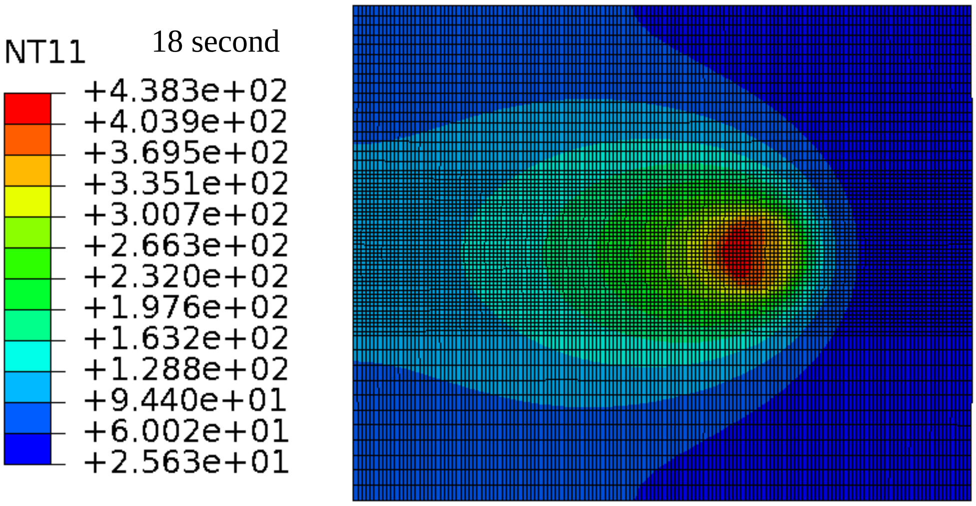
18 second

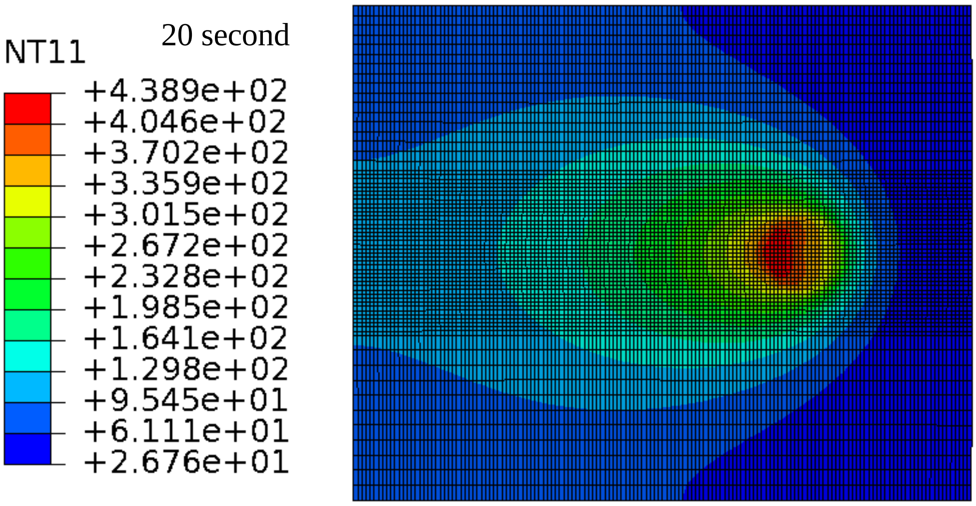

Figure 5-8 Temperature fields during heating process for the original model

A reference line is defined at position x=73 mm and 11 points A to K are selected in the line at 1mm interval, as shown in Figure 5-6, with point A on the welding path. The temperature-time curve of *Figure 5-9* shows that point A experiences the peak temperature at step time 14 seconds. At this moment, the tool center is at position x=80 mm, 7 mm ahead of point A. In this model, the tool center is the heat source center. The maximum temperature location lags the tool location and the lag time and distance are related to several factors, such as moving speed, conductivity of the material and the distribution of heat flux. Points B to J have a similar thermal history, in which they experience their peak temperature at the same step time of 14 second. These 10 points are selected as reference points and the longitudinal residual stress at these locations are defined as reference longitudinal residual stresses and the analysis of longitudinal residual stress distribution along the transverse direction is based on these. In general, these local points present the variation trend of global longitudinal residual stress.

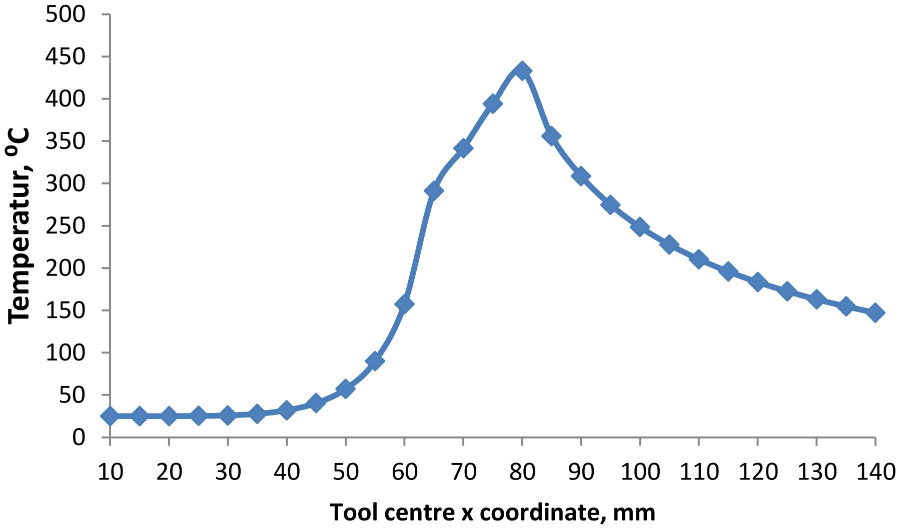

Figure 5-9 Temperature history of point A

The maximum value of longitudinal residual stress occurring in the entire model is defined as the global longitudinal residual stress, Global-S1. In the original model, Global-S1 is 169.1 MPa. The maximum longitudinal residual stress at the reference points are defined as Ref-S1, in this case, it is 168.1 MPa.

In the traditional cooling arrangement, a rectangular cooling area is located at a center to center distance of 35 mm from tool center, as shown in Figure 5-2, moving at the same speed as the tool. The cooling area dimensions are 20 mm*10 mm. Four different cooling rates are used: 0.5E4 $Wm^{-2}{}^{0}C^{-1}$, 0.8E4 $Wm^{-2}{}^{0}C^{-1}$, 1.0E4 $Wm^{-2}{}^{0}C^{-1}$ and 1.6E4 $Wm^{-2}{}^{0}C^{-1}$ and the whole cooling area is considered to have a uniform cooling rate. The corresponding effects on the temperature of the work piece and the residual stress were investigated. As shown in Table 5-2, it is found that maximum temperature and longitudinal residual stress at the reference points decrease with increasing cooling. This is consistent with findings reported in [5-15], which indicates that in a proper range higher cooling rate induce lower longitudinal residual stress.

Table 5-2 Maximum temperature and longitudinal residual stress varying with cooling rate in traditional active cooling models

Cooling rate	0.5E4	0.8E4	1.0E4	1.6E4
Max temperature	429.5	428.9	428.2	427.5
Global S1	156.6	151.1	149.0	145.8
Reference S1	151.2	142.9	139.3	135.2

The effect of the relative location of the rectangular cooling area and welding tool was also investigated. Figure 5-11 shows three temperature contour plots for the same cooling area with the same cooling rate of 0.8E4 $\mathrm{Wm}^{-20}\mathrm{C}^{-1}$ at distance 35 mm, 25 mm and 15 mm. The maximum temperature drops significantly as the center to center distance becomes smaller, especially when it approaches 15 mm. The longitudinal residual stress is also reduced, as shown in Figure 5-11. These findings agree with the results reported in [5-15] (with a different shape of the cooling area). However, from a practical perspective, too low a material temperature under the tool is detrimental to the welding process, as the material is harder when colder. Thus a balance between welding temperature and longitudinal residual stress is required when considering the location of the cooling area.

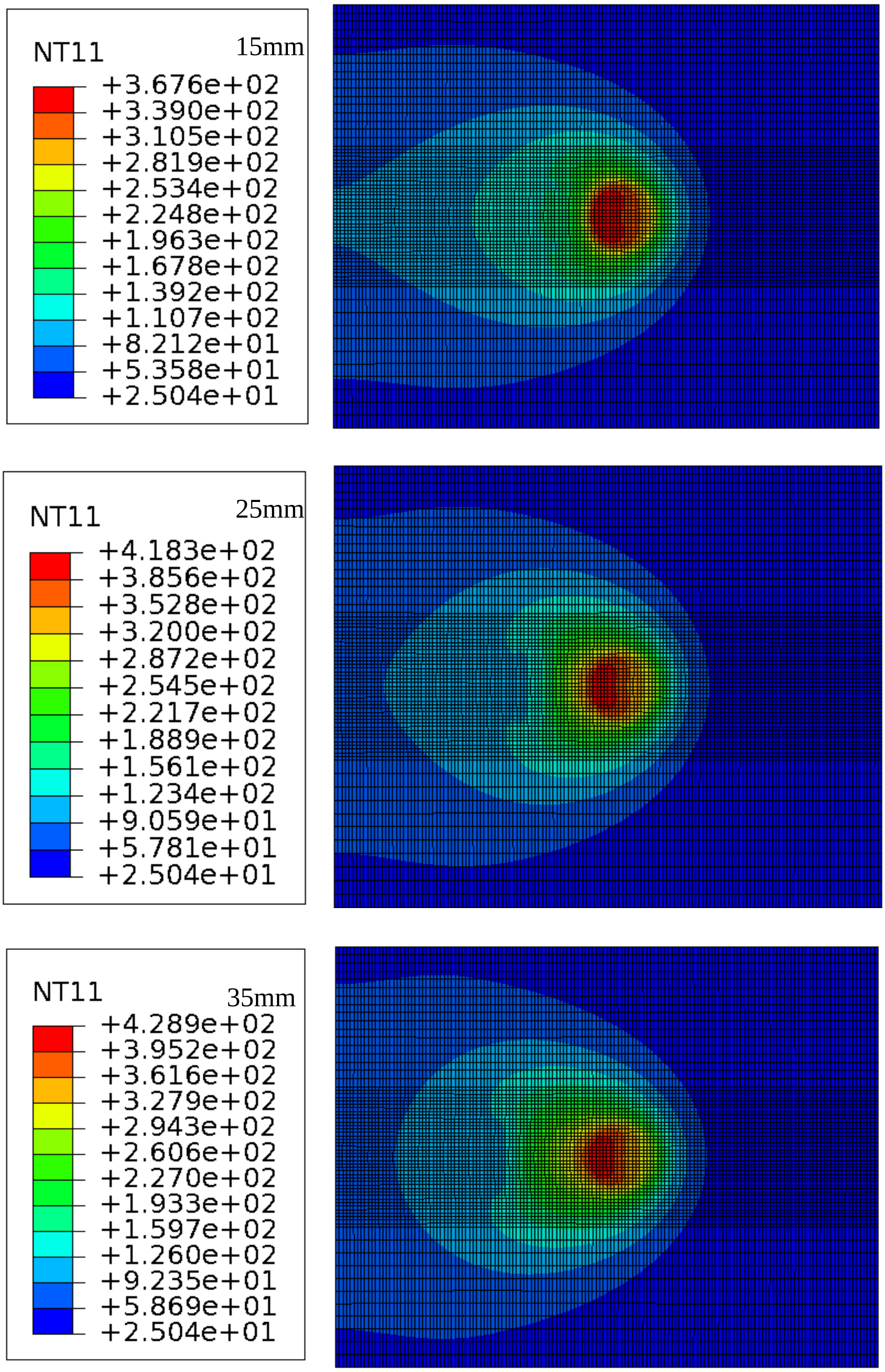

Figure 5-10 Comparison of temperature field for models with Dcc=15mm, Dcc=25mm and Dcc=35mm

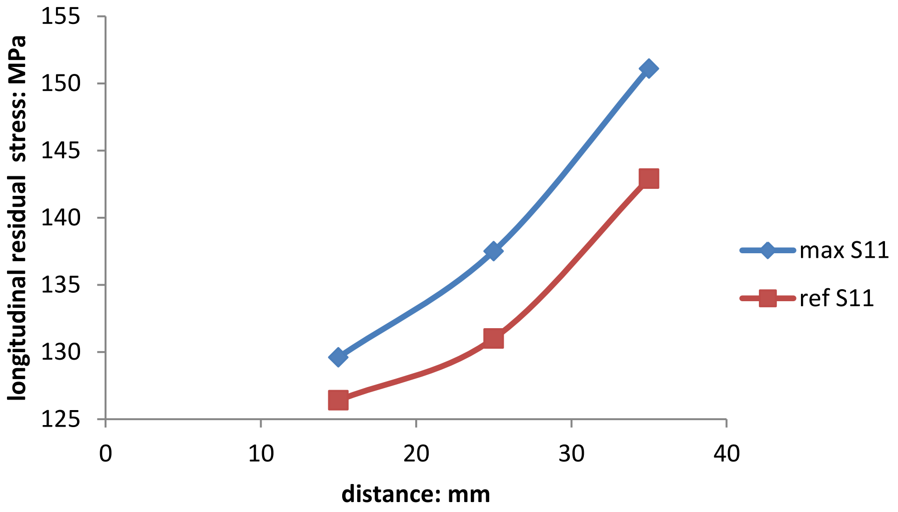

Figure 5-11 Influence of Dcc to global S1 and reference S1

The welding stage of the traditional (continuous) model can be considered to be quasi-static, as the temperature distribution associated with the moving coordinate system varies slowly with time and the cooling area influences the temperature of material under the tool center. This indicates active cooling affects the temperature in the cooling area and also changes the temperature in other location, such as under the tool. Here, the alteration of temperature in the cooling area is referred to as the *local effect* and the change of temperature under the tool is defined as the *remote effect*. The local effect is desirable but the remote effect is negative, since the drop in temperature may affect the quality of the weld. Although the remote effect can't be completely removed, it is possible to reduce and limit it.

In the discontinuous cooling model, the cooling is varied with time, aiming to maximize the local reverse temperature gradient and minimizing the remote effect. As shown in Figure 5-2, the cooling area applied is a rectangle with a center to center distance to the weld tool of 15 mm. The cooling frequency is set to 1 Hz. The cooling rate and duty vary but their production is kept constant, in accordance with the assumption that the average cooling media (liquid) volume flow is constant. Figure 5-12 shows the maximum temperature and longitudinal residual stress distribution at the reference points. The observed trend is that the temperature under the tool increases with increasing cooling rate and decreasing duty but the increment speed becomes slow when the duty drops to a low level. In practice, cooling rate can't increase infinitely and is, restricted by physical conditions. If the duty is too low the beneficial cooling effect may be limited, as less heat is absorbed per volume of cooling media and the cooling media may not be sufficiently utilized.

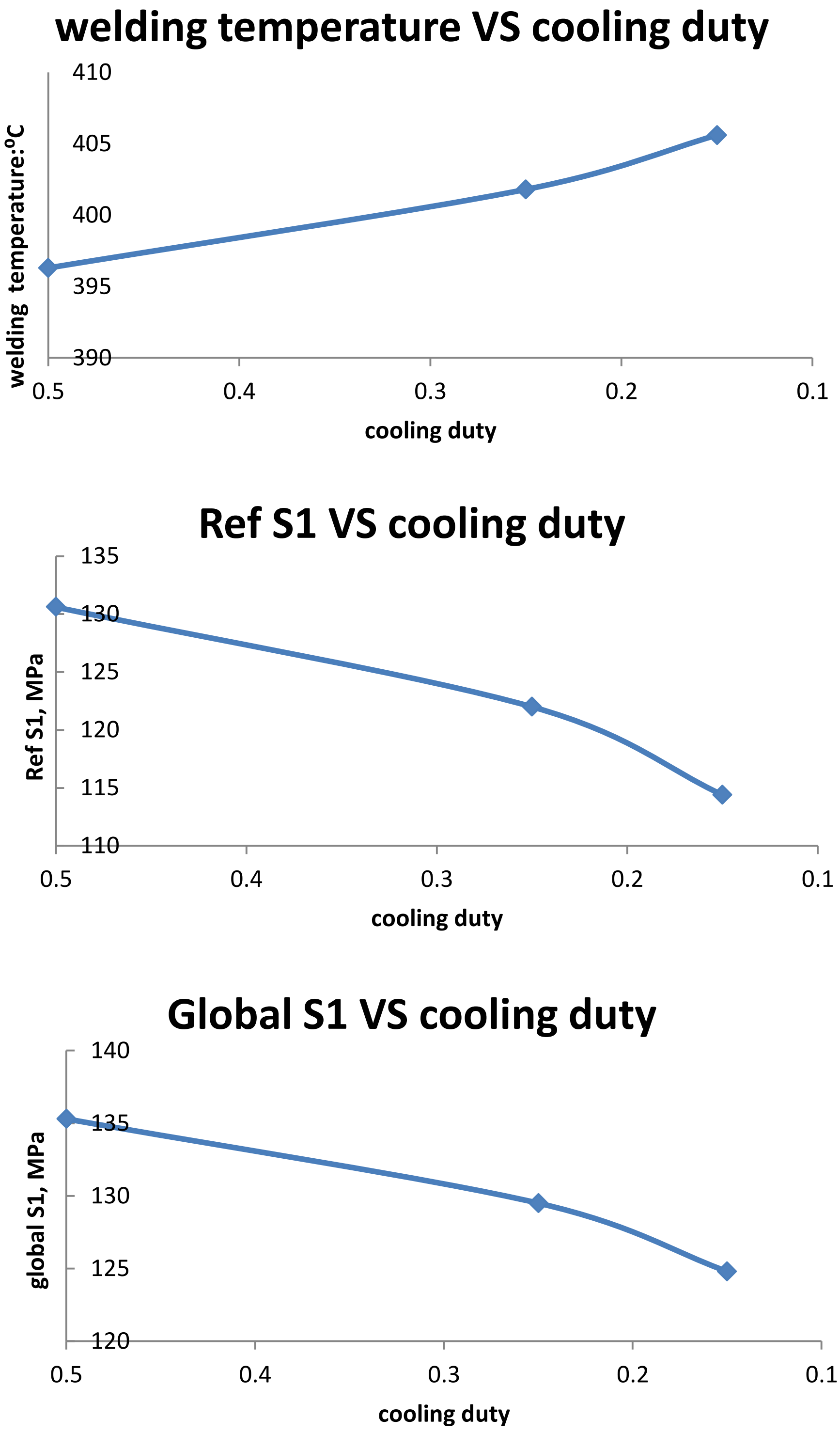

Figure 5-12 Variation of temperature, reference S1 and global S1 with duty decreasing

A comparison between discontinuous and traditional cooling with Dcc=15 mm and cooling rate 0.4 E4 Wm^{-2} $^{0}C^{-1}$, controlling the average production of cooling area and cooling rate, is shown in *Table 5-3*. Although the same cooling area is applied, the discontinuous cooling pattern with duty 0.25 exceeds the continuous cooling pattern in terms of both temperature drop and longitudinal residual stress. This confirms theoretical analysis in section 5.1.1 and addresses the issue of longitudinal residual stress in section 5.1.2.

Table 5-3 Maximum temperature and longitudinal residual stress for discontinuous and continuous cooling models

	Max temperature	Global S1	Ref S1
Discontinuous cooling /duty 0.25	401.8	129.5	122.0
Traditional cooling	388.7	143.4	141.4

In line with the analysis of section 5.1.1.2, the temperature gradient for the material between the tool and the nozzle in the discontinuous cooling model is greater than that of traditional cooling. Figure 5-13 shows the longitudinal direction temperature gradient at the reference points for step time 14.2 second, which is assumed to help reduce longitudinal residual stress. The temperature gradient here is quantified as the temperature different of two points 5 mm apart.

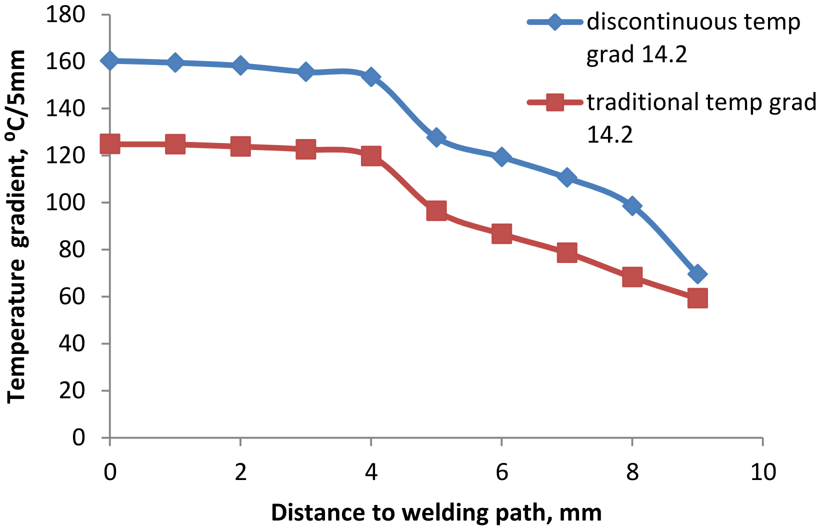

Figure 5-13 Temperature gradient comparison between discontinuous cooling and traditional cooling at 14.2 second

The welding temperature under the tool is shown in Figure 5-14. As expected from section 5.1.1, the temperature in the discontinuous cooling model is higher at the end of each cooling period than that of traditional cooling. It is also found that at step time 14.25 second, when the entire cooling medium in one cycle from step time 14 to 15 second has been applied to the workpiece, the welding temperature is still higher though the difference is smaller. This should be attributed to the accumulation of average temperature difference in previous cycles.

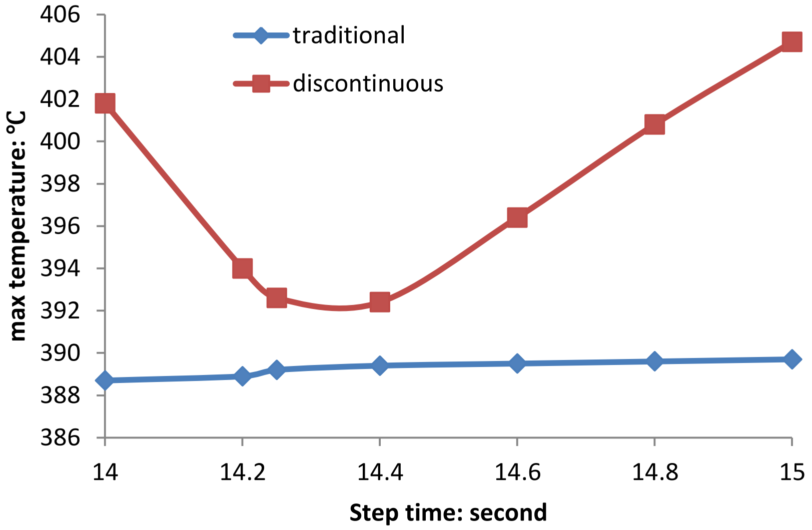

Figure 5-14 Welding temperature comparison for discontinuous and traditional cooling

5.1.4 Effectiveness of active cooling

The effectiveness of the cooling operation is defined as:

$$Eff = \frac{S_1^0 - S_1^c}{r_c * d_c} \quad \text{5-10}$$

where S_1^c and S_1^0 are longitudinal residual stress with and without active cooling applied, r_c presents the cooling rate, d_c is the cooling duty. In a continuous cooling pattern, the cooling duty is 1. The unit for effectiveness is 1E-4*MPa*W^{-1}m^{20}C.

The cooling effectiveness is significant as a more effective process requires less cooling medium for the same residual stress drop. In addition, less cooling medium applied may result in a lower drop in welding temperature if the Dcc is the same. Finally, since the cooling rate is usually limited by physical conditions, the cooling pattern with highest effectiveness can lead to the lowest longitudinal residual stress.

For traditional cooling, it is observed that the effectiveness decreases with increasing cooling rate, as shown in Figure 5-15. This may explain the inference in [5-15] that there appears to be a limit in active cooling r, beyond which additional cooling has little effect in reducing longitudinal residual stress.

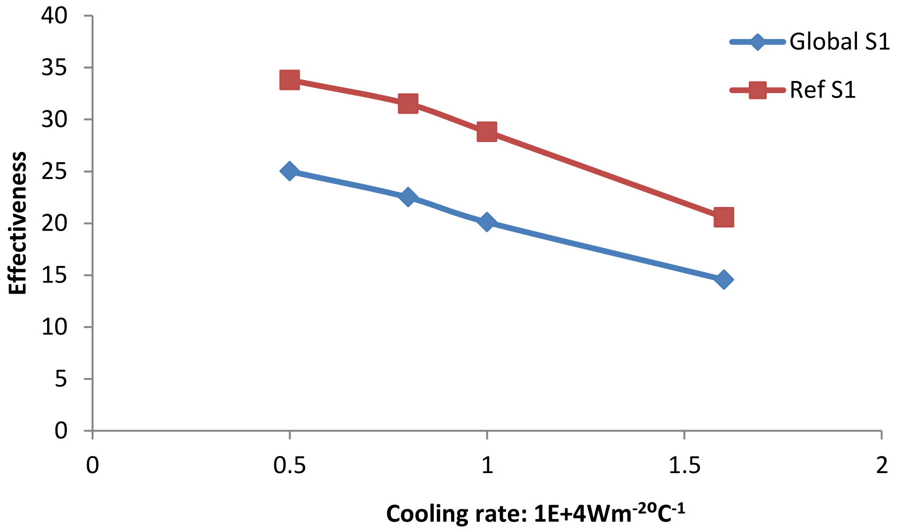

Figure 5-15 Variation of effectiveness with cooling rate for traditional cooling

It is also observed that the effectiveness increases with decreasing Dcc, as shown in Figure 5-16. This explains the phenomena identified in [5-15] that the smaller the Dcc is, the greater the decrease in longitudinal residual stress.

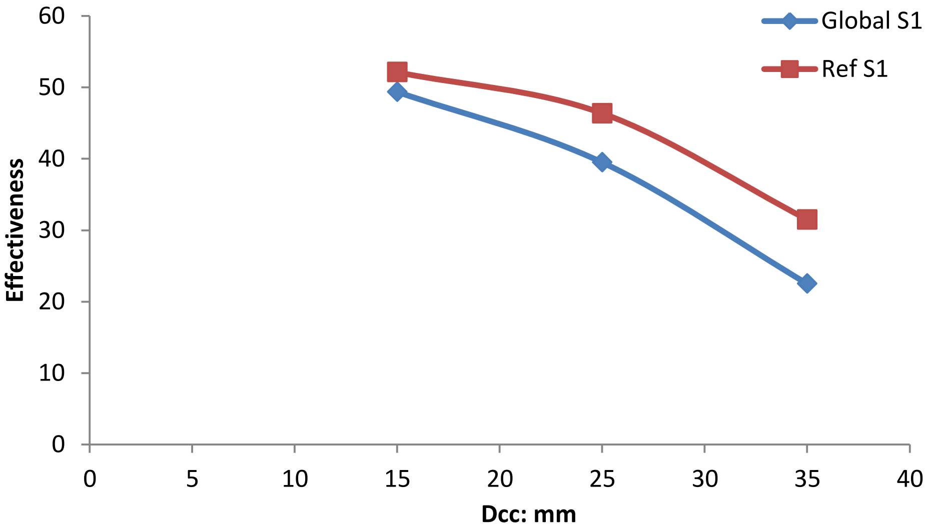

Figure 5-16 Variation of effectiveness with Dcc for traditional cooling

The investigation of discontinuous cooling indicates a high level of effectiveness, which increases with increasing cooling rate, as shown in Figure 5-17. This indicates a potential for further reduction in longitudinal residual stress when higher cooling is applied.

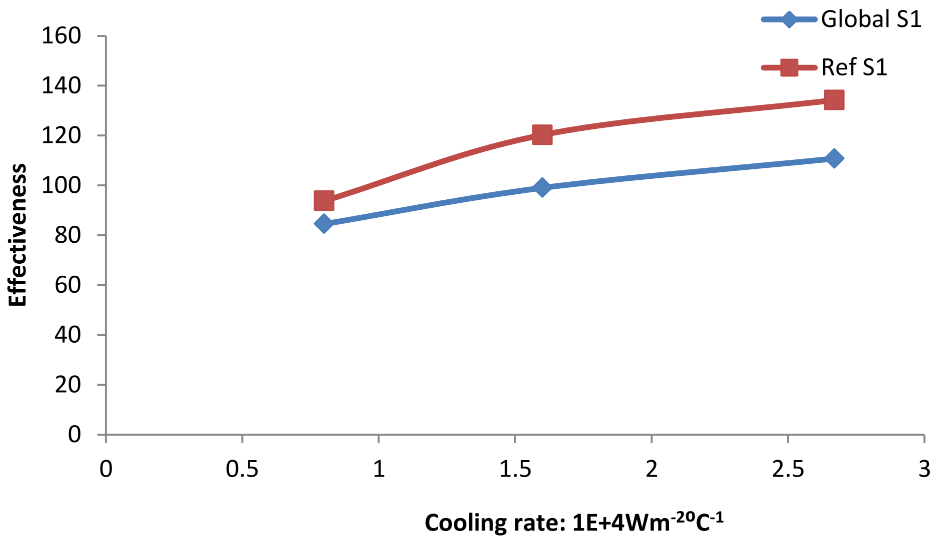

Figure 5-17 Variation of effectiveness with cooling rate for discontinuous cooling

Figure 5-18 is a comparison of effectiveness for the discontinuous cooling and continuous cooling patterns, with Dcc set to 15 mm and production of cooling and duty of 0.4E4 $Wm^{-2o}C^{-1}$.This case is the most effective traditional cooling case considered, since Dcc=15 mm is the smallest practical distance between the tool and cooling nozzle and the effectiveness increases with decreasing Dcc/ The cooling duty of 0.4E4 $Wm^{-2o}C^{-1}$ is the smallest in the cases investigated and effectiveness increases with decreasing cooling rate. The effectiveness of the discontinuous cooling is calculated from the model with duty 0.5 and cooling 0.8E4. Figure 5-18 clearly demonstrates the advantage of discontinuous cooling in terms of welding temperature and longitudinal residual stress reduction.

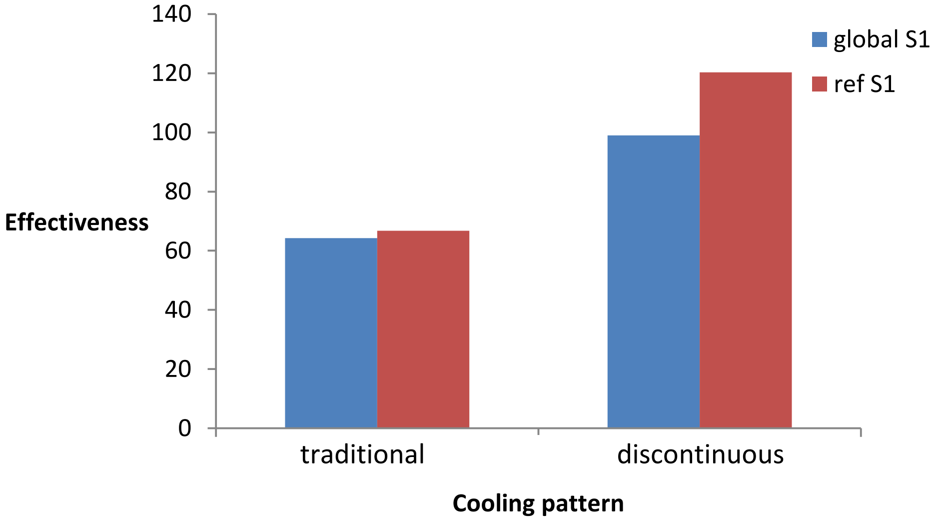

Figure 5-18 Comparison of effectiveness for traditional and discontinuous cooling

.

5.2 Distributed cooling

In the traditional active cooling, the cooling nozzle usually trails the welding tool and moves synchronously with it and the configuration is shown in Figure 5-1.

For investigation of distributed cooling, the rectangular cooling nozzle is divided symmetrically into 5 sections. A distributed cooling effect can be achieved by combinations of individual section cooling rate and/or position:

1. Cooling rate fixed, distance from tool varied, Figure 5-19a.
2. Distance from tool fixed, cooling rate varied, Figure 5-19b.
3. Both distance from tool and cooling rate varied.

Option 3 leads to a more complex optimization problem than options 1 and 2 and is not considered further here to simplify analysis and interpretation.

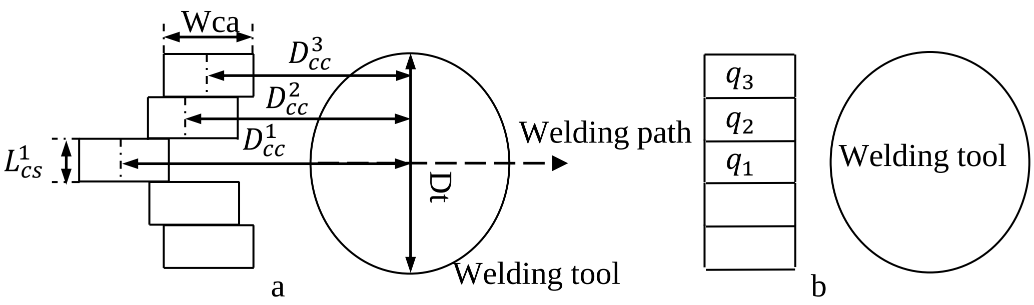

Figure 5-19 Schematics for distributed cooling

5.2.1 Welding temperature improvement

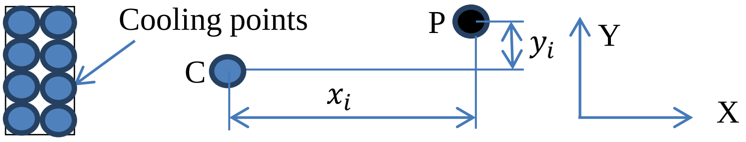

Figure 5-20 Schematic for welding temperature analysis

The cooling area is equally discretized into n cooling points, as illustrated in Figure 5-20. The temperature increment at a point P is related to each of the cooling points. Considering an arbitrary cooling point C with negative heat input rate during time period 0 and t_0:

$$T_{cool}^{nc} = \sum_{i=1}^{n} \int_0^{t_0} \frac{q^{nc}dt}{cp[4\pi\alpha(t_0-t)]^{3/2}} exp(\frac{-[\left(x_i^{nc}-vt\right)^2+y_i^{nc2}]}{4\alpha(t_0-t)}) \quad 5\text{-}11$$

$$T_{cool}^{dc} = \sum_{i=1}^{n} \int_0^{t_0} \frac{q^{dc}dt}{cp[4\pi\alpha(t_0-t)]^{3/2}} exp(\frac{-[\left(x_i^{dc}-vt\right)^2+y_i^{dc2}]}{4\alpha(t_0-t)}) \quad 5\text{-}12$$

where n is the number of discrete points, T_{cool}^{nc} and T_{cool}^{dc} are temperature increment from time 0 to t_0 for investigated point P, q^{nc} and q^{dc} are cooling rates for cooling point C in the non-distributed cooling model and distributed cooling model respectively, x_i^{nc}, $y_i^{nc}$and x_i^{dc}, y_i^{dc} are X and Y coordinate difference between cooling point C and investigated point P in the non-distributed cooling model and distributed cooling model respectively and c, p and α are constant material property parameters. (When t=t$_0$, $x_i^{nc} - vt > 0$)

For distributed cooling with different D_{cc}^{i}, $q^{dc} = q^{nc}$ in the whole cooling area and

$x_i^{dc} > x_i^{nc}$ in cooling section 1 and 2
$x_i^{dc} = x_i^{nc}$ and $y_i^{dc} = y_i^{nc}$ in cooling section 3

$$T_{cool}^{dc} > T_{cool}^{nc}$$

For distributed cooling with different cooling rates, $x_i^{dc} = x_i^{nc}$ and $y_i^{dc} = y_i^{nc}$ in the whole cooling area and

$q^{dc} > q^{nc}$ in cooling section 1 and 2
$q^{dc} = q^{nc}$ in cooling section 3

$$T_{cool}^{dc} > T_{cool}^{nc}$$

Consider changing cooling rate first as shown in Figure 5-21:

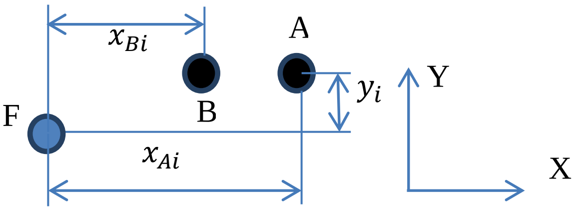

Figure 5-21 Schematic of temperature analysis (varying Dcc)

$$\Delta T_{cool}^{dc} = \sum_{i=1}^{n} \int_0^{t_0} \frac{q^{dc} dt}{cp[4\pi\alpha(t_0 - t)]^{3/2}} \exp\left(\frac{-\left[\left(x_{Ai}^{dc} - vt\right)^2 + y_i^{dc^2}\right]}{4\alpha(t_0 - t)}\right)$$
$$- \sum_{i=1}^{n} \int_0^{t_0} \frac{q^{dc} dt}{cp[4\pi\alpha(t_0 - t)]^{3/2}} \exp\left(\frac{-\left[\left(x_{Bi}^{dc} - vt\right)^2 + y_i^{dc^2}\right]}{4\alpha(t_0 - t)}\right)$$

$$\Delta T_{cool}^{nc} = \sum_{i=1}^{n} \int_0^{t_0} \frac{q^{nc} dt}{cp[4\pi\alpha(t_0 - t)]^{3/2}} \exp\left(\frac{-\left[(x_{Ai}^{nc} - vt)^2 + y_i^{nc^2}\right]}{4\alpha(t_0 - t)}\right)$$
$$- \sum_{i=1}^{n} \int_0^{t_0} \frac{q^{nc} dt}{cp[4\pi\alpha(t_0 - t)]^{3/2}} \exp\left(\frac{-\left[(x_{Bi}^{nc} - vt)^2 + y_i^{nc^2}\right]}{4\alpha(t_0 - t)}\right)$$

Thus $\Delta T_{cool}^{dc} < \Delta T_{cool}^{nc}$

Increasing Dcc has the equivalent effect on temperature as decreasing the cooling rate:

$$\Delta T_{cool}^{dc} = \sum_{i=1}^{n} \int_0^{t_0} \frac{q_A^{dc} dt}{cp[4\pi\alpha(t_0 - t)]^{3/2}} \exp\left(\frac{-\left[\left(x_{Ai}^{dc} - vt\right)^2 + y_i^{dc^2}\right]}{4\alpha(t_0 - t)}\right)$$
$$- \sum_{i=1}^{n} \int_0^{t_0} \frac{q_B^{dc} dt}{cp[4\pi\alpha(t_0 - t)]^{3/2}} \exp\left(\frac{-\left[\left(x_{Bi}^{dc} - vt\right)^2 + y_i^{dc^2}\right]}{4\alpha(t_0 - t)}\right)$$

$$q_A^{dc} > q_B^{dc}$$

$$\Delta T_{cool}^{dc} < \sum_{i=1}^{n} \int_0^{t_0} \frac{q_A^{dc} dt}{cp[4\pi\alpha(t_0 - t)]^{3/2}} \exp\left(\frac{-\left[\left(x_{Ai}^{dc} - vt\right)^2 + y_i^{dc^2}\right]}{4\alpha(t_0 - t)}\right)$$
$$- \sum_{i=1}^{n} \int_0^{t_0} \frac{q_A^{dc} dt}{cp[4\pi\alpha(t_0 - t)]^{3/2}} \exp\left(\frac{-\left[\left(x_{Bi}^{dc} - vt\right)^2 + y_i^{dc^2}\right]}{4\alpha(t_0 - t)}\right)$$

$$q_A^{dc} > q^{nc}$$

Thus $\Delta T_{cool}^{dc} < \Delta T_{cool}^{nc}$

In practice, precise control of the individual nozzle section cooling rates would be more difficult than changing the individual section distance to the tool, Dcc. The latter option is therefore selected for detailed investigation.

5.2.2 Longitudinal residual stress profile

It has been shown that active cooling can reduce longitudinal residual stress near the centre of the weld; however it is more difficult to reduce residual stress in material near the tool edge [5-34]. Theoretical analysis indicates that the edge area is cooler than the center area, so the material is harder and the yield strength relatively high. It is therefore difficult to produce tensile plastic strain or reduce compressive plastic strain in the edge area after the peak temperature has passed.

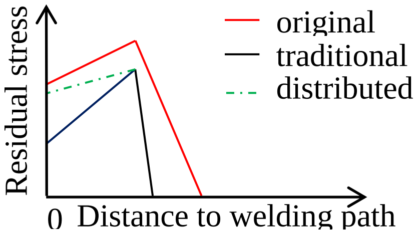

Figure 5-22 Analysis of potential for active cooling

As shown in Figure 5-22, the longitudinal residual stress distribution associated with non-distributed cooling has an M-shape profile, with low residual stress in the center area and high residual stress in both sides. Edge areas are therefore critical to fatigue performance since the grain size is coarser and residual stress is high. This section investigates the possibility of developing a more balanced residual stress profile by applying different cooling rates across the weld, with lower cooling rates (or increase Dcc) towards the center region.

The basic object of optimizing residual stress by distributed cooling is to reduce the temperature drop and lower residual stress, such that the optimized residual stress is no higher than that without optimization.

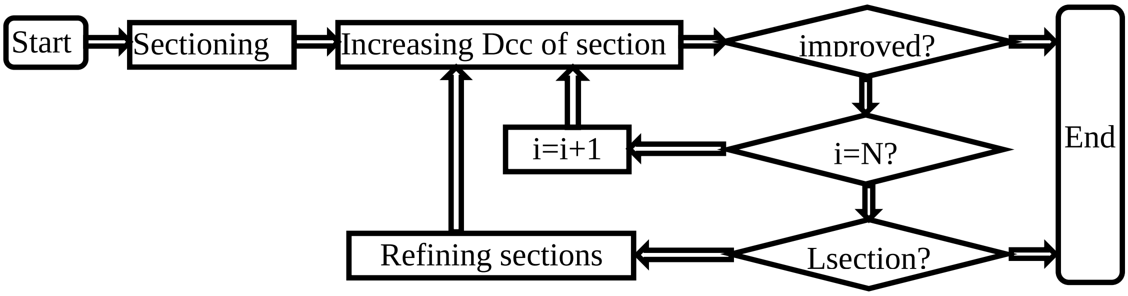

Figure 5-23 Flow chart for distributed cooling optimization

The optimization procedure is shown in Figure 5-23:

- Step1, section the cooling area and number the sections, with the central section numbered as section 1.
- Step 2, keeping other sections constant, increase Dcc of the ith section, (move the ith section away from the welding tool). Initially i is equal to 1.
- Step 3, if S11 is smaller than the previous S11, continue to step 4, otherwise exit the optimization progress.
- Step 4, if current optimized section is the last section, continue to step 5, otherwise optimize the next section and jump to step 2.
- Step 5, if section factor is smaller than criterion, resection the cooling area and jump to step 2 with parameter I equal 1, otherwise exit the optimization progress.

A general progressive procedure of this type could be costly in term of computational requirements and time. A more practical approach is to first define an optimization zone and only optimize for this zone. Any optimization applied outside this zone would contribute less to welding temperature improvement and reduced longitudinal residual stress. The zone is named as optimization region. Optimizing within this region under the condition that the optimized residual stress is no greater than the non-optimised stress is a safe procedure. And the size of safe zone should be located in the center and might take the distribution of longitudinal residual stress into account.

As shown in Figure 5-24:

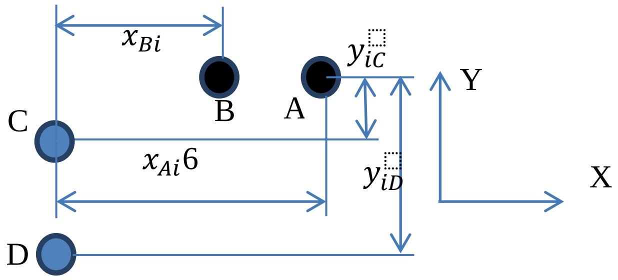

Figure 5-24 Sensitivity of temperature gradient to different zones

$$\Delta T_C^{dc} = \sum_{i=1}^{n} \int_0^{t_0} \frac{q^{dc} dt}{cp[4\pi\alpha(t_0 - t)]^{3/2}} \exp\left(\frac{-\left[\left(x_{Ai}^{dc} - vt \right)^2 + y_{iC}^{dc\,2} \right]}{4\alpha(t_0 - t)} \right)$$

$$- \sum_{i=1}^{n} \int_0^{t_0} \frac{q^{dc} dt}{cp[4\pi\alpha(t_0 - t)]^{3/2}} \exp\left(\frac{-[\left(x_{Bi}^{dc} - vt \right)^2 + y_{iC}^{dc\,2}]}{4\alpha(t_0 - t)} \right)$$

$$\Delta T_D^{dc} = \sum_{i=1}^{n} \int_0^{t_0} \frac{q^{dc} dt}{cp[4\pi\alpha(t_0 - t)]^{3/2}} \exp\left(\frac{-\left[\left(x_{Ai}^{dc} - vt \right)^2 + y_{iD}^{dc\,2} \right]}{4\alpha(t_0 - t)} \right)$$

$$- \sum_{i=1}^{n} \int_0^{t_0} \frac{q^{dc} dt}{cp[4\pi\alpha(t_0 - t)]^{3/2}} \exp\left(\frac{-[\left(x_{Bi}^{dc} - vt \right)^2 + y_{iD}^{dc\,2}]}{4\alpha(t_0 - t)} \right)$$

As $\Delta T_C^{dc} < \Delta T_D^{dc}$, the temperature gradient can be reduced by decreasing the cooling rate in zones close to critical zone to the same degree as in the safe zone.

When the effect of temperature improved gained by moving the safe zone is less than the negative effect of the decreased temperature gradient, the safe zone is no long safe and optimization should stop (it is possible to find refined safe zone in the central area).

5.2.3 FEA model

To compare the difference between conventional FSW welding without active cooling, FSW welding with non-distributed cooling and FSW welding with distributed cooling, a simplified thermal stress coupled finite element model without the mechanical action of the welding tool was created. The material investigated is AA2024, with temperature dependent yield strength. The welding and natural cooling process is in two steps. In the welding step, heat input and active cooling (except original welding model) are applied, while all loads and boundary conditions are released in a natural cooling step. To ensure the temperature of the workpiece drops to ambient temperature, the natural cooling step is set to 174 seconds. The welding start point is set to 10 mm away from the edge, as shown in Figure 5-5 and the welding stop point is 40 mm away from the other edge.

The model is comprised of two plates with dimensions 50 mm * 150 mm * 3 mm, as shown in Figure 5-5. The welding direction is the positive X axis. Only half geometry is modeled, as the geometry, load and boundary conditions are symmetric.

The thermal conductivity is 121 $Wm^{-1}{}^{0}C^{-1}$, density 2780 kg/m^{3}, specific heat capacity is 875 $JKg^{-1}{}^{0}C^{-1}$, Young's modulus 73.1 GPa , Poisson’s ratio are 0.33 and thermal expansion coefficient 2.268E-5 ${}^{0}C^{-1}$. Temperature dependent plastic properties are listed in [5-35] as shown in Table 5-4, which is slightly different from the material properties used in discontinuous cooling models.

Table 5-4 Temperature dependant yield strength

Temperature/°C	25	100	149	204	260	315	371	424
Yield strength/MPa	324	310	248	131	62.0	41.0	27.6	15.3

Figure 5-25 shows the boundary conditions and loads of the FEM. Physically the workpiece would be supported by a rigid plate and usually modeled as contact interaction. As use of a contact algorithm in FEM is time consuming, the support from the rigid plate is simplified to a constraint of Z direction displacement of the workpiece bottom face. Complex heat transfer from faces other than the bottom face to air is simplified to a convection model, with ambient temperature $25^{0}C$ and film coefficient of 15 $Wm^{-2}{}^{0}C^{-1}$. The heat exchange rate between the bottom surface and the virtual supporting plate should be larger than the other surfaces since both materials are metal with relative high conductivity and they are contact pairs. In the welding step, the heat exchange rate for the area of bottom face directly under the welding tool should be larger than other areas because contact in this area is tighter due to the Z axis force from the welding tool, which is supported by results in [5-5]. Here, the film coefficient is set to 500 $Wm^{-2}{}^{0}C^{-1}$, while in other unpressurized areas it is assumed to be 200 $Wm^{-2}{}^{0}C^{-1}$. The total heat input rate is 700 W, with surface heat flux linearly distributed in an area of radius 10 mm, which is equivalent to the radius of tool shoulder. The welding speed is set to 5 mm/s. In the non-distributed cooling model and distributed cooling model, the cooling area projected by the cooling nozzle has the same velocity as the tool. Y direction of the surface parallel to welding line is constrained. In natural cooling step, all heat input and active cooling are removed, as well as the constraint of Y direction for the parallel surface.

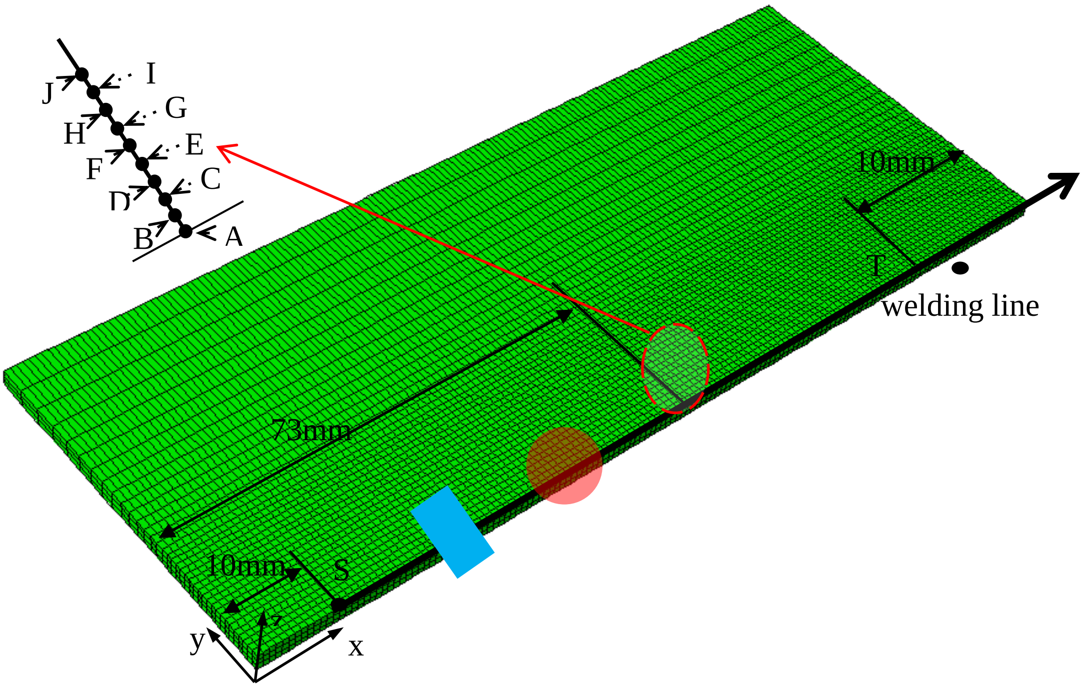

Figure 5-25 Finite element model for FSW

Points A to J are reference points and points S and T are the welding start and end points. The red circle and blue rectangle in Figure 5-25 represent the moving welding tool and cooling nozzle respectively.

To reduce CPU time, geometry remote from the welding path is coarsely meshed. A mesh convergence study was performed to determine a suitable mesh density at the center. The model contains 16200 elements and 22348 nodes in total.

The time increments in both the welding and natural cooling steps are automatically controlled, with maximum increment limited to be 0.1 second in the welding step and 1 second in nature cooling step, taking account of precision for thermal prediction. Calculated results are written every 1 second in the welding step and every 20 seconds in natural cooling step.

5.2.4 FE Results

Figure 5-26 shows the isotherm profile for the model without active cooling has an approximately oval form. The temperature field from step time 14 seconds can be treated as quasi-static with moving coordinate system attached to the welding tool. The rate of change of welding temperature is low, no more than 2 °C/s from step time 14 second. To simplify the investigation, a reference line is chosen at location X=63 mm, as shown in Figure 5-5 and 10 reference points are set at 1 mm interval. All reference points achieve their maximum temperature at step time 14 second and the distribution of longitudinal residual stress across the reference points represent the trend of longitudinal residual stress distribution within the whole weld (except the start section and end section) in the transverse direction.

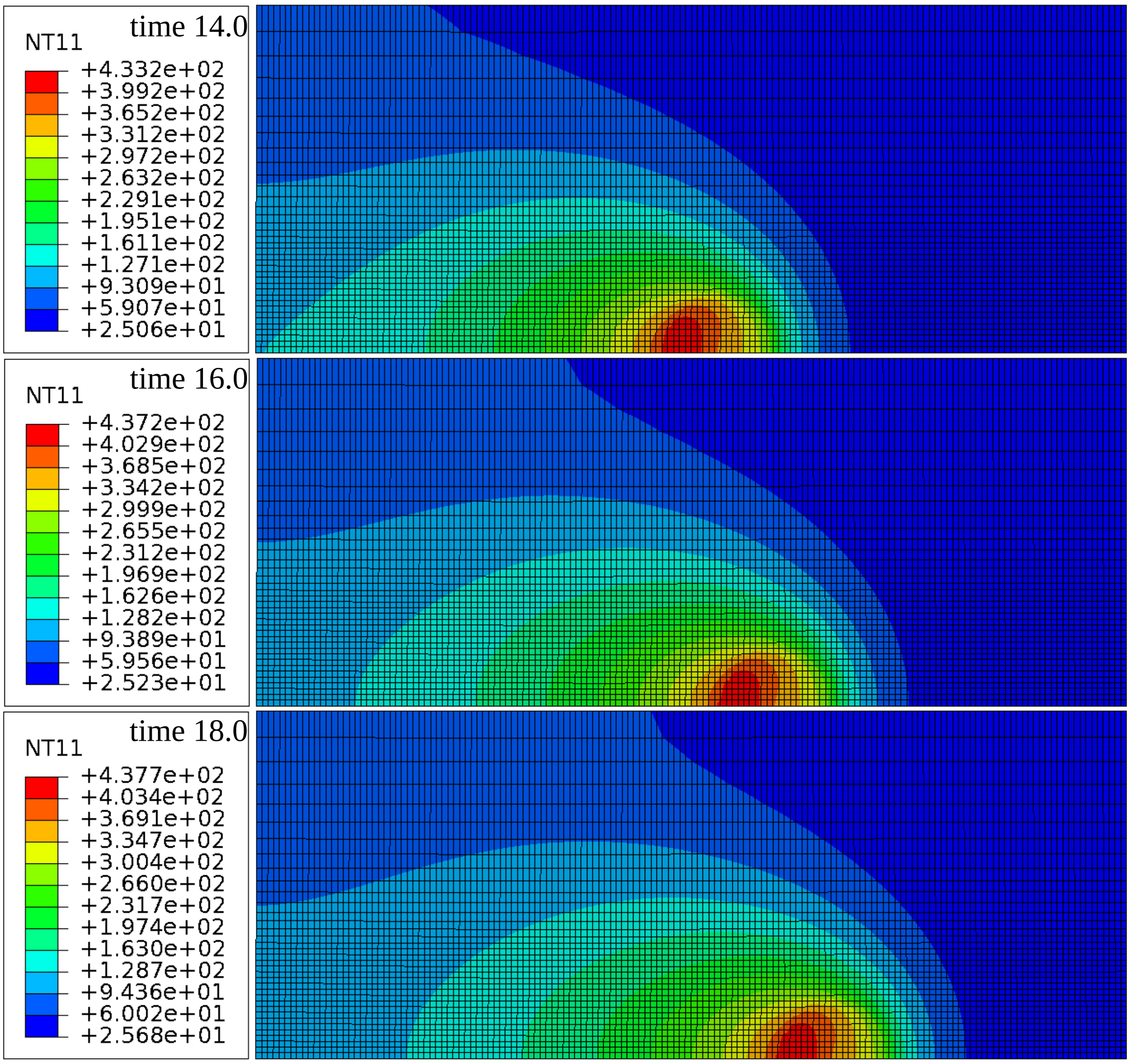

Figure 5-26 Temperature field for original model at different step time

The maximum longitudinal residual stress for original model is 176.5 MPa. As shown in Figure 5-27, the longitudinal residual stress of the weld is tensile with the exception of the welding start section and unwelded section. The transverse distribution is uneven, with high longitudinal residual stress near the tool edge.

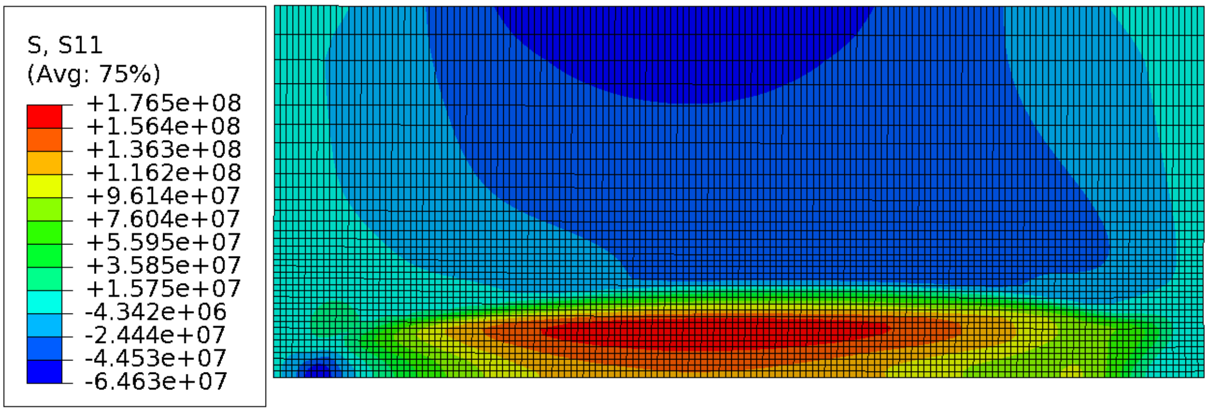

Figure 5-27 Longitudinal residual stress for original model

The S11 distribution along reference line exhibits the expected M profile. In Figure 5-28, the peak longitudinal residual stress is located 8mm from the welding line, while the tool radius is 10 mm.

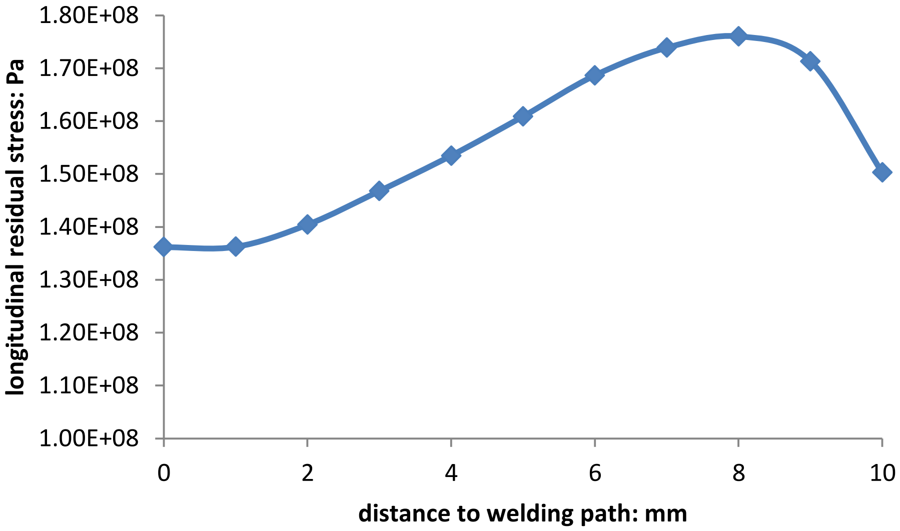

Figure 5-28 Longitudinal residual stress distribution along reference line for original model

The isotherm profile for non-distributed cooling has a different form to that of the original model, with the active cooling altering the, temperature field near the cooling nozzle. The welding temperature under the tool is lower than the original model.

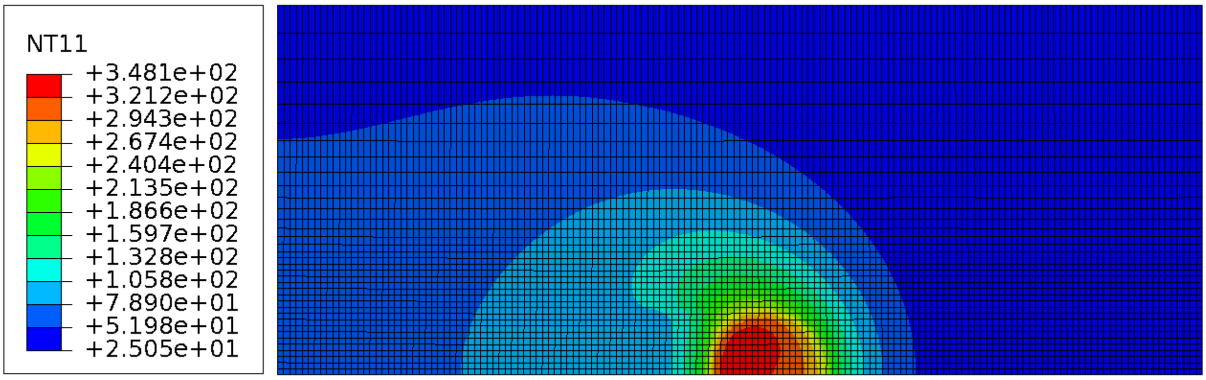

Figure 5-29 Temperature field for non-distributed cooling with Dcc=15mm and cooling rate=1.6E4

As shown in Figure 5-29, addition of active cooling lowers the longitudinal residual stress. In the case of Dcc=15 and cooling rate set to 1.6E4 Wm$^{-2 0}$C^{-1}, the max longitudinal residual stress is 128.8 MPa, which is significantly less than that of the original model. The longitudinal residual stress distribution along transversal direction is also different. As shown in Figure 5-30, the longitudinal residual stress at the tool center and edge is increased; on the reference line the value is 101 MPa compared to 40 MPa in the original model.

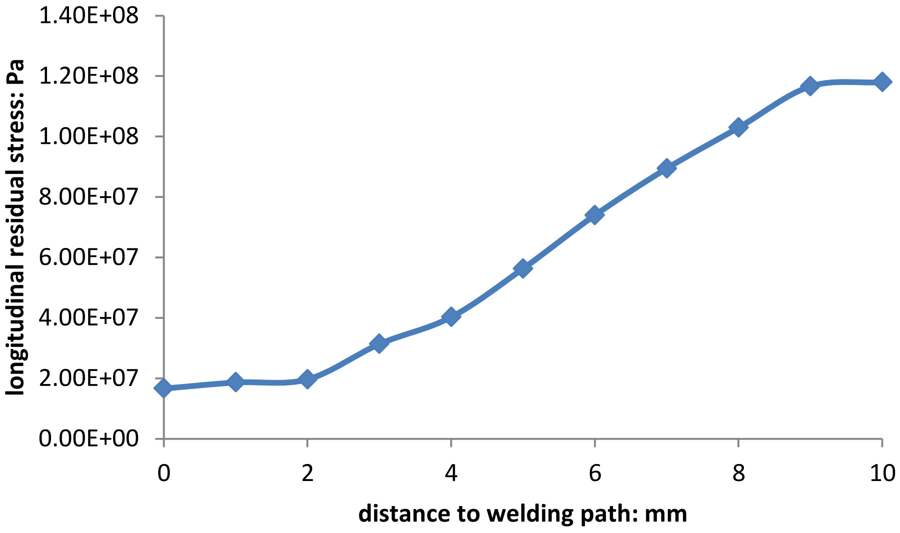

Figure 5-30 Longitudinal residual stress distribution along reference line for non-distributed cooling

The welding temperature drops dramatically when decreasing Dcc, though longitudinal residual stress is also decreasing, as shown in Figure 5-31 and Figure 5-32. When Dcc=15 mm, the welding temperature at step time 14 second drops form original 433.2 ºC to 348.1 ºC. The phenomenon found in [5-34] agrees well with these findings.

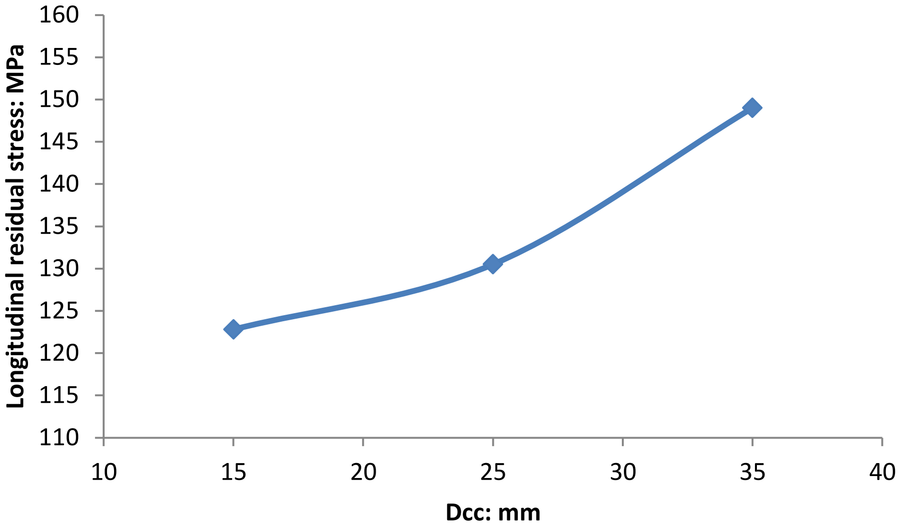

Figure 5-31 Longitudinal residual stress variation with Dcc for non-distributed cooling

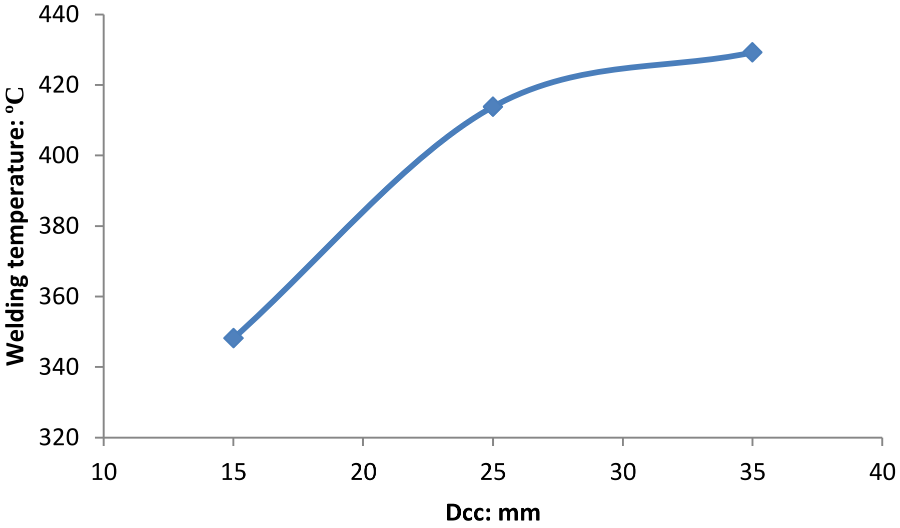

Figure 5-32 Welding temperature variation with Dcc for non-distributed cooling

The temperature field for distributed cooling differs from non-distributed cooling. In non-distributed cooling, the isotherm influenced by cooling nozzle is rectangular, while in distributed cooling the influenced area is smaller and irregular. The welding temperature has risen as shown in Figure 5-33.

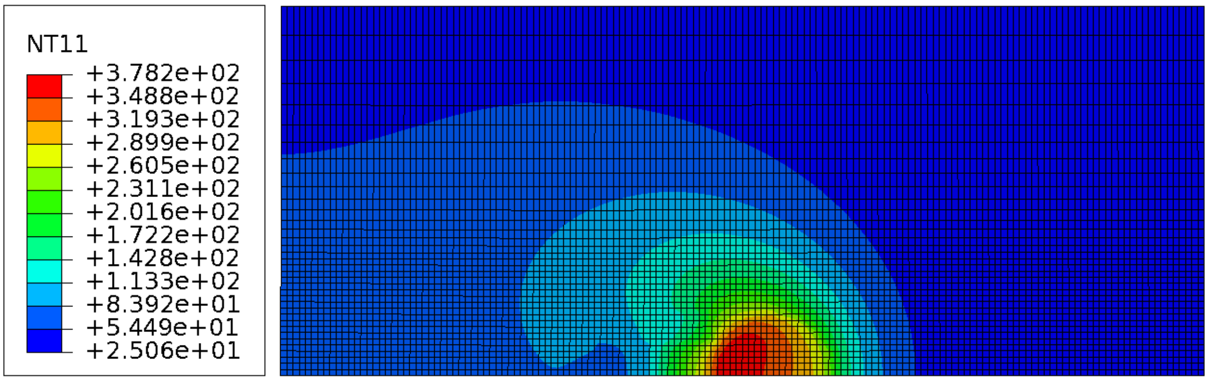

Figure 5-33 Temperature field for distributed cooling with Dcc=15mm, rate=1.6E4

The non-distributed model with Dcc=15 mm and cooling rate=1.6E4 Wm^{-20}C^{-1} was optimized according to the method described in section 5.1.3.4. Sectioning is based on the longitudinal residual stress distribution of the non-distributed cooling model of section 5.2.6.2, at intervals of approximate 40 MPa. Section 1 is from center to 5 mm (not included), section 2 is from 5 mm to 7 mm (not included) and from 7 mm to 10 mm is section 3. The optimization moves section 1 backward at intervals of 2 mm. The first and second moves succeed without increasing the maximum longitudinal residual but increased the temperature of material under the tool center. In the reference line, the welding temperature is improved from 348.1 ºC to 378.2 ºC at the second move. Though further movement of cooling section 1 could further improve welding temperature, the longitudinal residual stress is increased compared to the second moving. Thus the optimized Dcc for cooling section 1 is considered to be 15+4=19 mm. The details are shown in Figure 5-34 and Figure 5-35.

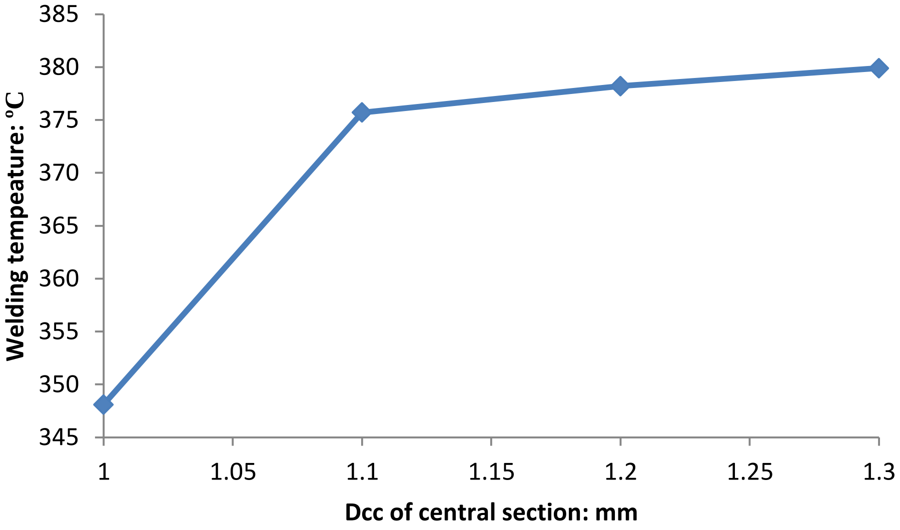

Figure 5-34 Welding temperature variation with increasing Dcc for central section

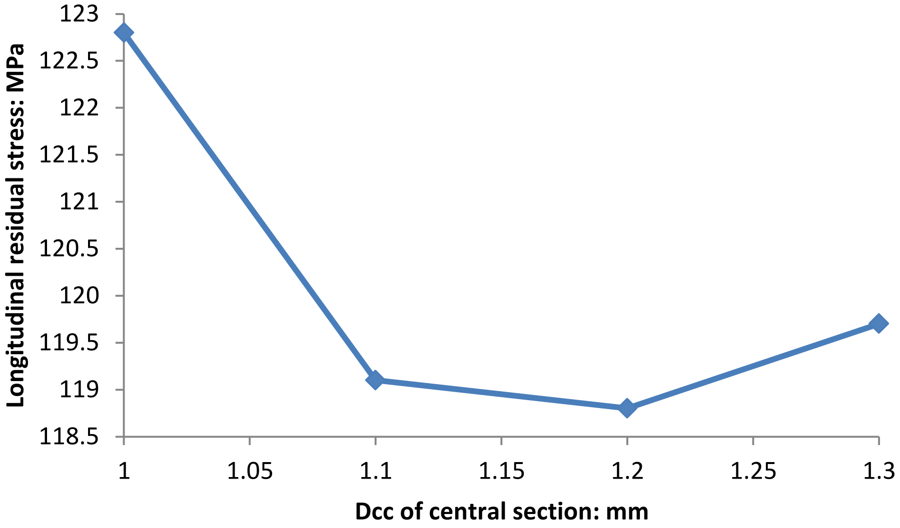

Figure 5-35 Longitudinal residual stress variation with increasing Dcc for central section

From Figure 5-36a, it can be observed that the welding temperature in the distributed cooling model is improved by an average of 25 ºC. This is contributed by the increased Dcc of the central cooling sections. While Figure 5-36b shows the temperature gradient is decreased in distributed cooling, it means the tensile stress, which should be good for reducing compressive plastic strain, is smaller. The opt3 and opt4 are corresponding to the distributed cooling configurations Dcc 1.2mm and Dcc 1.3mm in Figure 5-35.

These results show that under distributed cooling, the welding temperature and temperature gradient are affected and their influence on longitudinal residual stress conflict. As Dccs increases, the welding temperature improvement is limited.

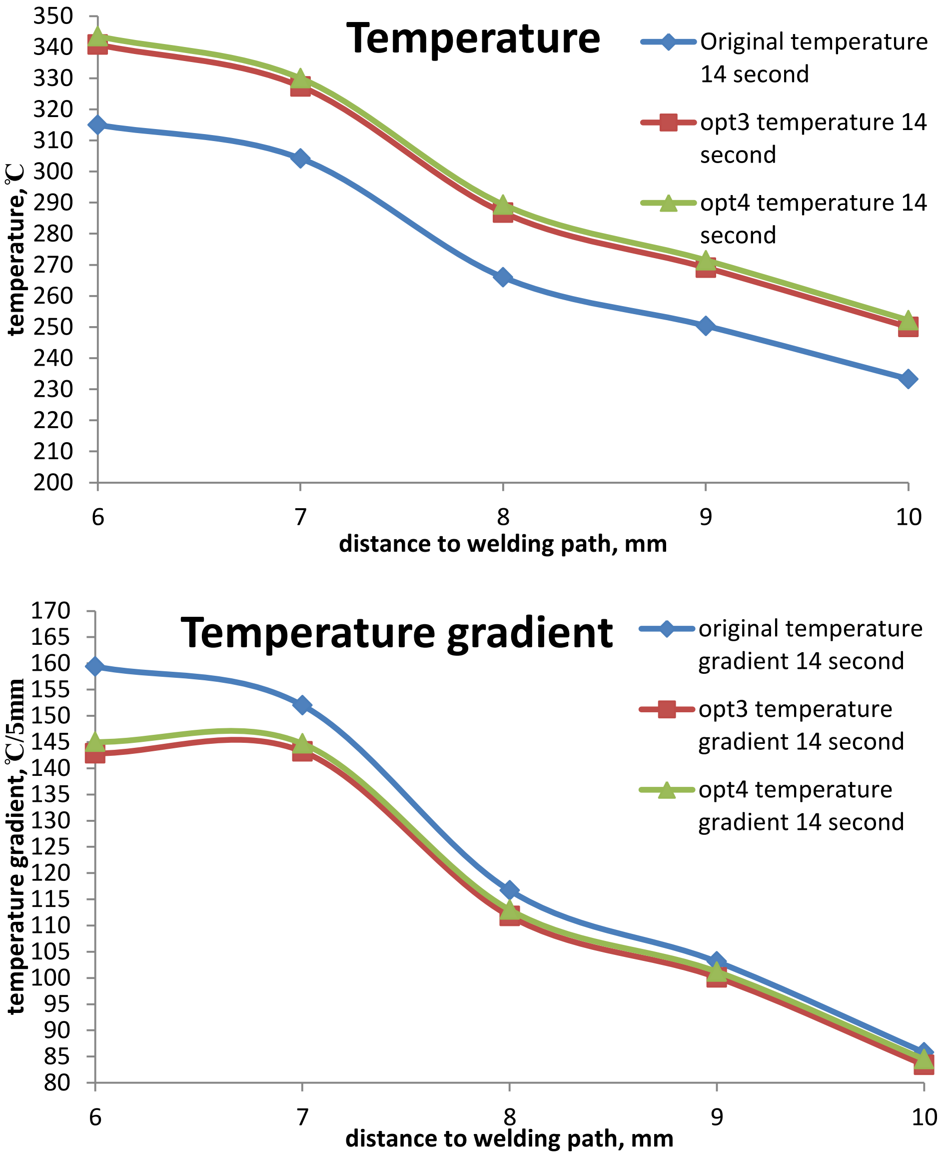

Figure 5-36 temperature and temperature gradient analysis for distributed cooling

The maximum longitudinal residual stress is reduced to 118.8 MPa as shown in Figure 5-37. Difference in longitudinal residual stress at the tool center and edge has also been reduced compared to the non-distributed cooling model. In the reference line, the difference is 36.5 MPa while in non-distributed cooling it is 101 MPa. This phenomenon agrees well with the analysis presented in section 5.1.1.

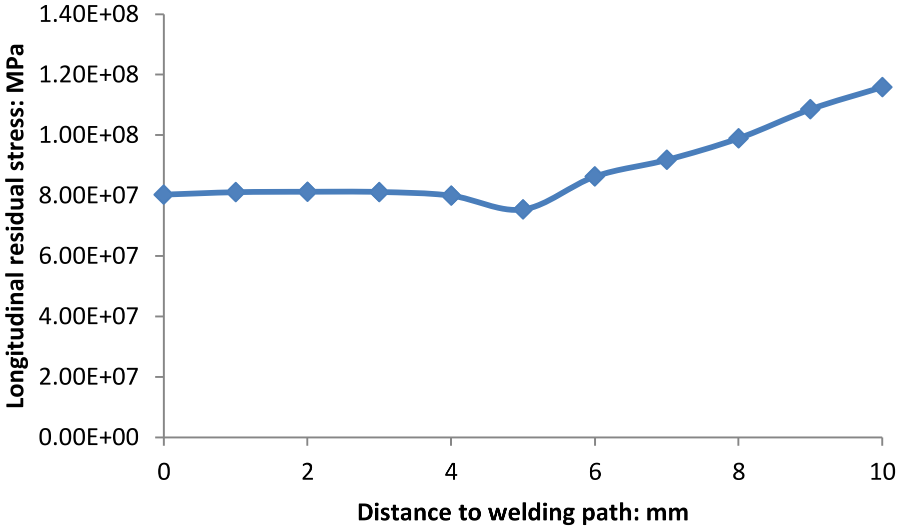

Figure 5-37 Longitudinal residual stress distribution on reference line for optimized distributed cooling

After optimization of cooling section 1, a trial of moving backward cooling section 1 was made but it was found that the longitudinal residual stress is a little bigger that previous result. Thus it is concluded that the model can't be further optimized by distributed cooling with the provided sectioning and Dcc intervals.

5.2.5 Trade-off ratio investigation

Trade-off ratio is defined as:

$$R_{trad} = \frac{(S^0 - S^c)/S^0}{(T^0 - T^c)/T^0} \quad 5\text{-}13$$

where S^c and $S11^0$ are longitudinal residual stress with and without active cooling applied, T^0 and T^c present Welding temperature with and without active cooling applied.

For non-distributed cooling, the ratio decreases quickly as Dcc is decreased, which means the temperature drops dramatically though longitudinal residual stress is reduced, as shown in Figure 5-38. When Dcc gets to its theoretical limit value 15 mm, the ratio has dropped to 8.1% compared to ratio for Dcc=35 mm.

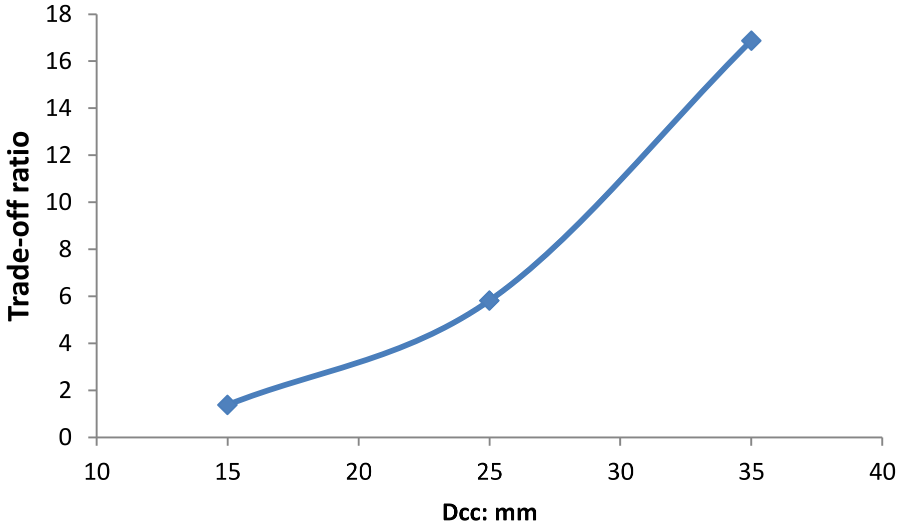

Figure 5-38 Trade-off ratio variation with Dcc for non-distributed cooling

Distributed cooling clearly optimizes the ratio, as shown in Figure 5-39. For Dcc=15 mm, the ratio of distributed cooling has improved 87%, with potential improvement if the cooling area is subdivided.

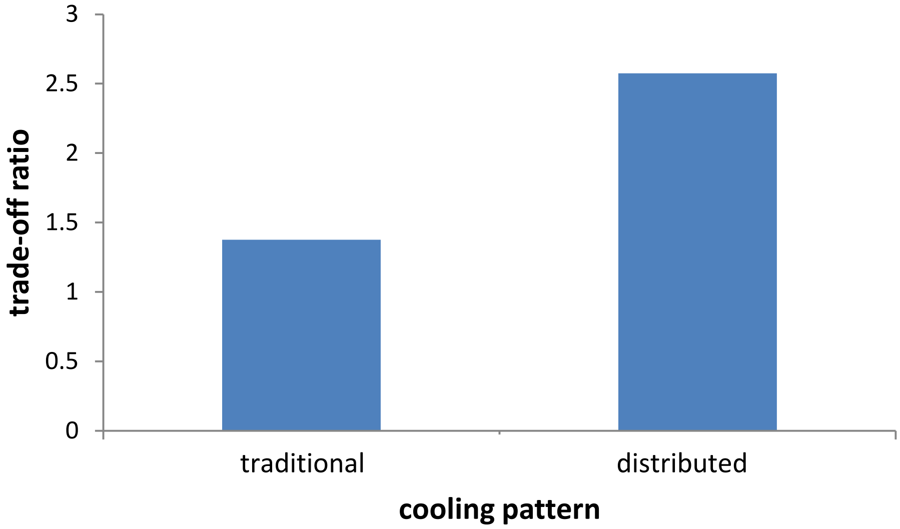

Figure 5-39 Trade-off ratio comparison between distributed cooling and non-distributed cooling with Dcc=15mm

5.3 References

[5-1] R.S. Mishra, Z.Y. Ma, Friction stir welding and processing, Materials Science and Engineering: R: Reports, Volume 50, Issues 1–2, 31 August 2005, Pages 1-78, ISSN 0927-796X, 10.1016/j.mser.2005.07.001.

[5-2] H.W. Zhang, Z. Zhang, J.T. Chen, The finite element simulation of the friction stir welding process, Materials Science and Engineering: A, Volume 403, Issues 1–2, 25 August 2005, Pages 340-348, ISSN 0921-5093, 10.1016/j.msea.2005.05.052.

[5-3] Mir Zahedul H. Khandkar, Jamil A. Khan, Anthony P. Reynolds, Michael A. Sutton, Predicting residual thermal stresses in friction stir welded metals, Journal of Materials Processing Technology, Volume 174, Issues 1–3, 25 May 2006, Pages 195-203, ISSN 0924-0136, 10.1016/j.jmatprotec.2005.12.013.

[5-4] Chen, C. (2003). Finite element modeling of friction stir welding—thermal and thermomechanical analysis. International Journal of Machine Tools and Manufacture, 43(13), 1319-1326

[5-5] Soundararajan, V., Zekovic, S., & Kovacevic, R. (2005). Thermo-mechanical model with adaptive boundary conditions for friction stir welding of Al 6061.International Journal of Machine Tools and Manufacture, 45(14), 1577-1587.

[5-6] A. Bastier, M.H. Maitournam, F. Roger, K. Dang Van, Modelling of the residual state of friction stir welded plates, Journal of Materials Processing Technology, Volume 200, Issues 1–3, 8 May 2008, Pages 25-37, ISSN 0924-0136, 10.1016/j.jmatprotec.2007.10.083.

[5-7] G. Buffa, L. Fratini, S. Pasta, R. Shivpuri, On thermo-mechanical loads and the resultant residual stresses in friction stir processing operations, CIRP Annals - Manufacturing Technology, Volume 57, Issue 1, 2008, Pages 287-290, ISSN 0007-8506, 10.1016/j.cirp.2008.03.035

[5-8] Livan Fratini, Gandolfo Macaluso, Salvatore Pasta, Residual stresses and FCP prediction in FSW through a continuous FE model, Journal of Materials Processing Technology, Volume 209, Issues 15–16, 1 August 2009, Pages 5465-5474, ISSN 0924-0136, 10.1016/j.jmatprotec.2009.05.001.

[5-9] G. Buffa, A. Ducato, L. Fratini, Numerical procedure for residual stresses prediction in friction stir welding, Finite Elements in Analysis and Design, Volume

47, Issue 4, April 2011, Pages 470-476, ISSN 0168-874X, 10.1016/j.finel.2010.12.018.

[5-10] Weifeng Xu, Jinhe Liu, Hongqiang Zhu, Analysis of residual stresses in thick aluminum friction stir welded butt joints, Materials & Design, Volume 32, Issue 4, April 2011, Pages 2000-2005, ISSN 0261-3069, 10.1016/j.matdes.2010.11.062.

[5-11] G Bussu, P.E Irving, The role of residual stress and heat affected zone properties on fatigue crack propagation in friction stir welded 2024-T351 aluminum joints, International Journal of Fatigue, Volume 25, Issue 1, January 2003, Pages 77-88, ISSN 0142-1123, 10.1016/S0142-1123(02)00038-5.

[5-12] Altenkirch, J., Steuwer, A., Withers, P. J., Williams, S. W., Poad, M., & Wen, S. W. (2009). Residual stress engineering in friction stir welds by roller tensioning. Science and Technology of Welding and Joining, 14(2), 185-192.

[5-13] D.G. Richards, P.B. Prangnell, S.W. Williams, P.J. Withers, Global mechanical tensioning for the management of residual stresses in welds, Materials Science and Engineering: A, Volume 489, Issues 1–2, 20 August 2008, Pages 351-362, ISSN 0921-5093, 10.1016/j.msea.2007.12.042.

[5-14] Staron, P. (2004). Residual stress in friction stir-welded Al sheets. Physica B: Condensed Matter, 350(1-3), E491-E493.

[5-15] D.G. Richards, P.B. Prangnell, P.J. Withers, S.W. Williams, T.Nagy, S.Morgan, Efficacy of active cooling for controlling residual stresses in friction stir welds, Science and Technology of Welding & Joining, Vol. 15, No. 2, pp. 156-165.

[5-16] Li, T., Shi, Q. Y., & Li, H. K. (2007). Residual stresses simulation for friction stir welded joint. Science and Technology of Welding and Joining, 12(8), 664-670.

[5-17] Q.Lin, J.Chen and H.Chen, Possibility of inducing compressive residual stresses in welded joints of SS400 steels, Journal of Material Science and Technology, Vol.17 No.6, 2001

[5-18] H.Chen, W.Fricke and A.Krohn, Experimental study of Inducing Compressive Stress by Anti-welding Heating Treatment in a Thin Plate Weldment with Variant Temperatures, Journal of Material Science and Technology, Vol.18 No.2, 2002

[5-19] W.Zhang, Heat transfer for welding, Tianjin: Mechanical Industry Press, 1987

[5-20] R.S. Mishra, Z.Y. Ma, Friction stir welding and processing, Materials Science and Engineering: R: Reports, Volume 50, Issues 1–2, 31 August 2005, Pages 1-78, ISSN 0927-796X, 10.1016/j.mser.2005.07.001.

[5-21] H.W. Zhang, Z. Zhang, J.T. Chen, The finite element simulation of the friction stir welding process, Materials Science and Engineering: A, Volume 403, Issues 1–2, 25 August 2005, Pages 340-348, ISSN 0921-5093, 10.1016/j.msea.2005.05.052.

[5-22] Mir Zahedul H. Khandkar, Jamil A. Khan, Anthony P. Reynolds, Michael A. Sutton, Predicting residual thermal stresses in friction stir welded metals, Journal of Materials Processing Technology, Volume 174, Issues 1–3, 25 May 2006, Pages 195-203, ISSN 0924-0136, 10.1016/j.jmatprotec.2005.12.013.

[5-23] Chen, C. (2003). Finite element modeling of friction stir welding—thermal and thermomechanical analysis. International Journal of Machine Tools and Manufacture, 43(13), 1319-1326

[5-24] Soundararajan, V., Zekovic, S., & Kovacevic, R. (2005). Thermo-mechanical model with adaptive boundary conditions for friction stir welding of Al 6061.International Journal of Machine Tools and Manufacture, 45(14), 1577-1587.

[5-25] A. Bastier, M.H. Maitournam, F. Roger, K. Dang Van, Modelling of the residual state of friction stir welded plates, Journal of Materials Processing Technology, Volume 200, Issues 1–3, 8 May 2008, Pages 25-37, ISSN 0924-0136, 10.1016/j.jmatprotec.2007.10.083.

[5-26] G. Buffa, L. Fratini, S. Pasta, R. Shivpuri, On thermo-mechanical loads and the resultant residual stresses in friction stir processing operations, CIRP Annals - Manufacturing Technology, Volume 57, Issue 1, 2008, Pages 287-290, ISSN 0007-8506, 10.1016/j.cirp.2008.03.035

[5-27] Livan Fratini, Gandolfo Macaluso, Salvatore Pasta, Residual stresses and FCP prediction in FSW through a continuous FE model, Journal of Materials Processing Technology, Volume 209, Issues 15–16, 1 August 2009, Pages 5465-5474, ISSN 0924-0136, 10.1016/j.jmatprotec.2009.05.001.

[5-28] G. Buffa, A. Ducato, L. Fratini, Numerical procedure for residual stresses prediction in friction stir welding, Finite Elements in Analysis and Design, Volume

47, Issue 4, April 2011, Pages 470-476, ISSN 0168-874X, 10.1016/j.finel.2010.12.018.

[5-29] Weifeng Xu, Jinhe Liu, Hongqiang Zhu, Analysis of residual stresses in thick aluminum friction stir welded butt joints, Materials & Design, Volume 32, Issue 4, April 2011, Pages 2000-2005, ISSN 0261-3069, 10.1016/j.matdes.2010.11.062.

[5-30] G Bussu, P.E Irving, The role of residual stress and heat affected zone properties on fatigue crack propagation in friction stir welded 2024-T351 aluminium joints, International Journal of Fatigue, Volume 25, Issue 1, January 2003, Pages 77-88, ISSN 0142-1123, 10.1016/S0142-1123(02)00038-5.

[5-31] Altenkirch, J., Steuwer, A., Withers, P. J., Williams, S. W., Poad, M., & Wen, S. W. (2009). Residual stress engineering in friction stir welds by roller tensioning. Science and Technology of Welding and Joining, 14(2), 185-192.

[5-32] D.G. Richards, P.B. Prangnell, S.W. Williams, P.J. Withers, Global mechanical tensioning for the management of residual stresses in welds, Materials Science and Engineering: A, Volume 489, Issues 1–2, 20 August 2008, Pages 351-362, ISSN 0921-5093, 10.1016/j.msea.2007.12.042.

[5-33] Staron, P. (2004). Residual stress in friction stir-welded Al sheets. Physica B: Condensed Matter, 350(1-3), E491-E493.

[5-34] D.G. Richards, P.B. Prangnell, P.J. Withers, S.W. Williams, T.Nagy, S.Morgan, Efficacy of active cooling for controlling residual stresses in friction stir welds, Science and Technology of Welding & Joining, Vol. 15, No. 2, pp. 156-165.

[5-35] Li, T., Shi, Q. Y., & Li, H. K. (2007). Residual stresses simulation for friction stir welded joint. Science and Technology of Welding and Joining, 12(8), 664-670.

6 Optimization Oriented Multi-physics Modelling

Large structures, such as airplane fuselages made of AA2024, are commonly manufactured using welding processes to join multiple components or parts together. In practice, post welding heat treatment may be expensive and difficult to achieve for large structures. Therefore, it is strongly desirable that the mechanical performance of the structures should be optimized at the stage of welding process design to eliminate or minimize post welding treatment. Residual stress and inappropriate material properties due to microstructure alteration during friction stir welding are significant factors in the structure’s mechanical performance, fatigue and corrosion performance for instance, and the main concerns in this Chapter.

Investigations of residual stress of friction stir welding in the past decades could be classified into either experiment methods or simulation methods. H. Lombard *et al* systematically examined the correlation between mid-length residual stress profile and welding parameters rotational speed and welding velocity by non-destructive synchrotron X-ray radiation. It was found that the width of tensile stress region and magnitude of peak tensile residual stress are linearly dependent on heat input per unit length. W. Xu *et al* measured temperature and bottom surface and top surface residual stress for 12 mm thick AA2219 friction stir butt welding, and revealed different residual stress profile on bottom and top surface by hole-drilling method. It was also indicated that the longitudinal residual stress of the top surface decreased with increasing rotational speed, while the longitudinal residual stress increased with increasing rotational speed. Residual stress numerical models mainly focused on thermal stress, which is considered to be dominated. T. Li *et al* predicted residual stress of 3mm thick AA2024-T3 friction stir butt welding, and compared the results with or without accounting for mechanical load from the tool. Despite of that the model with tool force was thought to be more realistic, magnitude of longitudinal residual stress for the model with only thermal load agreed well with experimental measurement, and this finding was frequently confirmed and commonly recognized.

For microstructure evolution and properties investigation for welding, age hardening aluminum alloys were one of the most interesting fields. C. Chen et.al analyzed the pre-existing phases in AA2024-T3 with differential scanning calorimetry (DSC), and temperature field of HAZ is simulated by Gleeble. It is found that material experiencing different peak temperature resulted in different hardness and hardness recovery one month after welding, and it is linked to phases' dissolution and precipitation. I. Khan *et al* investigated the microstructural evolution of AA2024-T351 during variable polarity plasma arc welding to predict the hardness and yield strength. Approximations have been proposed to improve the computational efficiency. H. Shercliff *et al* applied a simplified semi-analytical dissolution model for AA2014-T6. The dissolution model introduced a reference temperature and corresponding reference full dissolution time, with the kinetic hardness calculated as a ratio to the reference hardness. The predicted hardness after 1 week natural ageing near the weld center is close to the measured hardness. Microstructure models had already been reported to successfully predict mechanical properties for several alloys, and basically the microstructure is calculated increment by increment.

Recently integrated models combining thermal-mechanical analysis and microstructure analysis have become popular. The advantages of integrated models are the capability to predict various statuses of welded components or structures, such as residual stress, grain size, precipitation size, micro hardness, tensile strength and even corrosion properties. But it is noted that integrated models were usually time expensive due to the complexity involved in kinetic microstructure prediction and material property prediction.

In this Chapter, an optimization oriented integrated model for AA2024-T3 friction stir welding, incorporating thermal stress coupled model, temperature history based simplified microstructure model and the novel discontinuous cooling method described in Chapter 5, is proposed for computational efficiency.

The welding temperature involved in the FSW process is high and the heating duration is short. The peak material temperature in the weld is usually higher than heat treatment temperature: for AA2024, the solution heat treatment temperature is 493 ºC and artificial aging process temperature is 191 ºC. But the welding process can't be considered as a standard heat treatment process since the 'hold' time is so short that the precipitations couldn't achieve an equilibrium status, in other words, precipitation evolution is kinetic instead of quasi-static and it is dependent on peak temperature and hold duration.

Here, a simplified integrated model is presented, as shown in Figure 6-1. The heat input rate from the tool and the welding velocity are defined as model parameters. The novel discontinuous active cooling method is introduced to reduce the residual stress and alter the thermal cycles to influence microstructure evolution; thus the cooling rate, cooling duty and frequency are also defined as model parameters. These parameters, in combination with the thermal material properties, determine the temperature cycles. For the residual stress model, only thermal stress is considered and the material properties, including thermal conductivity and yield strength, are obtained via published data. For the microstructure model, the temperature history data of each location is compared to a reference curve, whose mechanical properties such as hardness and tensile strength are known experimentally.

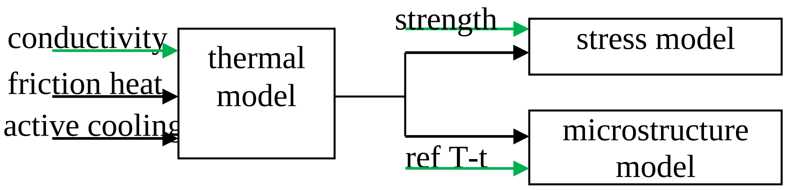

Figure 6-1 Schematic of integrated model

The microstructure model is based on the following analysis. For material from a certain batch, the chemistry composition is evenly distributed and the initial microstructure is uniform. The ultimate mechanical performance of any location is then dependent on the temperature history curve it experienced if work hardening occurred. For FSW, work hardening in the TMAZ and HAZ is negligible compared to SZ (nugget zone) and usually no recovery occurred [6-28]. For AA2024-T3, the contribution to hardness and strength of the precipitation evolution is dominant compared to solid solution [6-28]. In temperature range 262 ^{0}C to 400 ^{0}C, which is the peak temperature range for TMAZ and HAZ in FSW, precipitates are mainly subject to coarsening as identified in [6-25]. The hardness and strength vary linear with precipitate volume fraction and

$$X_d \approx K\Omega\tau^n \quad 6\text{-}1 \quad [6\text{-}29]$$

$$\tau = \frac{Dt}{R^2} \quad 6\text{-}2 \quad [6\text{-}29]$$

Where K is a kinetic constant, Ω is dimensionless supersaturation, n is a time exponent and n<1, D is kinetic and dependent on temperature T, R is the initial particle radius.

Analytic solution of X_d is complex and the following simplification has been made: the peak temperature of reference temperature history curve is referred to as the reference temperature and the duration of reference temperature above 262 ^{0}C is set as the reference duration. Other curves may have a difference peak temperature and its equivalent reference duration is proportional to its peak temperature, as shown in Equation 6-3.

$$t_{ref}^{e} = t_{ref}T_{ref}/T \quad 6\text{-}3$$

Where $t_{ref}$is the reference duration, T_{ref} is the reference temperature and t_{ref}^{e} and T are equivalent reference duration and peak temperature for temperature history curves other than the reference curve.

The volume fraction of precipitates is a linear function of its actual duration, as shown in Equation 6-4.

$$f = k_0 t/t_{ref}^{e} \quad 6\text{-}4$$

Where *t* is the time duration for other curves above 262 ^{0}C, k_0 is a constant.

In the FEM, computational cost is a power function of the number of degrees of freedom. For large welding models, the computing time or cost is highly dependent on the number of elements and nodes. Generally, the welding process can be considered to be a quasi-static thermal process from the view of the moving coordinate system bound to the welding tool, so the residual stress and microstructure distribution shouldn’t change too much along the welding path except at the start position and stop positions. Therefore, to reduce computation cost, relatively small geometry can be used to represent the residual stress and microstructure of large size model by reduce the size along welding path in addition to commonly used techniques such as symmetrical modeling.

It is not necessary to apply the microstructure model to all material since peak temperatures experienced by most base material are too low to make obvious microstructure alteration. For temperatures under 262 ^{0}C, microstructure alteration is not considered here and this condition is named as the temperature boundary. The mechanical properties in the stir zone are usually better than in the TMAZ or HAZ [6-32], so SZ is not considered in detail and the location of TMAZ/HAZ is defined as the geometry boundary. The geometry boundary is 3 dimensional and complex but here it is simplified to a 1D problem: that is, the TMAZ/HAZ geometry boundary is assumed to be parallel to the welding line through the thickness. Based on these boundaries, a zone of interest is established according to location (coordinates) and history peak temperature.

6.1.1 Numerical model

The numerical model simulates the dwell and welding stage of a physical friction stir butt welding process and the plunge and retrieve stage are ignored. The workpiece consists of two AA2024-T3 plates. The dimensions of the two parts are 125 mm * 200 mm * 3 mm, modeled as continuum solids. As the plates are identical, symmetric boundary conditions are applied to reduce computational cost. The element used is C3D8RT and the mesh near the seam is refined to 1 mm* 1 mm* 1 mm. The total number of elements and nodes in the model are 20904 and 15000 respectively.

The heat generated by the tool can be divided into two parts: friction heat between the shoulder and component material and friction heat between the probe and component material. The total heat input rate from the shoulder is 670 W and its heat flux distribution is linear to the radius, as shown in Figure 6-2. The total heat input from the probe is 230 W and it is assume to be uniformly distributed body heat flux among the cylinder. Diameters for the shoulder and probe are 16 mm and 5 mm separately.

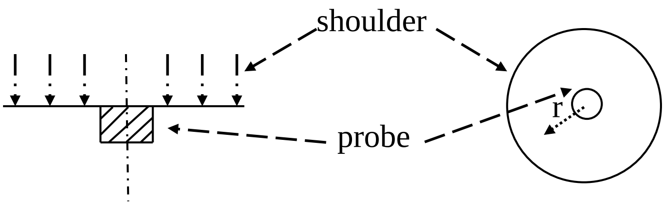

Figure 6-2 Heat source model for FSW

The discontinuous active cooling is modeled as a surface convection and implemented by user defined subroutine FILM. The temperature of cooling source is -72 ^{0}C and the film coefficient varies with time, as shown in Figure 6-3. The cooling source is rectangular and moves synchronously with the welding tool. The distance between the tool center and cooling source center is 13 mm. The frequency of discontinuous cooling is 1 Hz and aligned with step time, so that the active cooling would be applied at the very beginning of each second. Cooling duty is from 0.1 to 0.2 at an interval of 0.05.

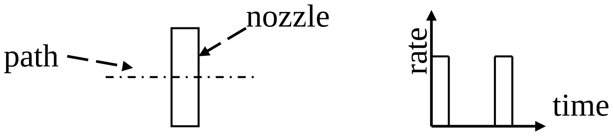

Figure 6-3 Cooling source model for discontinuous cooling

A Symmetry boundary condition is applied to the cross section along the welding path, as shown in Figure 6-4. Face A is restricted from moving in the transverse direction. The backing plate is simplified to a rigid support at the Z axis and the bottom surface is restricted from moving up or down. The heat transfer rate between the component and clamping parts is 500 Wm^{-2}^{0}C^{-1}and for surface exposed to air the heat transfer rate is 25 Wm^{-2}^{0}C^{-1}.

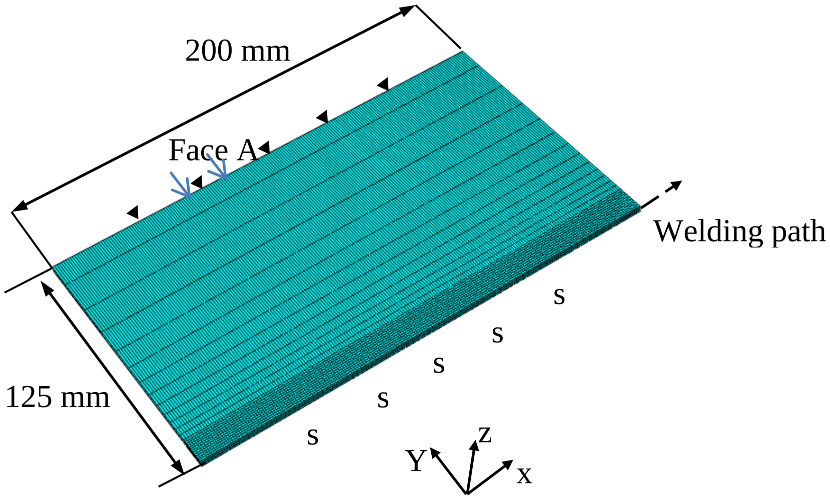

Figure 6-4 Geometry, mesh and boundary condition for numerical model

The mass density of AA2024-T3 is 2780 kg/m^3, specific heat capacity is 875 Jkg^{-1}^{0}C^{-1}, Young's module and Poisson’s ratio are 73.1 GPa and 0.33 respectively and the thermal expansion coefficient is 2.268E-5 ^{0}C^{-1}. The thermal conductivity is temperature dependent, as shown in *Table 6-1*. And yield strength is temperature history dependent, as shown in Figure 6-5. During the heating stage of each material point, the yield strength is determined by its current temperature. For the cooling stage of each material point, the yield strength is not only related to current temperature but also the peak temperature in history. The plastic behavior is described by a perfect plasticity model.

Table 6-1 Temperature dependent conductivity

temperature	25	25<T<500	500
conductivity	120	120*(T-25)/475	240

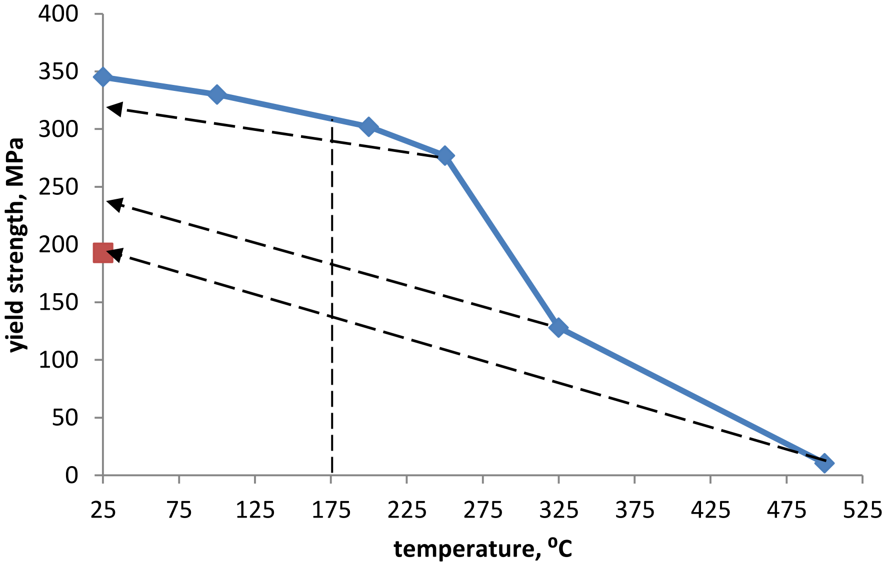

Figure 6-5 Temperature history dependent yield strength [6-19] for AA2024-T3

To reduce computational cost, the microstructure model is only applied to a small zone of the component material, which is called the interest zone. The geometry boundary of the interest zone is based on the size of the welding tool, especially the diameter of probe. Here, the probe diameter is 2.5 mm and the geometry boundary is 3mm from the welding line. The temperature boundary is determined by the material chemical composition: for AA2024, the critical temperature is 262 ^{0}C, as precipitation coarsening is accelerated for material experiencing temperature above 262 ^{0}C.

The reference temperature history curve is shown in Figure 6-6. Peak temperature is 375 ºC and the welding duration is 6 seconds. The corresponding micro hardness was measured experimentally and the Hv micro hardness value is 123.5. If peak temperature in interest zone is no less than 375 ºC, the equivalent reference time is larger than 6 seconds as calculated by equation6-3, otherwise, equivalent reference duration is less than 6 seconds. The micro hardness of corresponding microstructure is determined by actual welding duration and equivalent reference duration, as shown in equation 6-4.

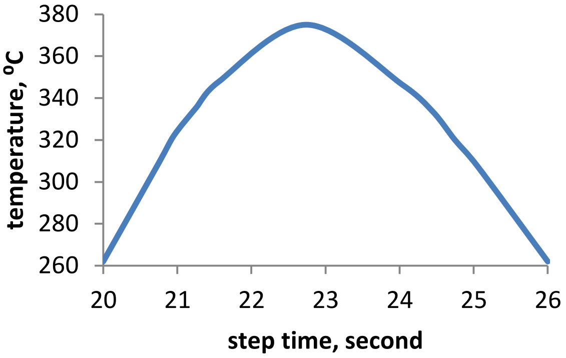

Figure 6-6 Reference temperature history data

6.2 Results and discussion

The numerical model results are compared with the experimentally measured residual stress and the simulated microstructure is analyzed. *Table 6-2* is time cost list of the various models used in the present work. Basically, computational time cost for each model is around 3 hours on a 4-core Intel computer at 2.93 GHz.

Table 6-2 Time cost of integrated models

Model name	M1	M2	M3	M4
time cost	3h6m09s	3h16m11s	3h3m37s	3h3m48s

M1: duty 0.15, welding speed 2.5 mm/s, M2: duty 0.20, welding speed 2.5 mm/s, M3: duty 0.10, welding speed 3.00 mm/s, M4: duty 0.10, welding speed 3.5 mm/s

6.2.1 Residual stress

The history peak temperature of each material point is plotted in Figure 6-7. The isotherm lines are parallel to the welding path except the start point and terminal point. This indicates that the heating progress for each material point is similar and the moving temperature field is stable. The peak temperature observed in the model without discontinuous cooling is 471 ºC.

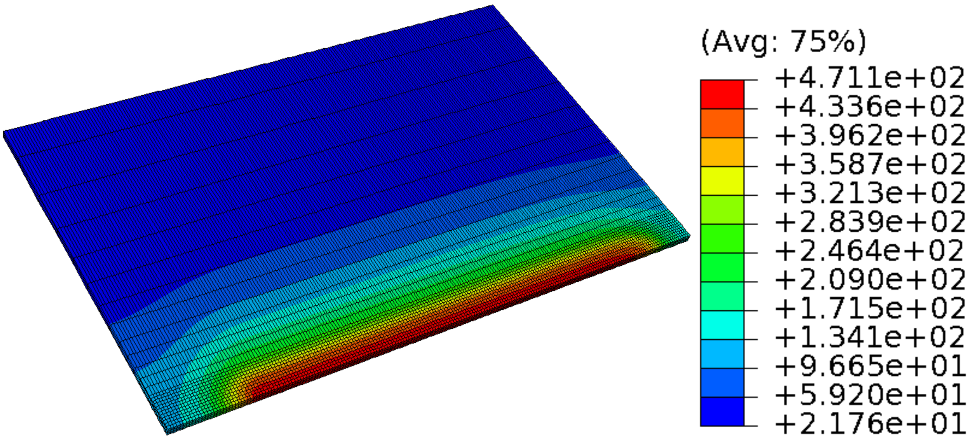

Figure 6-7 History peak temperature field

The residual stress in the middle of mid-thickness layer is shown in Figure 6-8. The longitudinal residual stress has a typical M profile and the predicted peak longitudinal residual stress is 174 MPa located in the position 6 mm from the welding line.

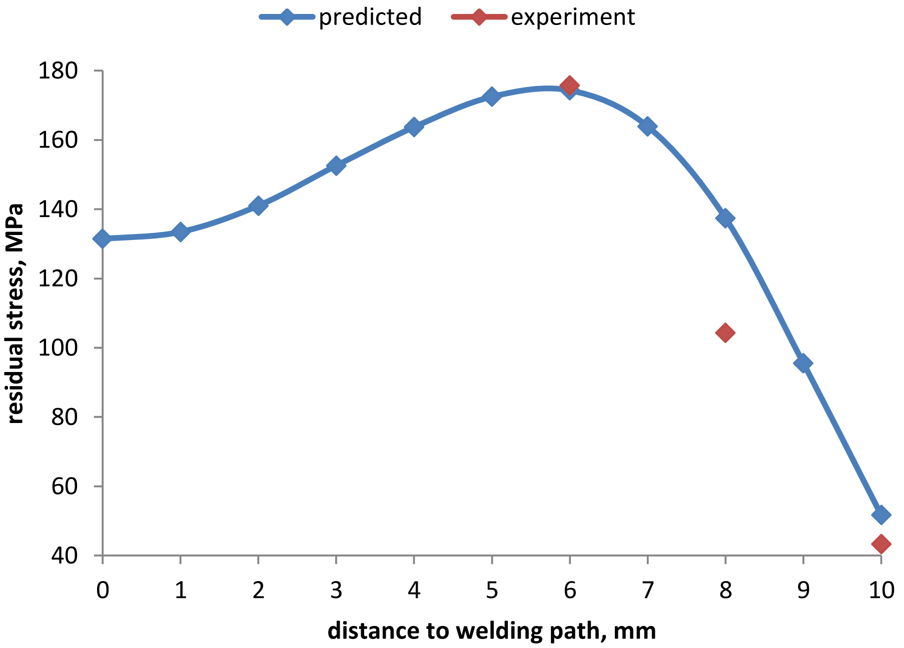

Figure 6-8 Longitudinal residual stress distribution at the middle of mid-thickness layer

The results from the model are compared to experiment results for the same welding velocity, the same material AA2024 and the same nominal heating power from the welding tool, shown in Figure 6-8. The dimensions of the plates used in the experiment are 1000 mm*125 mm*3 mm and the length is much bigger than that in this section. However, the observed peak temperature, magnitude of longitudinal residual stress of mid-thickness layer and its corresponding position are similar. The peak temperature in the experiment is 468 °C, compared to 471 °C in the model and the magnitude of longitudinal residual stress is 176 MPa compared to 174 MPa. The position corresponding to the peak longitudinal residual stress is 6 mm, compared to 6 mm. The minor difference of magnitude and position of peak longitudinal residual stress could be caused by ignoring mechanical effect of the welding tool.

6.2.2 Microstructure

As shown in Figure 6-9, the temperature boundary of interest zone is 12 mm from the welding line, which agrees well with reported findings that the dimension of HAZ is almost linear to the size of the welding tool shoulder.

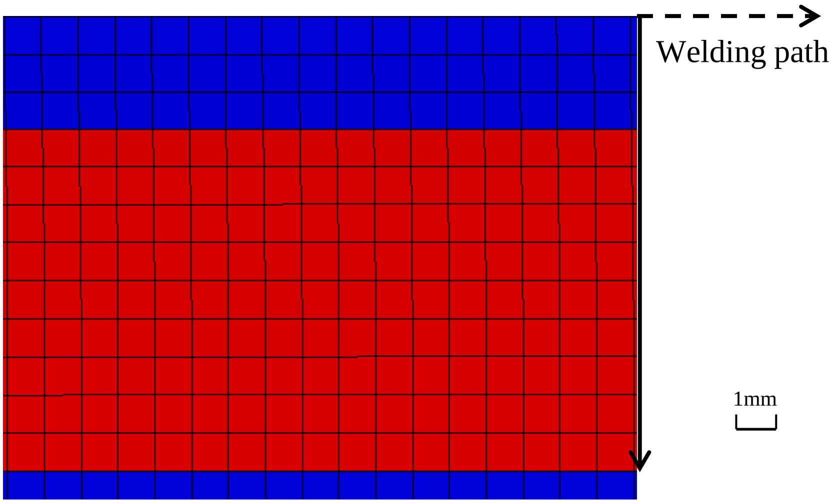

Figure 6-9 Interest zone dimension (top surface)

red: interest zone, blue: non-interest zone

The predicted micro hardness of the SZ and TMAZ interface is plotted in Figure 6-10 and it is observed that the micro hardness near the interface is much smaller than reference hardness. This reflects the physical phenomena that the interface between SZ and TMAZ is usually a weak zone if no fault [6-27] occurred during welding. Another interesting phenomenon is that the width of the interface varies with welding velocity. As shown in Figure 6-11, the interface zone width increased with decreasing welding velocity. Physically, decreasing welding velocity would increase the welding duration and coarsen the precipitation thus the micro hardness would drop.

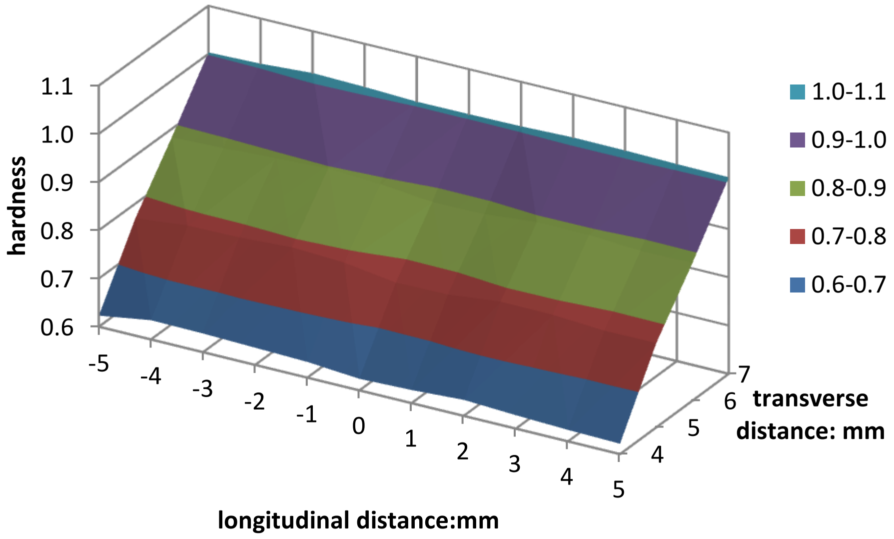

Figure 6-10 Predicted hardness for SZ and TMAZ interface zone

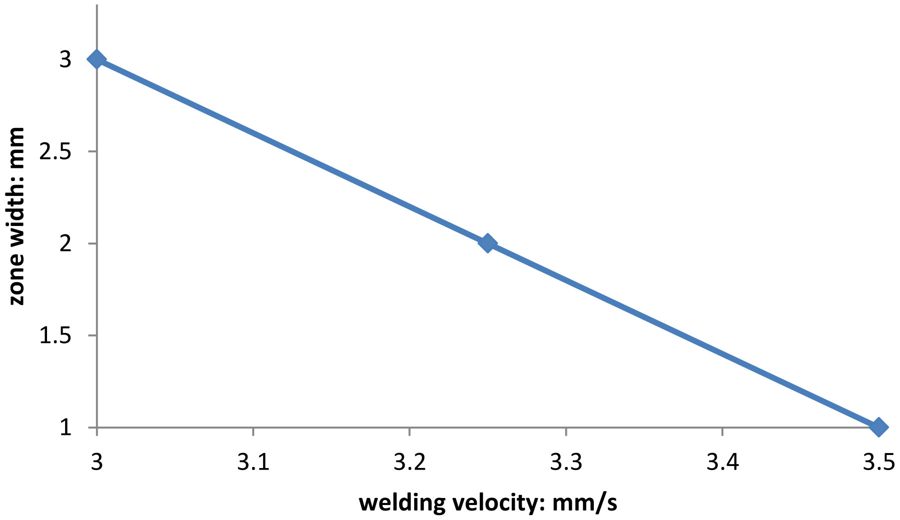

Figure 6-11 Variation of predicted hardness width (average) in the interface zone with welding velocity

6.2.3 Effect of Active cooling on width of interface

Appling discontinuous cooling to FSW decreases the width of interface zone, as shown in Figure 6-12. The average micro hardness of the interface zone increased.

Further increasing cooling duty results in a narrower interface zone, as shown in Figure 6-13. And the interface zone can even disappear if the discontinuous cooling is strong enough.

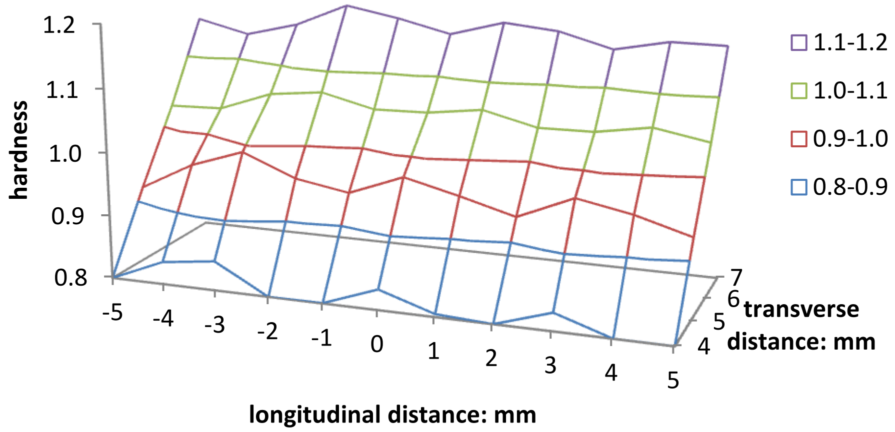

Figure 6-12 Hardness in the interface zone with discontinuous cooling

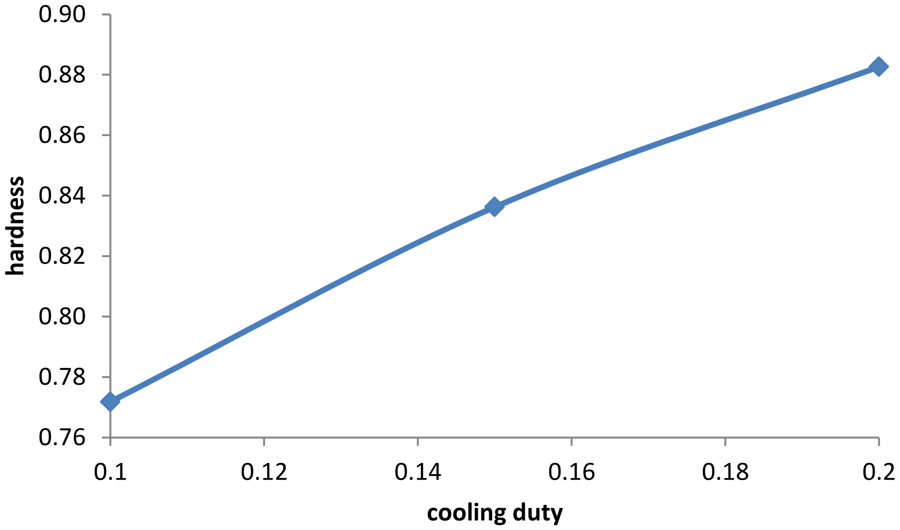

Figure 6-13 Hardness in the interface zone with increasing cooling duty (minimum)

The temperature history curve close to the geometry boundary is influenced by addition of discontinuous cooling. As shown in Figure 6-14, discontinuous cooling has little influence on the heating stage but enhances cooling progress, which significantly reduces the total welding duration.

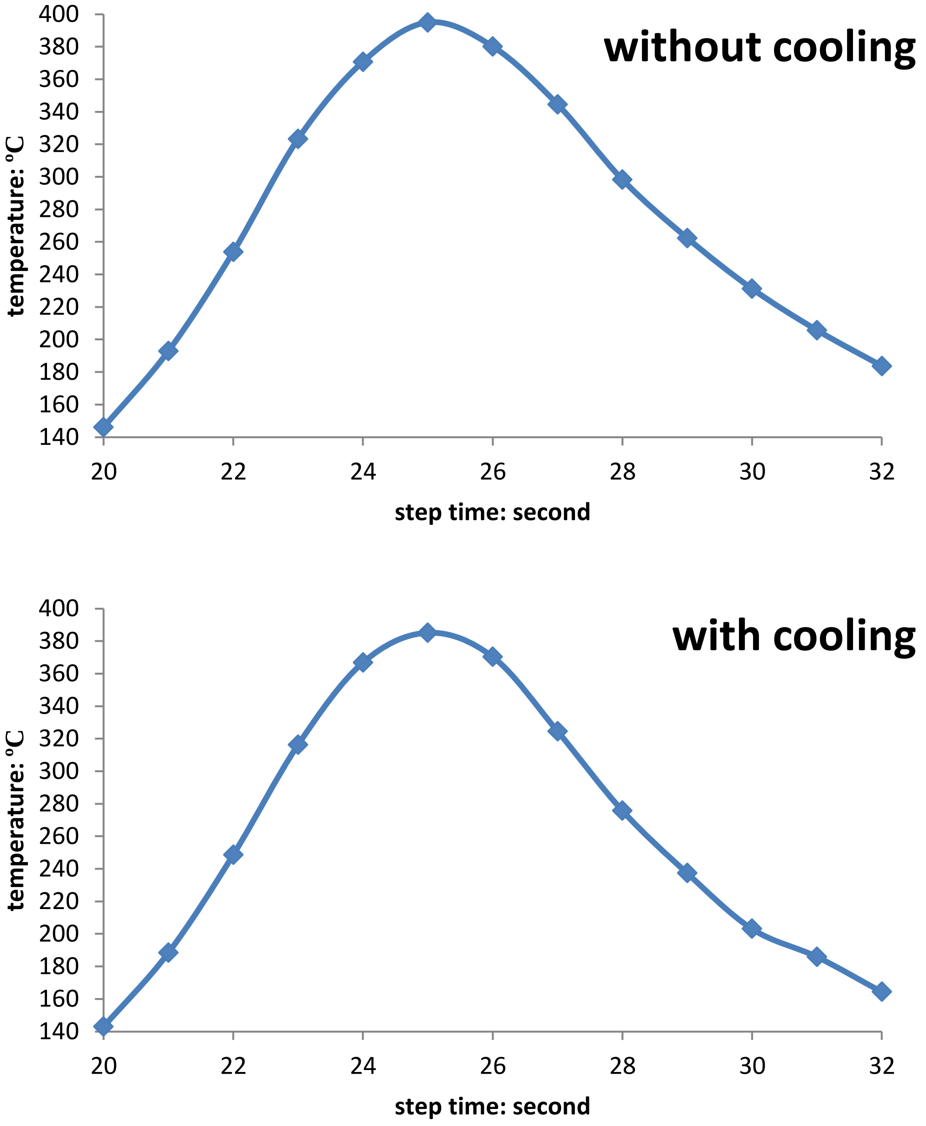

Figure 6-14 Temperature history curve with/without discontinuous cooling

6.2.4 Micro hardness distribution

Figure 6-15 shows the micro hardness contour. The contours are parallel to the welding line, due to the fact that isotherm lines are parallel to the welding line. The micro hardness distribution at transverse direction is shown in Figure 6-15. This indicates that the hardness increases with increasing distance from the welding line. This is explained by the fact that the history peak temperature decreases with increasing distance, thus the precipitation coarsening rate decreases.

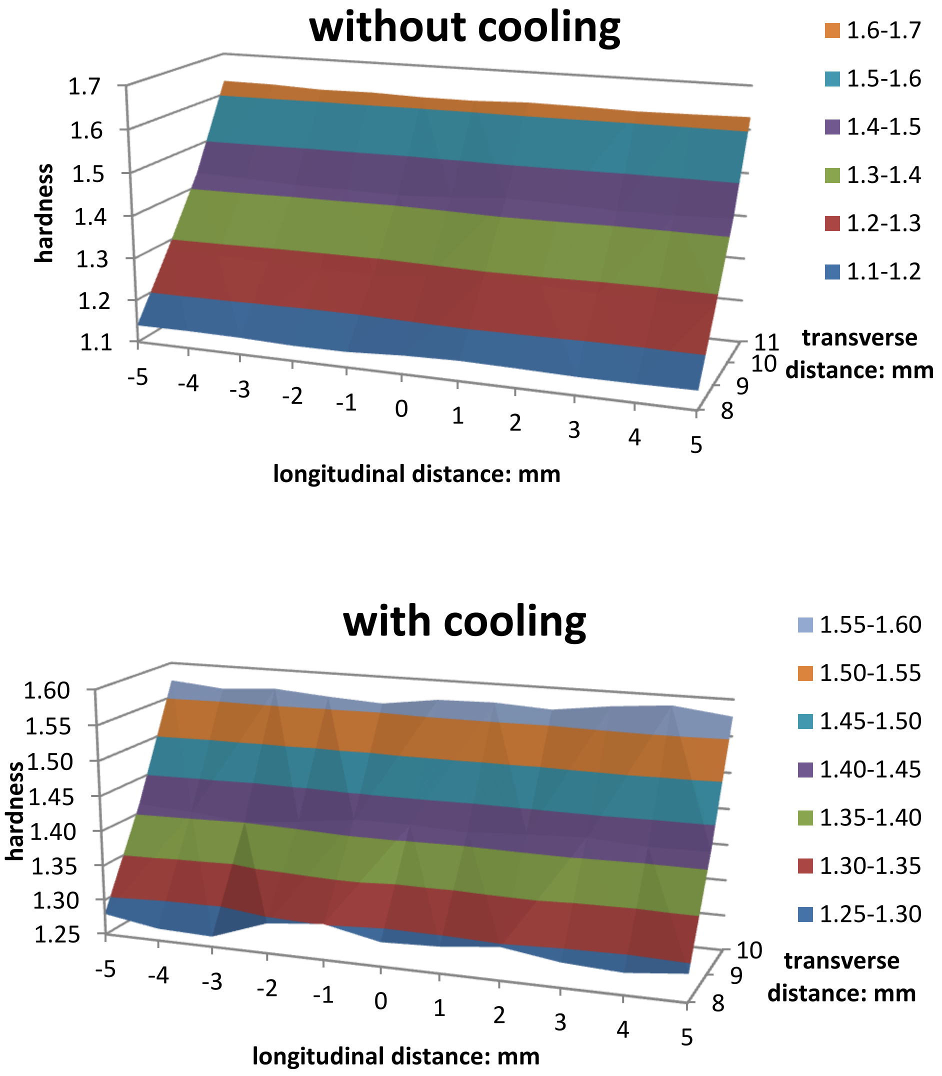

Figure 6-15 Micro hardness distribution

The hardness is compared to published data [6-28], which used the same material AA2024-T3, but with welding velocity mm/s, as shown in Figure 6-16. The experimentally measured data shows an approximate linear relationship between the hardness and the distance to the welding line from the interface zone (between NZ and HAZ), which agrees well with hardness profile calculated here. The difference in slope could be contributed to the welding velocity difference.

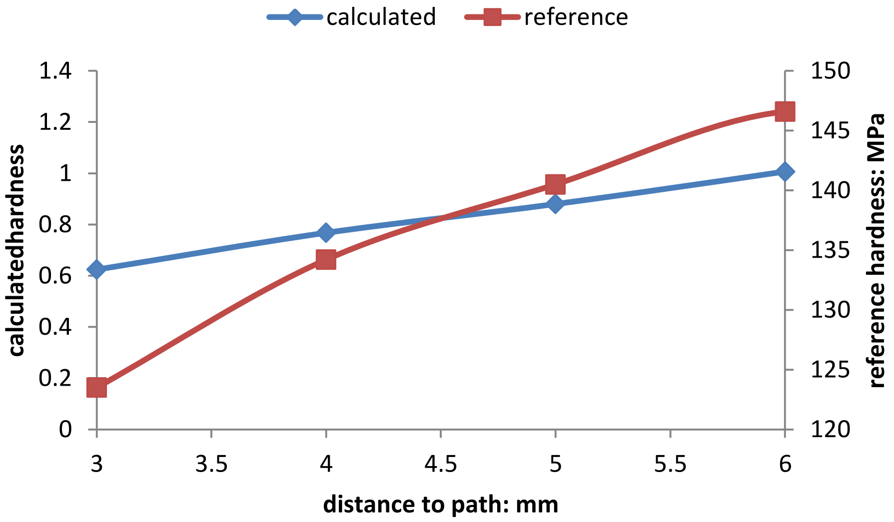

Figure 6-16 Comparison of calculated hardness profile and referrence hardness profile

6.3 References

[6-1] Q.Lin, J.Chen and H.Chen, Possibility of inducing compressive residual stresses in welded joints of SS400 steels, Journal of Material Science and Technology, Vol.17 No.6, 2001

[6-2] H.Chen, W.Fricke and A.Krohn, Experimental study of Inducing Compressive Stress by Anti-welding Heating Treatment in a Thin Plate Weldment with Variant Temperatures, Journal of Material Science and Technology, Vol.18 No.2, 2002

[6-3] W.Zhang, Heat transfer for welding, Tianjin: Mechanical Industry Press, 1987

[6-4] Van der Aa, E.M. (2007), Local Cooling during Welding: Prediction and Control of Residual Stresses and Buckling Distortion, PhD thesis, Delft University of Technology, UK

[6-5] H. Lombard, D.G. Hattingh, A. Steuwer, M.N. James, Effect of process parameters on the residual stresses in AA5083-H321 friction stir welds, Materials Science and Engineering: A, Volume 501, Issues 1–2, 15 February 2009, Pages 119-124

[6-6] Weifeng Xu, Jinhe Liu, Hongqiang Zhu, Analysis of residual stresses in thick aluminum friction stir welded butt joints, Materials & Design, Volume 32, Issue 4, April 2011, Pages 2000-2005

[6-7] Li, T.; Shi, Q.Y.; Li, H.-K., Residual stresses simulation for friction stir welded joint, Science and Technology of Welding & Joining, Volume 12, Number 8, November 2007 , pp. 664-670(7)

[6-8] Khan, I.N. and Starink, M.J. (2008) Microstructure and strength modelling of Al-Cu-Mg alloys during non-isothermal treatments: part 1 – controlled heating and cooling. Materials Science and Technology, 24, 1403-1410

[6-9] Khan, I.N., Starink, M.J., Sinclair, I. and Wang, S.C. (2008) Microstructure and strength modelling of Al-Cu-Mg alloys during non-isothermal treatments: part 2 - Welds. Materials Science and Technology, 24, 1411-1418

[6-10] Yutaka S. Sato, Hiroyuki Kokawa, Masatoshi Enomoto and Shigetoshi Jogan, Microstructural evolution of 6063 aluminum during friction-stir welding. METALLURGICAL AND MATERIALS TRANSACTIONS A, Volume 30, Number 9 (1999), 2429-2437

[6-11] Williams, S. W., Colegrove, P. A., Shercliff, H., Prangnell, P., Robson, J., & Withers, P. (2006). Integrated Modelling of the Friction Stir Welding Process.Elements.

[6-12] A. Simar, Y. Bréchet, B. de Meester, A. Denquin, C. Gallais, T. Pardoen, Integrated modeling of friction stir welding of 6xxx series Al alloys: Process, microstructure and properties, Progress in Materials Science, Volume 57, Issue 1, January 2012, Pages 95-183

[6-13] R.S. Mishra, Z.Y. Ma, Friction stir welding and processing, Materials Science and Engineering: R: Reports, Volume 50, Issues 1–2, 31 August 2005, Pages 1-78

[6-14] Zacharia, T.; Radhakrishnan, B.; Paul, A. J.; Cheng, C. An integrated model for optimizing weld quality. Modeling of Casting, Welding and Advanced Solidification Processes 7, London, England, 10-15 Sep. 1995

[6-15] M. A. Sutton ; A. P. Reynolds ; D.-Q. Wang, A Study of Residual Stresses and Microstructure in 2024-T3 Aluminum Friction Stir Butt Welds. Journal of Engineering Materials and Technology. 2002, 124(2)

[6-16] I.N. Khan et al., 2006, A Multi-Mechanistic Model for Precipitation Strengthening in Al-Cu-Mg Alloys during Non-Isothermal Heat Treatments. Materials Science Forum, 519-521, 277

[6-17] D.E. Boyce, P.R. Dawson, B. Sidle, T. Gnäupel-Herold, A multiscale methodology for deformation modeling applied to friction stir welded steel, Computational Materials Science, Volume 38, Issue 1, November 2006, Pages 158-175

[6-18] E. Hersent, J. H. Driver, D. Piot, C. Desrayaud, Integrated modelling of precipitation during friction stir welding of 2024-T3 aluminium alloy. Material Science and Technology 2011 26(11) 1345-1352

[6-19] R.V. Preston, H.R. Shercliff, P.J. Withers, S. Smith, Physically-based constitutive modelling of residual stress development in welding of aluminium alloy 2024, Acta Materialia, Volume 52, Issue 17, 4 October 2004, Pages 4973-4983

[6-20] Preston, RV; Shercliff, HR; Withers, PJ; Smith, SD, Finite element modelling of tungsten inert gas welding of aluminium alloy 2024. SCIENCE AND TECHNOLOGY OF WELDING AND JOINING. 2003;8:10-18.

[6-21] Laurent Dubourg et al., 2010, Prediction and Measurements of Thermal Residual Stresses in AA2024-T3 Friction Stir Welds as a Function of Welding Parameters. Materials Science Forum, 638-642, 1215

[6-22] D.G. Richards, P.B. Prangnell, S.W. Williams, P.J. Withers, Global mechanical tensioning for the management of residual stresses in welds, Materials Science and Engineering: A, Volume 489, Issues 1–2, 20 August 2008, Pages 351-362

[6-23] Axel Steuwer et al., 2006, Aspects of Residual Stress Determination Using Energy-Dispersive Synchrotron X-Ray Diffraction. Materials Science Forum, 524-525, 267

[6-24] DA Price, SW Williams, A Wescott, CJC Harrison, A Rezai, A Steuwer, et al. Distortion control in welding by mechanical tensioning, Science and Technology. 12 (2007) 620-633

[6-25] Saad Ahmed Khodir, Toshiya Shibayanagi and Masaaki Naka, Control of Hardness distribution in friction stir welded AA2024-T3. 2006 57(6) 1560-1567

[6-26] Benavides, S.; Li, Y.; Murr, L. E.; Brown, D.; McClure, J. C, Low-Temperature Friction-Stir Welding of 2024 Aluminum. METALLIC MATERIALS. 1999 14(8) 809-815

[6-27] Genevois, C., et al., Quantitative investigation of precipitation and mechanical behaviour for AA2024 friction stir welds. Acta Materialia, 2005. 53(8): p. 2447-2458

[6-28] Saad Ahmed Khodir*, Toshiya Shibayanagi and Masaaki Naka, Microstructure and Mechanical Properties of Friction Stir Welded AA2024-T3 Aluminum Alloy. Materials Transactions. 2006 47(1) 185-193

[6-29] O.R. Myhr, Ø. Grong, Process modelling applied to 6082-T6 aluminium weldments—I. Reaction kinetics, Acta Metallurgica et Materialia, Volume 39, Issue 11, November 1991, Pages 2693-2702

[6-30] H.J Liu, H Fujii, M Maeda, K Nogi, Tensile properties and fracture locations of friction-stir-welded joints of 2017-T351 aluminum alloy, Journal of Materials Processing Technology, Volume 142, Issue 3, 10 December 2003, Pages 692-696

[6-31] H.R. Shercliff, M.J. Russell, A. Taylor, T.L. Dickerson, Microstructural modelling in friction stir welding of 2000 series aluminium alloys. Mec Ind, 6 (2005), pp. 25-35

[6-32] Chen, C S; Yang, J G; Tan, A H, Study of welding peak temperatures on microstructures and hardness of heat affected zone in 2024-T3 aluminium alloy. 2009 2597) 896-904

7 Small Punch Beam Test Method

Standard testing methods usually require relatively large material specimens and the characterized properties can be volume-averaged, so it is difficult to apply standard testing methods to identify material property distribution in friction stir welds, which is composed by several small zones.

In this chapter, a small punch testing system based on a small beam shape specimen and punch similar to that of SPPS is presented in the first section. Material properties are evaluated from the deformation through comparison with multi-linear strain hardening Finite Element analysis of specimen deformation and a genetic algorithm utilizing a cost function based on the relative difference between the experimental and testing forces at the top center of the beam. The small punch beam testing tool design is presented in the Section 7.1.2, while the experiment procedure is given in Section 7.1.3. FEM modeling is presented in Section 7.1.4, material property characterization using a genetic algorithm method in section 7.1.5 and results in section 7.1.6.

In the second section, the average plastic properties of a Friction Stir Welded (FSW) material are characterized using a procedure combining small punch beam testing, finite element analysis and a neural network algorithm. The base test-piece is a FSW sheet of 2024-T3 Aluminum alloy: length 500 mm, width 60 mm and thickness approx. 1.6 mm. The FSW parameters used were: rotational speed 800 rpm and welding speed 100 mm/min. Diameter of the welding tool's shoulder is 8 mm. No post welding heat treatment was applied. Methodology is introduced in section 7.2.1, including experiment setups and numerical methods. Then the results are presented and discussed in section 7.2.2.

In the third section, small punch beam test method is applied to characterize friction stir welds, which is comprised of several different material zones. The advantages and application of this study is introduced and then methodology is presented in section 7.3.1. The next two sections are numerical results and discussion of error factors for this study.

7.1 Plastic Property Characterisation

7.1.1 Small Punch Beam Testing Tool Design

The standard the small punch test (SPT) tool employs an upper and a lower hollow cylindrical shape die and a cylindrical punch with hemispherical punch head. To avoid the high cost and low accuracy for manufacturing hemispherical punch head, the new designed tool testing system shown in Figure 7-1 has been developed. The tool consists of top and a bottom blocks, each having a narrow through slot. The test beam specimen is located in a shallow slot perpendicular to the through slot. The punch is a rectangular bar with a half-cylinder profile contact surface, overcoming the manufacturing difficulties associated with a hemispherical punch. The radius of the punch head is 1.25 mm and the width of the punch is 8 mm. The test specimen shown in Figure 7-2 is a beam with rectangular cross section with width of 2 mm and height of 1.6 mm. The height of the beam is slightly greater than the depth of the shallow slot, such that when the four fixing screws are tightened the beam sample is fully clamped. The central part of the beam is 8mm and an additional 4 mm or more of material is included at both ends to hold the beam. Chamfers with size 0.2 mm * 45^o were created on the bottom slot to avoid stress singularity. The four screws were tightened with equal torque using a torque wrench to keep the top and bottom surfaces parallel. The punch is guided by the slot in the top block. The bottom block is made of two pieces, making the chamber easier to manufacture. The top and bottom blocks and punch are made of stainless steel, while the tested specimen is aluminum AA2024 with chemical composition in weight percentage shown in *Table 7-1*. The specimen material Young’s modulus and Poisson’s ratio are 73.1 GPa and 0.3 respectively. Lubricant was applied to the punch top surface and the side surface to reduce the friction between the punch and specimen and punch and the top block slot.

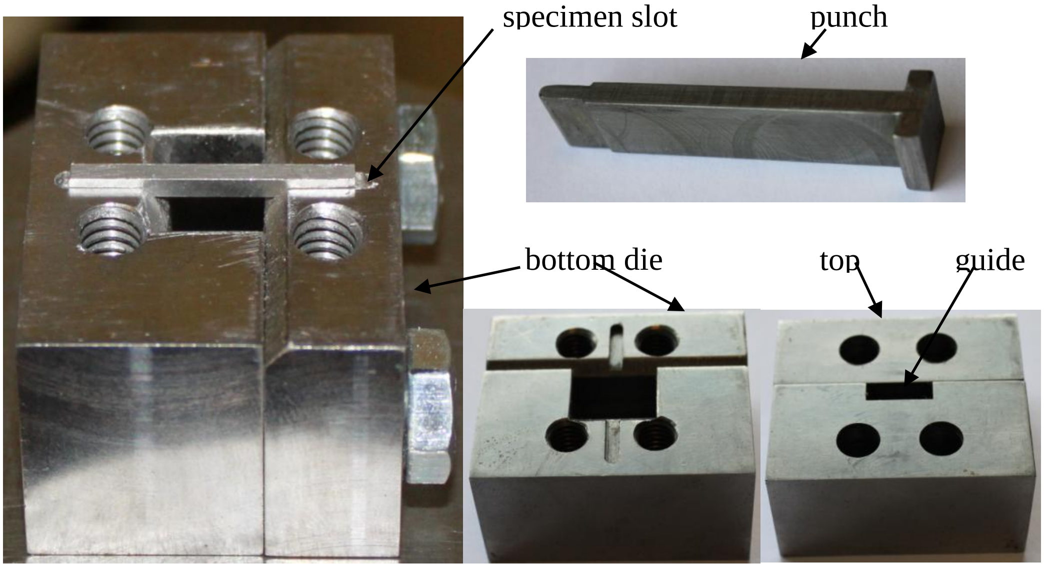

Figure 7-1 small punch beam test tool system

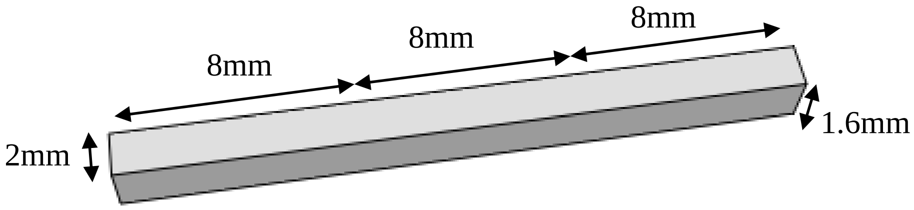

Figure 7-2 Specimen for small punch beam test

Table 7-1 Chemical composition of AA2024 in Wt.%

Componente	Al	Mg	Si	Cr	Mn
Wt. %	90.7-94.7	1.2-1.8	Max 0.5	Max 0.1	0.3-0.9
Componente	Ti	Cu	Zn	Fe	Other
Wt. %	Max 0.15	3.8-4.9	Max 0.25	Max 0.5	Max 0.15

7.1.2 Experiments

The small punch beam testing tool system was fitted to a Denison Mayes material testing machine and the force applied to the punch and the displacement of the machine movement were recorded. The maximum speed of the press head was set to 1 mm per minute; therefore, the strain rate of the specimen is small and dynamic effects are not considered. The test was terminated when the press head displacement reached 0.9 mm and then the press head was released.

The recorded force and displacement were the force applied onto the specimen and displacement of the central point on the beam top surface: friction, punch weight and the elastic deformation of punch are assumed to be negligible. The typical punch force-displacement is shown in Figure 7-3. The specimen initially deformed elastically in region A, followed by elastic and plastic deformation in region B. In region C, when large deformation occurs, damage is accumulated within the specimen and the material shows softening behavior with the total force decreasing. In the final region D, specimen fails as the critical crack length is reached.

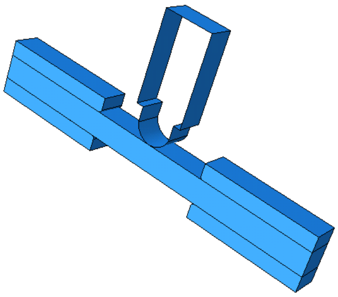

Figure 7-3 FEM Geometrical model

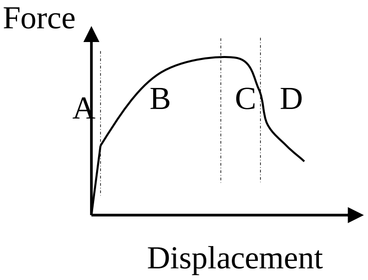

Figure 7-4 Typical the small punch testing force vs. displacement curve

A: elastic region, B: elastic-plastic region, C: damage region, D: failure

7.1.3 FEM modeling

The aim of the investigation is to characterize material plastic properties through the comparison between numerical and experimental results. The FEM model shown in Figure 7-4 consists of a specimen, a top block, a bottom block and a punch. The ABAQUS/implicit finite element code was used for the simulation. The steel punch is treated as a rigid body as it is significantly stiffer than the aluminum test specimen. The top and bottom blocks were modeled as elastic bodies. The length between the two inner surfaces of the bottom block is 8 mm and the width and the height of the beam cross section are 1.6mm and 2 mm respectively. Since lubricant is applied to the punch-specimen interface, the contact between punch head and specimen is considered as frictionless. And the friction coefficient between the dies and specimen are investigated later in section 7.1.5.

As the specimen is aluminum AA2024-T3, an oxide layer was formed on its surface when it was exposed to the atmosphere. As this oxide layer is very thin, its influence on the mechanical properties of specimen was not considered. The multi-linear strain hardening material model shown in Figure 7-5 was used in the ABAQUS numerical simulation, with S1, S2 and S3 representing the initial yield stress, proof stress (at 0.2% plastic strain) and ultimate tensile strength respectively. The material will yield and plastic deformation occurs when von Mises stress reaches the yield surface, which is assumed to be a function of equivalent plastic strain. The von Mises stress σ is represented as

$$\sigma = \sqrt{\frac{1}{2}\left[(\sigma_1-\sigma_2)^2+(\sigma_2-\sigma_3)^2+(\sigma_3-\sigma_1)^2\right]} \qquad 7\text{-}1$$

Whereσ_1, σ_2 and σ_3 are the principle stresses.

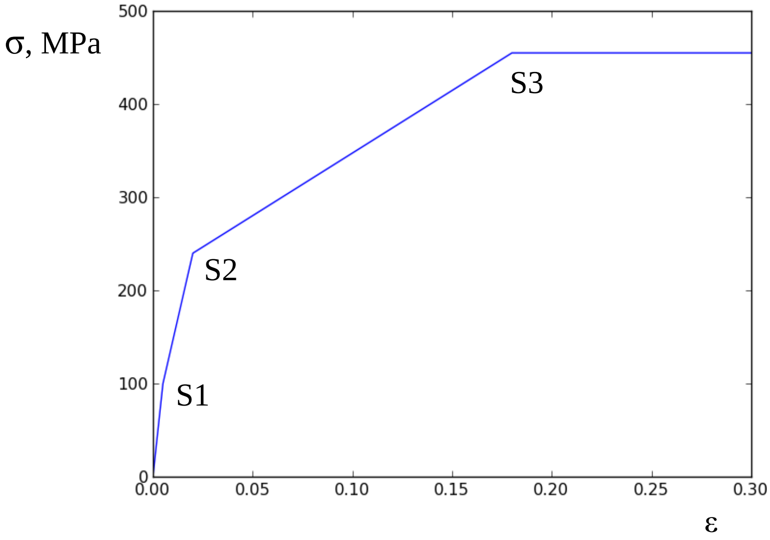

Figure 7-5 Material stress vs. strain relationship

Both top block and bottom blocks were fully constrained. The punch is assumed to be a rigid body and a reference point assigned to it in ABAQUS, such that only this reference point is required to be constrained. The three rotation degrees of freedom and the two translation degrees of freedom within the horizontal plane were set to 0. The load applied to the specimen was replaced by vertical displacement control of the punch. The reaction force from the ABAQUS model corresponding to this constraint corresponds to the force applied to the specimen.

Contact between the punch head and specimen top surface, specimen and top block and specimen and bottom block were considered in the ABAQUS model. The influence of the friction coefficient on the punch force versus the top surface middle point displacement was investigated. As lubricant was applied to punch top, the friction coefficient was assumed to be zero, while the friction coefficient between the top block and specimen, bottom block and specimen were finally set at 0.3. The default penalty formulation in ABAQUS/Standard implicit codes was applied.

The ABAQUS three dimensional brick element C3D20R with reduced integration was used in the analysis. Four discretization cases, as shown in Figure 7-6(a) to (d), were investigated. The mesh used in characterization of material properties by the Genetic Algorithm method was selected by considering the CPU requirements and the accuracy of the analyses, as reported in Section 7.1.2.

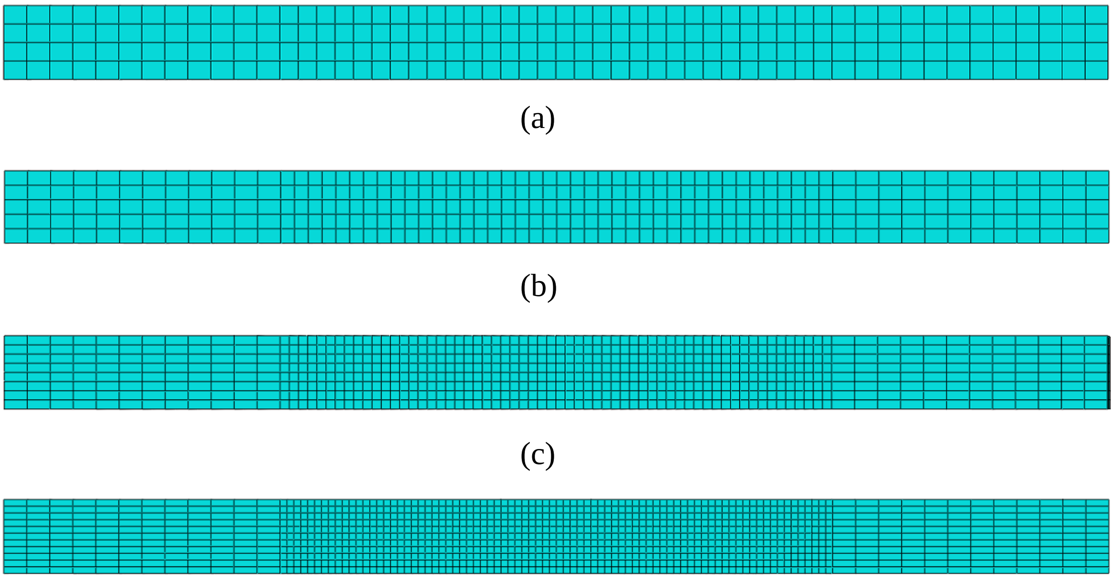

(a)

(b)

(c)

(d)

Figure 7-6 FEM model with different mesh size near the beam centre

(a) 0.4mm, (b) 0.3mm, (c) 0.2mm and (d) 0.15mm

7.1.4 Material properties characterization using genetic algorithm method

The Genetic Algorithm (GA) [7-20] optimization method is based on a simple natural rule: survival of the fittest. The fitter creatures will have more chances to survive and to produce off-spring. The GA method is applied to characterize the material nonlinear plastic parameters. The aim is to use the GA to search for the best values for a set of material parameters by comparing the finite element and experimental results. The total displacement is discretized uniformly into "*n*" segments; therefore, without considering the initial point, there are "*n*" values of displacement u_i (i=*1*,*2*,…,*n*) and their corresponding force values are F_i (i=*1*,*2*,…,*n*). However, as the experimental and FEM results may not fall exactly at the discretized displacement point, a linear interpolation method is used to obtain the corresponding force value. Shown in Figure 7-7, assuming u_i falls within the experimental or FEM consecutive points u_j and u_{j+1}, the force F_i corresponding to u_i can be calculated as

$$F_i = F_j + \frac{u_i - u_j}{u_{j+1} - u_j} * (F_{j+1} - F_j) \quad \text{7-2}$$

A flow chart of a general GA optimization procedure is given in Figure 7-8. Equation 6-3 shows the formulation of the objective function Φ, which is defined as the square root of the average of the summation of the square of the relative difference between the experimental and numerical results. The fitness is chosen as the inverse of the objective function, i.e. $f = \frac{1}{\Phi}$.

$$\Phi = \sqrt{\frac{1}{n}\sum_{i=1}^{n}\left(\frac{F_i^{cal} - F_i^{\exp}}{F_i^{\exp}}\right)^2} \quad \text{7-3}$$

Where $F_i^{\exp}$ and F_i^{cal} are the experimental and FEM punch forces corresponding to the i^th^ displacement u_i. For this case, the linear interpolation method was used.

Smaller values of the objective function correspond to the larger values of the fitness. The general GA procedure consists of initialization, selection, crossover and mutation, with a higher fitness seed having more chance to be selected and one of the fittest off-spring at each generation always being kept. The GA procedure stops when the convergence criterion is satisfied.

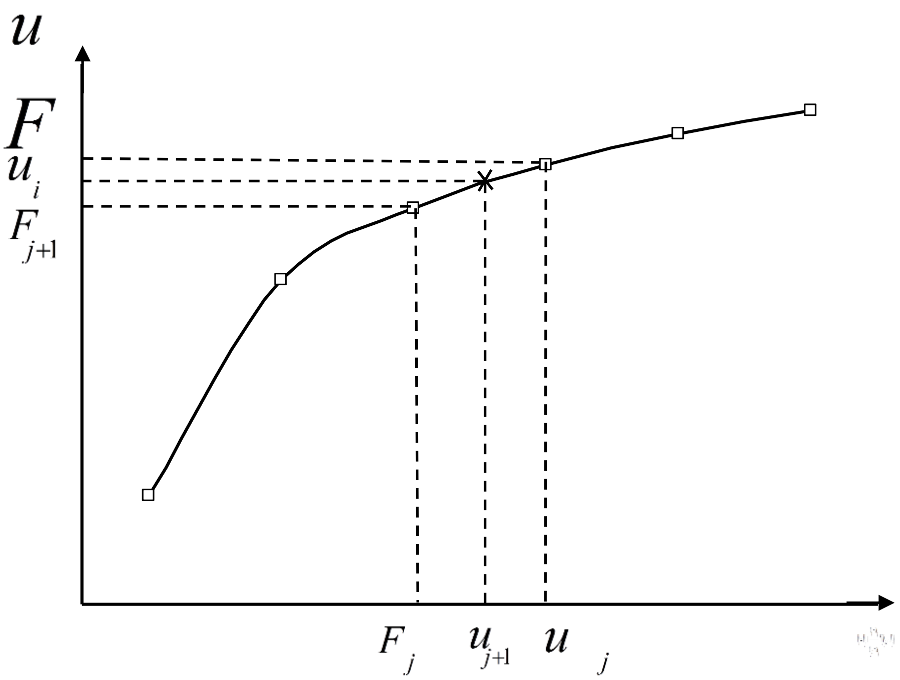

Figure 7-7 Displacements and their corresponding forces

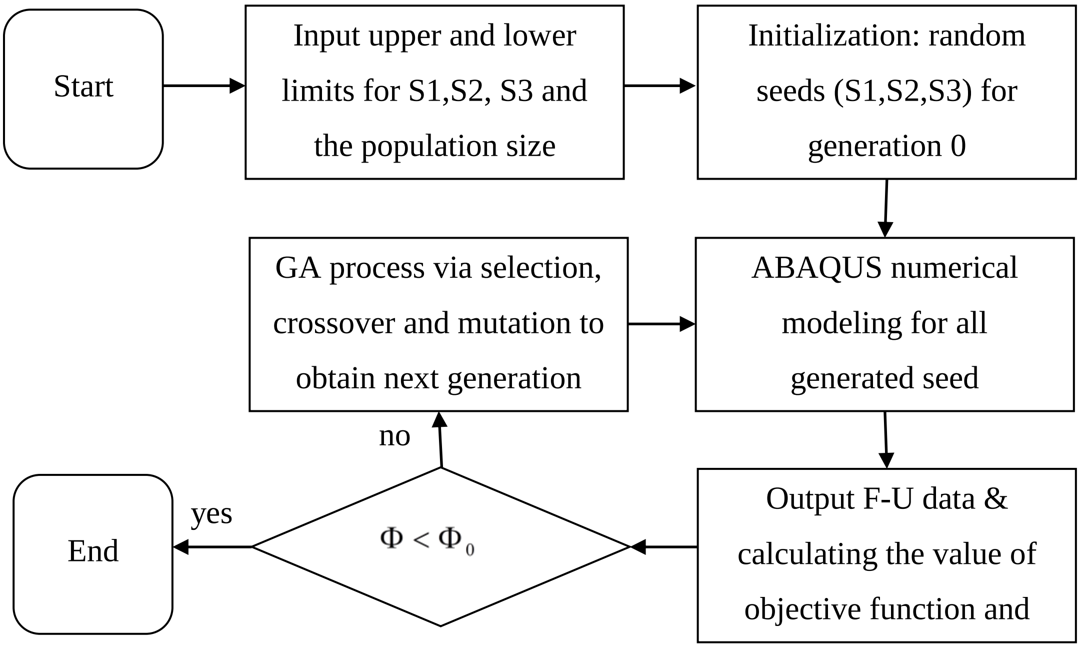

Figure 7-8 Flow chart of the genetic algorithm

One example of selection, cross over and mutation from generation 0 to generation 1 of the GA method, is described as follows. As the material properties to be characterized are S1, S2 and S3, the range of their values are set at start. For initialization, S1, S2 and S3 are randomly assigned an integer from 0 to 255. At the start, chromosomes with the integers from 0 to 255 are represented as 8-digit binary strings. At iteration 0, there are 20 seeds for each set of S1, S2 and S3 and each seed can be linearly mapped to the parameters S1, S2 and S3 used in the FE models, as shown in Figure 7-9. These 20 seeds are ranked according to the objective function value calculated from the corresponding FE analysis: the seed with the smallest objective function ranks first, while the seed with the largest objective function ranks last. The selection operator is to delete the last seed for preparation of the next procedure cross over. The cross over procedure randomly selects a pair of seeds from seed numbers 1 to 18 and exchanges their genes at a random position. This procedure is continued until all seeds from seed number 1 to 18 are selected and crossed-over, giving new seeds numbered from 1 to 18. Finally, three seeds from 0 to 18 are randomly selected and mutated at random positions to obtain S1, S2 and S3 respectively and the newly generated seed is numbered as 19. Totally 20 new seeds for the next iteration are then prepared.

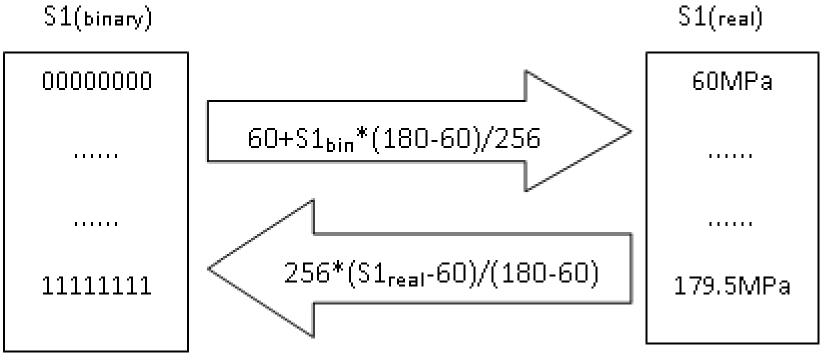

Figure 7-9 Mapping parameters from integers to real values

7.1.5 Results

Two tests were performed and the test results shown in Figure 7-10. Due to the accuracy of the testing machine, the testing results fluctuate. However, from this figure, it can be seen clearly that the test results are quite consistent. In this section, we aim to present a novel design and a GA method to characterize material plastic parameters; therefore, only the specimen 2 results were used for this purpose. To make the comparison easier, the average experimental results were compared with FEM results.

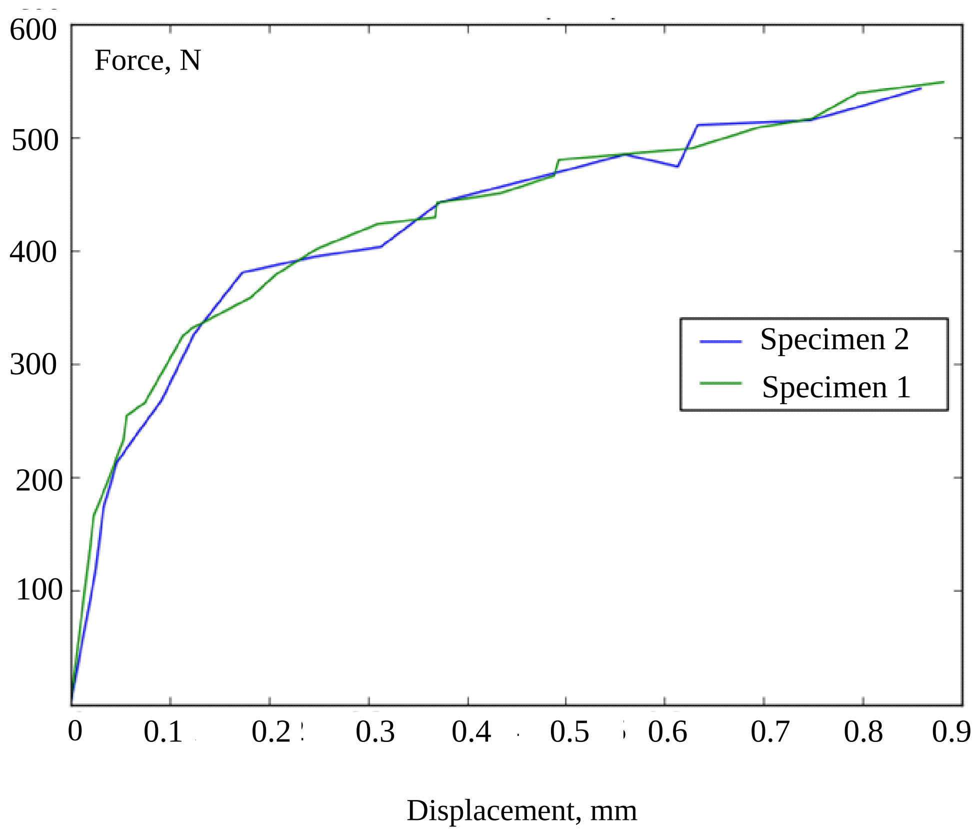

Figure 7-10 The two experiment force vs. displacement results

Figure 7-6(a) to (d) show the meshes with element size of 0.4 mm, 0.3 mm, 0.2 mm and 0.15 mm for the central part of the beam. *Table 7-2* displays the punch force corresponding to punch vertical displacement of 0.9 mm under different element size. The relative difference of the reaction force to the finest mesh is also shown in this Table. From this table, it can be concluded that the model with mesh size of 0.2 mm, Figure 7-6(c) gives a good balance between accuracy and CPU time and the results reported here were based on this mesh.

Table 7-2 Comparison of punch force at different mesh size

Case number	1	2	3	4
Mesh size (mm)	0.4	0.3	0.2	0.15
Load force (N)	455.12	495.428	500.601	500.398
Relative difference (%)	9.05	0.99	-0.04	NA

To investigate the influence of the friction coefficient on the punch force-displacement curve, different friction coefficients between upper die and specimen and lower die and specimen were assigned to the FE model. The simulation results are shown in *Table 7-3*, from which it can be seen that the punch force increases with increasing of friction coefficient. By comparing these results, it is found that the maximum relative difference is less than 4.5%. In this section, friction coefficient of 0.3 is used.

Table 7-3 Influence of friction coefficient on the punch force at displacement of 0.85 mm

Friction coefficient	0.1	0.2	0.3	0.4
Punch force, N	490.9	500.0	508.7	513.9

7.1.5.1 GA method results

Table 7-4 shows the history of evolution of the minimum objective function Φ of generation varying with iteration number. At the beginning of the GA procedure, all seeds are randomly generated and the lowest objective function value is 0.0817. The binary string for the best seed is [01011101], [01000100] and [00000011] and their corresponding S1, S2 and S3 values are 103.6 MPa, 239.8 MPa and 401.4 MPa. From Table 7-4, it can be seen that generally the minimum value of the objective function decreases as the iteration number increases. The value of the minimum objective function will eventually reach a certain value, leading to the convergence of the GA. In this section, after evolution of 20 generations, the minimum Φ reaches 0.0612. The binary strings for this generation are [01011010], [00100010] and [11101010] and their corresponding S1, S2 and S3 values are 102.2 MPa, 219.9 MPa and 509 MPa respectively. The ultimate tensile strength is very close to the 496 MPa report in [7-21].

Table 7-4 Objective function Φ varies with iteration number

Iteration No	0	5	10	15	20
Objective function Φ	0.0817	0.0749	0.0731	0.0686	0.0612

Comparison of the experimental and finite element punch force-displacement curves is shown in Figure 7-11, from which it can be seen that the predicted results are in good agreement the experimental results.

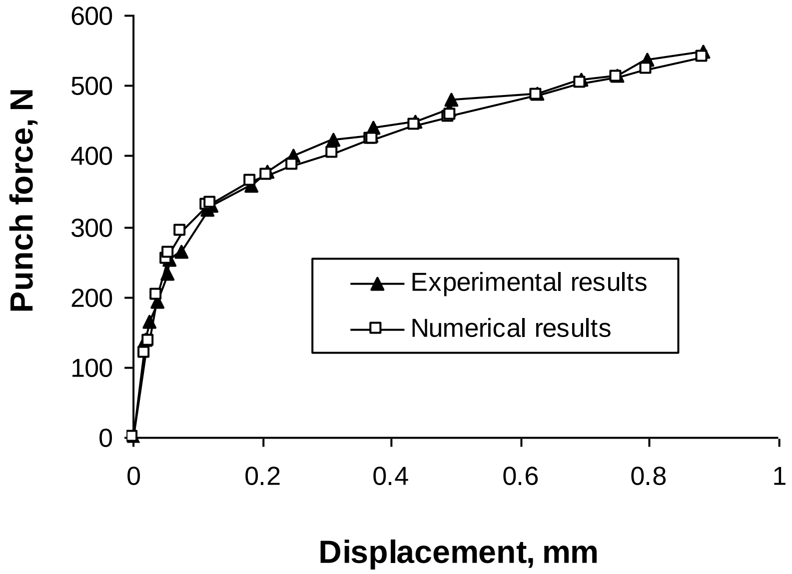

Figure 7-11 Comparison between experiment and FEM numerical force vs. displacement results

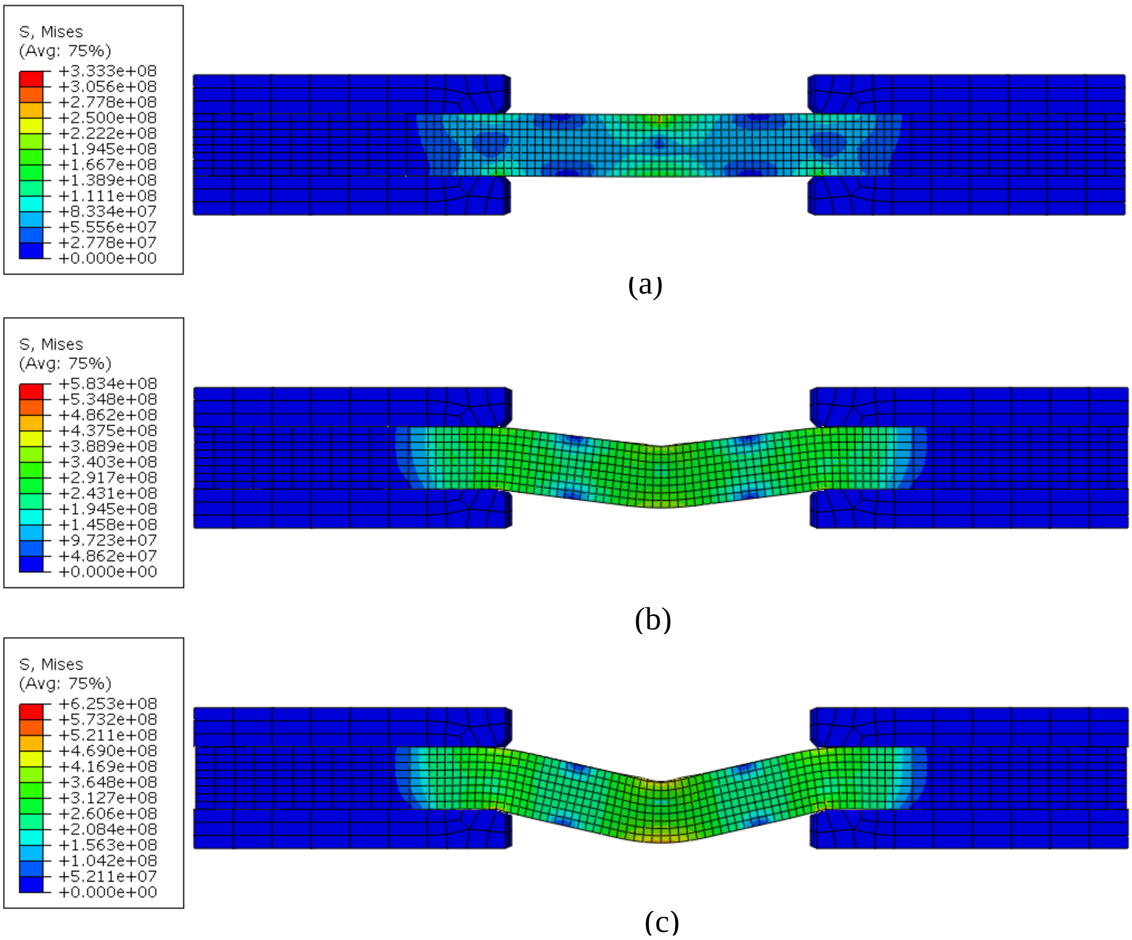

Figure 7-12 Von Mises stress contours of the specimen at different displacements

(a) 0.025 mm displacement, (b) 0.5 mm displacement and (c) 0.89 mm displacement

After obtaining the material plastic parameters, the FEM simulation results produced using the optimal parameters values were re-investigated. Figure 7-12(a) to (c) show the stress contours at the top surface middle point displacement of 0.025 mm, 0.5 mm and 0.89 mm respectively. From Figure 7-12(a), it can be seen that apart from the contact point between punch and specimen, the maximum stress was less than the 0.2% proof stress and the high stresses occurred in elements close to the middle points of the top and bottom surfaces. This shows the beam deformation behavior. By checking the punch force versus specimen top surface middle point displacement, it is found that this stage corresponds to linear elastic deformation in the specimen. With higher punch force applied onto the specimen, the maximum von Mises stress exceeded the yield stress and plastic deformation developed in the specimen. From Figure 7-12(b) and (c), it is clear that the location of high stress in the elements expanded from the middle points of the top and bottom surfaces to the center of the specimen and the areas near the bottom support regions also have high stresses.

7.2 Identifying plastic properties of friction stir welded material by small punch beam test

Artificial neural network algorithms provide an advanced alternative to genetic algorithms for approximating complex functions. Abendroth and Kuna employed a neural network to predict the parameters of a material hardening law and hence define strain-stress curves for steel in [7-27]. The simulated load-displacement curves obtained agreed well with experiment data for the three test specimens investigated. The elastic-plastic properties and failure properties for 10MnMoNi55, 18Ch2MFA and StE-90 using a disk specimen of diameter 8mm and thickness 0.5 mm were investigated in [7-28] and [7-29], with load deformation curves again showing good agreement with experimental results.

In this section, the average plastic properties of a Friction Stir Welded (FSW) material are characterized using a procedure combining small punch beam testing, finite element analysis and a neural network algorithm. The base test-piece is a FSW sheet of 2024-T3 Aluminum alloy: length 500 mm, width 60 mm and thickness approx. 1.6 mm. The FSW parameters used were: rotational speed 800 rpm and welding speed 100 mm/min. Diameter of the welding tool's shoulder is 8 mm. No post welding heat treatment was applied.

7.2.1 Methodology

The proposed procedure for material plastic property characterization shown in Figure 7-13 consists of consecutive and parallel actions of sampling, modeling, testing, building a neural network and finally property characterization.

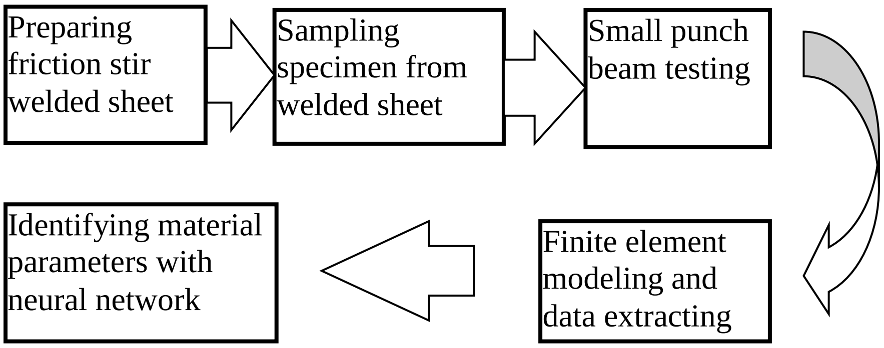

Figure 7-13 Procedure of identification

7.2.1.1 Experimental Arrangement

The base AA2024-T3 material comprises of three layers, as illustrated in Figure 7-14. The two external layers are pure aluminum material and the internal layer is aluminum alloy. The thickness of the external layers is around 50 μm.

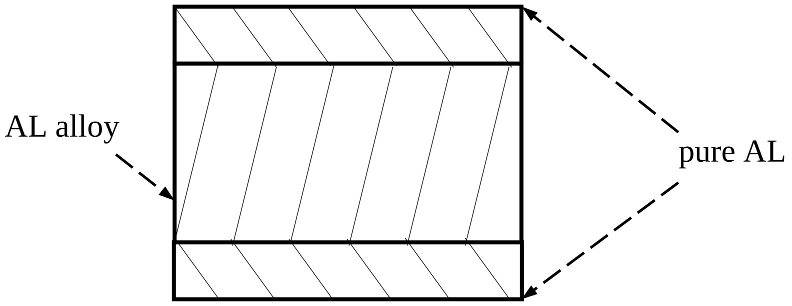

Figure 7-14 Three layer structure of AA2024-T3 cross section

Small rectangular beam test specimens were cut from the FSW sheet using a disc cutting machine. The nominal length and width of the cut samples were 25 mm and 1.95 mm respectively. Two specimens identified as B1 and B2 in Figure 7-15 were prepared. During cutting, the work-piece was water cooled and the cutting speed was limited to 1 mm per minute to avoid distortion and residual stress from the cutting procedure.

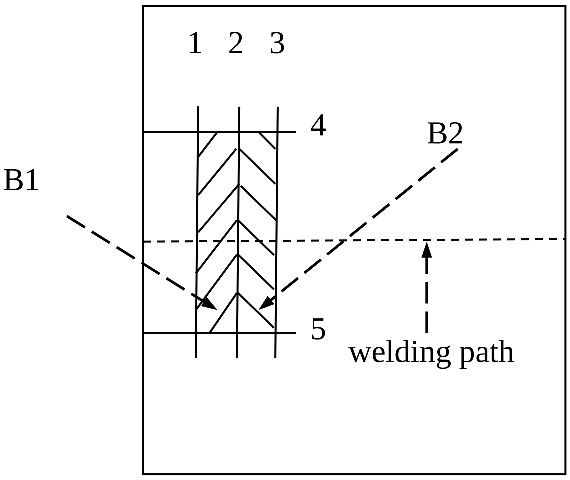

Figure 7-15 Specimen cutting procedure

1, 2, 3, 4 and 5 denote the cutting sequence

One of the specimens cut from the welded plate is shown in Figure 7-16: the central part is welded material and the outer parts are base material.

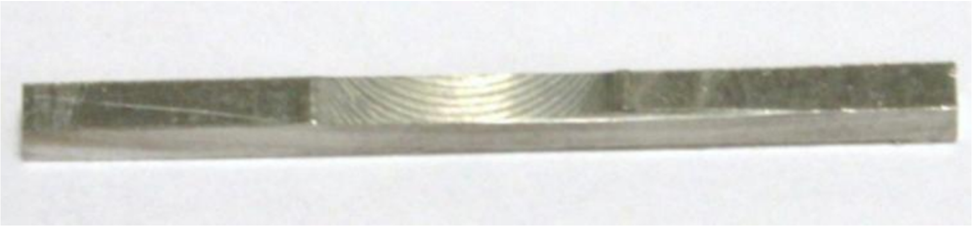

Figure 7-16 Small beam test specimen cut from FSW plate

The material thickness near welding path varies due to the mechanical action of the welding tool. The specimen top and bottom surfaces were grinded at a low speed for duration of 30 seconds under 100 N load to produce a uniform specimen thickness, removing the external layers. The specimens were protected by silicon oil after grinding to avoid oxidation. The width and height of the specimens were then measured in three different positions. The measured dimensions and their averaged values for the two samples are shown in Table 7-5.

Table 7-5 Dimensions of samples B1 and B2

Sample	Length/mm	Width /mm				Height /mm			
		W1	W2	W3	average	H1	H2	H3	average
B1	24.93	1.85	1.89	1.90	1.88	1.33	1.33	1.27	1.31
B2	24.93	1.89	1.91	1.93	1.91	1.29	1.27	1.16	1.24

The small punch beam test system consists of a Tinius Olsen H25KS load frame with 0.1N force resolution and 0.001 mm displacement resolution and a small punch beam test tool, as illustrated in Figure 7-17. The tool includes a top die, a bottom and a punch (tool design details are given in [7-26]).

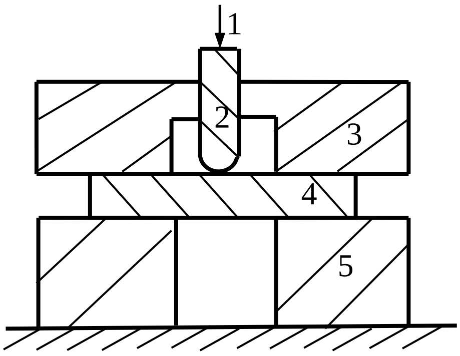

Figure 7-17 Small punch beam test system

1- Force from press machine 2- punch 3- top die 4- specimen 5- bottom die

The punch force and punch head displacement are recorded automatically by the machine. Assuming the test frame is rigid, the displacement of the punch corresponds to the central point displacement of the specimen.

The specimen material within 6 mm of the welding path consists of the weld nugget zone, thermal mechanical affected zone and heat affect zone. In the material characterization considered here, these individual zones are represented by a single homogenous material with average elastic-plastic properties. The specimen material is therefore considered to consist of two regions: welded material and base material.

Figure 7-18 illustrates the location of the test specimen in the small punch beam test tool. The base material is located beyond the supporting points and fixed by top and bottom dies. It is therefore assumed that deformation will be largely restricted to the central welded material and the deformation of base material is negligible. The specimen deformation and associated punch force will therefore be determined by material properties of the welded material. Based on this assumption, the material model for the whole specimen is considered to be homogenous and isotropic.

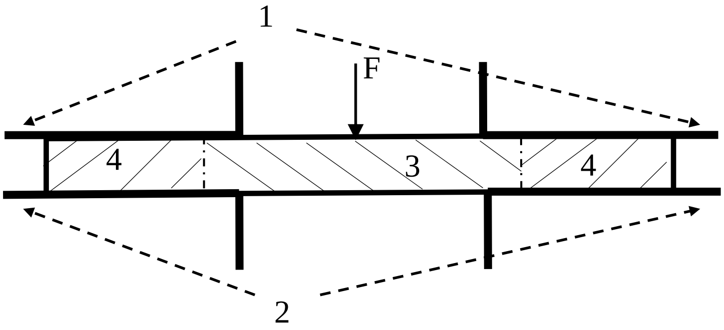

Figure 7-18 SPBT FEA model schematic

1- top die, 2- bottom die, 3- welded material of specimen,

4- base material of specimen, F- load

7.2.1.2 Numerical simulation

The deformation of the clamped small beam specimen subject to the central punch force is simulated by a multi-linear hardening Finite Element Analysis. The strain hardening material model is defined by three parameters: yield stress S1, proof stress S2 and tensile strength S3, as defined in Table 7-6. The commercial finite element program ABAQUS was used. The aluminum alloy beam specimen was meshed using 20-node brick elements and the steel punch modeled as a rigid body. Mesh convergence tests were performed to establish appropriate mesh density: the simulation results reported here were obtained using the converged finite element mesh.

Table 7-6 Multi-linear material model defined by S1, S2 and S3

True stress	Plastic strain	Total strain
S1	0.0%	S1/E
S2	0.2%	S2/E+0.002
S3	18.0%	S3/E+0.180

7.2.1.3 Neural network

Neural networks are adaptive systems demonstrating a self-learning capability that can be used to model complex relationships that can’t be expressed explicitly [7-30]-[7-38]. Here the FEA material model parameters S1, S2 and S3 are identified using a neural network following the procedure outlined in the flow chart of Figure 7-19. The first step is to define the range for each parameter. Definition ranges should cover all possible values of the parameters and can usually be obtained from references or empirical data. The definition range used for S1 was from 40 to100 MPa, for S2 from 150 to 300 MPa and for S3 from 400 to 500 MPa.

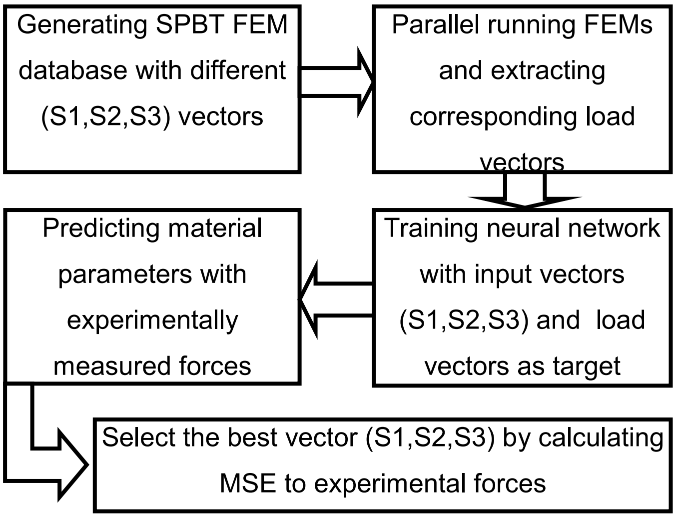

Figure 7-19 Flow chart of parameter identification

Each definition range is divided evenly by 5 section points, such that a full array contains 5*5*5=125 material vectors **S**. The vectors are then applied to the parametric finite element model to calculate reaction forces **F**, such that a training database with 125 **S** vectors and corresponding reaction **F** vectors is established. Finally a back propagation neural network is trained by the database and the trained neural network used to predict values of material vector $\mathbf{S_0}$ corresponding to the experimentally measured punch force vector $\mathbf{F_0}$.

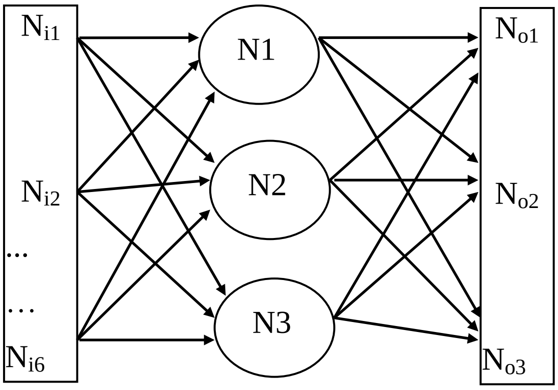

Figure 7-20 Neural network schematic diagram

A schematic diagram for a typical three layer BP neural network is shown in Figure 7-20. The first layer is the input layer. The input vector of this layer is the normalized force vector $\mathbf{F_{nor}}$ (F1, F2,,, F6). The second layer is a hidden layer and the input data of this layer is the output of the input layer. The last layer is the output layer and the input data of this layer is the output of the hidden layer. The output data of the output layer is the normalized material vector $\mathbf{S_{nor}}$, (S1, S2,,, S6). $\mathbf{F_{nor}}$ and $\mathbf{S_{nor}}$ are determined by equation 7-4:

$$\mathbf{S_{nor}} = \frac{\mathbf{S}}{max(\mathbf{S})}, \mathbf{F_{nor}} = \frac{\mathbf{F}}{max(\mathbf{F})} \quad 7\text{-}4$$

Where **S** and **F** are material vectors and corresponding force vectors in the training database and max(**S**) and max(**F**) represent the maximum value of elements in **S** and **F** separately.

The numbers of neurons of the input layer and output layer is determined by the dimensions of $\mathbf{F_{nor}}$ and $\mathbf{S_{nor}}$ individually, here 6 and 3 respectively. The function of each neuron can be described as a linear operator followed by a non-linear operator. The linear operator [7-30] is:

$$u_k = \sum_{i=1}^{n}(w_{ki}I_i + b_{ki}) \quad 7\text{-}5$$

Where u_k is the linear operator output of neuron *k*, *n* is the dimension of input vector and w_{ki} and b_{ki} are the weight and bias for each input I_i of neuron k.

The nonlinear operator [7-30] is:

$$\varphi_k = \frac{exp(u_k)-exp(-u_k)}{exp(uk)+exp(-u_k)} \quad 7\text{-}6$$

Where φ_k is the output of neuron *k* and u_k is the output of the linear operator.

Initially all weight and bias values are randomly assigned. After it is trained using a database containing normalized input vector $\mathbf{F_{nor}}$ (6D load forces) and normalized output vector $\mathbf{S_{nor}}$ the BP neural network adjust the weight and bias values based on the mean square error (MSE) of the calculated output vectors and training output vectors from the database. The value adjustment continues until the MSE reaches a designated goal. The training algorithm used is the default MATLAB 'trainlm' function, which updates weight and bias values according to the Levenberg-Marquardt algorithm.

When MSE reaches the set goal, the neural network is an approximate function of $\mathbf{S_{nor}} = f(\mathbf{F_{nor}})$ and can therefore be used to predict approximate values of S1, S2 and S3 for AA2024-T3 weld material.

Due to the complexity of the relationship between force vectors **F** and corresponding material vectors **S**, the difference between FE models and the physical experiment and the error between the simplified elastic-plastic material model and the complicated physical material behavior, the trained neural network suffers noise and the prediction of material parameters contains random errors. To optimize the results, the predicted material vectors **S** of the neural network for multiple runs are recorded and applied to the FEM to calculate corresponding force vectors **F.** Each vector **F** is compared to the experimental force vector $\mathbf{F_0}$ and the best fit is determined by equation 7-7:

$$\Phi = \sqrt{\frac{1}{n}\sum_{i=1}^{n}\left(\frac{F_i^{cal} - F_i^{\exp}}{F_i^{\exp}}\right)^2} \tag{7-7}$$

Where F_i^{cal} presents the i^th^ element of calculated vector **F** and $F_i^{\exp}$ is the i^th^ element of experimental vector $\mathbf{F_0}$. The lower the Φ value, the better the predicted $\mathbf{S_0}$.

7.2.1.4 Results and Discussion

The experimental displacement of the specimen center under varying load is shown in Figure 7-21. It is observed that the specimen B1 load is higher than the specimen B2 load for the same displacement. This difference is in good agreement with the slight difference in dimensions between the two specimens, as shown in *Table 7-5*, (the average height of B1 and B2 are 1.31 mm and 1.24 mm respectively). The difference in the two curves is largest when the displacement is small, as the effect of the elastic stiffness of the beams reduces with increasing plastic deformation.

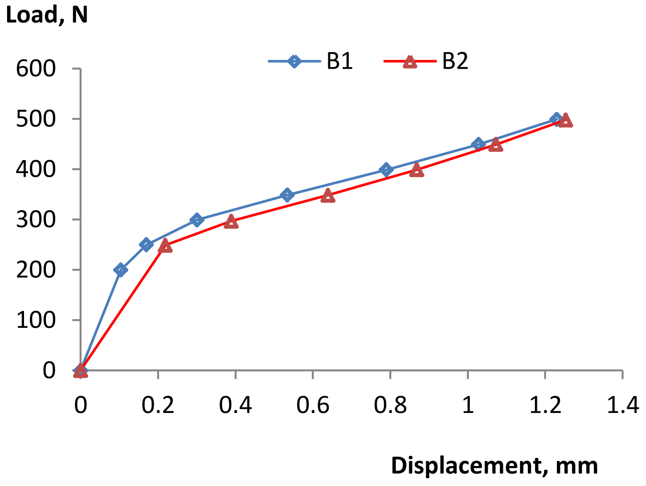

Figure 7-21 Load-displacement curve for specimen

The neural network was implemented using the MATLAB neural network toolbox. The MSE goal was set to 1.1E-3. The experimental force vector $\mathbf{F_0}$ from specimen B1 is selected to predict material vector $\mathbf{S_0}$. The predicted results for S1, S2 and S3 are 94.98 MPa, 251.67 MPa and 636.56 MPa respectively. For S2, minimum tensile yield strength for 2024-T3 (base material) is reported to be in the range between 207 MPa and 338 MPa [7-39], [7-40], indicating the predicted S2 value 251.67 MPa is reasonable. In addition, compared to the base material properties predicted using a genetic algorithm [7-26], both yield strength S2 and ultimate strength S3 of the welded material are higher than that of the base material, 219.9 MPa and 509.0 MPa respectively, which indicates the effect of grain size refinement during FSW.

The force vector **F** calculated from the predicted material parameters 94.98 MPa, 251.67 MPa and 636.56 MPa is compared with experiment force $\mathbf{F_0}$ in Figure 7-22. It is observed that the predicted forces and experimental forces agree well except for some slight difference at the initial deformation stage. The relative error calculated by equation 6-7 is 5.4%.

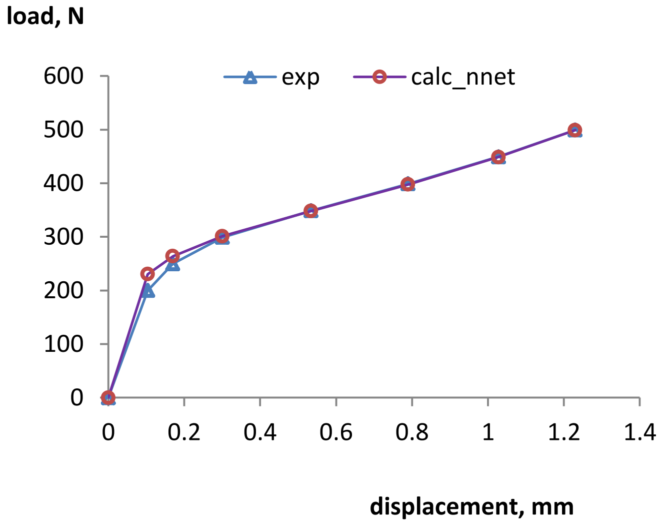

Figure 7-22 Comparison of experiment and predicted load-displacement data

The procedure proposed here assumes that the difference in material properties between welded material and base material will have a negligible effect on the calculated load-displacement curve. The validity of this assumption can be investigated by comparing the experimental and numerical results. Figure 7-23 shows the deformed specimen shape obtained experimentally and by FEA. It is seen that the material clamped by the dies does not exhibit significant deformation, whilst large deformation is observed in the central section.

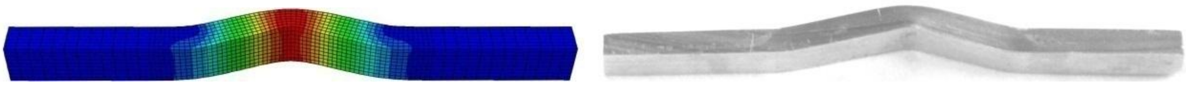

Figure 7-23 Specimen deformation of FEM and experiment

A quantitative comparison of the effect of parent material properties was obtained by performing FEA of similar models with and without different base material properties. The base material properties [7-26] and welded material properties obtained in the present investigation are given in *Table 7-7*.

Table 7-7 Base material properties [7-26] and welds properties

	S1/MPa	S2/MPa	S3/MPa
Base material	102.2	219.9	509.0
Welded material	94.98	251.67	636.56

Table 7-8 shows a comparison of load-deformation results from the two analyses, where *d* is the specimen top center displacement, *f1* is the corresponding force assuming the uniform material properties and *f2* is the corresponding force assuming

different properties for the welded and base materials. The maximum different in force between the two models is less than 0.1%, indicating the validity of the homogeneous material model used.

Table 7-8 Load-displacement data comparison

d/mm	0.534	1.028	1.230	1.484
f1/N	347.7	448.3	498.5	578.2
f2/N	347.8	448.5	498.8	577.6

7.3 Identifying property distribution: SPBT for welded material

Large structures or devices, such as power plants, usually should be regularly maintained to ensure their safety, or evaluated to estimate their residual life after designed life circle or severe geological disasters. This kind of evaluation involves material property characterization for critical components and requires non-destructive techniques to avoid interruption of service.

In maintenance of nuclear power plants, reactors as critical components are one of the main research fields. Nuclear reactors are large pressure vessels and commonly manufactured by welding several parts together, thus performance evaluation of welds is significant. C. Rodriguez *et al* [7-1] applied the small punch test to characterized mechanical properties of heat affected zone for steels; yield strength, ultimate tensile strength and elongation are predicted for welded 30CrMo5-2 steel. The 4.5mm HAZ zone are even divided into 3 smaller subzones and the difference between these HAZ subzones is successfully identified. Jerome Lsselin et al. [7-42] tested crack initiation resistance for 316L stainless steel subject to constant temperature 288 and pressure 9 MPa to simulate boiling water reactor environment with the small punch test facility. Base material, heat affect zone and weld zone were examined separately and the results indicated that the HAZ was more likely to be the crack initiation position. D. Blagoeva [7-43] presented small punch creep test to characterize properties for base material, service exposed material, weld material and HAZs with coarse and fine grains separately. The sampling plan to cut thin disc specimen is detailed introduced and the material was sampled at thickness direction to get different specimen at different small zones as Figure 7-24a shows. HAZ material is identified as one of the weakest zones under 600 ^{0}C temperature.

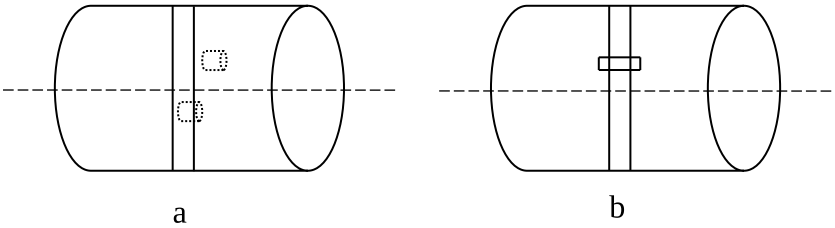

Figure 7-24 Sampling patterns for SPT and SPBT

Aforementioned references commonly indicated that HAZ is a critical zone for welds and the presented sampling pattern requires 6-10 mm material in wall thickness direction of components, which weakens structures' strength and may influence their safety.

In this section, the novel small punch beam test is applied to characterize weld properties in different zones and the sampling plan is shown in Figure 7-24b. The largest dimension of specimens is aligned with reactors' height instead of thickness direction and the thickness of specimens is only 2 mm, so the material removed from components in wall thickness direction is much smaller compared to Figure 7-24a. Apparently, the sizes of removed rectangular specimen are relatively ignorable in all three directions compared to corresponding dimensions of the reactors. In addition, applicability of the novel small punch beam test to distinguish the material property difference in HAZ and weld nugget zone in a single test is investigated.

Methodology for identifying plastic properties of HAZ and weld nugget zone with small punch beam test is introduced first, including finite element modeling, sensitivity analysis and material property distribution characterization procedure in virtual experiment with aiding of neural network algorithm and extended Latin Hypercube Sampling (LHS) algorithm. Then results are presented and discussed including geometric material distribution determination method and evaluation of possible experiment error factors.

7.3.1 Methodology

Figure 7-25 shows the flow of characterizing material properties of HAZ and NZ by neural network and virtual experiment. Firstly a parametric numerical model for small punch beam test is built, which is implemented by ABAQUS and represented by a text file physically. Other FEMs in next steps are built based on the parametric model by assigning values to the parameters embedded in the text file. The parametric model helps to reduce the time cost of building different the small punch test models for different materials and make it possible to produce a procedure to automatically fulfill the characterization progress. Secondly sensitivity of load displacement curves to material parameters is analyzed. The sensitivity analysis investigates the feasibility for small punch beam test to identify transverse distribution of material properties and determines the proper range of load displacement for characterization. Next neural network algorithm is employed to approximate the relationship between load displacement curves and the corresponding material properties and predict plastic properties for a virtual experiment. Since the total number parameters and fragments of each parameter in this section are relatively big and it would take considerable time to prepare the database for training neural network, Latin Hypercube Sampling (LHS) is employed to reduce size of and time cost for preparing the database. The procedure of neural network algorithm and LHS are presented in detail in section 7.3.1.4. Finally the neural network is trained and the values of material property parameters are predicted using load displacement curve from virtual the small punch testing.

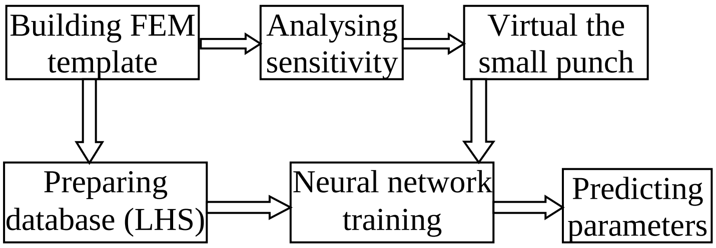

Figure 7-25 Flow chart of characterization for small punch beam test

7.3.1.1 FEM

The FEM is a simplified model of a small punch beam test system, which consists of a top die, a bottom die and a punch [7-56]. Specimen is a rectangular beam with dimensions 24 mm*1.9 mm*1.33 mm. Deflection of specimen tool center point is recorded as displacement to present the deformation of the specimen and the reaction force of the tool is recorded as load force.

The material model for the specimen in the FEM template is complicated. Generally the specimen can be divided into three zones, namely the base material zone and the weld nugget zone. As reported in [7-57], the base material property has little influence to load displacement relationship, thus it is described as simplified multi-linear strain stress curve [7-56]. The material in welded zone is partitioned symmetrically into three zones as shown in Figure 7-26, since it is well known that the weld contains weld nugget zone near the welding path and heat affected zone located between the weld nugget zone and base material. The sizes of weld nugget zone and heat affected zone are 6 mm and 3 mm separately. Locations of weld nugget zone and HAZ zone are symmetric to the welding line. Details of determining sizes and location of these zones are discussed in section 3.1. Material law is Ramberg-Osgood model which is expressed as

$$\varepsilon = \frac{\sigma}{E} + \varepsilon_y \left(\frac{\sigma}{\sigma_0}\right)^n \quad 7\text{-}8$$

Where ε is the true strain, σ is the true stress, E is Young's modulus, σ_0 is yield strength and ε_y is yield offset.

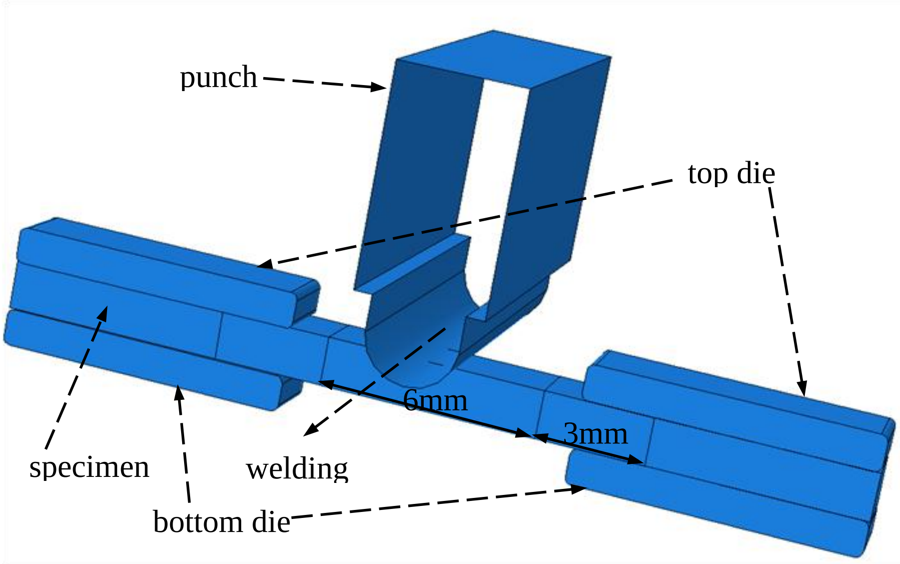

Figure 7-26 Schematic of small punch beam test model

7.3.1.2 Sensitivity analysis

It is necessary to investigate the sensitivity of load displacement to material properties. The feasibility of identify two different material in one specimen in single test should be discussed and also the proper range of load displacement curves to be utilized to character the specimen should be determined. The sensitivity of parameters s and n and location sensitivity are investigated separately.

7.3.1.2.1 Yield stress sensitivity of NZ and HAZ material

Yield strength of NZ material is varying from 210 MPa, 200 MPa to 180 MPa and the corresponding load displacement curves are shown in Figure 7-27 (m1 indicates the NZ material). As expected, load forces for material models with lower yield strength are generally lower when the displacements are the same. Also, it is observed that the curve with displacement from 0 to 0.05 mm is not sensitive to plastic property changes. This phenomenon is mainly due to the fact that the initial deformation is dominated by elastic properties. Relatively, load forces are more sensitive to changes of plastic properties when displacements are increasing. After transiting from elastic-plastic stage, most welded material of specimen is plasticized and the force differences between different material models are getting stable.

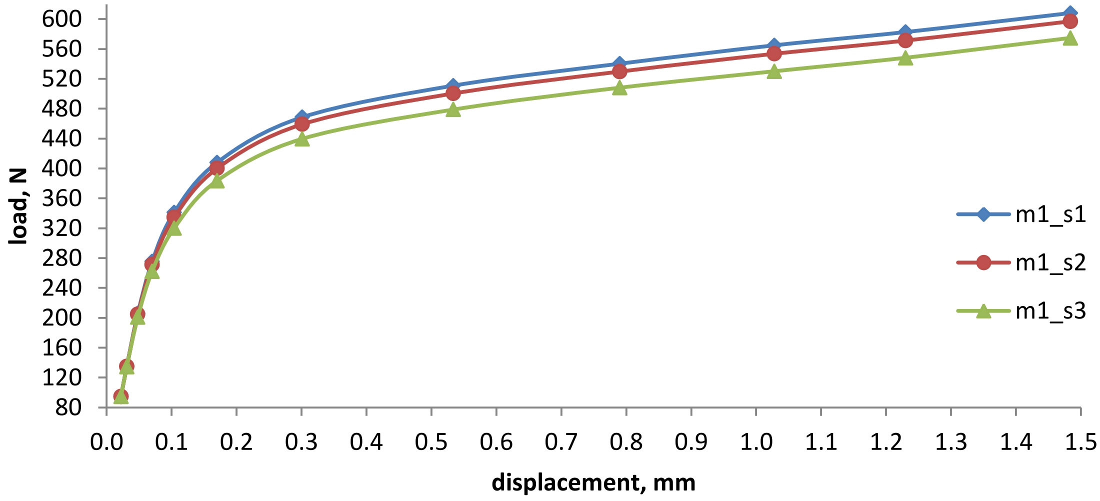

Figure 7-27 Sensitivity of yield strength for welded material

m1_s1: 210 MPa, m1_s2: 200 MPa, m1_s3: 180 MPa

The findings for altering yield strength for HAZ are similar as shown in Figure 7-28 (m2 indicates HAZ material), though the specific values are different. It is noticed that in elastic deformation zone, effect of decrease of yield strength to load forces is less than 1 N. In elastic-plastic deformation regime, the influence of yield strength begins to get larger. When most material of specimen is plasticized, the force difference between the curves is almost constant.

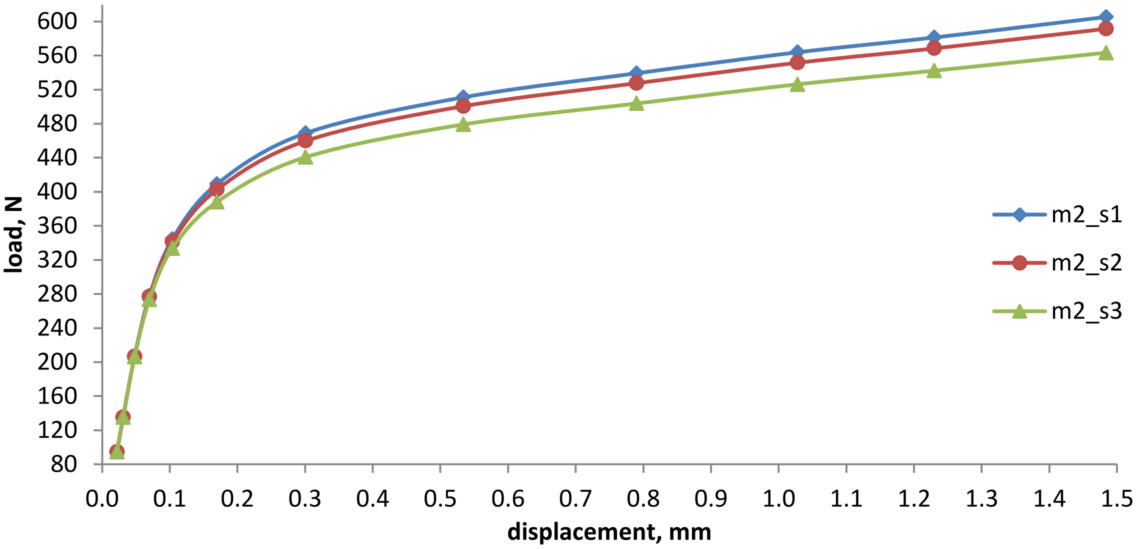

Figure 7-28 Sensitivity of yield strength for HAZ material

m2_s1: 210 MPa, m2_s2: 200 MPa, m2_s3: 180 MPa

Through comparison of load displacement curves with different yield strength, it is found that the load forces are sensitive to elastic-plastic deformation zone and plastic deformation zone.

7.3.1.2.2 Power index n sensitivity of NZ and HAZ material

Power index n for Ramberg-Osgood model is varying from 11, 10 to 9 for NZ and HAZ materials and yield strength is kept the same. As shown in Figure 7-29, NZ materials with lower n are actually harder and it is reflected by the increased forces. Distinguished from sensitivity analysis of yield strength, load forces are not sensitive to altering of power index n in both elastic deformation stage and early elastic-plastic deformation stage. This is due to the fact that the true strain stress curve before yield strength has little relevance to power index n; instead, it is highly related to yield strength. It is also noticed that sensitivity, measured by force per percentage of variables, is bigger for power index n than that for yield strength in plastic deformation stage.

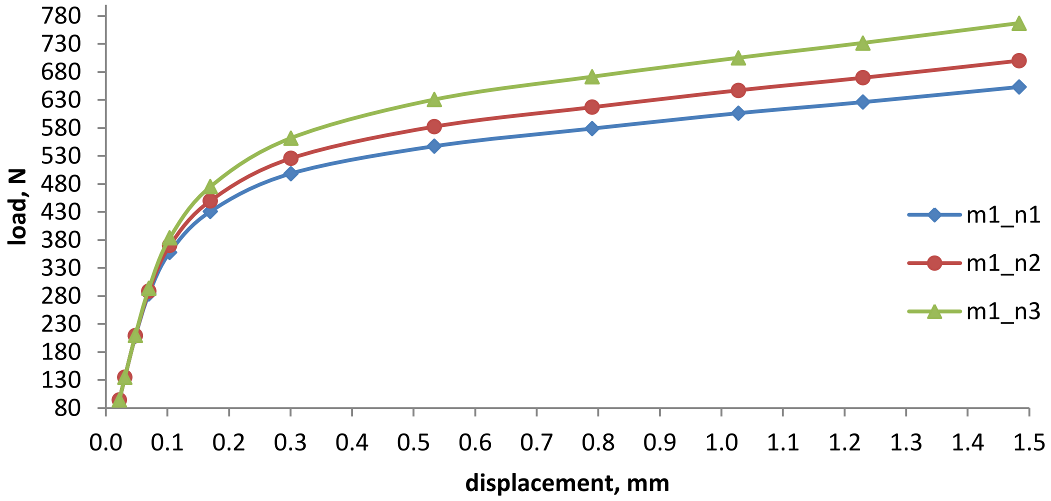

Figure 7-29 Sensitivity of power index n for weld material

m1_n1: 11, m1_n2:10, m1_n3:9

The sensitivity of power index for HAZ is similar to that for weld material as shown in Figure 7-30. Load forces are not sensitive when displacement is less 0.1 mm, but the difference between curves with different material models goes quickly as displacement is increasing.

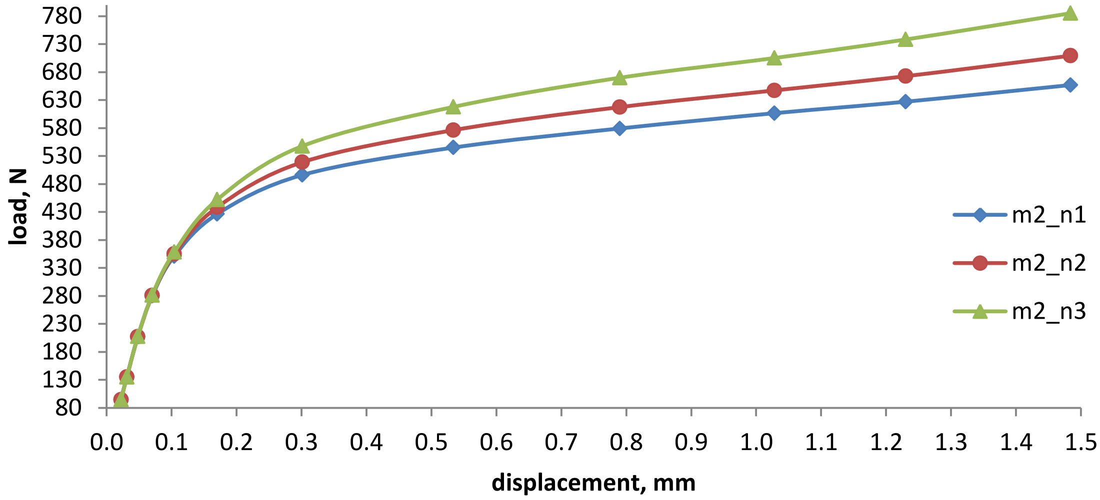

Figure 7-30 Sensitivity of power index n for HAZ material

m1_n1: 11, m1_n2:10, m1_n3:9

7.3.1.2.3 Location sensitivity

Though sensitivity analysis in section 7.3.1.2.1 and 7.3.1.2.2 shows that the load displacement curves are sensitive to all four material parameters in elastic-plastic deformation zone and plastic deformation zone, it doesn't necessarily mean that the two different materials can be precisely characterized. In addition to aforementioned sensitivity analysis, the location sensitivity should be investigated.

From Figure 7-31 it is observed that the two materials located in the two zones have different contribution to load displacement curves. In elastic-plastic deformation zone and early plastic deformation zone, the contribution of weld material is relatively larger. When displacement continues to increase, the load force is more sensitive to HAZ material. This phenomena is in good agreement with observation that displace of central material of specimen is relative larger at early stage and then as displacement increasing, deformation of HAZ material is getting larger. Thus it can be speculated that it is hardly to find alternative materials to generate the same load displacement curve from the early elastic-plastic deformation zone to plastic deformation zone.

The differences of curves are shown in Figure 7-31 and the amplitude is observed in range 0.1 N, which can be easily measured by modern test machines, for instance, Tinius Olsen H25KS model.

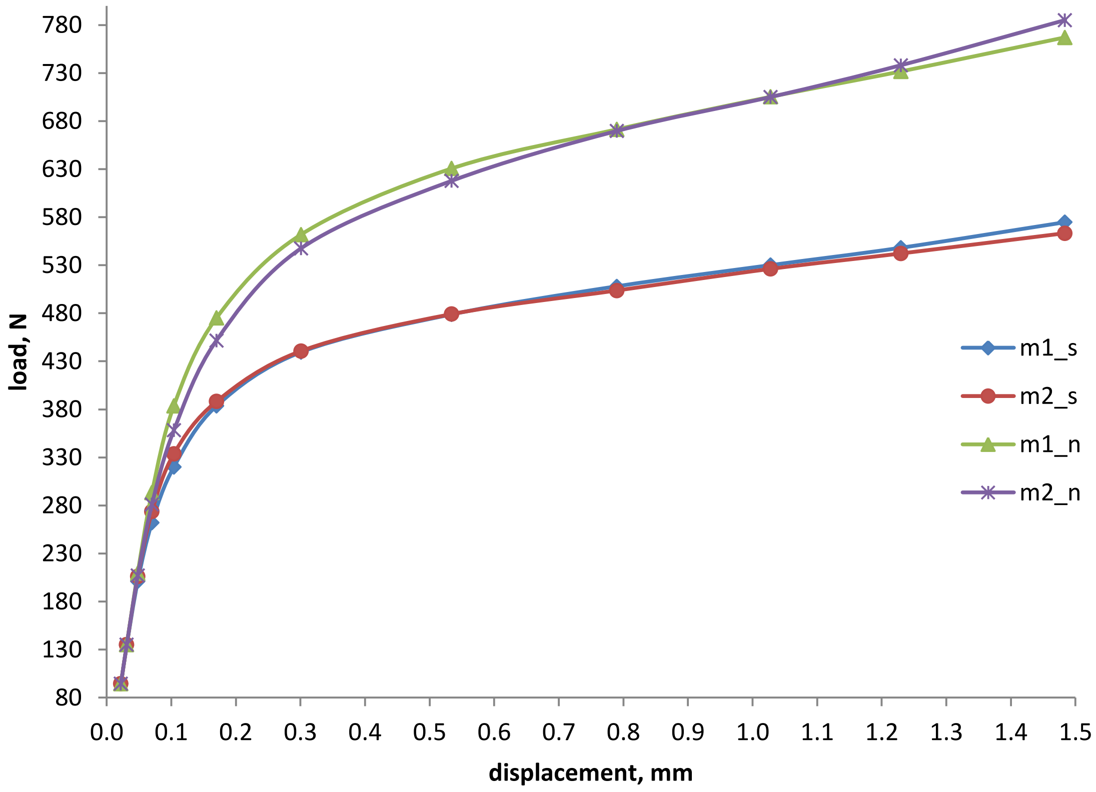

Figure 7-31 Comparison of sensitivity of HAZ and NZ materials

m1_s: s=180, m2_s: s=180, m1_n: n=9, m2_n: n=9

Based on sensitivity analysis of m1_s, m1_n, m2_s, m2_n and sensitivity comparison of the two materials, the load displacement curve from displacement 0.07 to 1.484 are selected as object to identify material properties.

7.3.1.3 LHS and Neural Network Procedure

Though neural network is proven to be capable to approximate complex relationship between material parameters and the punch forces in small punch beam test [7-57], when the quantity of material parameter n or the fragment m of each factor is increased to take more factors into consideration and establish a more accurate neural network, size of training database increases rapidly since the size could be expressed by m^n. It requires much more time to prepare for a larger database, which might even make it impractical to prepare the database and prevent researchers from taking advantage of neural network algorithm. Introduction of Latin hypercube Sampling

(LHS) method [7-45] relieved this problem (a detailed introduction of LHS) and the size of LHS database is linear to dimension and fragment of material parameters.

The procedure of the LHS algorithm is shown in Figure 7-32. The first step is to normalize the parameters according to their definition range and make the normalized values are in range of 0 to 1. The normalization can be expressed as:

$$P_i^{nor} = \frac{P_i - P_{min}}{P_{max} - P_{min}} \quad 7\text{-}9$$

In the second step, the definition range of each parameter is divided equally by 100 fragment points. In the following steps, the fragment points are randomly selected sequentially. In this section, there are four parameters in total, thus when n equals 4, the first sample is obtained and then it is denormolized. Then the sample counter is increased by 1 and the randomly selected values are excluded from sampling in next cycle. The sampling progress stops when the sample counter equals 100, which means totally 100 samples are obtained.

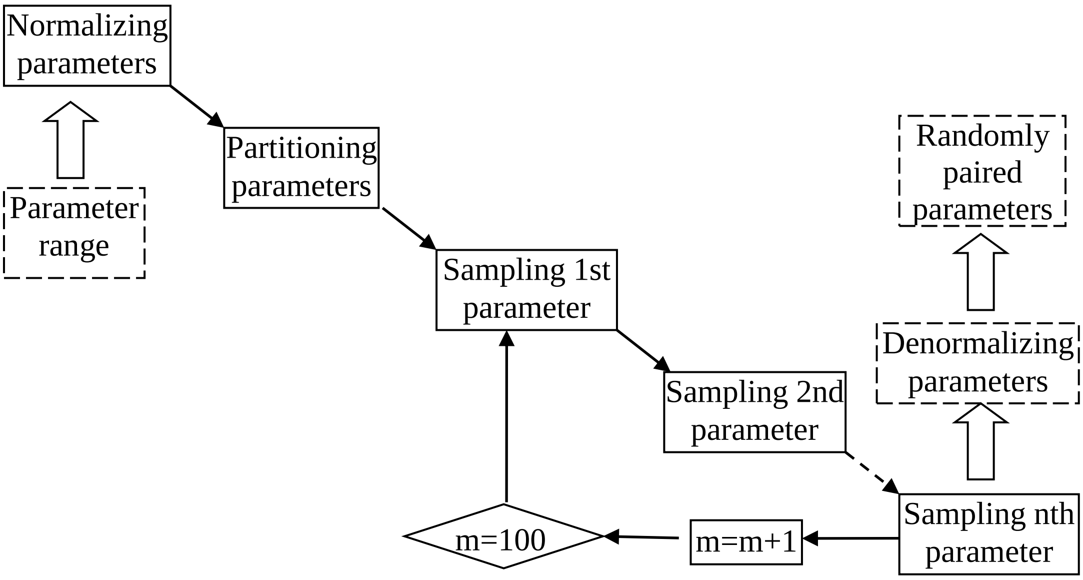

Figure 7-32 LHS flow chart

It is still possible to get localized database since the sampling progress is actually random. Thus an extended LHS [7-44] method is proposed, in which the spatial distance of sampling points is monitored. In this chapter, the distance of sampling points is calculated by

$$d_{LHS} = \sqrt{(s_1^i - s_1^j)^2 + (n_1^i - n_1^j)^2 + (s_2^i - s_2^j)^2 + (n_2^i - n_2^j)^2} \quad 7\text{-}10$$

where s_1^i, s_1^j, n_1^i, n_1^j, s_2^i, s_2^j, n_2^i and n_2^j are weld zone and HAZ material parameters for any points i and j, 1<=i<=100, 1<=j<=100 and 1!=j.

The LHS algorithm is run by 20 times and the run with biggest minimum distance is selected.

The generated 100 material parameter vectors are then assigned to the FEM templates separately to calculate corresponding punch force vectors. Thus a database containing 100 pairs of material parameter vectors and punch force vectors is prepared. These vectors are used as output vectors and input vectors to train the neural network. To validate the effectiveness of the trained neural network, two material parameter vectors, whose value are in the definition range of the database but not identical to any vector in the database, are designed and the corresponding punch force vectors are calculated via FEM. Since the material parameters are not identical to any in the database, the corresponding force vectors could act as virtually measured force vectors in physical experiment. The last step is to use the virtually measured force vectors to predict corresponding material parameter vectors and compare them with the designed material parameter for validation of the capability of small punch beam test in identifying material property distribution.

The range of n and yield stress are 5 to 15 and 150MPa to 300 MPa separately, while the yield offset is defined as 0.2%. Details of the neural network model and its implementation can be found in [7-57].

7.3.2 Results

Figure 7-33 shows the distribution of material parameters from the training database. The pairs of material parameters are numbered sequentially from 1 to 100 and every parameter is normalized to the same range between 0 and 1 by linear matching from their definition range. This figure indicates that material parameters are evenly distributed between 0 and 1 with each grid containing 40 different values.

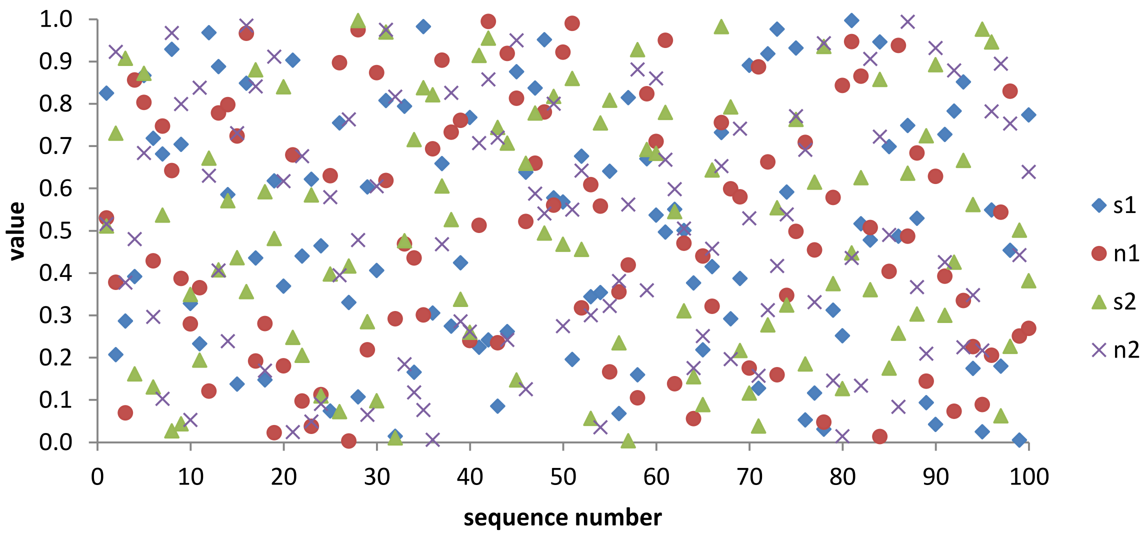

Figure 7-33 Distribution of normalized material parameters in training database

The training takes 82 iterations and the performance MSE (mean square error) reaches 4.95e-4 which is a little smaller than the goal 5e-4, as shown in Figure 7-34.

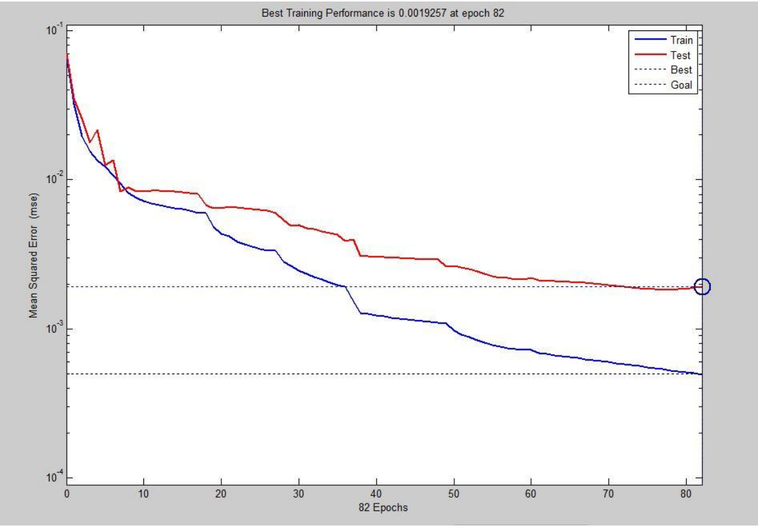

Figure 7-34 Training progress of BP neural network

From Figure 7-35 with combination of Figure 7-34, it can be observed that the trained neural network is very close to the relationship between F-U curve and material parameters.

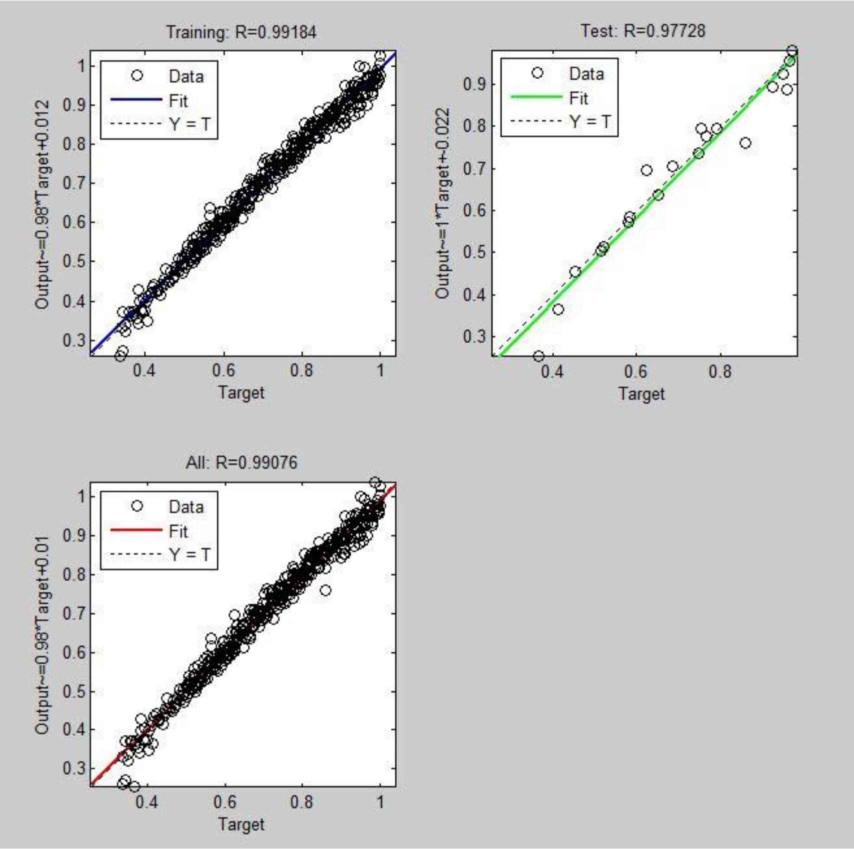

Figure 7-35 Training state of BP neural network

The predicted material parameters are 251.22 MPa, 11.2 and 218.87 MPa, 10.16. Strain stress curves for the virtual experiment specimen and predicted material model are compared in Figure 7-36 and it is found that they are very close to each other.

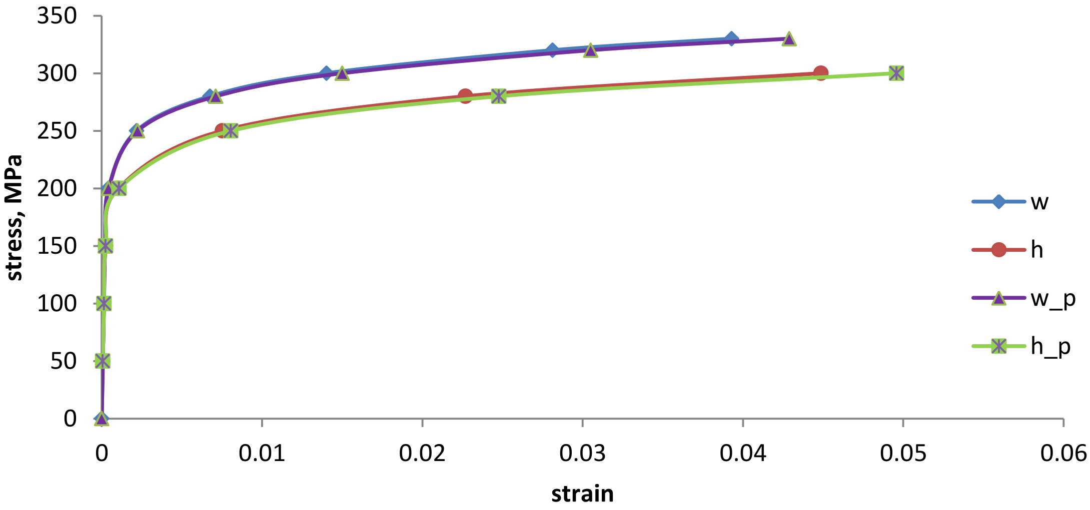

Figure 7-36 Material properties comparison of virtual specimen and predicted specimen

w: virtual NZ, h: virtual HAZ, w_p: predicted NZ, h_p: predicted HAZ

The corresponding load-displacement curve is also compared in Figure 7-37. Obviously, the F-U curve predicted by neural network algorithm is very close to the virtual experiment and the relative error is less than 3%.

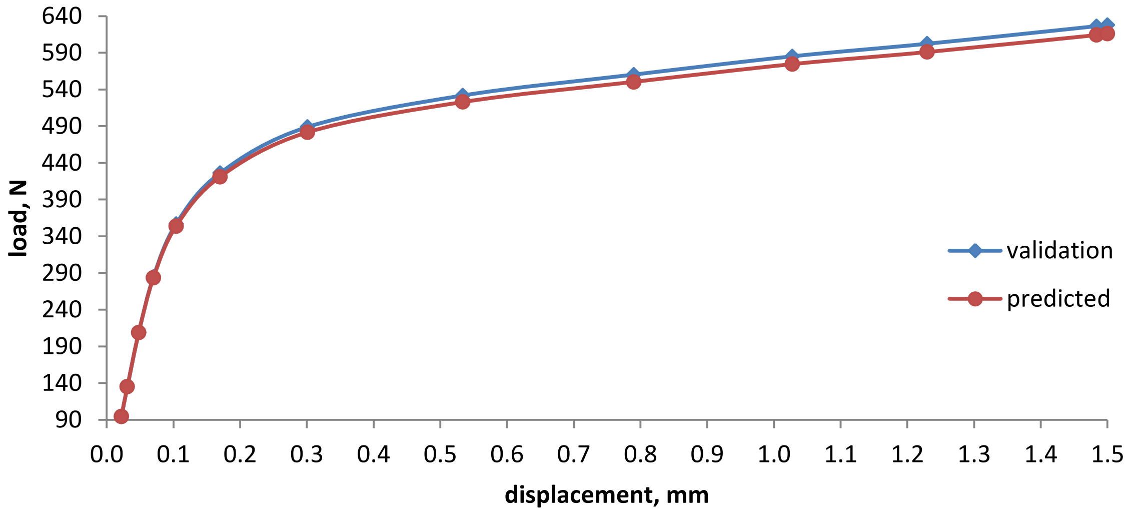

Figure 7-37 Comparison of virtual experiment and predicted load displacement curves

7.3.3 Discussion

One of the practical issues is to determine the size and location of different zones for SPBT specimen. Usually material properties are determined by microstructure and texture, such as grain size, precipitation size and volume fraction. The microstructure and texture can be observed by optical microscope and scan electron microscope etc. For a 2 mm wide and 2 mm thick specimen, it is reasonable to determine the distribution along width direction and thickness direction by observing microstructure of the cross sections as shown in Figure 7-38. The shape of different zones can be determined by linking the two cross sections.

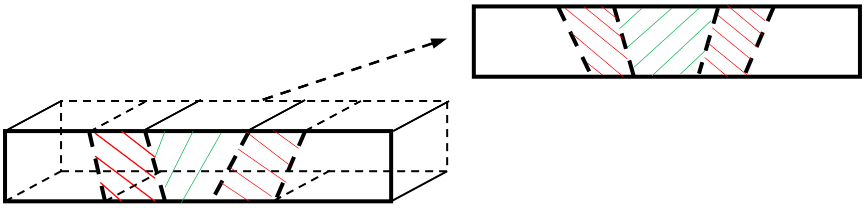

Figure 7-38 Size and location determination for NZ and HAZ

The results of section 7.3.1 indicate that the small punch test is applicable to identify material property distribution of longitudinal direction. For practical application, there are always errors between the physical test and the numerical model. Therefore, it is necessary to consider the factors that might influence load displacement curve and evaluate the significances.

Here, the precision of height for specimen and precision of span for the tool system are considered. For such a thin specimen, it is very common that the thickness along longitudinal direction is not uniform. For the tool system, the precision of span is significant.

The height of specimen and span are set to vary at 10% amplitude and the results are shown in Figure 7-39 and Figure 7-40. It is observed from Figure 7-39 that the load displacement curve is more sensitive to height variation, while the load displacement curves with the same amplitude variation of span are closer to the reference curve. Figure 7-40 is the relative error for load force at different displacement and it indicates that the relative error in elastic deformation zone is the biggest, so load displacement curve in elastic deformation zone could be used to calibrate the numerical model.

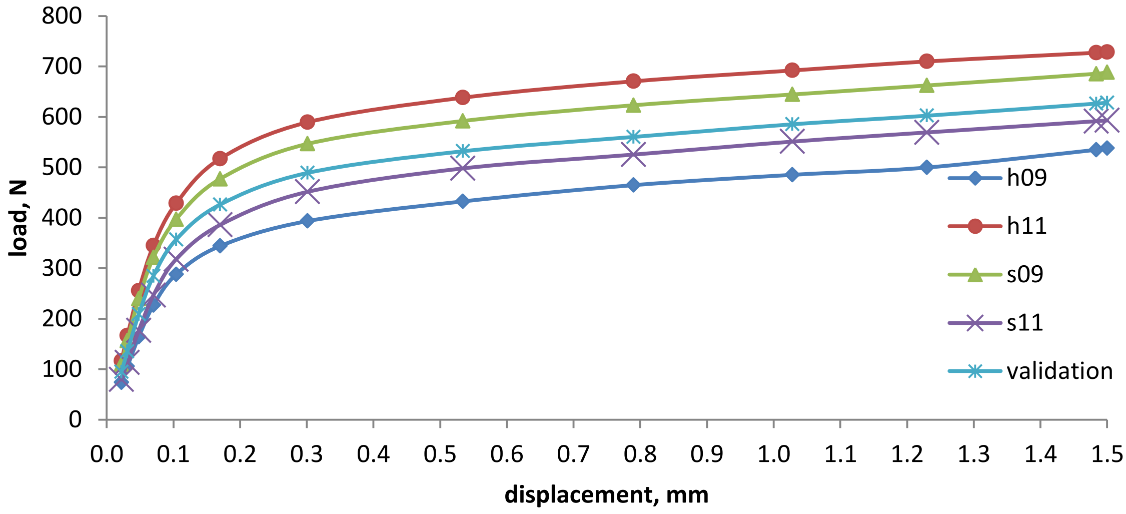

Figure 7-39 Load displacement variation for error analysis

h09: 90% of virtual specimen height, h11: 110% of virtual specimen height

s09: 90% of virtual specimen span, s11: 110% of virtual specimen span

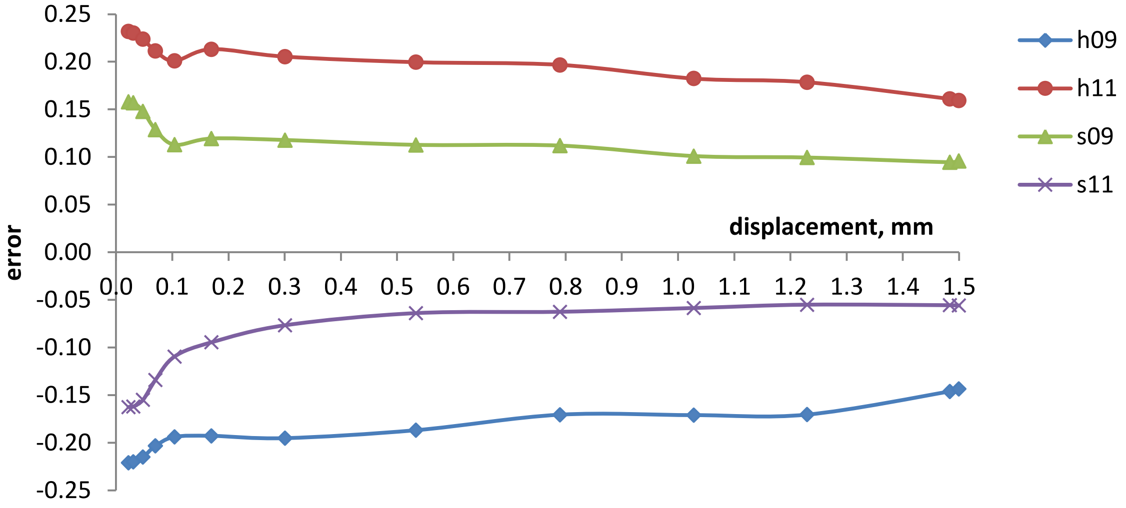

Figure 7-40 Load error variation with displacement for error analysis

h09: 90% of virtual specimen height, h11: 110% of virtual specimen height

s09: 90% of virtual specimen span, s11: 110% of virtual specimen span

7.4 References

[7-1] Manahan, MP, Argon, AS, Harling OK. The development of miniaturized disk bend test for the determination of postirradiation mechanical properties. J. of Nuclear Materials 1981: 103&104:1545-1550.

[7-2] Patrick Egan, Maurice P, Whelan, Fereydoun Lakestani, Michael J Connelly. The small punch test: An approach to solve the inverse problem by deformation shaper and finite element optimization. Computational Materials Science 2007:40: 33-39.

[7-3] J Isselin, A Iost, J Golek, D Najjar, M Bigerelle. Assessment of the conbstitutive law by inverse methodology: The small punch test and hardness. Journal of nuclear Materials 2006: 352:97-106.

[7-4] Steven M Kurtz, Jude R Foulds, Charles W Jewett, Sanjeev Srivastav, Avram A Edidin. Validation of a the small punch testing technique to characterize the mechanical behaviour of ultra-high-molecular-weight polyethylene. Biomaterials 1997: 18: 1659-1663.

[7-5] Karthik V, Visweswaran P, Vijayraghavan A, Kasiviswanathan KV, Baldev Raj. Tensile-shear correlations obtained from shear punch test technique using a modified experimental approach. Journal of Nuclear Materials 2009:393(3):425-432.

[7-6] Karel Milicka, Ferdonand Dobes. The small punch testing of P91 steel. International Journal of Pressure Vessels and Piping 2006:83: 625-634.

[7-7] Ken-ichi Kobayashi, Masaaki Tabuchi, Gavin C Stratford. Creep Rupture life of welding components in P92 Ferritic steel using small punch creep test. Metallurgical Journal 2010: LXIII: 54-58.

[7-8] DT Blagoeva, RC Hurst. Application of the CEN (European Committee for Standardization) small punch creep testing code of practice to a representative repair welded P91 pipe. Materials Science and Engineering 2009: A 510-511: 219-223.

[7-9] Mao X, Takahashi H. Development of a further-miniaturized specimen of 3 mm diameter for tem disk the small punch tests. J. of Nuclear Material 1987:150:44-52.

[7-10] J Foulds, R Viswanathan. The small punch testing for Determining the Material Toughness of Low Alloy Steel Components in Service. Journal of Engineering Material Technology 1994:116(4):457.

[7-11] LI Yingzhi, HURST Roger, MATOCHA Karel, CIZEK Peter, BLAGOEVA Darina. New Approach to Determine Fracture Toughness from the small punch test. Metallurgical Journal 2010: LXIII: 94-102.

[7-12] Takahashi H, Shoji T, Mao X, Hamaguchi Y, Misawa T, Saito M Oku T, Kodaira T, Fukaya, K Nishi H, Suzuki M. Recommended practice for small punch (SP) testing of metallic Materials, JAERI-M, 88-172, Sept. 1988.

[7-13] CEN, The small punch test Method for Metallic Materials. Part A: A Code of Practice for Small Punch Creep, 2005

[7-14] CEN, The small punch test Method for Metallic Materials. Part B: A Code of Practice for The small punch testing for Tensile and Fracture Behavior, 2006.

[7-15] ASTM F2183 - 02(2008) Standard Test Method for The small punch testing of Ultra-High Molecular Weight Polyethylene Used in Surgical Implants.

[7-16] Guan Kai-shu, Wang Zhi-wen, Xu Tong, Shou Bi-nan. Development of The small punch test in China. Czech Metallurgical Journal 2010: LXIII: 69-73.

[7-17] W. Pan, Jim Boyle, Mohd Ramlan, Craig Dun, Mohd Ismail, Kenji Hakoda. selected for Czech Metallurgical Journal 2010: LXIII:174-179.

[7-18] Sehgal DK, Husain A, Pandey RK. The Rectangular Shaped Miniature Specimen to study the Mechanical Behavior of Materials. In: Mechanical and Electronics Engineering (ICMEE) , 2nd International Conference, Vol.1, 196 -199, Kyoto, 2010.

[7-19] Abendroth M, Kuna M. Determination of deformation and failure properties of ductile materials by means of the small punch test and neural networks. Computational Materials Science 2003:28: 633-644.

[7-20] CF Castro, CAC Antonio, LC Sousa. Optimisation of shape and process parameters in metal forging using genetic algorithms. J. of Materials Processing Technology 2004:146:356-364.

[7-21] http://wenku.baidu.com/view/b70b8a5c3b3567ec102d8a44.html, access on 3rd Oct. 2010.

[7-22] Manahan, MP, Argon, AS, Harling OK. The development of miniaturized disk bend test for the determination of postirradiation mechanical properties. *J. Null. Mater.* 1981; 104:1545-1550.

[7-23] Krishna K.Dwivedi, Krishna K.Pathak, *et al*, http://scholarsresearchlibrary.com/aasr-vol2-iss6/AASR-2010-2-6-211-218.pdf, Influence of material parameters on the small punch test using curved specimens

[7-24] Pan W, Boyle J, Ramlan M, Dun C, Ismail M, Hakoda K. Material plastic properties characterization using a generic algorithm and FEM modeling of the plane-strain the small punch test. 2010. Paper presented at SPT Conference 2010, Ostrava, Czech Republic.

[7-25] Sehgal DK, Husain A, Pandey RK. The Rectangular Shaped Miniature Specimen to study the Mechanical Behavior of Materials. In: Mechanical and Electronics Engineering (ICMEE) , 2nd International Conference, Vol.1, 196 -199, Kyoto, 2010.

[7-26] Xingguo Zhou, Wenke Pan and Donald Mackenzie, Material plastic properties characterization by coupling experimental and numerical analysis of small punch beam tests, Computers and Structures: HWU special issue, 2012

[7-27] Abendroth, M. and Kuna, M. Determination of Ductile Material Properties by Means of the small punch test and Neural Networks. *Advanced Engineering Materials* 2004; 6: 536–540.

[7-28] Abendroth M, Kuna M. Identification of ductile damage and fracture parameters from the small punch test using neural networks, *Engineering Fracture Mechanics*, 2006; V73: 710-725.

[7-29] Abendroth M, Kuna M, Determination of deformation and failure properties of ductile materials by means of the small punch test and neural networks. *Computational Materials Science* 2003; 28: 633-644.

[7-30] Documentation of MATLAB 2007b, neural network toolbox user's guide

[7-31] Neural network design, Martin T. Hagan, Howard B. Demuth, Mark H. Beale, 2002, ISBN: 0-9717321-0-8

[7-32] Rumelhart, David E.; Hinton, Geoffrey E., Williams, Ronald J. Learning representations by back-propagating errors. Nature 323 1986; 6088: 533–536.

[7-33] P. Werbos. Beyond Regression: New Tools for Prediction and Analysis in the Behavioral Sciences. PhD thesis, Harvard University, Cambridge, MA, 1974.

[7-34] Thomos Poppe et al., Estimating material properties for process optimization, Proceedings of the ICANN-93, Gielen S. and Kappen B. (eds), Springer, Heidelberg, pp. 795-798

[7-35] Charalambous, C., "Conjugate gradient algorithm for efficient training of artificial neural networks," Circuits, Devices and Systems, IEE Proceedings G , vol.139, no.3, pp.301-310, Jun 1992

[7-36] Hagan, M.T.; Menhaj, M.B.; , "Training feedforward networks with the Marquardt algorithm," Neural Networks, IEEE Transactions on , vol.5, no.6, pp.989-993, Nov 1994

[7-37] http://www.inb.uni-luebeck.de/publikationen/pdfs/MaPo94.pdf, accessed on 2012-04-26

[7-38] http://wenku.baidu.com/view/6e75648302d276a200292e4d.html,accessed on 2012-04-26, accessed on 2012-04-06

[7-39] W.P. Achbach, R.J. Faver and W.S. Hyler, Materials property design for metals part IV, p44, Oct. 1957, Battelle Memorial Institute

[7-40] Atlas of Stress-Strain Curves, second edition, ASM International, 2002

[7-41] C. Rodríguez, J. García Cabezas, E. Cárdenas, F. J. Belzunce, and C. Betegón. Mechanical properties characterization of heat-affected zone using the small punch test. Welding Journal (Miami, Fla), 88(9), 2009.

[7-42] Jerome Isselin, Tetsuo Shoji, Crack initiation resistance characterization of weld by small-punch test in boiling water reactor environment, International Journal of Pressure Vessels and Piping, Volumes 93–94, May–June 2012, Pages 22-28

[7-43] D. Blagoeva, Y.Z. Li, R.C. Hurst, Qualification of P91 welds through Small Punch creep testing, Journal of Nuclear Materials, Volume 409, Issue 2, 15 February 2011, Pages 124-130

[7-44] Fasihul M. Alam, Ken R. McNaught, Trevor J. Ringrose, A comparison of experimental designs in the development of a neural network simulation metamodel, Simulation Modelling Practice and Theory, Volume 12, Issues 7–8, November 2004, Pages 559-578

[7-45] Zhao, M. Cui, W.-c., Application of the optimal Latin hypercube design and radial basis function network to collaborative optimization, JOURNAL OF MARINE

SCIENCE AND APPLICATION, Volume 6, numb 3, 2007, pages 24-32, ISSN 1671-9433

[7-46] Atlas of Stress-Strain Curves, second edition, ASM International, 2002

[7-47] Dam, E.R. van & Rennen, G. & Husslage, B.G.M.,Bounds for maximin Latin hypercube designs, Operations Research, Volume 57, issue 3, May-June 2009, pages 595-608

[7-48] Coit D W, Jackson B T, Smith A E, Static neural network process models: consideration and case studies, International Journal of Production Research, Nov 1998, Volume: 36 Issue: 11 pp.2953-2967

[7-49] C.J. Sallaberry, J.C. Helton, S.C. Hora, Extension of Latin hypercube samples with correlated variables, Reliability Engineering & System Safety, Volume 93, Issue 7, July 2008, Pages 1047-1059

[7-50] Jung Hwan Lee, Young-Don Ko and Ilgu Yun, Comparison of Latin Hypercube Sampling and Simple Random Sampling Applied to Neural Network Modeling of HfO2 Thin Film Fabrication, Transactions on Electrical and Electronic Materials, Volume 7, issue 4, August 2006, page 210-214

[7-51] C. Schmitt, P. Lipinski, Modelling of the elasto-plastic behavior of rolled aluminium alloy for forming applications, Journal of Materials Processing Technology, Volume 74, Issues 1–3, February 1998, Pages 14-22

[7-52] C. Cervellera, A. Wen, and V. Chen. Neural network and regression spline value function approximations for stochastic dynamic programming. Computers & Operations Research, 34(1):70–90, January 2007

[7-53] Jeong-Soo Park, Optimal Latin-hypercube designs for computer experiments, Journal of Statistical Planning and Inference, Volume 39, Issue 1, 1 April 1994, Pages 95-111

[7-54] M. Mohri, H. Odagiri, T. Satake, T. Yamashina, H. Oikawa, Kanedo, Surface characterization of aluminum alloy 2017 as a vacuum vessel for nuclear fusion devices, Journal of Nuclear Materials, Volume 122, Issues 1–3, 2 May 1984, Pages 164-168

[7-55] Lebedev, V. M. Lebedev, V. T. Ivanova, I. N. Orlov, S. P. Orlova, D. N., Structure of aluminum alloys irradiated with reactor neutrons, PHYSICS OF THE

SOLID STATE C/C OF FIZIKA TVERDOGO TELA, 2010, VOL 52; NUMBER 5, pages 996-999

[7-56] Xingguo Zhou, Wenke Pan and Donald Mackenzie, Material plastic properties characterization by coupling experimental and numerical analysis of small punch beam tests, Computers and Structures: HWU special issue, 2012

[7-57] SPBT on welded material-JMDA

8 Conclusions

The research reported in this thesis includes development of a range of numerical models (thermal, thermal-stress and thermal-stress-microstructure models) for the FSW process, application of genetic algorithms to implement an automatic procedure to identify the model parameters, proposed new discontinuous cooling and distributed cooling methods to optimize residual stress in welds and development of the small punch beam test method to characterize the material properties of base metal and welded metal. The following conclusions are drawn from the research outcomes presented:

A. The proposed automatic procedure for identifying FSW model parameters was successfully implemented. The procedure coupled experimentally measured temperature history data and FEM analysis, introducing the genetic algorithm to find the values of unknown model parameters. It took advantages of HPC and the identification progress was accelerated by parallel computation. By using the predicted parameters from one set of experiment results, the temperature distribution at other points were predicted and in good agreement with the experimental results.

B. The discontinuous cooling method is an effective method to reduce the residual stress for FSW. Analytic and numerical analysis indicated the welding temperature was improved compared to the conventional active cooling method. Numerical analysis results demonstrated that the residual stress with discontinuous cooling method is lower than that in the conventional active cooling method. It was also shown the welding temperature and residual stress could be further improved by increasing the cooling rate in discontinuous cooling method, while keep the time-averaged cooling media flow unchanged. The effectiveness of discontinuous cooling method was much higher than conventional active cooling method.

C. The distributed cooling method provided another effective method for reducing the residual stress for friction stir butt welding. To make the distributed cooling more applicable, the optimization region and associated identification procedure were proposed and discussed. Numerical simulation results optimization in the proper region could increase the welding temperature and the residual stress could be also reduced. The balance between the welding temperature and the residual stress was discussed and the trade-off ratio for the distributed cooling is higher than conventional active cooling.

D. The computational efficient multi-physical model was successfully built and the discontinuous cooling was found to be positive to microstructure evolution with respect to hardness/strength. A novel reference based microstructure model is proposed, which predicts reference micro hardness of interest zone by analyzing temperature history data of each material point and the reference temperature history curve. This model successfully predicts the size of interest zone, the distribution among the interest zone and the trend of micro hardness variation when welding speed varies and discontinuous active cooling is applied. The computational time cost was also reduced to a level feasible for optimization by analysis. In addition, Introducing discontinuous into friction stir welding effectively lowers the residual stress and interface width, and the micro hardness in the interface (TMAZ) zone increases with increasing cooling duty.

E. The small punch beam test method was developed for characterizing mechanical properties using miniaturized beam shape specimen. The tool system was designed and manufactured, primary test results presented good consistency with load-displacement curves. The genetic algorithm was introduced to characterize the plastic properties of base material aluminum alloy 2024-T3 using simplified multi-linear hardening model. The predicted numerical load-displacement was in good agreement with the experimental data.

F. The small punch beam test was also applied to characterize mechanical properties of welded material. Consistence of the testing system was also observed in the load-displacement curves. It was found by properly sampling specimen, influence of the mechanical properties of base material is ignorable when characterizing properties of the welded zone, such it was unnecessary to take the properties of base material as a prior, which made the characterizing procedure more convenient. Average plastic properties of the welded zone were successfully identified with the artificial neural network algorithm.

G. The applicability of the small punch beam test to characterize mechanical property difference of different zones in a single test was investigated. The proper range of load displacement for characterizing plastic properties is determined by analysing the sensitivity of material model parameters. The error between virtual experiment material properties and the predicted material properties are very close, and the predicted load displacement curve is in good agreement with virtual experiment. Error factors for SPBT were investigated and it was found that the load displacement curve is sensitive to both specimen thickness and tool's span. It was necessary to precisely measure the thickness and tool's span to minimize the error between numerical model and physical tests.

In the future, other issues might be further researched. A cooling nozzle capable of jetting liquid carbon dioxide continuously and periodically could be designed and made to build an experimental platform. The effect of discontinuous cooling method and conventional active cooling method could be compared experimentally and the underlying mechanics of residual stress could be further revealed.